Spring 2003

Numerical Studies on Supersonic Mixing and Combustion Phenomena

Tarek M. Abdel-Salam
Old Dominion University

NUMERICAL STUDIES ON SUPERSONIC MIXING AND COMBUSTION PHENOMENA

by

Tarek M. Abdel-Salam
B.S. July 1988, Cairo University, Egypt
M.S. March 1994, Cairo University, Egypt

A Dissertation Submitted to the Faculty of
Old Dominion University in Partial Fulfilment of the
Requirement for the Degree of

DOCTOR OF PHILOSOPHY

MECHANICAL ENGINEERING

OLD DOMINION UNIVERSITY
May 2003

Approved by:

Surendra N. Tiwari (Director)

Tajeldin O. Mohieldin (Co-Director)

Sushil K. Chaturvedi (Member)

Arthur C. Taylor, III (Member)

ABSTRACT

NUMERICAL STUDIES ON SUPERSONIC MIXING AND COMBUSTION PHENOMENA

Tarek M. Abdel-Salam
Old Dominion University
Director: Dr. Surendra N. Tiwari

A numerical study is conducted to investigate the mixing, combustion, and flow characteristics of different scramjet-combustor configurations. Three-dimensional models for the combustors have been used. Numerical results are obtained using a finite volume computational fluid dynamics (CFD) code with unstructured grids with sizes between 200,000 and 400,000 cells.

In the first part of the current study, the effects of the side angle of the fuel injectors in both mixing and combustion processes are investigated. Raised (compression) and relieved (expansion) wall-mounted ramps are used with side angles of 0 (unswept), 5, and 10 degrees. Results are obtained for nonreacting flows as well as for reacting flows. Hydrogen is used as the fuel in all reacting cases. It is noted that the side angle highly affects the mixing process. The results show clearly that increasing the side angle of the ramps leads to better mixing and further increase of the angle will slightly improve the mixing rate.

In the second part, two dual-mode scramjet-combustor models are investigated. In the first model, fuel is injected through a single unswept wall-mounted ramp parallel to the airstream. In the second model, fuel is injected behind a rearward facing step normal to the airstream. The effects of the combustor length, the equivalence ratio, the number, and the arrangements of the fuel injectors are investigated. Also, the effect of the initial

boundary layer thickness is studied. Results show that improved combustion efficiency is obtained by increasing the length of the combustor. For the same amount of injected fuel, increasing the number of injectors improves the combustion efficiency. Asymmetric flow and significant upstream interaction are seen in the isolator section of the second model when using initial boundary layer at the inlets. Furthermore, high degree of upstream interaction is obtained by increasing the number of injectors.

Co-Director of Advisory Committee: Dr. Tajeldin O. Mohieldin

ACKNOWLEDGEMENTS

I express my appreciation and gratitude to the faculty and staff members of the Mechanical Engineering Department at Old Dominion University for their guidance and support.

I would like to express my intimate appreciation, sincere indebtedness, gratitude, and deep thanks to my advisor, Dr. Surendra N. Tiwari, Eminent Professor of Mechanical Engineering, for his continuous guidance, helpful advice, and sincere supervision which guided me throughout the period of this research and for his effort that helped in bringing the present work to its final form.

I deeply touched by the kind support, care, and encouragement of Dr. Sushil K. Chaturvedi, Professor and Chair of the Mechanical Engineering Department. I express my thanks for his sincere guidance which greatly aided the progress and completion of this work. I would also like to acknowledge Dr. Tajeldin O. Mohieldin, Professor of Engineering Technology, for his assistance and guidance during this research and the course of my graduate studies. My appreciation extends to Dr. Arthur Taylor, Associate Professor of Mechanical Engineering, who served as a member of my dissertation committee.

Finally, I cannot forget to pray to Allah for giving me a wonderful family. I would like to acknowledge my father, Prof. Mohamed Abdel-Salam, and my mother, Prof. Ragaa Osman, who have always supported and encouraged me and who have done thousands of other things to make my life better. I express my deep thanks to my wife, Nehad, and my daughters, Rana and Menna, for their support during this research. And

last but not least, I thank my brothers, Dr. Omar and Hisham, for their help and encouragement.

This work was supported in part by the Old Dominion University's Institute for Scientific and Educational Technology (ISET) through NASA Langley Research Center, Cooperative Agreements NCC1-231 and NCC1-349. The Cooperative Agreement was monitored by Dr. Samuel E. Massenberg, Director, Office of Education.

TABLE OF CONTENTS

Page

LIST OF TABLES

LIST OF FIGURES

Page

Page

Page

Page

LIST OF SYMBOLS

A	area
C_p	specific heat capacity
d	jet diameter
F_x	streamwise thrust
g_i	external force
h	step height; also helicity
$\overline{h}$	mass-averaged helicity
h_j^o	enthalpy of formation of species j
H	ramp height; also total enthalpy
k	thermal conductivity
K	turbulent kinetic energy
L_c	combustor length
m_j	mass fraction of species j
$\dot{m}^o$	mass flow rate
M	molecular weight; also Mach number
$\overline{M}$	mass-averaged Mach number
P	pressure
$\overline{P}$	mass-averaged pressure
R	universal gas constant
R_j	rate of species generation
S_{ij}	mean strain-rate tensor

t	time
T	temperature
u_i	velocity components(u,v,w)
U	streamwise velocity
X	axial distance from centerline
Y	lateral distance from centerline
Z	vertical distance from surface

Greek Symbols

δ	boundary layer thickness
δ_{ij}	Kronecker delta
ε	dissipation rate
ζ	vorticity magnitude
η_c	combustion efficiency
η_{cl}	local combustion efficiency
μ	dynamic viscosity
ν	kinematic viscosity
ρ	density
σ_k	turbulent Prandtl number
τ_{ij}	specific Reynolds-stresses tensor
φ_l	local equivalence ratio
ϕ	total equivalence ratio
χ	mole fraction

Subscripts

i	inlet
j	jet
o	total condition
s	static condition
t	turbulent

Chapter I

INTRODUCTION

1.1 Motivation

In the past several years, there has been a great deal of research toward the development of airbreathing hypersonic vehicles. Airbreathers are engines that use the air through which the vehicle is flying both as a source of oxidizer for the fuel in the combustion process and as a working fluid for generating power or thrust [1]*. The ramjet engines are appropriate to supersonic speed flights, where the air becomes sufficiently compressed to overcome the need of mechanical compression. If flight speed is so high that fuel combustion must occur supersonically, the engine is called a scramjet, for supersonic combustion ramjet. Hypersonic flight utilizing airbreathing propulsion requires the development of scramjet technology. Scramjet propulsion differs substantially from lower speed concepts in that the propulsion flow path is highly integrated with the vehicle external aerodynamics. The flow is compressed under the vehicle forebody from the nose of the aircraft and though the inlet to the combustor, and expanded through the nozzle to provide the overall performance. In the combustor, fuel is injected at sonic or supersonic speeds into a shock dominated supersonic airstream where it mixes and burns [2]. A critical element in the design of the scramjet engine is detailed understanding of the complex flow field present in different regions of the system over a range of operating conditions. Constraints on system size and weight have led to the need to improve technology for analyzing and designing such systems. One of the

* The *AIAA Journal* format is followed in this dissertation.

characteristics of hypersonic airbreathing vehicles is that the combustor length remains virtually constant at 2-6 ft for most hypersonic vehicles, suggesting that the supersonic combustion processes are inherently mixing-limited. In order to meet these requirements, improved combustion systems are required. There is still serious question as to whether or not stable supersonic combustion is possible over the range of expected operating conditions. Recently, the National Aeronautics and Space Administration (NASA) initiated several hypersonic technology programs. One of these programs is the Hyper-X program. The program focus is to extend scramjet powered vehicle technology to flight, elevating as much as technology as possible, and validating, in flight, the design systems, computational fluid dynamics (CFD), analytical, and experimental methods required for this complex multidisciplinary problem [3]. The scramjet offers a method of propulsion, which, in principle, is able to operate up to any flight speed and, in fact, seems likely to be effective for flight speeds approaching 5 km/s. A considerable amount of research has been done on the components of scramjets, with the inlet, the combustion chamber, and the thrust nozzle all receiving attention. The components have also been coupled together to make a complete scramjet engine. Various forms of this type of engine have been subjected to experimental scrutiny [4]. With increasing combustor Mach number, the degree of fuel-air mixing that can be achieved through the natural convective and diffusive processes is reduced, leading to an overall decrease in combustion efficiency and thrust. Because of these difficulties, attention turned to the development of techniques for enhancing the rate of fuel-air mixing in the combustor. Numerical methods must also be used to improve the understanding of fuel-air mixing. Studies are currently underway to explore the physics of mixing. Chemical reaction has also been

included in some of those studies, but such studies are limited by the large number of spatial scales that are present and must be resolved [5].

The ramjet engines were designed for flights in the Mach number range 3-5, while the scramjet engines are designed to be suitable for flight Mach number over 6. For these reasons, in order to avoid having to carry two engines for ramjet and scramjet modes in the same vehicle, the concept of dual-mode combustion has been introduced in the late 1960's [6]. The dual-mode scramjet engine should be able to operate in both subsonic combustion as well as supersonic combustion modes. In the dual-mode engine a constant area diffuser called isolator is placed upstream the combustor to isolate the inlet flowfield from any combustor-generated upstream interaction in order to prevent the inlet unstart. A constant area duct combustor follows the isolator. Fuel can be injected by different methods inside the combustor. The heat release due to combustion eventually expands the flow back to sonic conditions (thermally choked condition). An expanding duct is placed after the combustor in order to maintain flow expansion to supersonic conditions and delay the formation of thermal choke. In recent years, dual-mode combustion has received attention because of its application in particular flights. Dual-mode combustion, which is the primary motivation of this study, is a very challenging problem for computational fluid dynamics (CFD). This is due to the nature of the highly turbulent flow field associated with the extensive upstream interaction, and the downstream mixing and combustion at low Mach number. Moreover, the mixed supersonic and subsonic regions of the combustor require large sections of the flow to be solved simultaneously, forcing the use of efficient CFD codes, and suitable turbulence and combustion models.

1.2 Overview of Research

The method of fuel injection highly affects the efficiency of scramject engines. One objective of this research is to numerically investigate both supersonic mixing and combustion processes in scramjet engines. A detailed investigation is performed on the ramp fuel injectors where fuel is injected parallel to the airstream. Different ramp injectors with different side angles are investigated. In addition to supersonic combustion, dual-mode combustion is among one of the newly investigated areas. Research in this area has been relatively scarce; more research is required to study the complicated flow field inside the dual-mode combustors. The second part of this research attempts to fill this void in the literature by investigating the flowfield of the dual-mode scramjet combustors. Two different configurations with parallel and transverse fuel injectors are studied.

A comprehensive review of the relevant previous work is presented in Chap. 2. The chapter is divided into two sections. The first section reviews the previous research done in the area of supersonic mixing and combustion with special focus on injection and ramp fuel injectors. The second section of Chap. 2 reviews the previous work in the area of dual-mode combustion. Chapter 3 describes the physical models selected for the current study, governing equations, and numerical procedures. Numerical results are presented and discussed in Chaps. 4 and 5. Chapter 4 includes results of the Mach 2 scramjet combustor. Effects of grid size and turbulence modeling and comparisons with experimental work are presented in this chapter followed by the effects of ramp side angle on mixing and combustion for raised and relieved ramps. Chapter 5 presents results for dual-mode combustion. Results are presented for two combustor configurations.

Finally, some concluding remarks and recommendations for future work are presented in Chap. 6.

Chapter II

LITERATURE SURVEY

In this chapter, the relevant literature pertaining to supersonic mixing and combustion in scramjet engines and dual-mode combustion is reviewed. In the first section, only research treating supersonic mixing and combustion in pure scramjet engines is presented. Special attention is paid to the perpendicular fuel injectors and the wall-mounted ramps as they are the two types of injectors that are used in the current study. In the second section, relevant work done in the area of dual-mode combustion is reviewed.

2.1 Supersonic Mixing and Combustion

A significant amount of recent high-speed combustion research has been directed towards the optimization of the scramjet combustor, and in particular the efficiency of fuel-air mixing and reaction taking place in the engine. To a large extent, for a given condition, the net heat release achieved in a scramjet combustor is driven by the efficiency and effectiveness of the fuel injection [7]. Various injection schemes of different geometrical configurations and flow conditions have been investigated in the past two decades. Selected methods that have been used to enhance the mixing process in the scramjet engines are summarized and reported in Ref. 8.

2.1.1 Transverse Fuel Injection

The earliest scramjet combustor design evolved normal injection of fuel into supersonic airstream. Several investigations have visualized turbulent structures in a transverse jet using either planar Mie scattering or planar laser-induced fluorescence.

Lee et al. [9] experimentally investigated the normal injection. Their work showed that the injectant produces a detached shock wave upstream of the fuel jet giving rise to separated air zones both upstream and downstream of the jet. This translates to significant losses in total pressure and consequently scramjet cycle efficiency. However, combustion can be achieved within a very short length from injection since the separation zone works as flame holder. More experimental studies of transverse hydrogen injection in supersonic airflow were conducted in [10-13]. All of these studies produced instantaneous images that showed large-scale turbulent structures. Experiments of Segal et al. [10] were performed to determine the combustion efficiency and the combustor-inlet interactions at low temperature, lean mixture operational end of a scramjet constant-area combustor model. Due to the constant area of the combustor and the low initial temperature, upstream interaction had occurred at a very low equivalence ratios. Results showed that most of the fuel was burned behind the step and around the jets which is the high recirculation region. Hermanson and Winter [11] reported that structures develop at the jet/freestream interface in a periodic manner and persist far downstream of the injector. Gruber et al. [12] found similar large-scale structures. VanLerberghe et al. [13] reported that significant instantaneous mixing occurs in the region downstream the barrel shock region and below the jet centerline. Also, the counter-rotating streamwise vortex pair in the jet plume plays an important role in the scalar mixing processes. Several studies [14-19] have attempted to investigate the effect of injector geometry and the use of hydrocarbon fuels on both supersonic mixing and combustion. In the present work one dual-mode combustor has been investigated with transverse fuel injection behind a rearward-facing step.

2.1.2 Parallel Fuel Injection

Mixing enhancement by axial vortices, either in the fuel stream or in the airstream, was investigated by many researchers in the past fifteen years. During this period of time, parallel injection techniques were studied experimentally and numerically. Parallel injection may be useful at high speeds to extract energy from hydrogen that has been used to cool the engine and the airframe of a hypersonic cruise vehicle.

Gutmark et al. [20] studied tapered slot jet experimentally in nonreacting and reacting flows. An axial vorticity is induced in the parallel-flow fuel jet. It includes inducing axial vorticity through secondary flows which arises when supersonic fuel flows through a converging tapered slot jet. This involves which feature an elliptic-to-conical duct transition just before sonic injection of the fuel into the parallel airstream.

One of the first experimental studies of wall-mounted ramps had been conducted by Northam et al. [21]. Experiments were conducted with swept and unswept raised ramps to explore the mixing enhancement in a scramjet combustor. In both configurations, hydrogen was injected at Mach 1.7 in the Mach 2.0 airstream. The injector ramps were designed to yield a deflected shock wave from the duct top wall such that it passed just downstream of the barrel shock of the fuel injector. Perpendicular fuel injectors were added downstream of the swept ramps to determine if the wake flow generated by the parallel injector, with no fuel injection, is effective in enhancing mixing. In addition, three-duct configurations of the combustor were tested. Results showed that the swept ramp injector provided good flame holding and enhanced mixing. Also, the calculated combustion efficiencies for the swept ramp injectors were found higher in comparison

with those achieved with the unswept ramp injectors. A series of numerical studies have been performed and compared with the results of this work.

Supersonic combustion research related to hypersonic airbreathing propulsion has been actively underway at NASA Langley Research Center (LaRC) since the mid 1960's. Rogers et al.[22] had reviewed the LaRC experimental supersonic combustion research efforts. At NASA Langley Research Center, Drummond et al. [23] studied numerically fuel-air mixing in a model generic supersonic combustor with the CFD code SPARK. Two ramp configurations were studied and were taken from Ref. 21. Only fuel-air mixing was considered during this study. A structured grid was used and compressed near the injector region. Results from this numerical study confirmed the experimental results of Northam et al.[21]. However, the predicted shock angle in both cases was lower than that measured in the experiment of Ref. 21. Riggins et al. [24] extended the preliminary non-reacting investigation of Drummond et al. [23] and investigated the reacting flow with a finite rate two-step combustion model for hydrogen. Comparison with the non-reacting solution showed that combustion has a small effect of increasing the fuel mixing which could be due to either high combustion induced pressure gradient or pressure-induced "lifting" of the fuel jet away from the wall and into the dominant shed vortex from the ramp.

A method for analyzing flow losses and thrust potential in supersonic combustors has been presented by Reggins and McClinton [25, 26]. The method used in Ref. 26 relies on a complete and consistent one-dimensional representation of a three-dimensional flowfield. All mass (including individual species mass), momentum, and energy fluxes were integrated from the three-dimensional solution and defined in the one-dimensional

equivalent flow. Both swept and unswept ramp injectors taken from Ref. 21 were investigated based on the reacting solutions. In addition to the ramp injectors, a thirty-degree downstream-directed flush wall fuel injectors has been analyzed. The wall jet displayed slightly higher thrust potential than the swept ramp at the end of the combustor, although the swept ramp was markedly more effective in the early stages of the combustor. In an extension to this work, Riggins et al. [27] investigated the injection strategies for high Mach number flow. Swept ramp fuel injector was used for Mach 13.5 and Mach 17 flights. The evolution and distribution of thrust potential were investigated in details in order to explain and visualize combustor performance.

Waitz et al. [28] experimentally tested the performance of countered wall fuel injectors. The effects of incoming boundary layer height, injector spacing, and injectant to freestream pressure and velocity ratios were investigated. Performance was judged in terms of mixing, loss generation, and jet penetration. Strong dependence on injectant to freestream pressure ratio was found. Also, it was found that the injector performance strongly depended on the displacement effect of the hypersonic boundary layer. In addition, the boundary layer varied with injector spacing.

Donohue et al. [29] numerically investigated the three-dimensional nonreacting supersonic flow field produced by three parallel fuel injection schemes. Preliminary experimental results were also presented. Among three configurations, the ramp generated vorticity was found to be considerably large.

An experimental work was conducted by Stouffer et al.[30] to study the effects of compression and expansion ramp fuel injector configuration on scramjet combustion and heat transfer. Both compression (raised) and expansion (relieved) swept wall-mounted

ramps were tested. Results showed that auto-ignition occurred for the compression ramp injectors and the fuel began to burn immediately downstream of the injectors. For tests with expansion ramps, a pilot was required to ignite the fuel, and the fuel did not burn for a distance of at least gaps downstream of injectors. Another experimental study followed this work was conducted by Stouffer and Northam [31]. Three ramp injector designs were evaluated: an unswept-compression ramp, a swept-compression ramp, and a swept-expansion ramp. In addition, normal injectors were used in combination with the unswept-ramp injectors. Similar results to that of the previous work were obtained concerning the method of ignition. With the normal injectors, the calculated combustion efficiencies and pressure integrals showed that the unswept compression ramp performed better than the two swept configurations.

A scramjet combustor, with swept ramp injectors, has been analyzed by Cox et al.[32], Eklund and Stouffer[33], and Baurle et al.[34]. The flowfield has been analyzed using a two-equation k-ω turbulence model. An assumed probability density function (PDF) model has been used to account for turbulence-chemistry interactions. Results showed that the use of the PDF did not yield any significant improvements.

Researchers at the University of Virginia have investigated the supersonic mixing and combustion with the wall-mounted ramp injectors. Both experimental work using the planar laser-induced iodine fluorescence and numerical predictions have been conducted.

McDaniel et al. [35] studied experimentally the injection and combustion of hydrogen behind a 10-degree-compression, unswept ramp into Mach 2 air. The data obtained was the first available for the validation of CFD codes. All measured wall pressure distribution was used for a one-dimensional, equilibrium chemistry calculation of

combustion efficiency. This work was extended by Guba et al. [36]. Numerical results of both reacting and non-reacting flows were obtained with the SPARK three-dimensional CFD code. An eight–species, twelve-reaction model was used. A numerical solution was obtained with structured grids. Swept-compression ramp injector was investigated experimentally by Hartfield et al. [37]. The flow field has been investigated using both Mach 2.0 and 2.9 freestreams. The measurements illustrate the domination of the mixing process by streamwise vorticity generated by the ramp. The mixing rate was observed to be lower for Mach 2.9 freestream than that for Mach 2.0 freestream. Donohue et al. [38] investigated experimentally and numerically the swept-compression ramp injection into a supersonic flowfield. Numerical results obtained using the SPARK three-dimensional CFD code were compared to the experimental results. Donohue and McDaniel [39] extended the work of Ref. 37 and investigated the unswept-compression ramp fuel injector using air injected at Mach 2.0 into a Mach 2.9 freestream. The objective of this research was to make available an experimental data set with sufficient completeness and accuracy for future CFD validation. Both experimental and numerical results were obtained.

A numerical study of parallel and non parallel injection in supersonic flow was conducted by Sekar [40]. Results were obtained with the three-dimensional CFD code GASP and were compared with the experimental results of the University of Virginia Ref. 38. Further studies of the ramp injectors have been conducted by investigators in [42-44]. Haimovitch et al.[41] had investigated the effects of internal nozzle geometry on compression ramp mixing in supersonic flow. Drummond [42] described two mixing

enhancement techniques. One of them involves the use of swept ramps placed in the airstream to introduce longitudinal vorticity leading to large scale mixing enhancement.

Cox-Stouffer and Gruber [44-46] studied the effects of span wise injector spacing and the impact of design changes upon mixing and losses characteristics.

2.2 Dual-Mode Combustion

The flowfield of the dual mode engine is complicated due to the presence of the mixed characteristics of both supersonic and subsonic flows and the active transition between subsonic and supersonic combustion within the engine. Past research on dual-mode combustion has generally been focused on studying inlets, isolators, combustors, fuels, and fuel injection. Waltrup [47] reviewed extensively the past research up to 1987 on hypersonic inlets, isolators, liquid fuels, wall fuel injection, axial fuel injection, combustors, and exit nozzle. Billing et al. [48-49], and Waltrup and Billing [50-51] first provided analysis of experiments and analytical tools allowing the prediction of upstream interaction, required isolator length for mid-speed scramjet combustor configurations. Anderson [52] studied the dual-mode combustor performance and determined that expansion steps upstream of the combustor yielded some degree of isolation from pressure wave interaction in the upstream flow.

Isolators have been studied experimentally for a number of years. In the early stages of the supersonic combustion research, it was surmised that the shock-train structures, which had been observed in tests with fuel injection and combustion, could be duplicated in an underexpanded or throttled nonreacting flow [53]. Moreover, Reynolds and Mach numbers would be the fundamental correlating parameters, not pressure and temperature.

Stockbridge [54] experimentally investigated the compression fields in a supersonic flow through an annular duct. The investigated model simulates the combustor inlet flowfield in a dual-mode combustor. Shock wave-boundary layer interactions also had been investigated. From experimental measurements of more than 1250 shock trains, Stockbridge [54] derived a correlation that predicts the position of the leading shock wave in an annular duct. Carrol and Dutton[55] experimentally investigated multiple shock wave/turbulent boundary layer interactions in rectangular ducts. Two Mach numbers were considered, Mach 2.45 and Mach 1.6. They showed that the lower Mach number interaction is much steadier with the length of the interaction scaling directly with the level of flow confinement (the ratio of the undisturbed boundary-layer thickness to the duct half-height, δ/L). A two-dimensional numerical study of precombustion shock-trains in supersonic diffusers had been performed by [56]. The freestream Mach number range of the study was from 3 to 10. They reported that the shock trains are characterized by a high speed coreflow which does not adhere to the adjacent diverging walls. Also, they concluded that turbulence modeling is critical for accurate prediction of shock/boundary layer interactions in shock-train regions. Lin et al.[57] numerically investigated the shock wave/boundary layer interaction in a two-dimensional constant area diffuser at Mach 3. They examined the effects of back pressure, Mach number and boundary-layer momentum thickness on the shock train behavior. The shock train increases with the increase of the back pressure for a given Mach number, and decreases with the increase of Mach number at fixed back pressure. It also increases with momentum thickness for given Mach number and high back pressure. The isolator-combustor interaction in a dual-mode scramjet engine had been investigated by Pratt and

Heiser[58]. The objective the work was to present some ideas to clarify the relationships between component processes in a supersonic combustion system.

Experiment to study the effect of fuel injector geometry on scramjet combustor performance with an entrance Mach number of 2.5 was conducted by Chinzei et al. [59]. The study focuses on the effects of geometry on combustion-induced peak wall pressure and associated upstream influence, as well as on mixing/combustion characteristics. Five types of injector/combustor models were tested. They concluded that the injector model with the shortest isolator had the lowest peak pressures while that with the longest isolator had the highest peak pressure. Also, there is a high sensitivity of the fuel mixing to the length of the isolator, which is due to pressure and Mach number changes. Their calculations of the combustion efficiency showed that the combustion efficiency is the highest with the shortest isolator. Lin[60] extended the work of Ref. 57 to investigate the geometric effects on precombustion shock train in a constant area isolator. Numerical analysis was conducted for two-dimensional planar and cylindrical ducts at Mach 2.6. Results of Lin [60] showed that the geometric difference in constant area isolators can affect the type of the shock structures and the shock train length. For the same back pressure and inflow condition, the shock train length in cylindrical duct is shorter than that in the two-dimensional planar duct. Emami et al. [61] conducted experimental studies to investigate inlet-isolator performance in an airframe-integrated dual-mode engine. Results were obtained for cold flow at Mach number of 4.0. Their results reveal that the performance of each isolator is dependent not only on inlet geometry and forebody boundary-layer thickness but also on the isolator length and isolator step area change. The results also showed that the combined inlet isolator maximum back pressure

capability was increased with increasing isolator length and increasing inlet contraction ratio, and it was decreased by inlet distortion and rearward-facing step area increases in the isolator.

Different experimental and numerical studies have been conducted to study a dual-mode combustor model with aerodynamics ramp fuel injectors [62-65]. A dual-mode combustor with high upstream interaction was proposed and investigated at the National Aerospace Laboratory (NAL) in Japan. Fuel is injected normal to the airstream behind a backward facing step. Experimental studies have been performed in Refs. 66 and 67. This geometry is similar to one of the dual-mode models investigated in the current study. Moreover, different numerical studies have been conducted to study the same geometry [68-72]. The effect of the turbulence temperature fluctuation on the combustion process was investigated by Mizobuchi et al. [68]. The numerical results of Reggins[69] showed the development of substantial upstream interaction consisting of an oblique shock/expansion train. This shock train is generated by recirculation zones on both top and bottom isolator walls. Olynciw et al.[70] numerically investigated the possibility of scaling the computational domain to accelerate the convergence of the numerical solution in order to reduce the computational time. The study supports the usefulness of the numerical scaling in simulating dual-mode combustor flowfields. Rodriguez et al. [71] studied grid convergence, turbulence modeling, and wall temperature effects in terms of wall pressure. Several computational cases were examined; these cases include jet-to-jet symmetry and half duct modeling. Results showed the development of a large side-wall separation zone extending much further upstream than the separation zone at the duct centerline. Mohieldin et al. [72] studied numerically the same model. They have

investigated both two-dimensional and three-dimensional models. Their results showed high upstream interaction in the isolator section. Also, it was found that the symmetric flow structure no longer exists in the isolator as the length of the upstream interaction exceeds the isolator height.

Chapter III

PHYSICAL MODELS AND NUMERICAL PROCEDURE

In this chapter, the physical models selected for the current study are described followed by the governing equations used to describe the flow field and the numerical procedure.

3.1 Physical Models

Different configurations are considered in the present study. Two configurations of scramjet combustors are investigated with different wall-mounted ramps in addition to two dual-mode combustor configurations. All configurations are discussed in the following subsections.

3.1.1 Scramjet Combustor with Raised Ramps

The objective of the wall mounted ramp is to convert part of the flow energy in the air stream into tangential kinetic energy to create a pair of counter rotating vortices in order to hold the fuel jet and increase the mixing rate [6]. In the raised (compression) ramp configuration, shown in Fig. 3.1, an oblique shock wave stands at the base of the ramp where it rises from the wall. The air pressure at the top surface of the ramp becomes higher than that at both sides. Due to the difference in pressure, air at the top surface of the ramp spills over the ramp sides to the lower pressure zone creating a pair of counter-rotating vortices.

In the present study, three raised (compression) wall mounted ramps are considered with different side angles, 0 (unswept), 5 degrees, and 10 degrees. The ramps are located in a constant area duct combustor as shown in Figs. 3.2-3.4. The duct has a rectangular

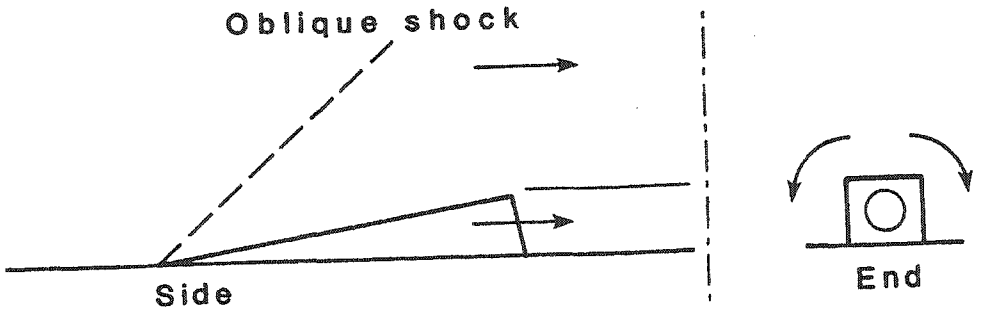

Fig. 3.1 Raised (compression) ramp configuration

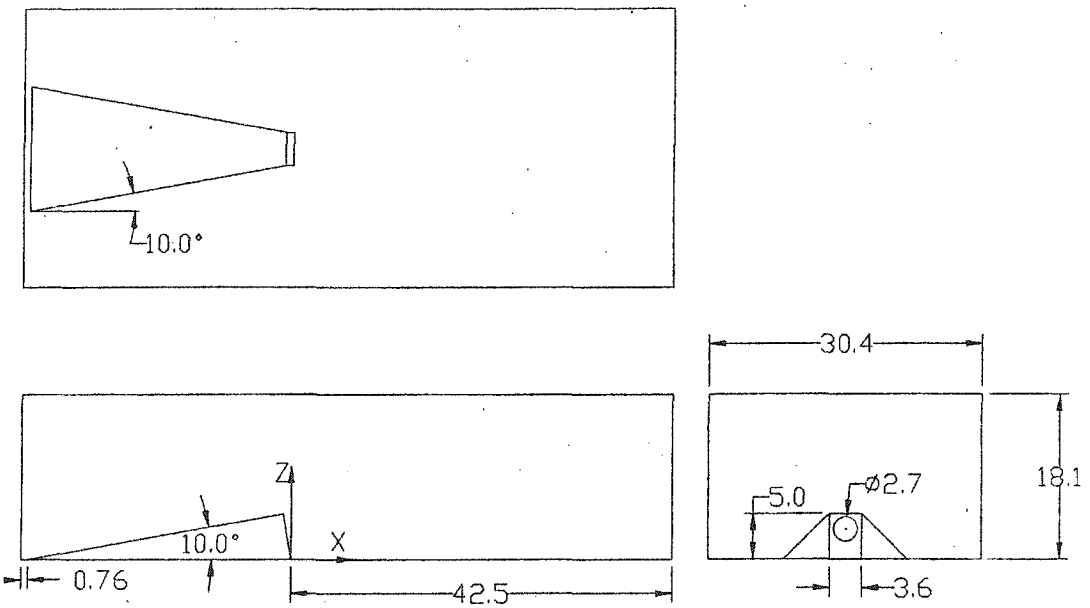

Fig. 3.2 Schematic of the 10-degree swept raised ramp

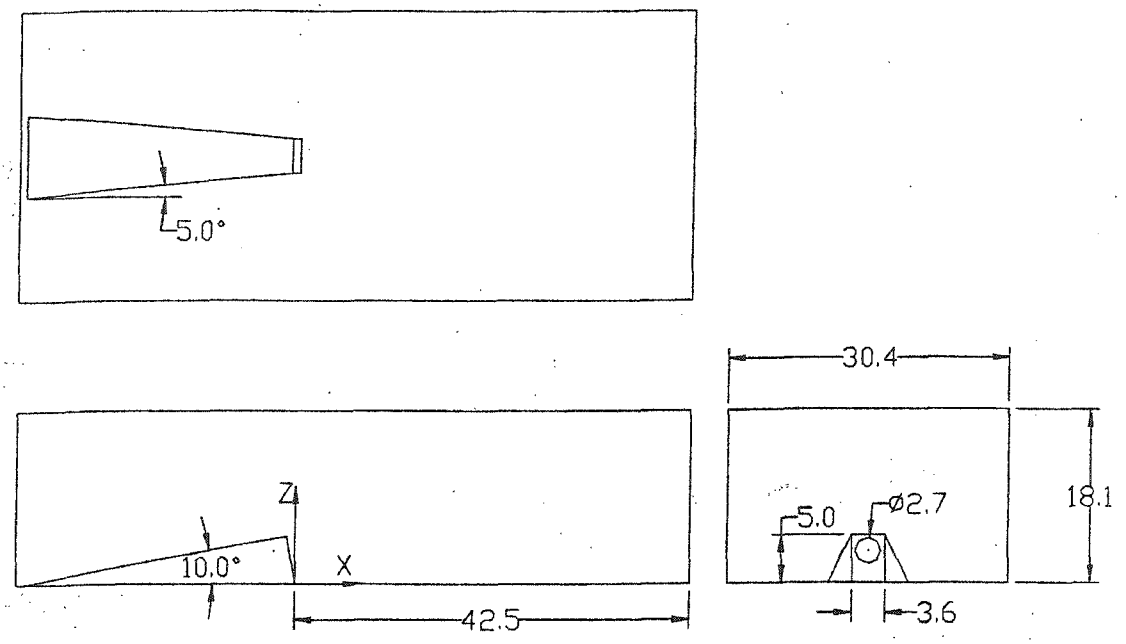

Fig. 3.3 Schematic of the 5-degree swept raised ramp

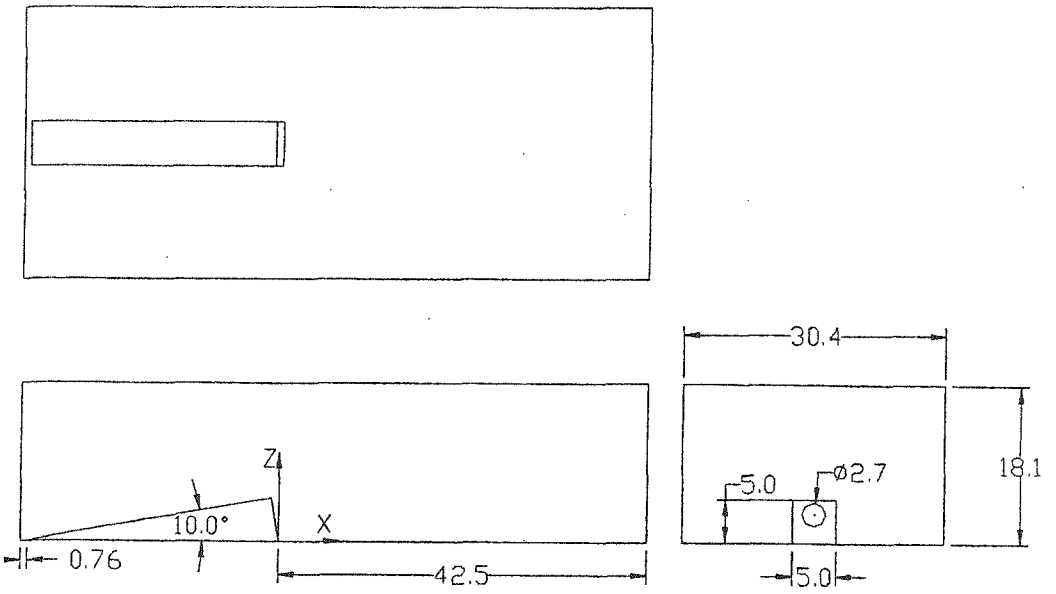

Fig. 3.4 Schematic of the unswept raised ramp

cross-section with an aspect ratio of 1.7. The ramps have a 10-degree compression angle. The fuel jet is 2.7 mm in diameter and the ramp height is 5mm. The jet is inclined at a 10-degree angle parallel to the ramp surface in the three ramps to keep the jet direction parallel to the air flow direction. The unswept compression ramp has an aspect ratio of 1.0. As reported by Nickol [73], the aspect ratio of 1.0 demonstrated the most rapid downstream decay of maximum injectant mole fraction and it is the most effective mixer among three unswept ramps with different aspect ratios. The geometry of the 10-degree swept ramp is selected identical to that of Donohue et al. [38] in order to be able to compare with the available experimental data.

3.1.2 Scramjet Combustor with Relieved Ramps

In this configuration, shown in Fig. 3.5, the wall is turned away from the flow, while the top surface of the ramp remains in the plane of the upstream wall. When the wall has relieved far enough to expose the fuel jet in the downstream end of the ramp, the wall turns back into the flow until it is again parallel with the plane of the upstream wall. A Prandtl-Meyer expansion fan is anchored at the upper edge of the inclined plane, causing a pressure difference between the flow on the upper ramp surface and the expanded flow along the side walls of the ramp [6]. The design goal is also to form counter-rotating pairs of axial vortices having the same sense of rotation as in the raised ramp.

In the present study, two relieved (expansion) wall-mounted ramps are considered with two side angles, 0 (unswept), and 5 degrees. The two configurations are shown in Figs. 3.6 and 3.7 respectively. The duct has a rectangular cross-section with an inlet aspect ratio of 1.7. The ramps have a 10-degree compression angle. The fuel jet is 2.7mm

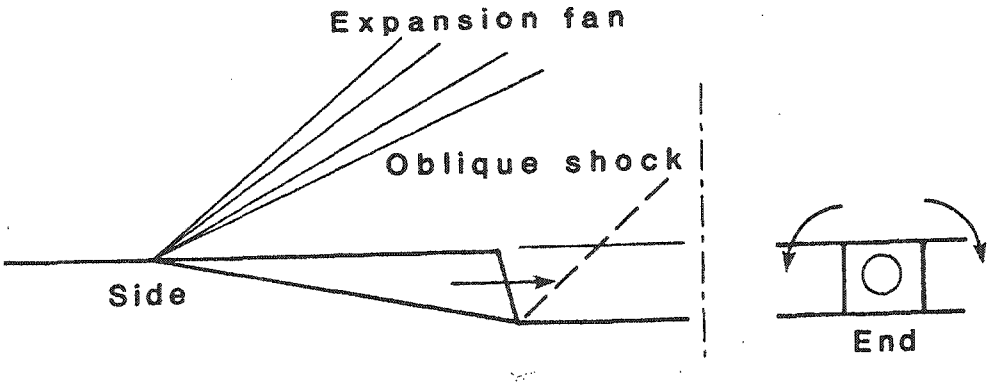

Fig. 3.5 Relieved (expansion) ramp configuration

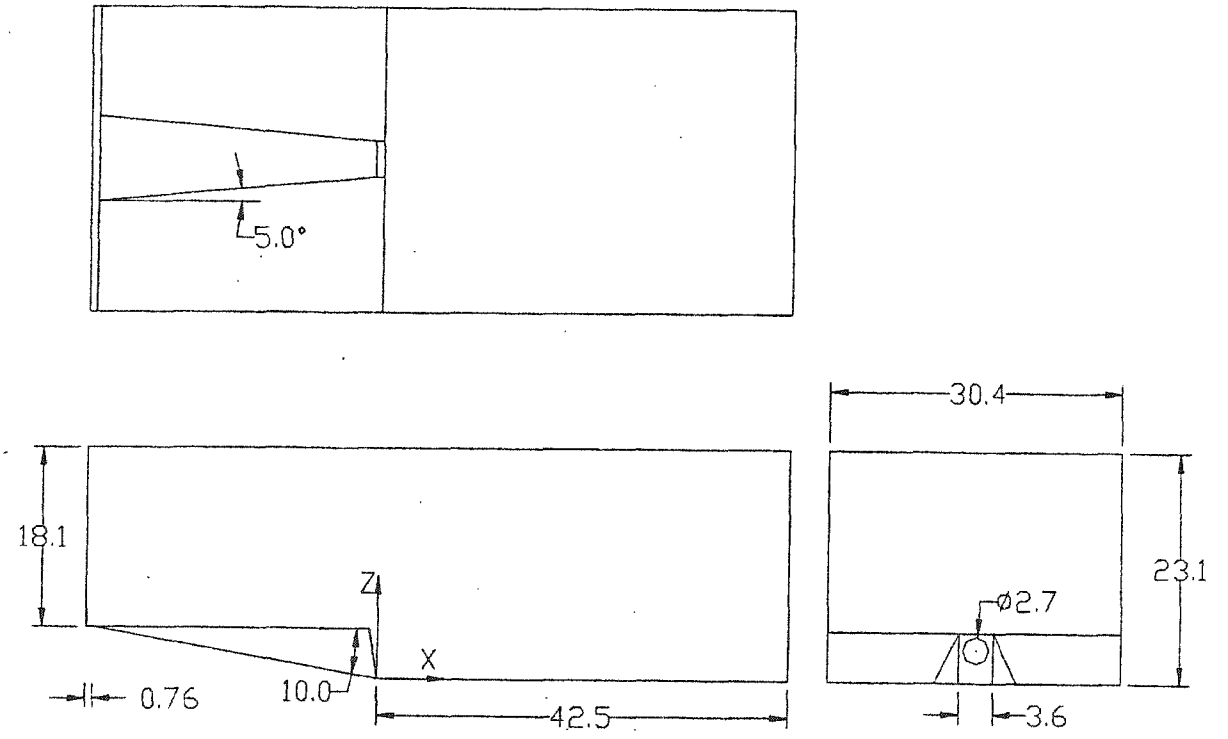

Fig. 3.6 Schematic of the 5-degree swept relieved ramp

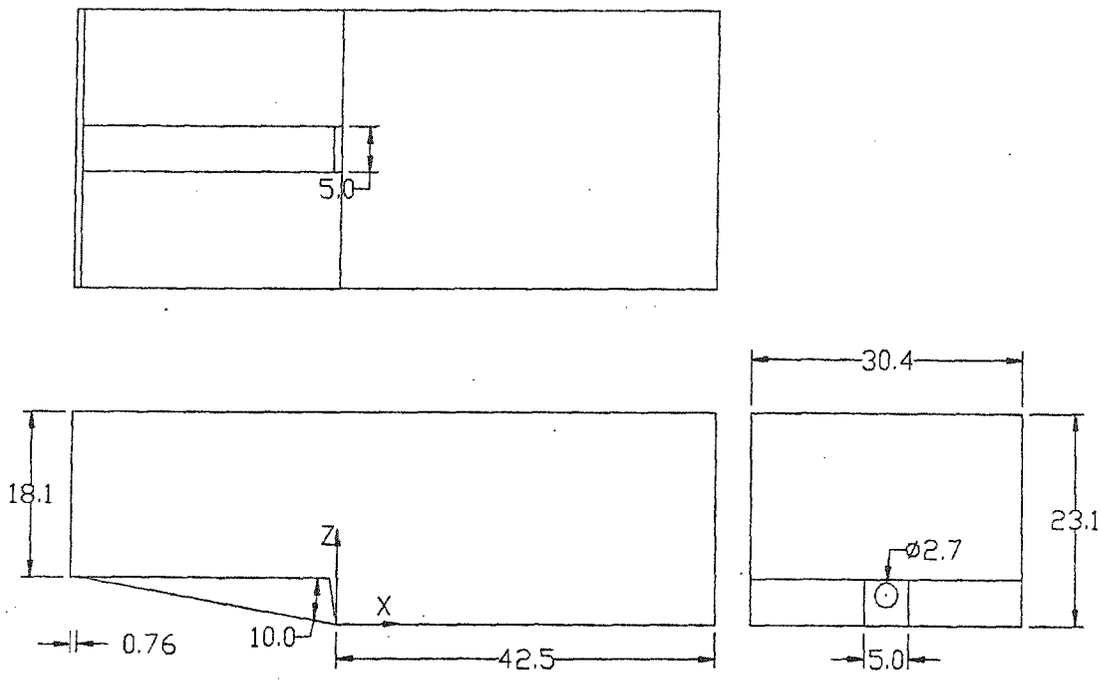

Fig. 3.7 Schematic of the unswept relieved ramp

in diameter and the ramp height is 5mm. The jet is inclined at a 10-degree angle parallel to the ramp surface in the two ramps.

3.1.3 Dual-Mode Combustor with Raised Ramps

The geometry is similar but not identical to the dual-mode combustor proposed by the University of Virginia [74]. The model consists of three parts, isolator, combustor, and expanding duct as shown in Fig. 3.8. The isolator is a constant area duct with aspect ratio of 1.7 placed before the combustor. Two combustors are investigated in this study with length of 10 and 20 ramp height. The combustors have the same aspect ratio of the isolator. Fuel is injected through an unswept compression ramp mounted on the bottom wall at the combustor inlet. An expanding duct with expansion angle of 2.9^{o} on the lower wall is placed after the combustor.

3.1.4 Dual-Mode Combustor with a Rearward Facing Step

The dual-mode combustor model is shown in Fig. 3.9. This model is similar to that investigated experimentally by Kumaro et al.[66] but with two different arrangements of the fuel injectors. The dual-mode combustor is a 147.3mm constant width rectangular duct. It consists of three parts, constant area duct isolator with aspect ratio 4.7, constant area duct combustor, and expanding duct. The isolator is 32 mm in height and 220 mm in length. There is a 3.2 mm steps on both upper and lower walls of the combustor. The length of combustor is 96 mm followed by a 350 mm expanding duct with expansion angle of 1.7^{o} on the upper and the lower walls. Fuel is injected through wall injectors on the upper and lower walls. Two different arrangements of fuel injectors inside the combustor are investigated. The first one has 18 injectors and the second one has 10

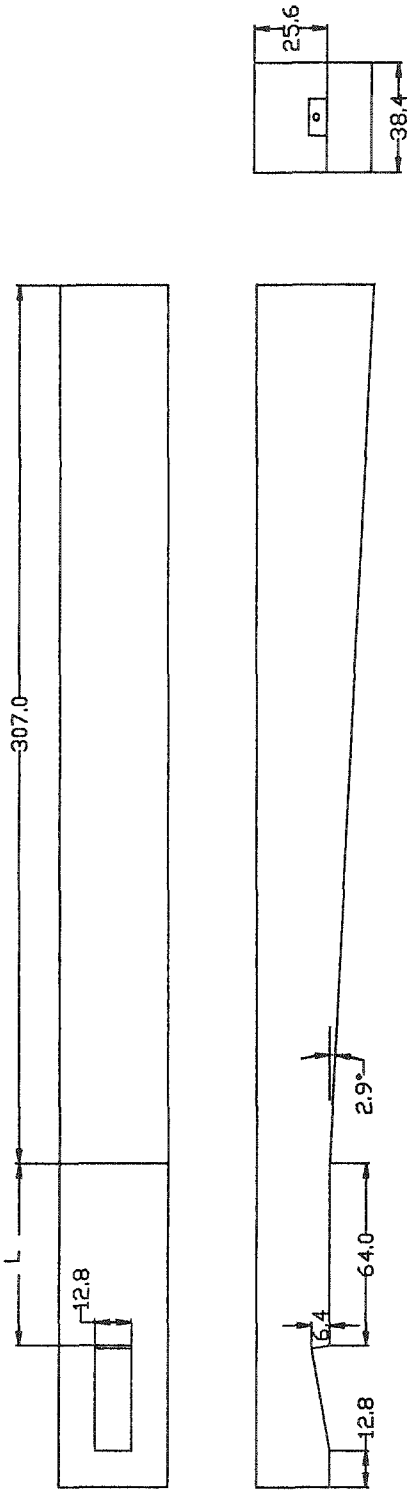

Fig. 3.8 Schematic of the dual-mode combustor

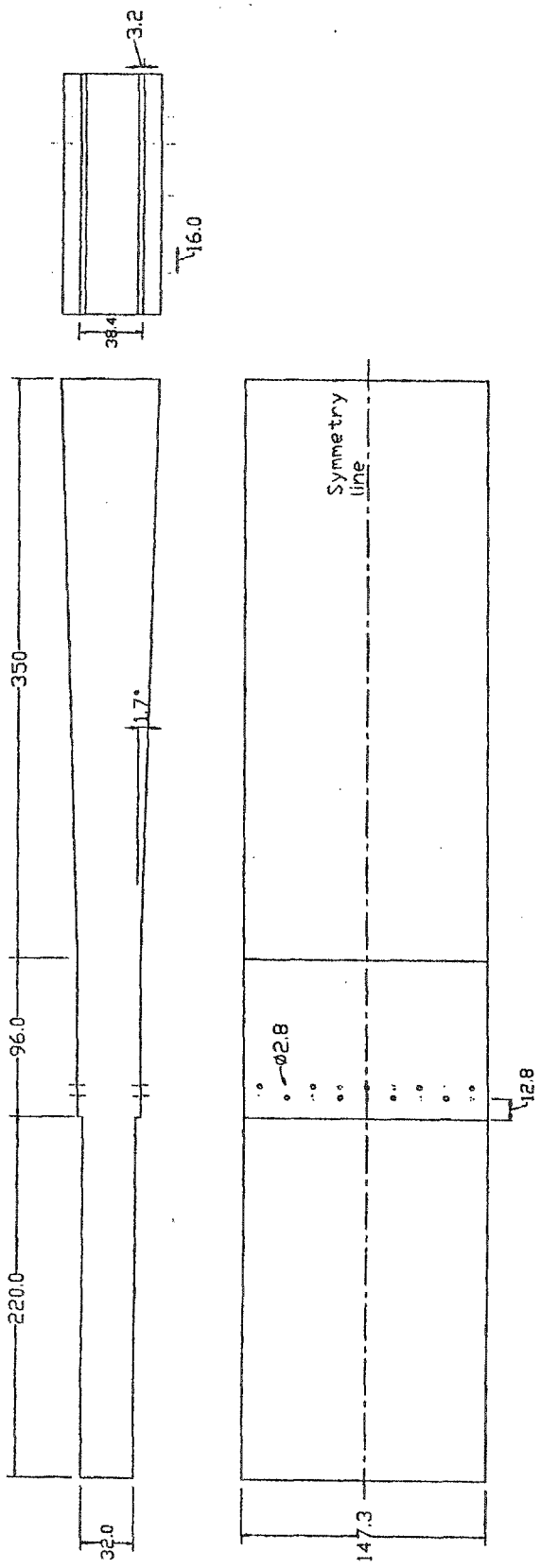

Fig. 3.9 Schematic of the dual-mode combustor with backward facing step

injectors. All injectors have the same diameter, 2.8 mm and 3.8 mm for the 18-injector combustor and the 10-injector combustor, respectively. Injectors are placed in two rows on each wall. The fuel injectors in each row are equally spaced. The injectors on both rows are staggered. The two rows are located at 128 mm and 192 mm downstream of the steps, respectively. The arrangement of the fuel injectors is intended to provide the same fuel flow rate on both walls in addition to increasing the surface area of the fuel in order to achieve good mixing and complete combustion. Figure 3.10 shows the distribution of the fuel injectors for both combustor configurations.

3.2 Governing Equations

The flow field of the combustor models is governed by the Reynolds averaged Navier-Stokes equation and the species continuity equation. According to Anderson [75], the main thrust of present-day research in computational fluid dynamics and heat transfer in turbulent flows is through the time-averaged Navier-Stokes equations. These equations are referred to as Reynolds averaged Navier-Stokes equations. The Reynolds averaged equations are derived by decomposing the dependent variables in the conservation equation into time-mean and fluctuating components and then averaging the entire equation. Equations for continuity, momentum, energy, and species continuity are expressed, respectively, as [75]

$$\frac{\partial \rho}{\partial t}+\frac{\partial}{\partial x_i}(\rho u_i)=0 \tag{3.1}$$

$$\frac{\partial}{\partial t}(\rho u_j)+\frac{\partial}{\partial x_i}(\rho u_i u_j)=-\frac{\partial p}{\partial x_j}+\frac{\partial}{\partial x_i}\left[\mu\left(\frac{\partial u_i}{\partial x_j}+\frac{\partial u_j}{\partial x_i}\right)\right]+\sum_{i=1}\rho_i g_i \tag{3.2}$$

18-injector combustor

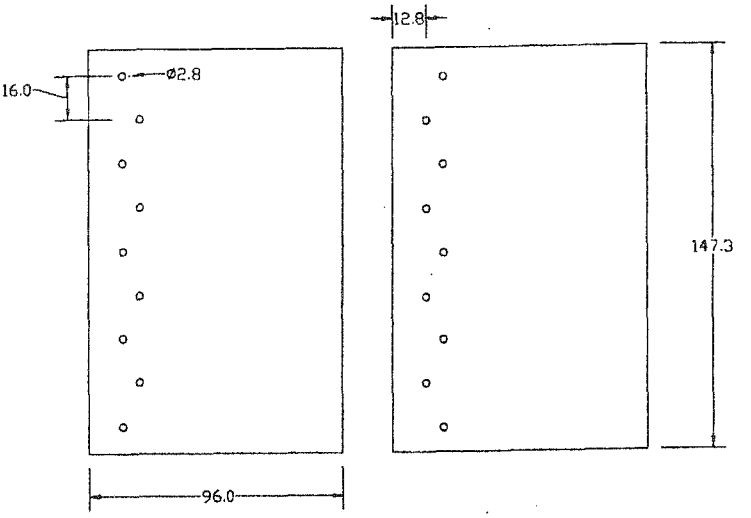

10-injector combustor

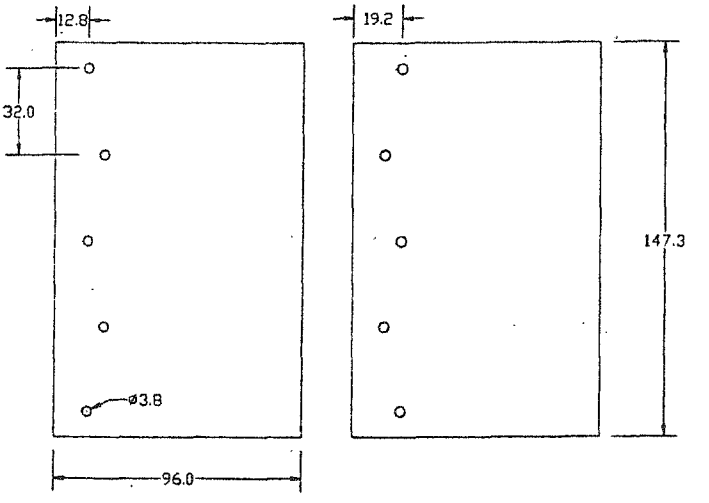

Fig. 3.10 Detailed of the 18-injector and the 10-injector combustors

$$\frac{\partial}{\partial t}(\rho H)+\frac{\partial}{\partial x_i}(\rho u_i H)=\frac{\partial}{\partial x_i}\left[\frac{k}{c_p}\frac{\partial H}{\partial x_i}\right]+\sum_j\left[\frac{h_j^o}{m_j}+\int_{T_{refj}}^{T_{ref}}C_{pj}dT\right]R_j \tag{3.3}$$

$$\frac{\partial}{\partial t}(\rho\, m_j)+\frac{\partial}{\partial x_i}(\rho\, u_i m_j)=R_j \tag{3.4}$$

where ρ is the density, t is the time, x_i is the coordinate axis (x, y, z), u_i is the velocity component (u, v, w), p is the static pressure, g_i is the external force, and H is the total enthalpy. The enthalpy of formation, the mass fraction, and the production rate of species j are presented by h_j^o, m_j, and R_j, respectively. The symbols μ, k, and c_p are the dynamic viscosity, the thermal conductivity, and the specific heat, respectively.

3.3 Numerical Procedure

3.3.1 Code Description

For the present study the numerical analysis is carried out using the CFD code FLUENT [76]. The FLUENT is a finite volume code for solving steady and unsteady three-dimensional Reynolds-averaged Navier-Stokes equations. The code uses first or second order finite volume discretization method coupled explicit or implicit solver. The code is capable of using structured as well as unstructured grids. The code can solve subsonic and supersonic flows. The program also has the ability to simulate chemical reactions. It has a large data base of chemical properties for many species and reactions. This feature is turned off in the nonreacting cases.

3.3.2 Turbulence Modeling

Turbulence modeling is a key element in computational fluid dynamics (CFD). Aside from any physical consideration, turbulence is inherently three dimensional and time dependent. Hinze [77] has provided a sharp definition of turbulence as "Turbulent fluid motion is an irregular condition of flow in which the various quantities show a random variation with time and space coordinates, so that statistically distinct average values can be discerned." Four main categories of turbulence models evolved by the early 1950's [78]: algebraic(zero-equation) models, one-equation models, two-equation models, and stress-transport models. With the coming of the age of computers, further development of all four classes of turbulence models has occurred. Unfortunately, no single turbulence model is universally accepted as being superior for all classes of problems. Thus, the choice of turbulence model will depend on different considerations such as the physics of the flowfield and the level of accuracy required. In the current study, the two-equation k-ε turbulence model is used. For this model, the Boussinesq approximation is assumed valid; it assumes that the turbulent stresses are proportional to the mean velocity gradients. Thus, specific Reynolds-stresses tensor and the turbulence kinetic energy can be calculated by the following equations [78]:

$$\tau_{ij} = 2\upsilon_t S_{ij} - \frac{2}{3}k\delta_{ij} \tag{3.5}$$

$$\frac{\partial k}{\partial t} + U_j \frac{\partial k}{\partial x_j} = \tau_{ij} \frac{\partial U_i}{\partial x_j} - \varepsilon + \frac{\partial}{\partial x_j}\left[(\upsilon + \upsilon_t / \sigma_k)\frac{\partial k}{\partial x_j}\right] \tag{3.6}$$

where ν_t is the kinematic turbulent viscosity (μ_t/ρ), S_{ij} is the mean strain-rate tensor δ_{ij} Kronecker delta, σ_k is the turbulent Prandtl number, and k is the turbulent kinetic energy.

Three different k-ε turbulence models are available in the FLUENT code. All three models have similar forms with transport equations for k and ε. The major differences in the models are the method of calculating turbulent viscosity, the turbulent Prandtl numbers governing the turbulent diffusion of k and ε, and the generation and destruction terms in the ε equation. An overview of issues related to these three turbulence models is given below.

The Standard k-ε Model

The standard k-ε model is a semi-empirical turbulent model based on model transport equation for the turbulent kinetic energy k and its dissipation rate ε [79]. The model transport equation for k is derived from the exact equation, while the model transport equation for ε is obtained using physical reasoning and bears little resemblance to its mathematically exact counterpart [76]. The turbulence kinetic energy is calculated from Eq.3.6 and the dissipation rate is calculated from

$$\frac{\partial \varepsilon}{\partial t} + U_j \frac{\partial \varepsilon}{\partial x_j} = C_{\varepsilon 1} \frac{\varepsilon}{k} \tau_{ij} \frac{\partial U_i}{\partial x_j} - C_{\varepsilon 2} \frac{\varepsilon^2}{k} + \frac{\partial}{\partial x_j} \left[(\upsilon + \upsilon_t / \sigma_\varepsilon) \frac{\partial k}{\partial x_j} \right] \tag{3.7}$$

where $C_{\varepsilon 1}$, $C_{\varepsilon 2}$ are constants and σ_ε is the turbulent Prandtl numbers.

By combining k and ε, the turbulent viscosity is calculated as

$$\nu_t = C_\mu k^2 / \varepsilon \tag{3.8}$$

where $C\mu$ is a constant.

The model constants have the following values [79]: $C_{\varepsilon 1}$= 1.44, $C_{\varepsilon 2}$=1.92, σ_ε= 1.3, σ_k= 1.0, and $C\mu$= 0.09. These default values have been determined from experiments. They have been found to work fairly well for a wide range of turbulent flows.

In the derivation of the model, the flow is assumed fully turbulent and the effects of molecular viscosity are negligible. Therefore, the standard k-ε model is valid only for fully turbulent flows.

Renormalization Group k-ε Model (RNG- k-ε)

The RNG k-ε is a more recent version of the k-ε model. The model was derived using a rigorous statistical technique called renormalization group theory [80]. This model is similar to the standard k-ε model but includes some refinements. The model includes additional term in its ε equation that significantly improves the accuracy. Also the effect of swirl turbulence is included which enhances the accuracy for swirling flow. These features make the RNG k-ε model more accurate and reliable for a wider class of flows than the standard k-ε model.

The turbulent kinetic energy k, the dissipation rate ε and the eddy viscosity are still given by Eqs.(3.6)-(3.8). However, the model uses a modified coefficient, $C_{\varepsilon 2}$ defined by

$$C_{\varepsilon 2} = \tilde{C}_{\varepsilon 2} + \frac{C_\mu \lambda^3 (1 - \lambda/\lambda_o)}{1 + \beta \lambda^3} \tag{3.9}$$

where

$$\lambda \equiv \frac{k}{\varepsilon}\sqrt{2S_{ij}S_{ji}}$$

The closure coefficients for the RNG k-ε model are[78]: $C_{\varepsilon 1}$= 1.42, $\tilde{C}_{\varepsilon 2}$=1.68, σ_ε= 0.72, σ_k= 0.72, Cμ= 0.085, β= 0.012, and λ_o=4.38.

Realizable k-ε Model

The term "realizable" means that this model satisfies certain mathematical constraints on Reynolds stresses consistent with the physics of turbulent flows. Neither the standard k-ε nor the RNG k-ε is realizable. The realizable k-ε model contains a new formulation for turbulent viscosity. Also, a new transport equation for the dissipation rate has been derived from an exact equation for the transport of the mean-square vorticity fluctuation. The eddy viscosity is computed from Eq.(3.8) as in other k-ε. The difference between the realizable and the other k-ε models is that C_μ is no longer constant. It is computed from

$$C_\mu = \frac{1}{A_o + A_s \frac{U^* k}{\varepsilon}} \tag{3.10}$$

where

$$U^* = \sqrt{S_{ij} S_{ji} + \tilde{\Omega}_{ij} \tilde{\Omega}_{ji}}$$

and $\tilde{\Omega}_{ij}$ is the rate of rotation tensor.

It can be seen that C_μ is a function of the mean strain and rotation rates and turbulence fields (k and ε). The model constants are $C_{\varepsilon 1}$= 1.44, $C_{\varepsilon 2}$=1.9, σ_ε= 1.2, σ_k= 1.0.

This model has been extensively validated for a wide range of flows. It more accurately predicts the spreading rate of both planar and round jets.

Both the realizable and the RNG k-ε models have shown substantial improvements over the standard k-ε model where the flow features include strong streamline curvature, vortices, and rotation. Initial studies have shown that the performance of both models provide good results for several validations of separated flows and flows with complex

secondary flow features. In the current study results are obtained for one case using the three k-ε model versions. Comparisons are presented in Sec. 4.3.

3.3.3 Chemistry Modeling

In this study a single-step chemistry model has been used for hydrogen–air combustion. In this global single-step mechanism, the hydrogen fuel is oxidized to water without taking into account the intermediate species such as OH, H, etc. The species transport model used for this study is the finite rate reaction model. The model solves for each species of the species considered in the study (H_2, O_2, N_2, and H_2O). The reaction rate is calculated with the Magnussen model to take into account the influence of turbulence. The nitrogen is carried as an inert species. The reaction and reaction rate are expressed as

$$H_2 + \frac{1}{2}O_2 \rightarrow H_2O \tag{3.11}$$

$$R_{H_2} = M_{H_2} A_1 C_{H_2}^{\alpha_1} C_{O_2}^{\beta_1} e^{\frac{-E_1}{RT}} \tag{3.12}$$

where M is the molecular weight of hydrogen and C_{H2} and C_{O2} are the concentrations of hydrogen and oxygen respectively. The symbols A_1, α_1, β_1 are imperical constants and are given in Table 3.1.

3.4 Grid Generation

The construction of a grid is one of the first steps in computing a numerical solution to the equations that describe the physical process. A poorly constructed grid leads to poor results and a lack to convergence. In the current study three-dimensional unstructured grids are generated. All grids are generated outside FLUENT with the

Table 3.1 One-step model for hydrogen/air

Constant	R_{H2}
A_1 (kg/m^3-s)	$6.32x10^5$
E_1 (J/kg-mol)	$1.2263x10^7$
α_1	1.6
β_1	1.6

preprocessor Gambit [81]. The grids generated in this study are in the range between 200,000 and 400,000 points. Grid convergence studies are performed for one geometry and these are presented in Sec. 4.1.

3.5 Boundary Conditions

In all modeled cases in this study, only half of the domain is computed due to the symmetry of the physical models. The symmetry condition is defined at y/2 for all cases. A uniform flow is assumed for the fuel jets. For the inlet air stream, either a uniform flow or a velocity profile is used at the inlet plane. A no-slip condition is used for the combustor walls. Walls are assumed either adiabatic, requiring the normal derivative of temperature to vanish, or isothermal. A non-reflective boundary condition is used at the outflow where the flow quantities are linearly extrapolated from the interior domain. Initial conditions are obtained by specifying freestream conditions throughout the flowfield.

3.6 Iteration Technique

3.6.1 Discretization

The FLUENT code uses a control-volume-based technique to convert the governing equations to algebraic equations that can be solved numerically. This control volume technique consists of integrating the governing equations about each control volume, yielding discrete equations that conserve each quantity on a control-volume basis. These discrete values are stored at the cell centers. Integration over the control volume requires calculation of the cell face values so that the convective and diffusive fluxes can be determined. This requires an interpolation from the values at the center to the cell face.

Different interpolation schemes are available in the code: first-order upwind, second-order upwind, power law, and QUICK. Higher order schemes present a better accuracy as a first order scheme introduces numerical diffusion when the flowfield is oblique to the grid alignment. However, high order schemes show a less stable solution procedure. In this work, both the first-order and the second-order upwind schemes are used.

3.6.2 Solver

The coupled solver of the FLUENT code is used in this study to solve the governing integral equations. The governing equations of continuity, momentum, energy, and species transport are solved simultaneously (coupled together). Governing equations for turbulence and other scalars are solved sequentially (segregated from one another and from the coupled set). Because the governing equations are non-linear (and coupled), several iterations of the solution is obtained. Each iteration consists of the steps shown in Fig 3.11 and outlined below:

1. Fluid properties are updated based on the current solution.
2. The continuity, momentum, energy, and species equations are solved simultaneously.
3. Turbulence equations are solved using the previously updated values of the other variables.
4. A check for convergence of the equation set is made.

These steps are continued until the convergence criteria are met.

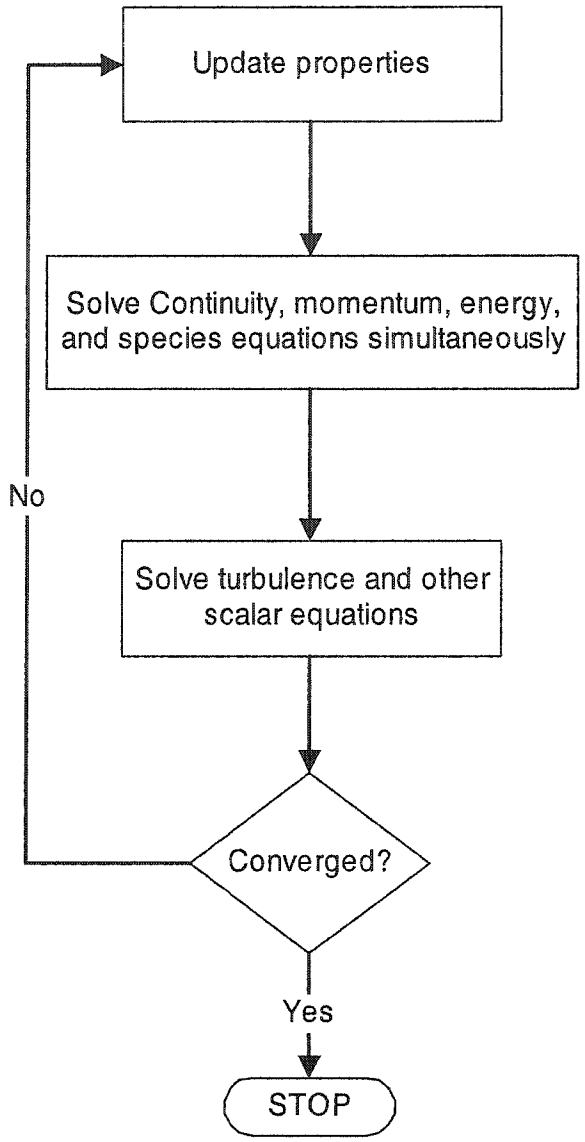

Fig. 3.11 Outline of the solution procedure

3.7 Convergence

In general, there are no universal metrics for judging convergence. In this study, the convergence of the solution is monitored and judged by four different criteria, namely the residuals of the flow properties, the mass conservation, and the profile of the mole fraction or the wall static pressure. The converged solution is assumed to be achieved after satisfying the following four conditions:

1- The residuals of the flow properties are less than 10^{-5} for nonreacting flows and less than 10^{-3} for reacting flows.

2- No changes in the wall static pressure profile are seen with the iterations.

3- Global mass balance at the inlets and the outlets is satisfied, i.e.,

$$\sum \dot{m}_{in} = \sum \dot{m}_{out} \tag{3.13}$$

4- Conservation of mass flow rates inside the computational domain is satisfied.

It is observed that the four conditions for convergence usually are achieved at the same time in all nonreacting cases. In the reacting cases, the last two conditions (3 and 4) are achieved after the first two conditions (1 and 2). For nonreacting cases, usually convergence achieved between 4,000-6,000 iterations while for reacting cases, convergence is achieved between 10,000- 40,000 iterations.

Chapter IV

RESULTS FOR SUPERSONIC MIXING AND COMBUSTION

In this chapter, results for supersonic mixing and combustion are presented. Two types of wall-mounted ramps, raised (compression) ramps, and relieved (expansion) ramps, are investigated. Results are presented for both reacting flow as well as non-reacting flow. Initially, results are obtained with different unstructured grids to examine the grid independence. The results for the non-reacting flow are extensively compared with the available experimental and numerical results for the case of raised ramp. The effects of changing the side angle of the ramp on both mixing and combustion, for the two types of ramps, are presented. Table 4.1 summarizes all of the cases presented in this chapter.

4.1 Effect of the Grid Size

The present results are compared extensively with both numerical and experimental results; these are presented in Sec. 4.3. However, a grid independence test has been conducted using one-ramp configuration. Different unstructured grids are used with the 10-degree raised ramp (Fig. 3.2) to investigate the effect of the grid size on the results. Before obtaining the final grids, an initial grid distribution test has been conducted for each grid size. Three grid sizes are investigated with sizes equal to about 200,000, 300,000, and 400,000 cells. Selected results are presented in Figs. 4.1-4.3 to give a clear idea about the effect of the grid. The figures demonstrate clearly the grid independence. Figure 4.1 shows the distribution of the injectant mole fraction near the nozzle along the vertical (Z) direction. Figure 4.2 shows the axial decay of the maximum injectant mole

Table 4.1 Summary of cases with ramp fuel injectors

Case	Ramp Type	Ramp Side Angle	Flowfield	Turbulence Model	Injectant Mach Number	Grid Size
1	Raised	10	Nonreacting	RNG k-ε	1.7	300,000
2	Raised	10	Nonreacting	RNG k-ε	1.7	200,000
3	Raised	10	Nonreacting	RNG k-ε	1.7	400,000
4	Raised	10	Nonreacting	RNG k-ε	0	300,000
5	Raised	10	Nonreacting	Standard k-ε	1.7	300,000
6	Raised	10	Nonreacting	Realizable k-ε	1.7	300,000
7	Raised	10	Reacting	RNG k-ε	1.7	300,000
8	Raised	5	Nonreacting	RNG k-ε	1.7	300,000
9	Raised	5	Reacting	RNG k-ε	1.7	300,000
10	Raised	0 (unswept)	Nonreacting	RNG k-ε	1.7	300,000
11	Raised	0 (unswept)	Reacting	RNG k-ε	1.7	300,000
12	Relieved	5	Nonreacting	RNG k-ε	1.7	300,000
13	Relieved	0 (unswept)	Nonreacting	RNG k-ε	1.7	300,000
14	Raised	10	Nonreacting	Laminar	1.7	300,000

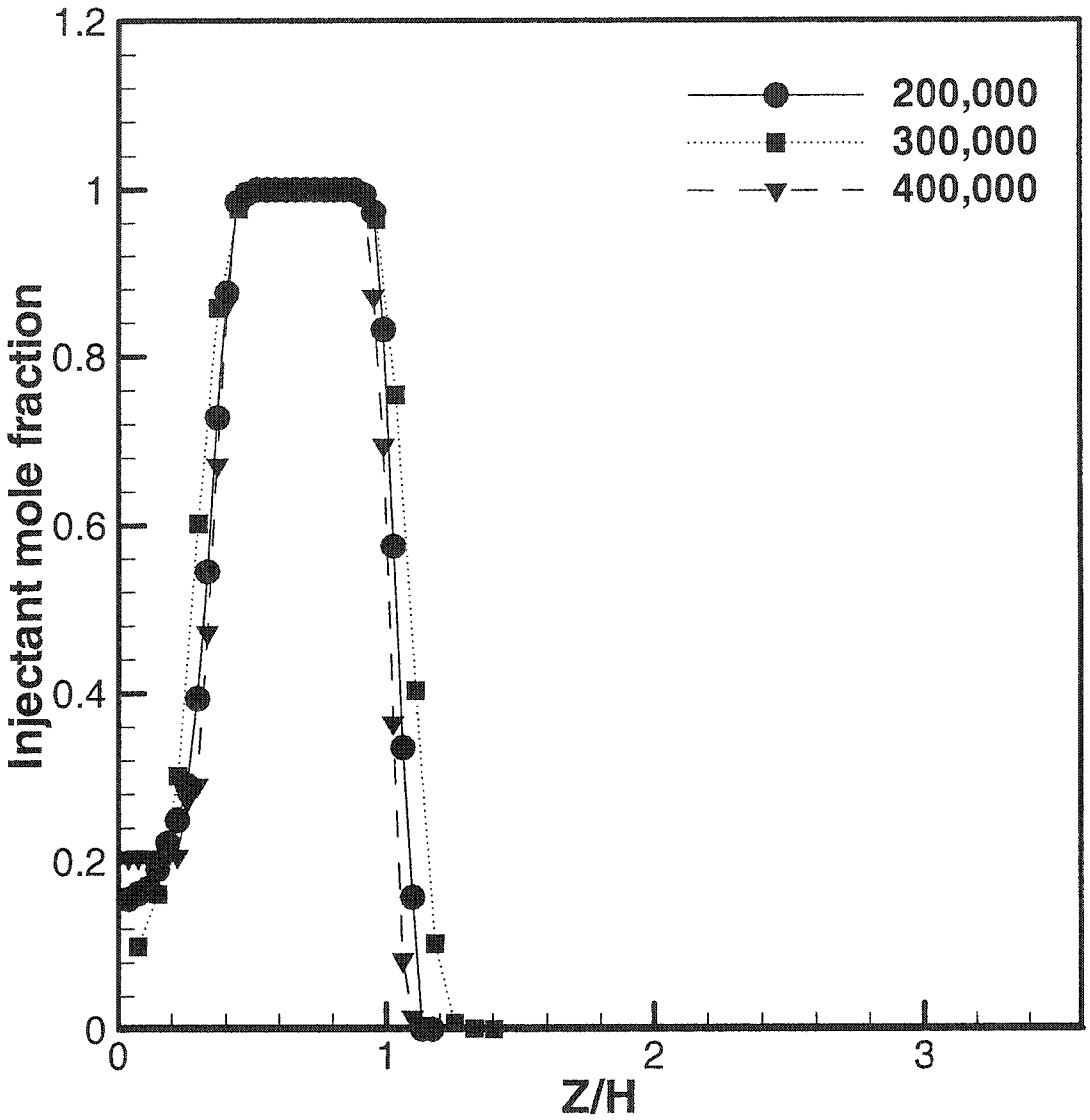

Fig.4.1 Mole fraction profile across the test section cutting through the jet core at X/H=0.5 and Y=0.0

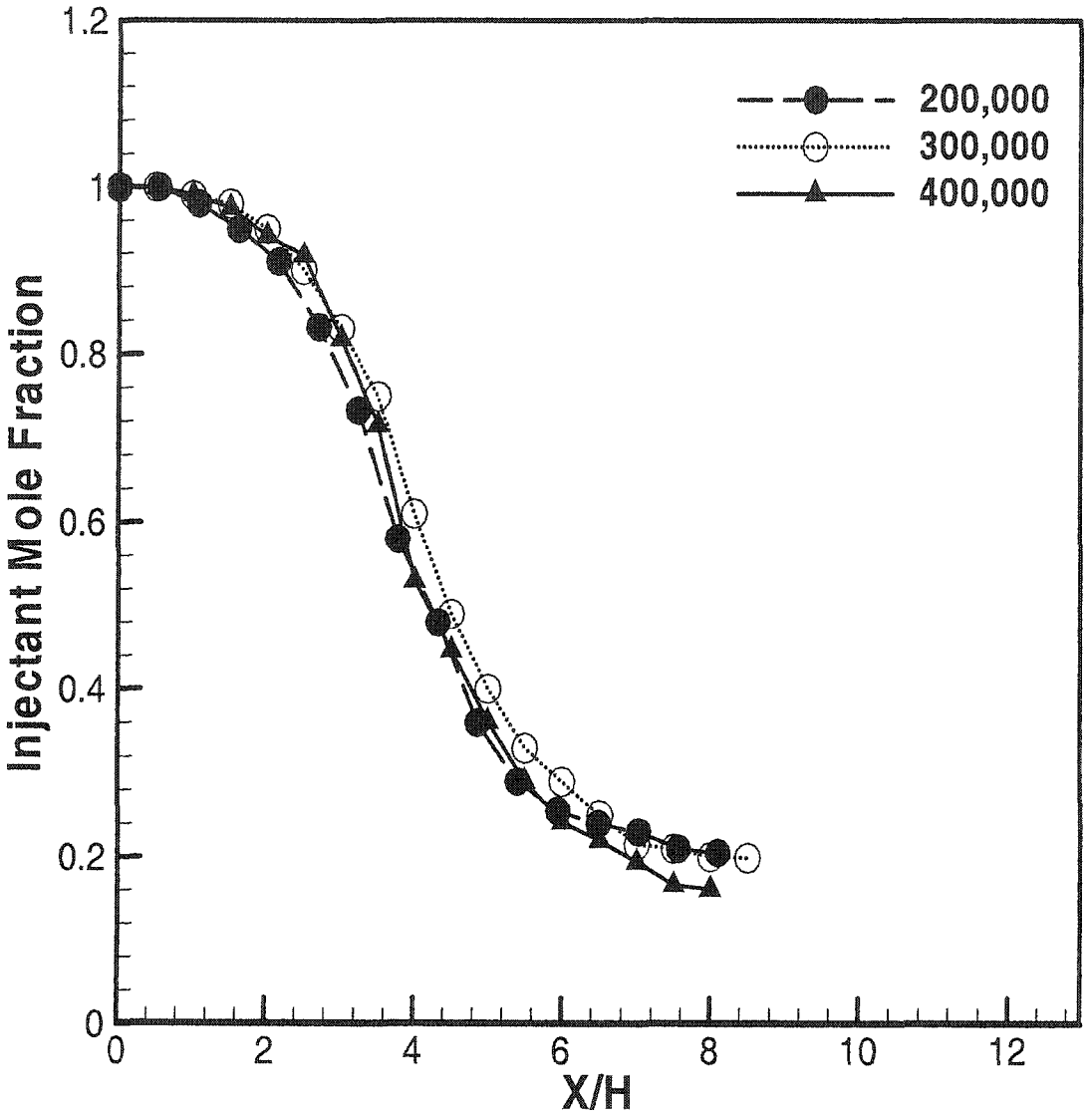

Fig.4.2 Axial distribution of maximum injectant mole fraction

200,000

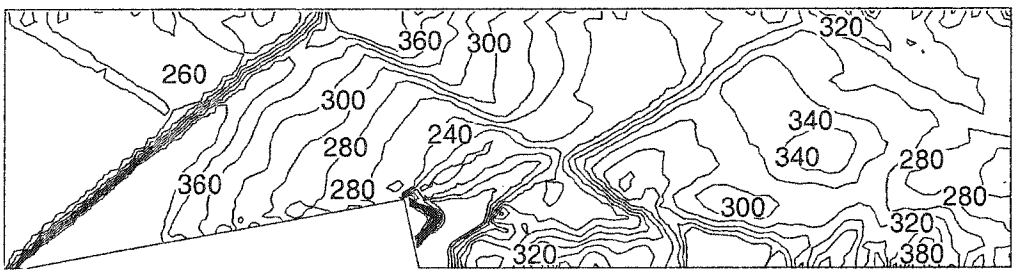

300,000

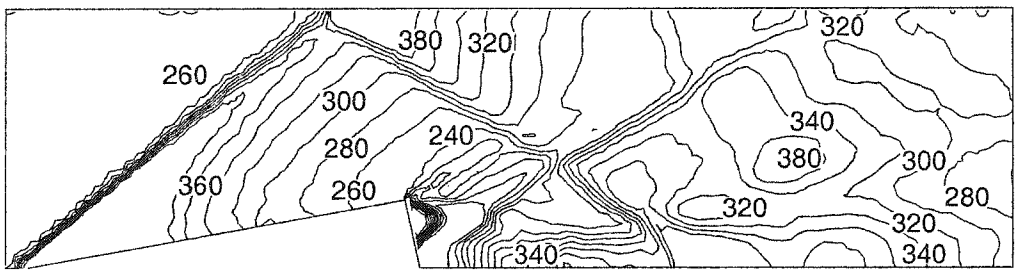

400,000

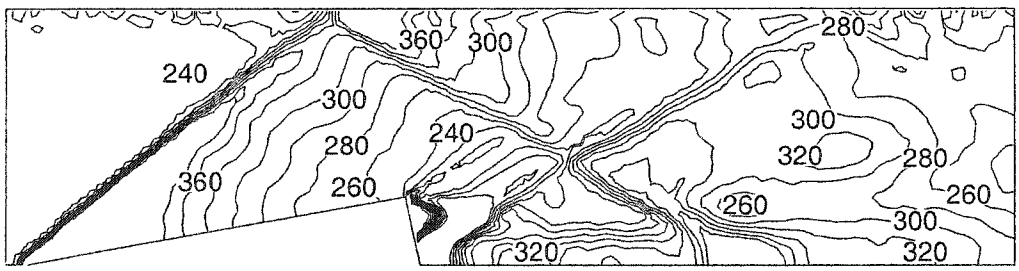

Fig. 4.3 Centerplane static pressure contours of different grids

fraction. The same results are obtained with the three grids with a very slight difference. Figure 4.3 shows the contours of the static pressure at the centerplane. The same values have been predicted with the three grids. The obtained results are very close, although the thinner shock wave is predicted with the 400,000 grid at the base of the ramp.

Unless otherwise noted, all results presented in the following sections, are obtained with a grid size equal to about 300,000 grid points.

4.2 Effects of Turbulence Modeling

As recommended by Donohue et al. [39] and others, a two-equation model, k-ε model, has been selected and used in the present study. The differences among different k-ε turbulence models have been investigated. Three k-ε models are used: the RNG k-ε model, the standard k-ε model, and the realizable k-ε model. In addition, laminar calculations are also performed and compared with the turbulent calculations. Results for laminar flows are presented before the comparison of the turbulence models. Contours of static pressure, static temperature, and stream wise velocity for both laminar and RNG k-ε model at the plane of symmetry are presented in Figs. 4.4 - 4.6.

Figures 4.4 and 4.5 show the contours of static pressure and temperature. At the combustor inlet, both the laminar and the turbulent calculations for the pressure and the temperature show almost the same values. The shock wave is much clearer in the turbulent results. At the exit section, the temperature is about 5% less in the laminar case than the turbulent case. The stream wise velocity is shown in Fig. 4.6. At the inlet section, it is about 6% less in the laminar case. The figures show that the resolution of the shock wave in the turbulent case is clearer than that in the laminar case.

Turbulent (RNG k-ε model)

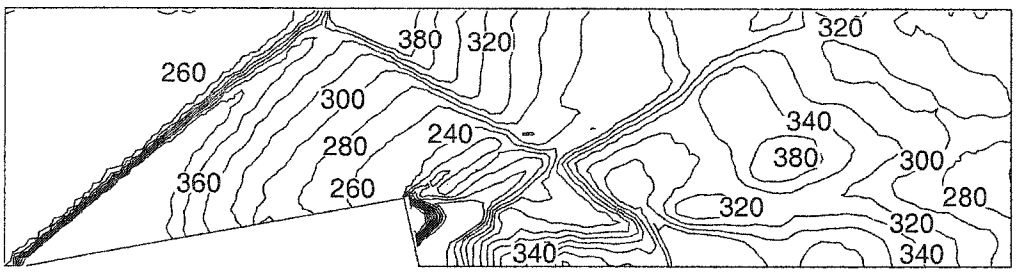

Laminar

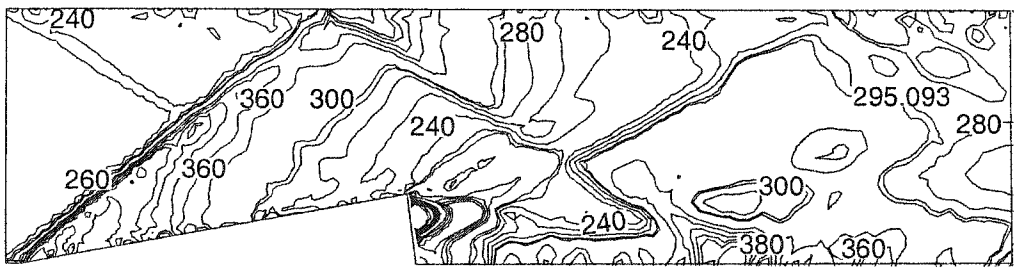

Fig. 4.4 Centerplane pressure contours of turbulent and laminar flows

Turbulent (RNG k-ε model)

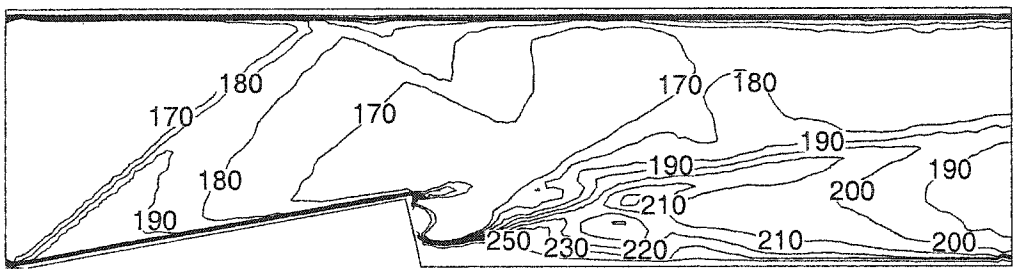

Laminar

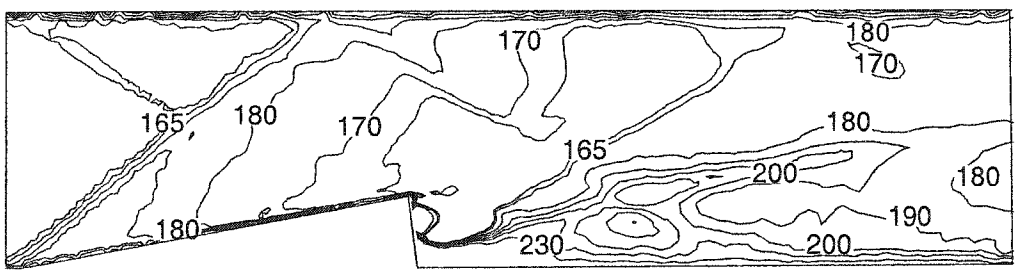

Fig. 4.5 Centerplane temperature contours ofturbulent and laminar flows

Turbulent (RNG k-ε model)

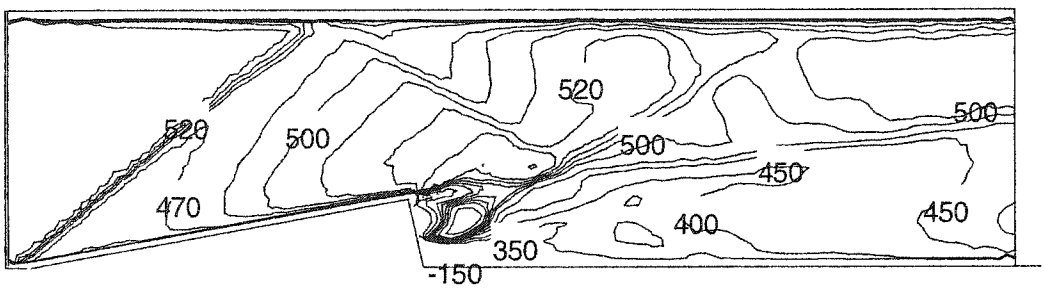

Laminar

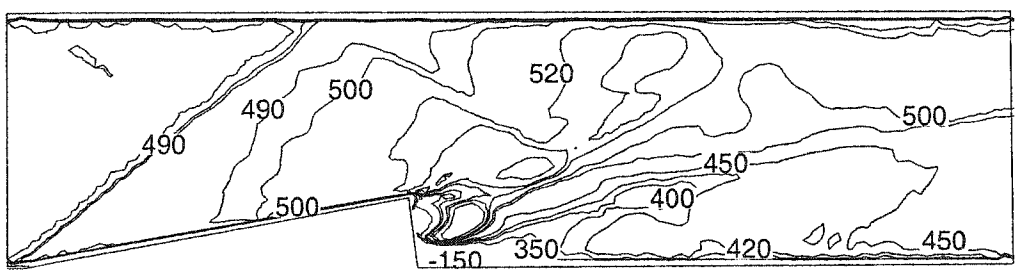

Fig. 4.6 Centerplane streamwise velocity contours of turbulent and laminar flows

Figures 4.7-4.9 show the decay of the maximum mole fraction, the mass-weighted averaged static pressure, and the mass-weighted averaged Mach number in the axial direction for the three turbulence models. The mass-weighted averaged pressure and Mach number are computed by using the following equations:

$$\overline{P} = \frac{\int P\rho\vec{V} \cdot d\vec{A}}{\int \rho\vec{V} \cdot d\vec{A}} \tag{4.1}$$

$$\overline{M} = \frac{\int M\rho\vec{V} \cdot d\vec{A}}{\int \rho\vec{V} \cdot d\vec{A}} \tag{4.2}$$

The figures show clearly that the three models give the same results. A slight difference is noted in the value of the maximum injectant mole fraction near the jet exit. Although the three turbulence models show no difference, the calculations in the current study are performed with the RNG k-ε model which is recommended in Ref. 76 for this type of flow problems.

4.3 Code Validation

Recently, computational fluid dynamics (CFD) has become an important tool in the design and the development of hypersonic propulsion systems. However, the results of any CFD code cannot be trusted until the code is validated with experimental results. The

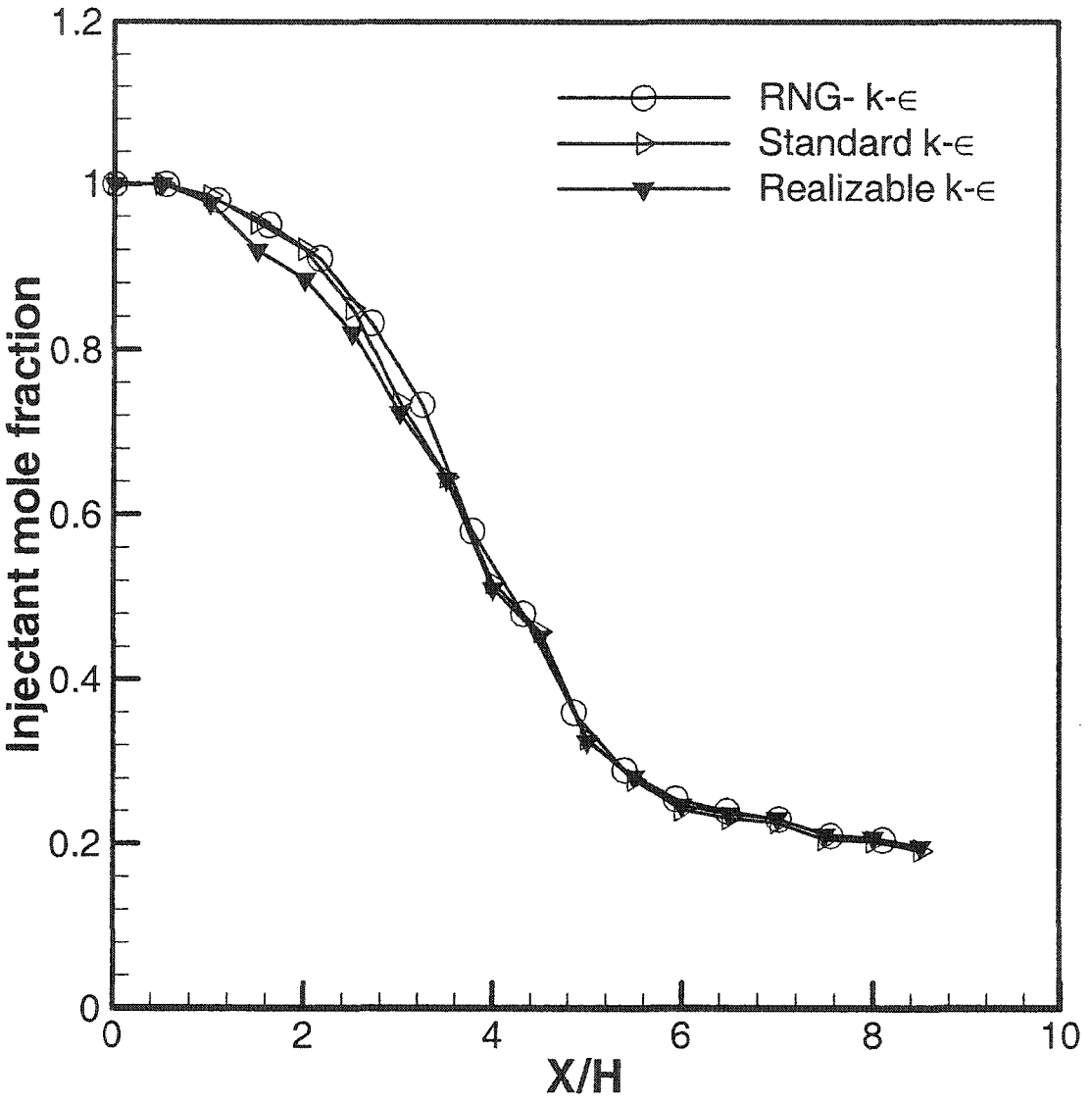

Fig. 4.7 Deacy of maximum injectant mole fraction along the axial direction

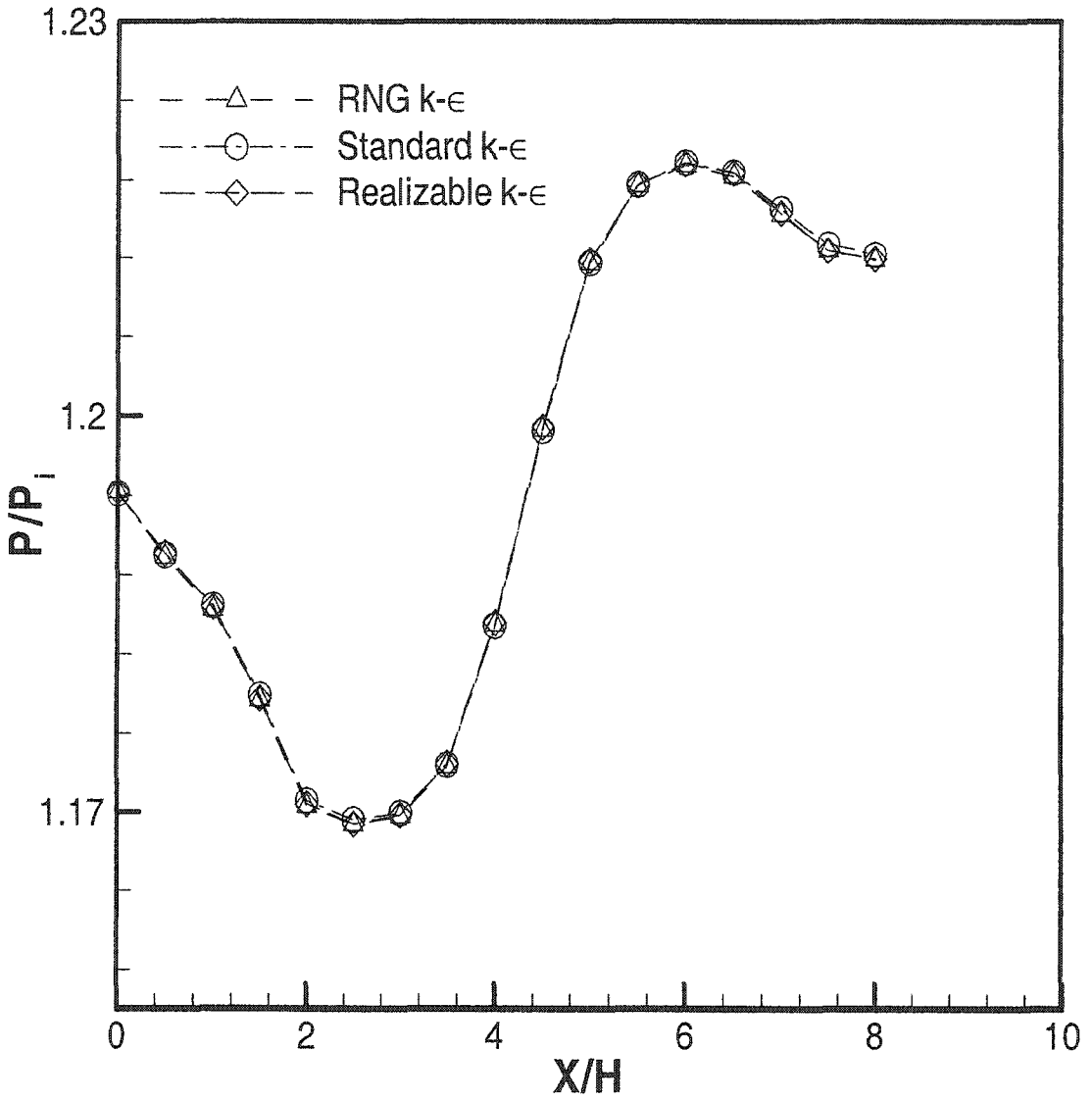

Fig. 4.8 Axial distribution of mass-averaged static pressure

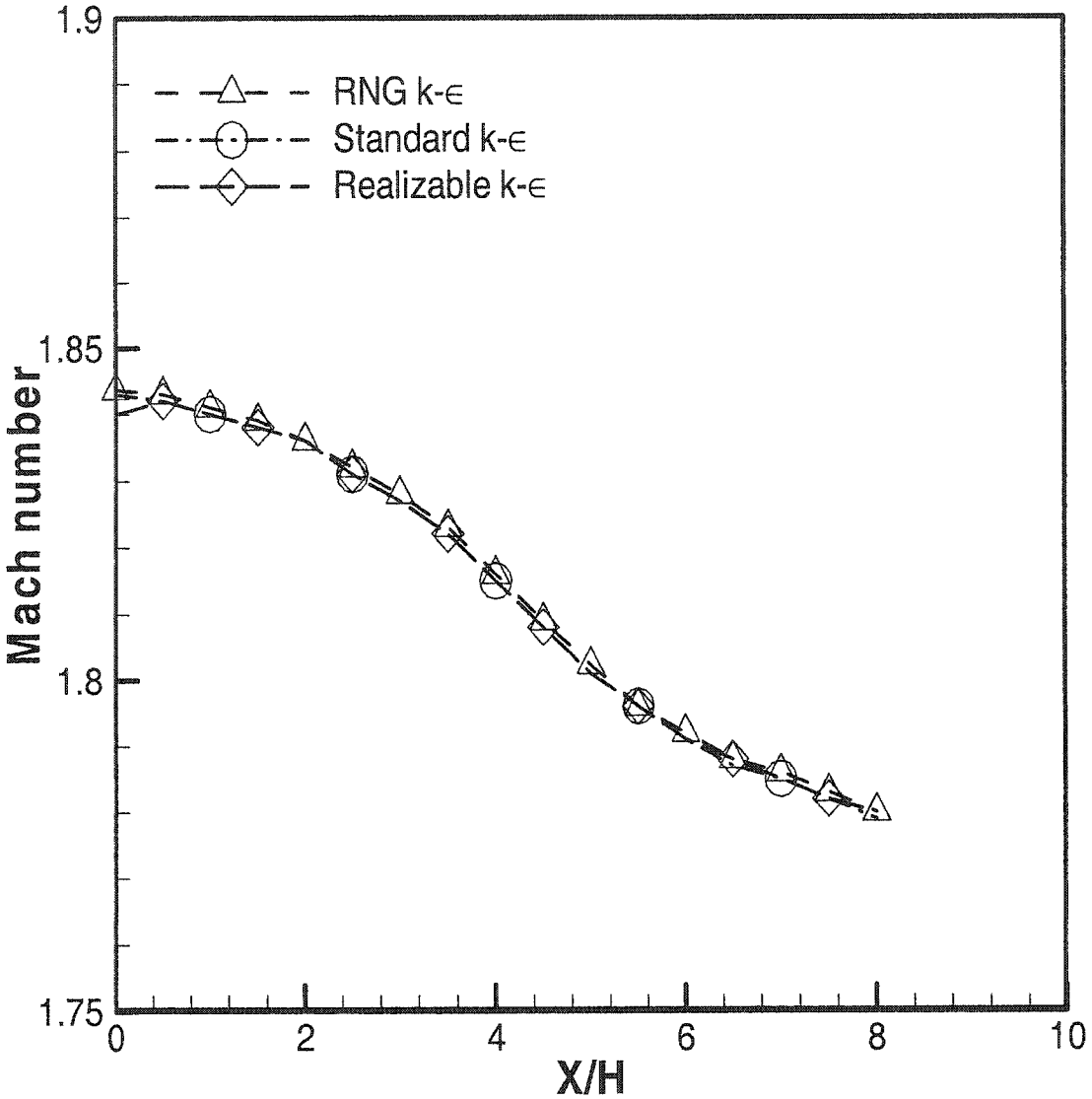

Fig. 4.9 Axial distribution of mass-average Mach number

validation of the CFD codes depends heavily on experimental data in carefully controlled experiment. The Fluent code has been validated for different applications. However, it is not completely validated for supersonic mixing before. Detailed comparisons have been made in the current study and will be presented in this section.

The results presented in this section represent the comparison with the available experimental results from the University of Virginia [37, 39]. Results of time-averaged measurements using the planar laser-induced fluorescence technique are presented. Iodine seeded air was used for optical measurement purposes. Iodine seeding has the advantage of accurate tracking through shock waves and other high-gradient regions. Furthermore, as reported by McDaniel et al. [35], the iodine seeding did not significantly change the thermodynamic properties of air.

In addition, the current results are compared with the numerical results of Mao [82]. The results of Mao [82] were obtained with a CFD code called GASP. A structured grid has been used with about 640,000 grid points. GASP solves Reynolds-Averaged Navier-Stokes equations. A cell-centered, finite-volume formulation was used with upwind-biased spatial discretization. Turbulence model was treated in his calculations with a two-equation k-ε model.

Comparisons are presented for the non-reacting flow. The ramp is a compression wall-mounted ramp with a 10-degree side angle. Calculations are performed by utilizing the RNG k-ε turbulence model. Flow conditions at the inlets are given in Table 4.2. Contours of static pressure, static temperature, mole fraction, and streamwise velocity are presented and are shown in Figs. 4.10-4.20. Comparisons are presented at the plane of symmetry as well as at different crossflow planes.

Table 4.2 Non-reacting freestream and injectant conditions

Parameter	Freestream conditions	Injectant conditions
P_o (kPa)	262	248
T_o (K)	300	300
P (kPa)	33.5	50.24
T (k)	163	189
Mach Number.	2.0	1.7
Turbulence Intensity	1.6%	5%

4.3.1 Results Near the Nozzle Exit

Profiles of streamwise velocity, injectant mole fraction, and pressure across the test section cutting through the jet core at X/H =0.5 and Y = 0 are given in Figs. 4.10 - 4.12. The figures compare the numerical results with the experimental results of Donohue et al. [39].

Figures 4.10 and 4.11 show the mole fraction and the stream wise velocity profiles. The stream wise velocity is normalized with respect to the inlet value, while the Z coordinate is normalized with respect to the ramp height. The agreement between the calculations and the experimental results is good. Small differences appear in the velocity profile near the location of the shock interaction. The pressure profile is shown in Fig. 4.12. The pressure is normalized with respect to the inlet pressure. The calculations do not show clearly the shock interaction between the fuel jet and the freestream as in the experiment. The flow field in this region is highly three-dimensional. For this reason, the differences could be due to the resolution of the grid at this location or due to some errors in the measurements. However, both the calculations and the experiment show the same trend. The differences seen in this figure are also clear in the results of the symmetry plane.

One of the methods that have been used to express the mixing rate of the fuel and the air is the decay of the maximum mole fraction downstream of the injector. Figure 4.13 compares the decay of the injectant mole fraction with the experimental results of Hartfield et al. [38] where a similar, but not identical, ramp has been used with a ramp side angle of 9 degrees. The figure shows excellent agreement except far downstream of the injector. Near the end of the combustor, approximately at X/H=7.0, the current

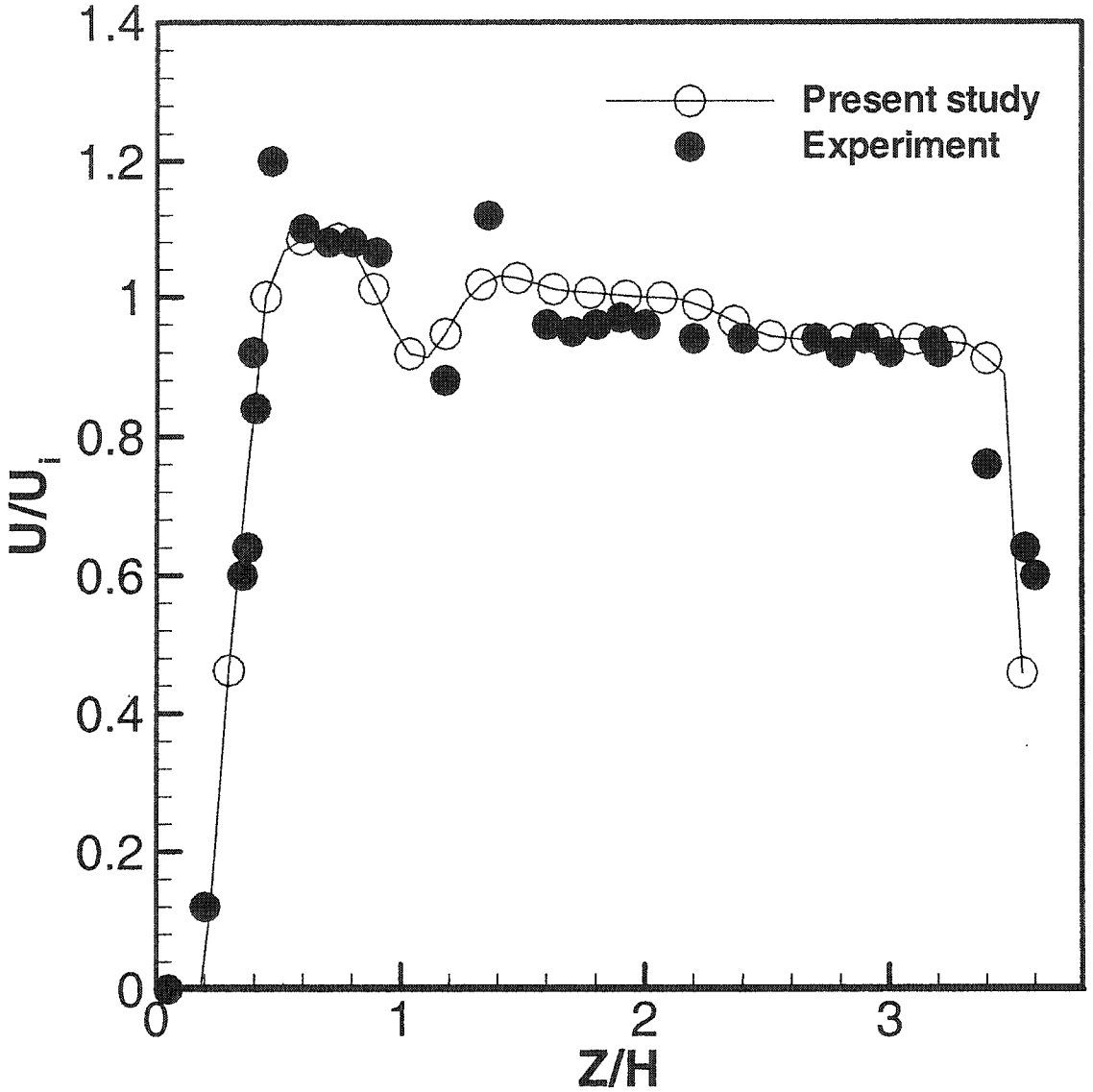

Fig.4.10 Axial velocity profile across the test section cutting through the jet core at X/H=0.5 and Y=0.0

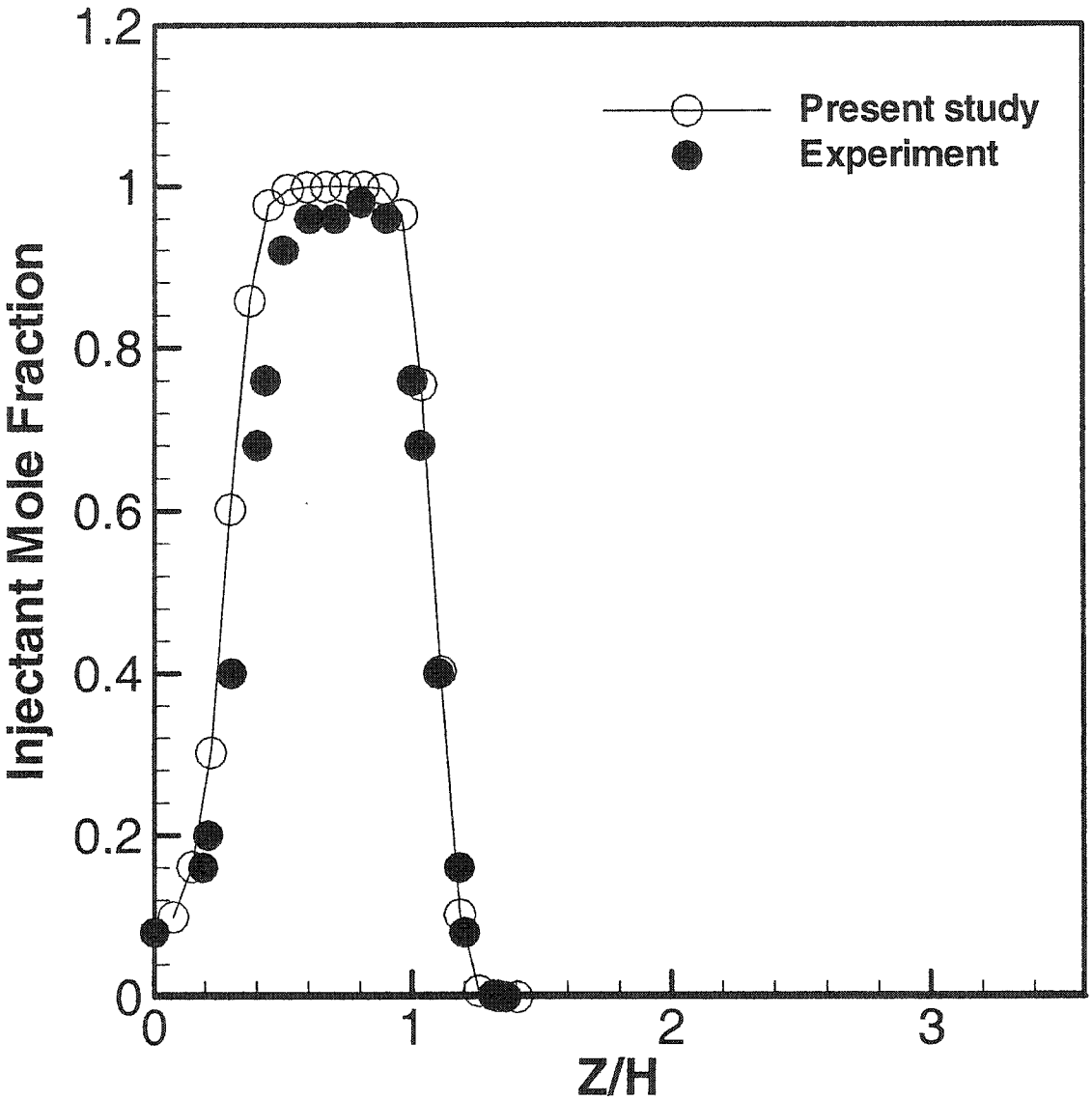

Fig.4.11 Mole fraction profile across the test section cutting through the jet core at X/H=0.5 and Y=0.0

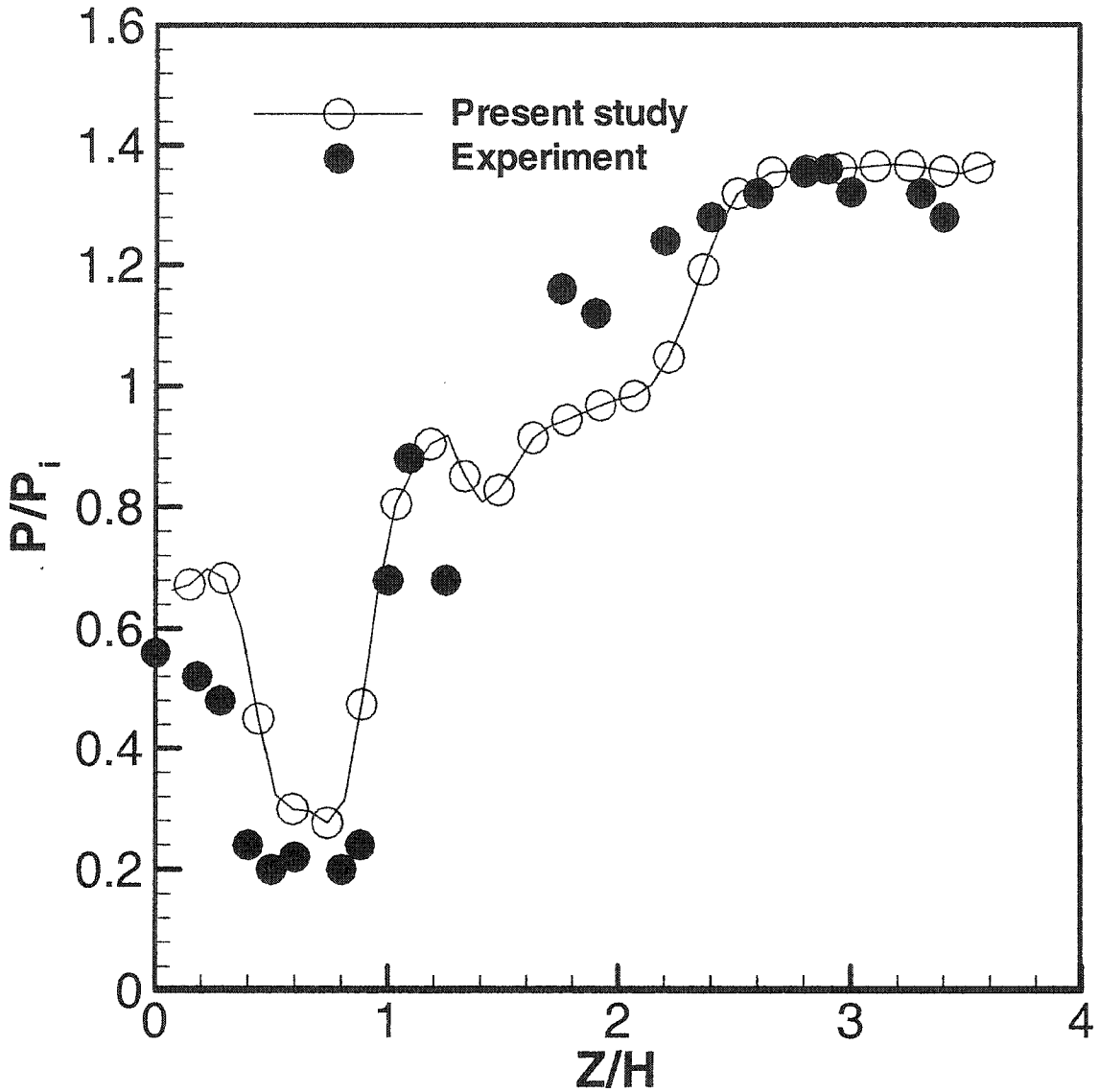

Fig.4.12 Static pressure profile across the test section cutting through the jet core at X/H=0.5 and Y=0.0

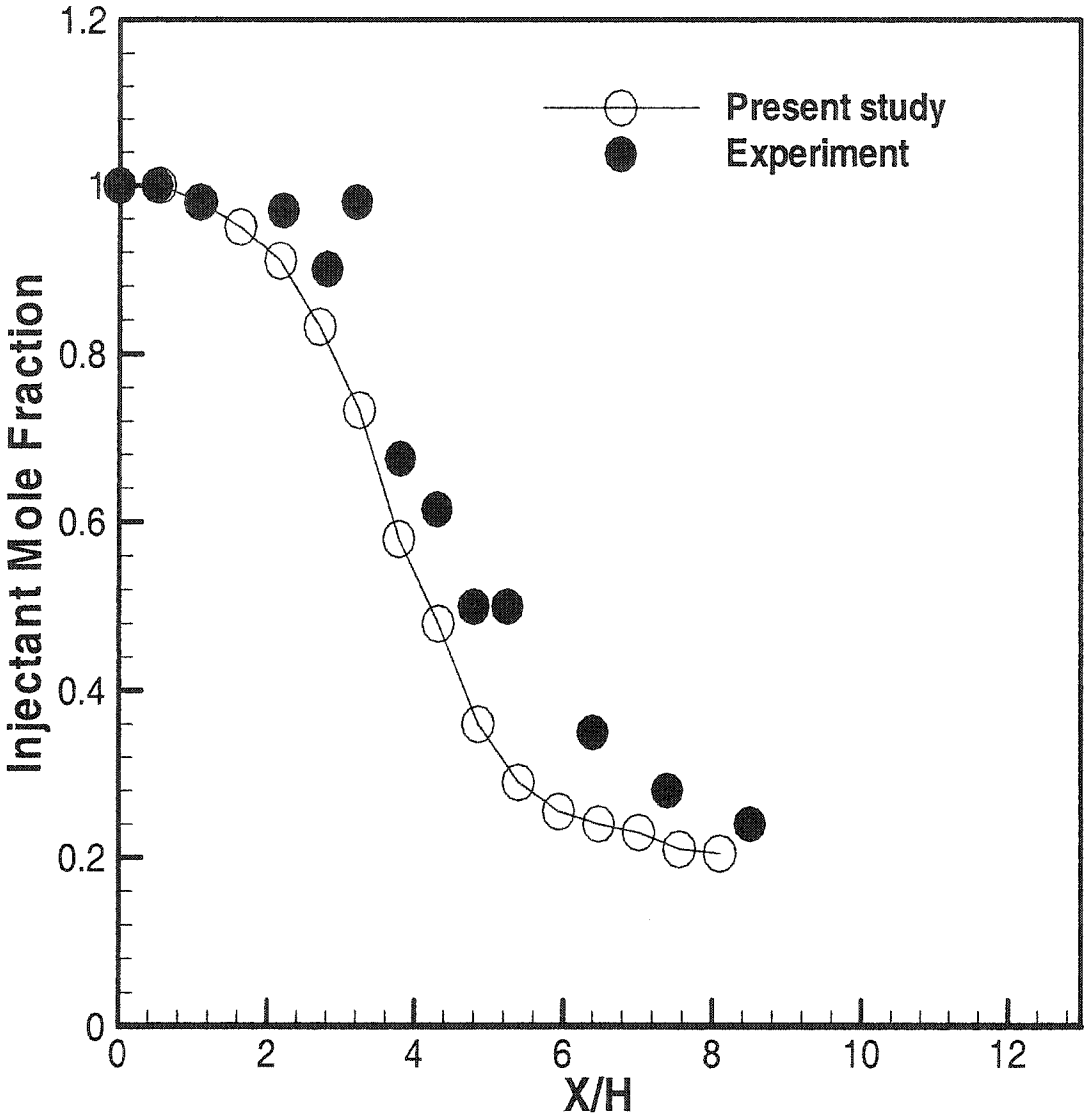

Fig.4.13 Decay of maximum injectant mole fraction along the axial direction

calculations show about 6% less in the maximum mole fraction than the experimental results. The difference at this section could be due to the slight difference in the side angle as it is shown in the following section. Another reason is the distribution of the grid at this section.

4.3.2 Results at the Symmetry Plane

Figure 4.14 compares the pressure on the tunnel centerplane. The agreement between the experiment and numerical results is generally very good, with differences mostly confined to specific regions. Shocks are captured with varying resolution in the calculation. Both codes captured well the ramp compression shock and its reflection from the opposing wall. The pressures in the near wake region agree well though GASP shows higher values in the jet core before the Mach disk. Downstream, current calculations predict well the reflected shock off the top surface. However, GASP calculation shows a weakly reflected shock, probably the results of insufficient grid resolution in the far field. Numerical results show that the pressure levels (the magnitudes of the pressure) are very close to the experimental values. Although the numerical results do not capture the second reflection near the top wall completely, there is still good agreement with the experimental results.

The centerplane temperatures are compared in Fig 4.15. The agreement between the two numerical results is very good. However, the agreement with the experiment is only fair. As indicated in Ref. [39], there are discrepancies attributed to light scattering near the surfaces during measurement. Along the top wall, in the three cases, temperature contours turn parallel to the wall. The values of the temperatures predicted by the two codes are almost the same. Both codes predict higher temperatures in the ramp base

Experiment

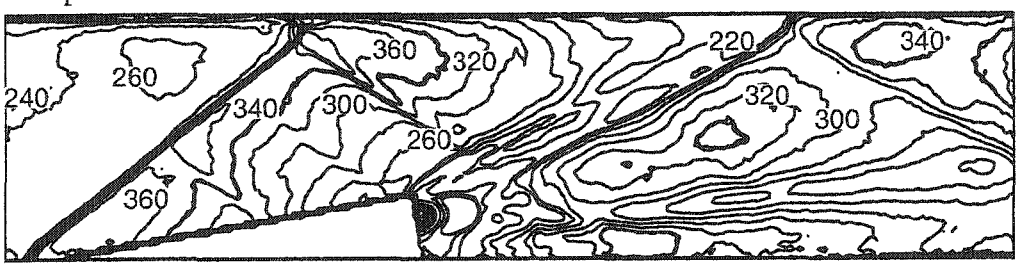

GASP

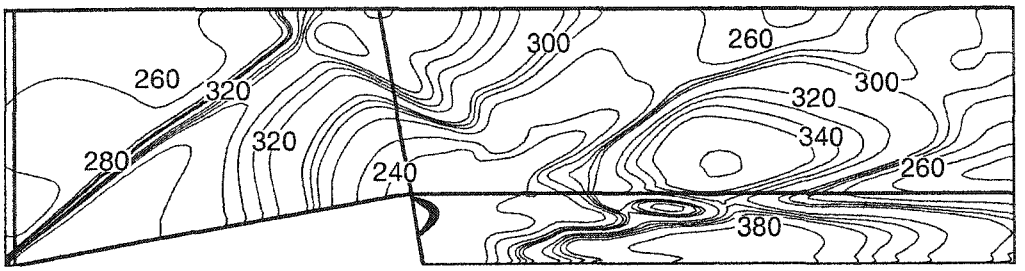

Present study

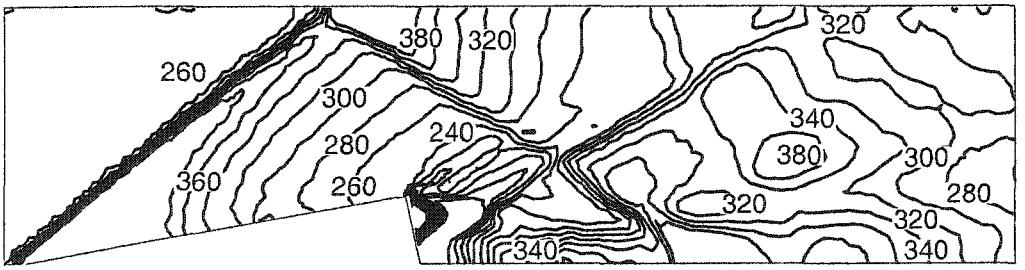

Fig. 4.14 Centerplane static pressure contours

Experiment

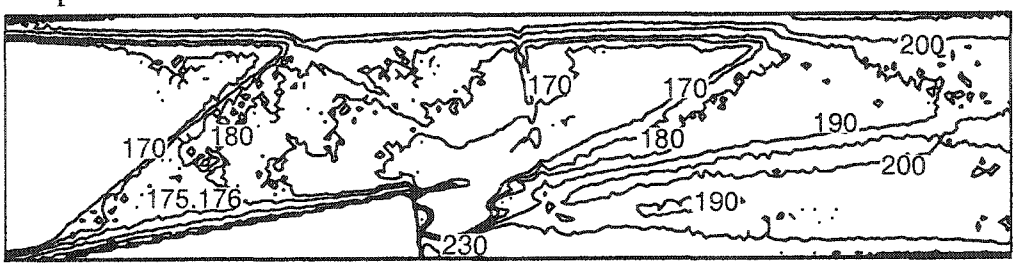

GASP

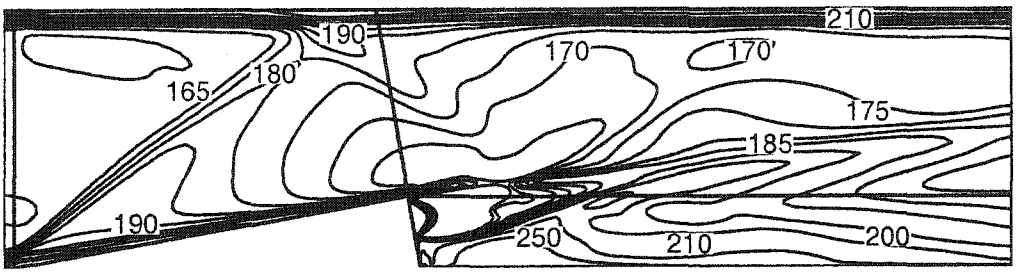

Present study

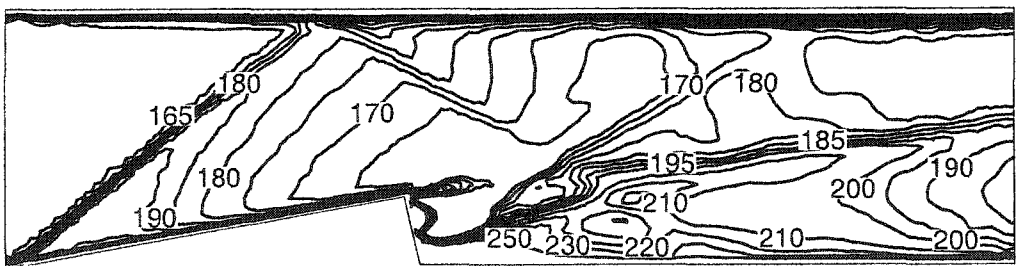

Fig. 4.15 Centerplane static temperature contours

recirculation region than the measured temperatures. The current calculations clearly predict the oblique shock wave at the ramp as well as the shock reflection. The thermal boundary layer of the top wall, in all cases, becomes thick at shock reflection.

Figure 4.16 presents the centerplane streamwise velocity contours. Generally, the agreement between the experiment and numerical results obtained by both codes is very good. Again, the oblique shock waves and the shock reflections are well captured by the current calculations. The results of GASP slightly show the reflections. In general, the values of the velocities in the three cases are very close. However, the velocities at the base of the ramp are about 4% higher in the calculations than in the experiment. The calculated and the measured velocities in the region near the jet agree very well. Near the exit plane, the current code shows excellent agreement with the results of GASP. However, both codes show poor agreement with the experiment in this region. The velocity is 10% less than that in the experiment.

The injectant mole fraction distributions at the centerplane are shown in Fig. 4.17. The present results agree well with both the GASP results and the experimental data. The penetration of the jet plume into the freestream and the core decay are well captured. Values of the mole fraction are almost the same. However, the decay in the experiment is faster than that predicted by the two numerical codes.

4.3.3 Results at Crossflow Planes

Experimental data are available for three crossflow planes, namely, X/H=0.5, X/H=2.0, and X/H=8.0. These crossflow planes results will give an idea about the flowfield near the fuel jet and far downstream of the fuel jet.

Experiment

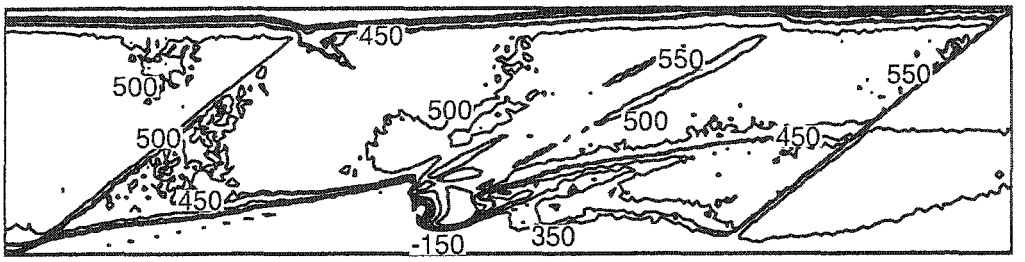

GASP

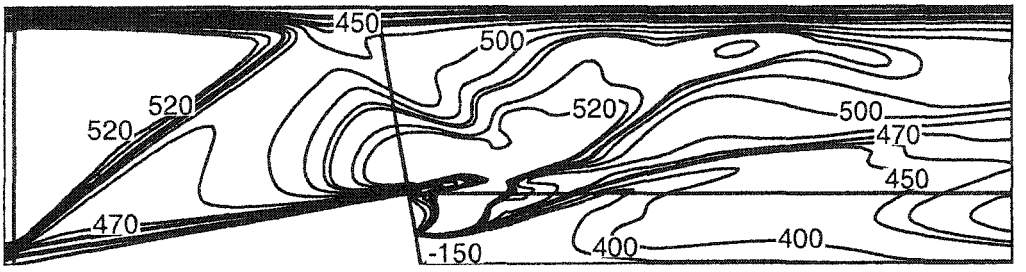

Present study

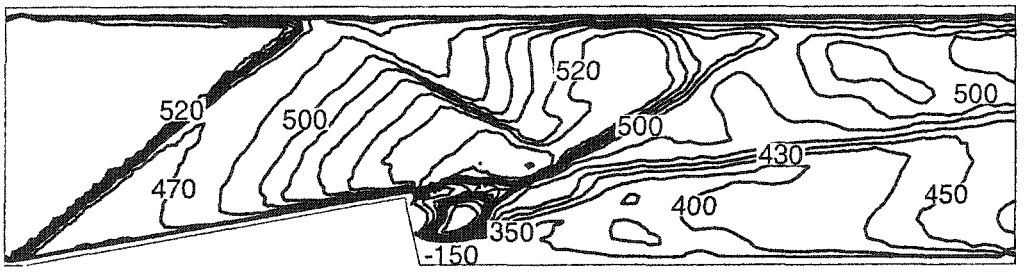

Fig. 4.16 Centerplane u-velocity contours

Experiment

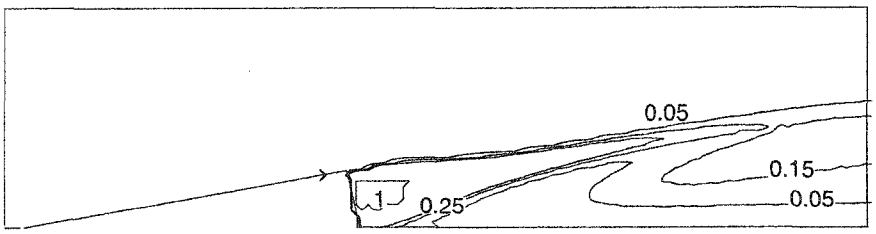

GASP

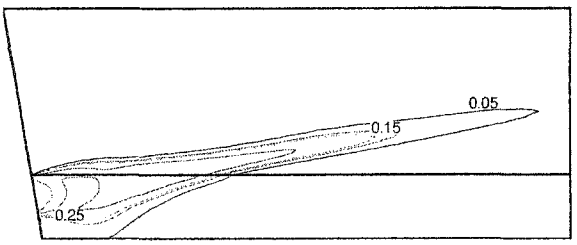

Present study

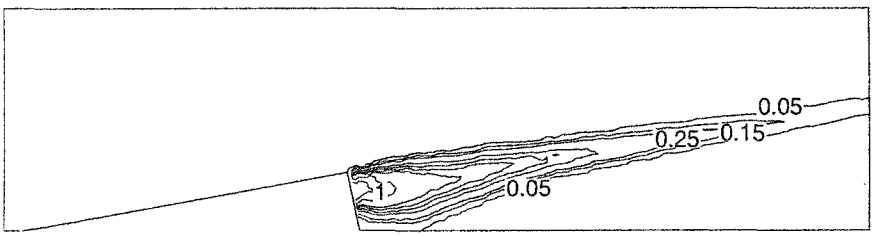

Fig.4.17 Centerplane injectant mole fraction

The pressure contours in the three crossflow planes are shown in Fig. 4.18. The pressure agreement is good. The flowfield features, such as shock locations and the position and strength of the vortices, are apparent in the pressure field. Although both codes predict higher pressure gradients in the measured vortex core, the current calculations indicate higher pressure in the core of the jet than the experiment, specially at the X/H = 2 plane. As mentioned before, this could be due to the grid resolution in the crossflow plane.

The temperature distributions in the same crossflow planes are compared in Fig. 4.19. The temperature agreement is fair. The numerical results obtained from the current calculations and GASP codes are similar. However, both codes predict higher temperature than the measured temperature in the ramp base recirculation region. As indicated in Ref. 6, there are discrepancies attributed to light scattering near the surfaces during measurement.

The injectant mole fraction distribution at three crossflow planes is shown in Fig. 4.20. Fuel injected from the base region of the ramp is mixed into the freestream air by the ramp-generated vortices. The results from both codes agree well with the experimental data. At X/H =2, the experimental plume displays slightly more curling. The penetration, spreading, and locations of maximum concentrations are in very good agreement. At X/H= 8.0, current calculations slightly under predict the peak mole fraction. The kidney-shaped structure is still shown in the calculations, while in the experiment the lobes have merged.

Finally, from the above comparisons it can be concluded that the current code is predicting well the complex three-dimensional compressible flow field around the ramp

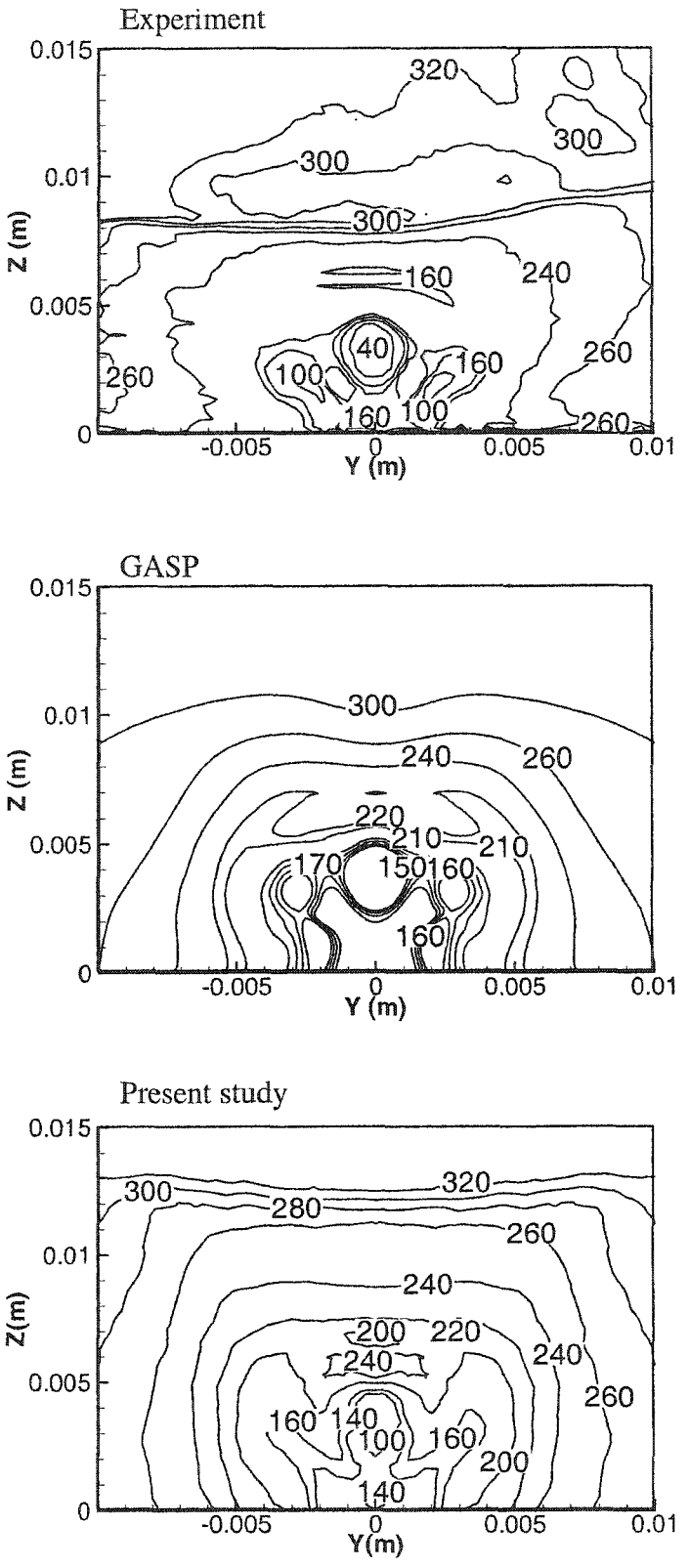

a. cross-section at X/H=0.5.

Fig. 4.19 Contours of constant static temperature

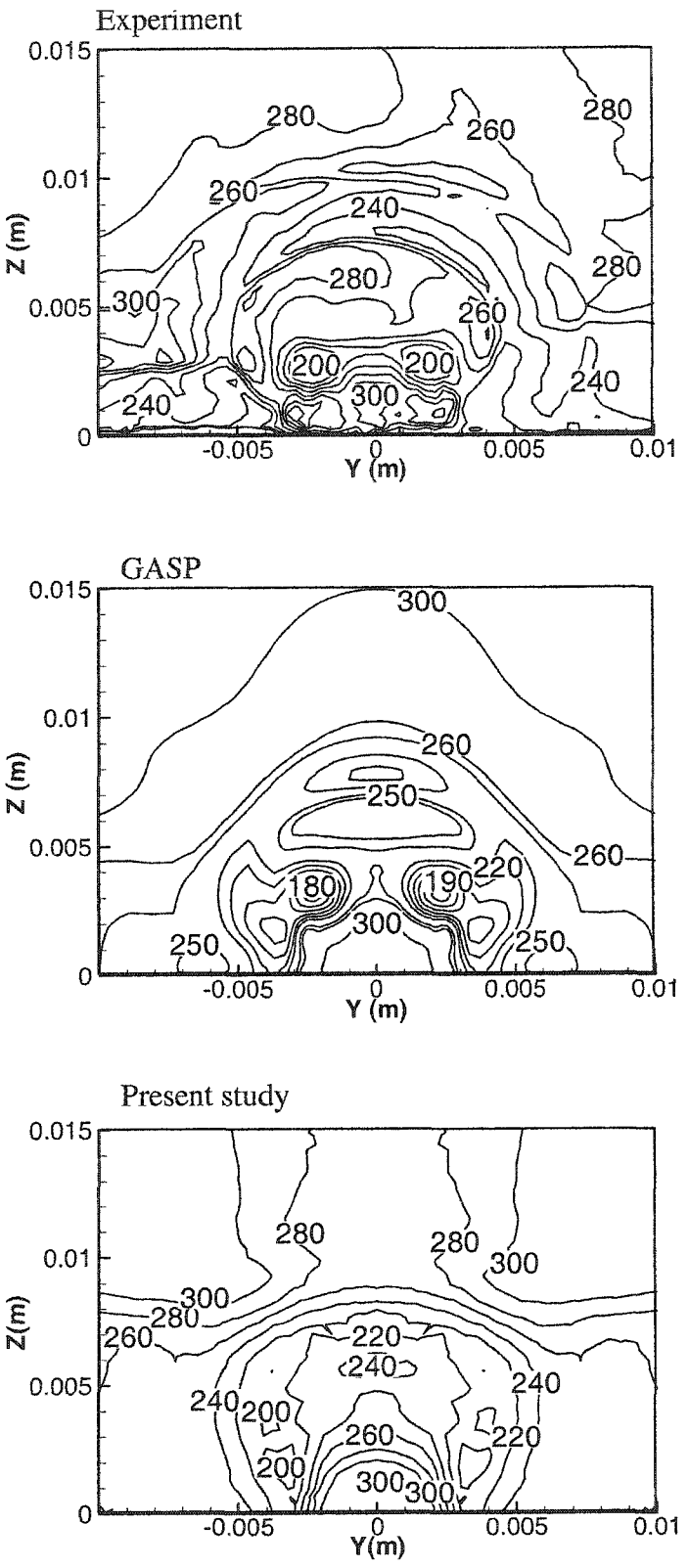

b. cross-section at X/H=2.0.

Fig. 4.19 (contd.) Contours of constant static temperature

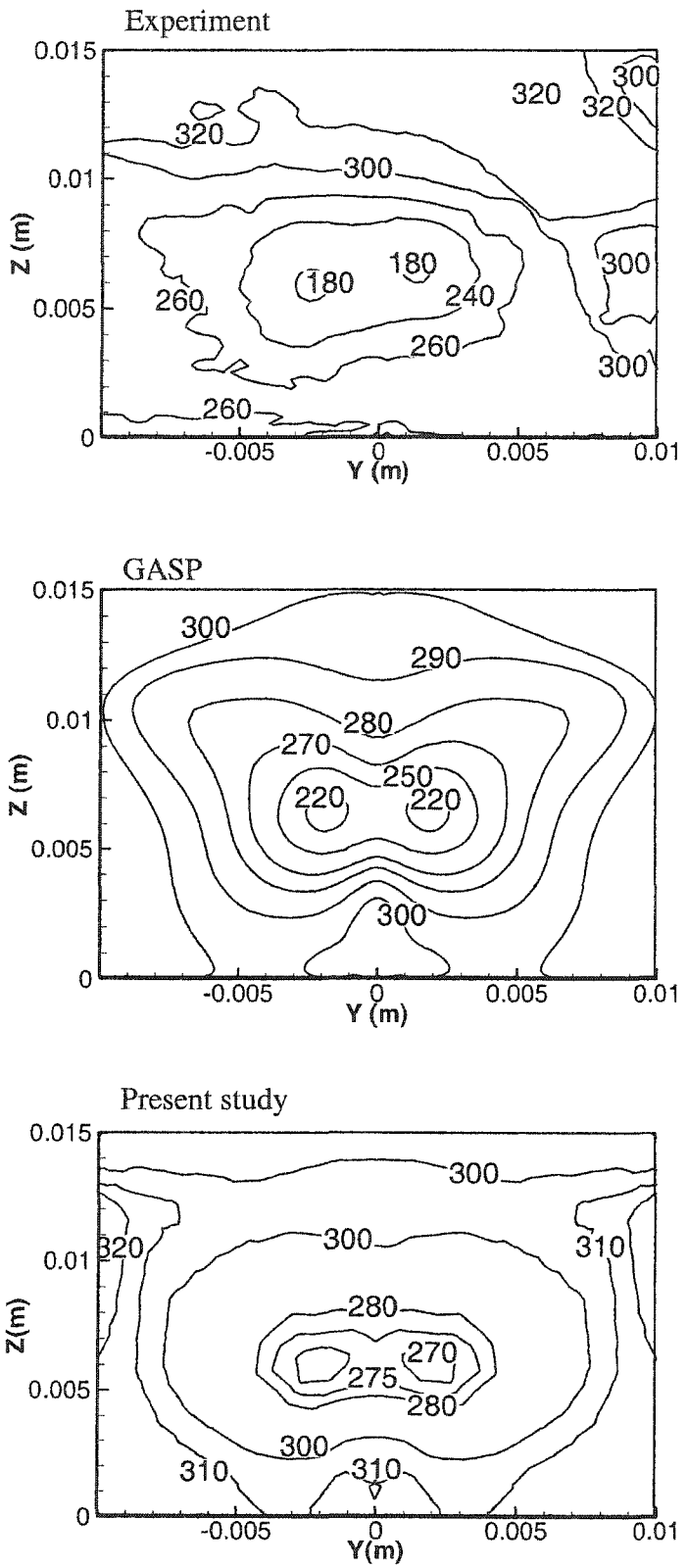

c. cross-section at X/H=8.0.

Fig. 4.19 (contd.) Contours of constant static temperature

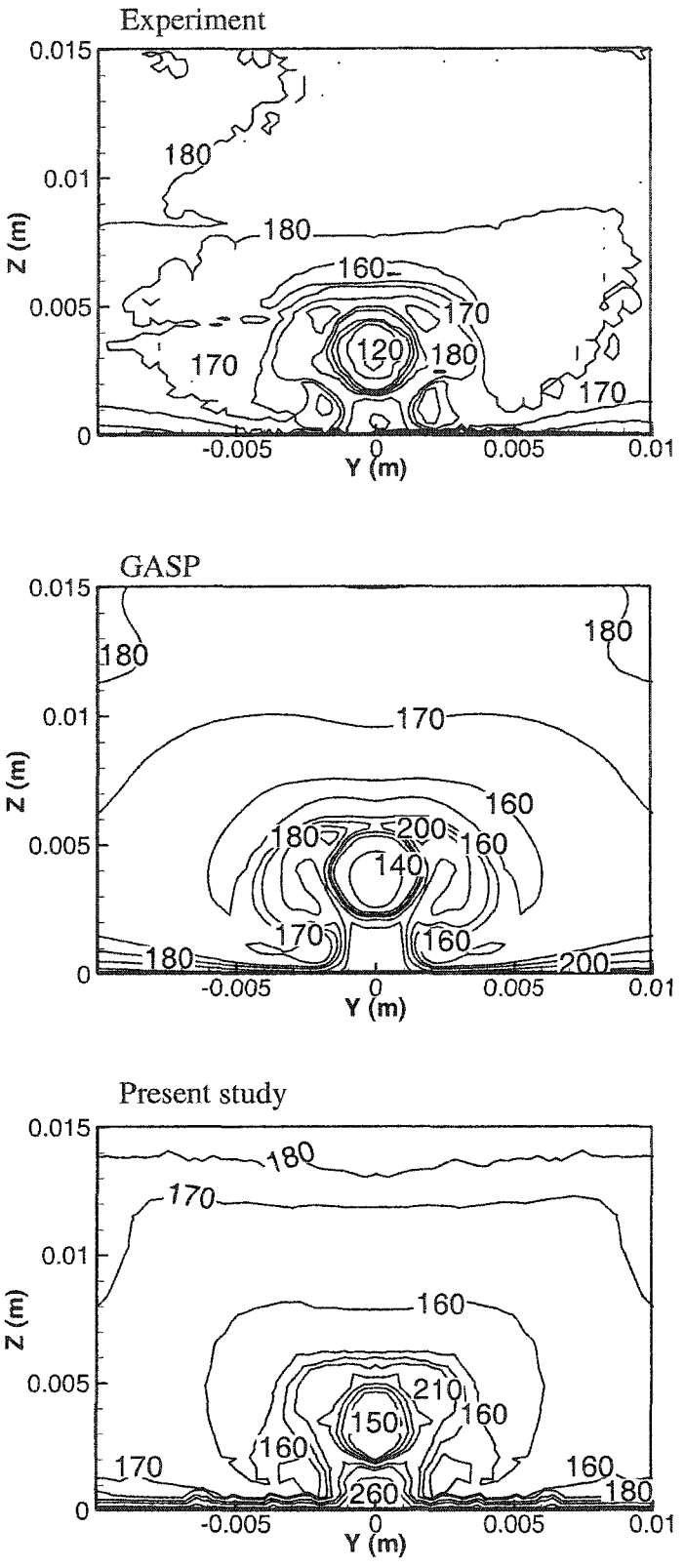

a. cross-section at X/H=0.5.

Fig. 4.18 Contours of constant static pressure

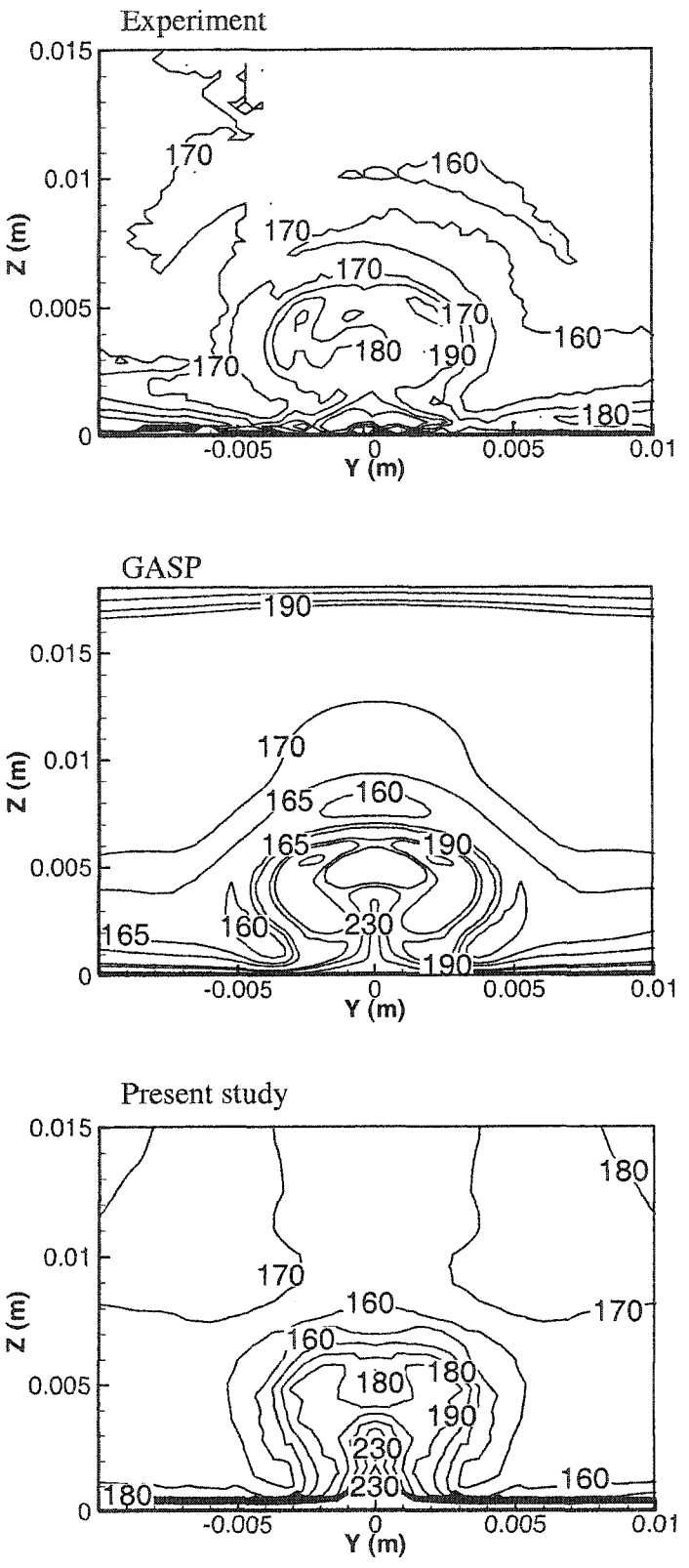

b. cross-section at X/H=2.0.

Fig. 4.18 (contd.) Contours of constant static pressure

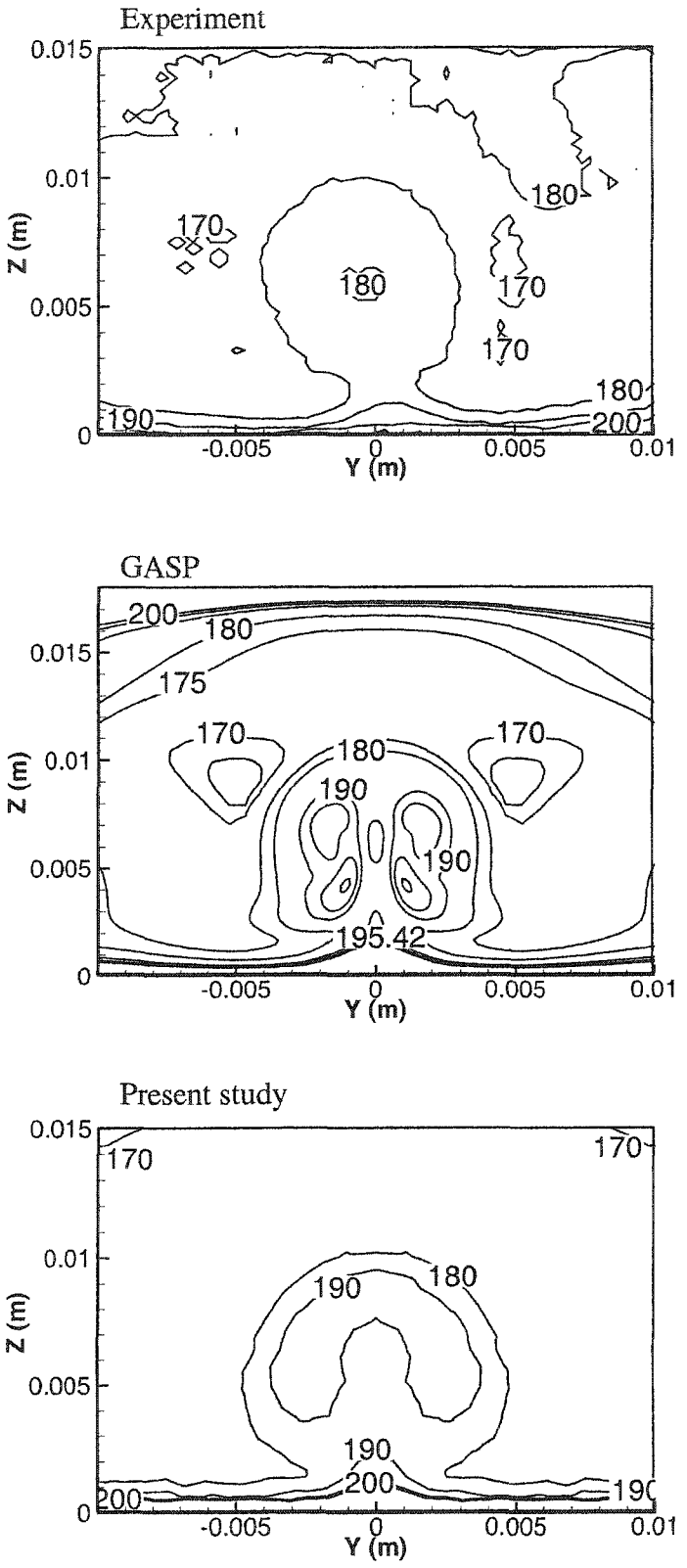

c. cross-section at X/H=8.0.

Fig. 4.18 (contd.) Contours of constant static pressure

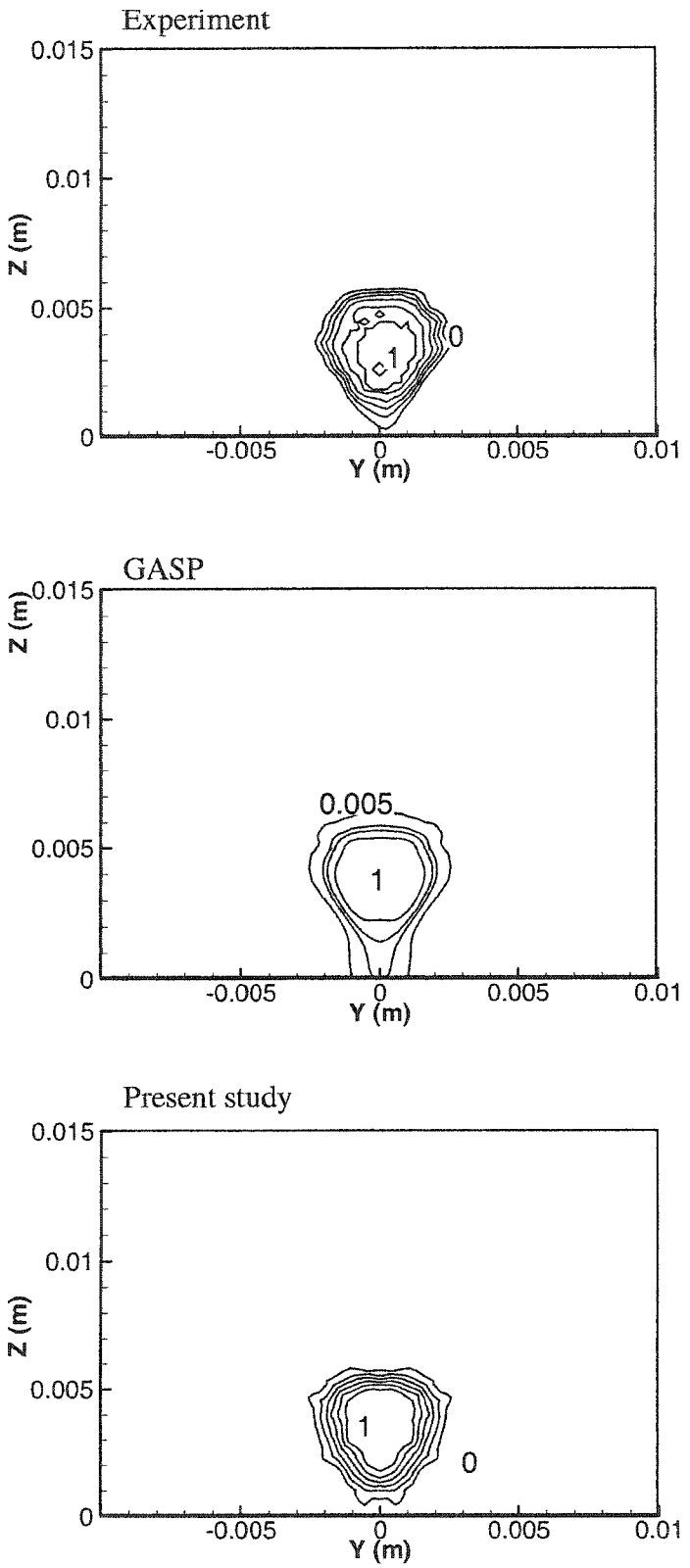

a. cross-section at X/H=0.5.

Fig. 4.20 Contours of constant injectant mole fraction

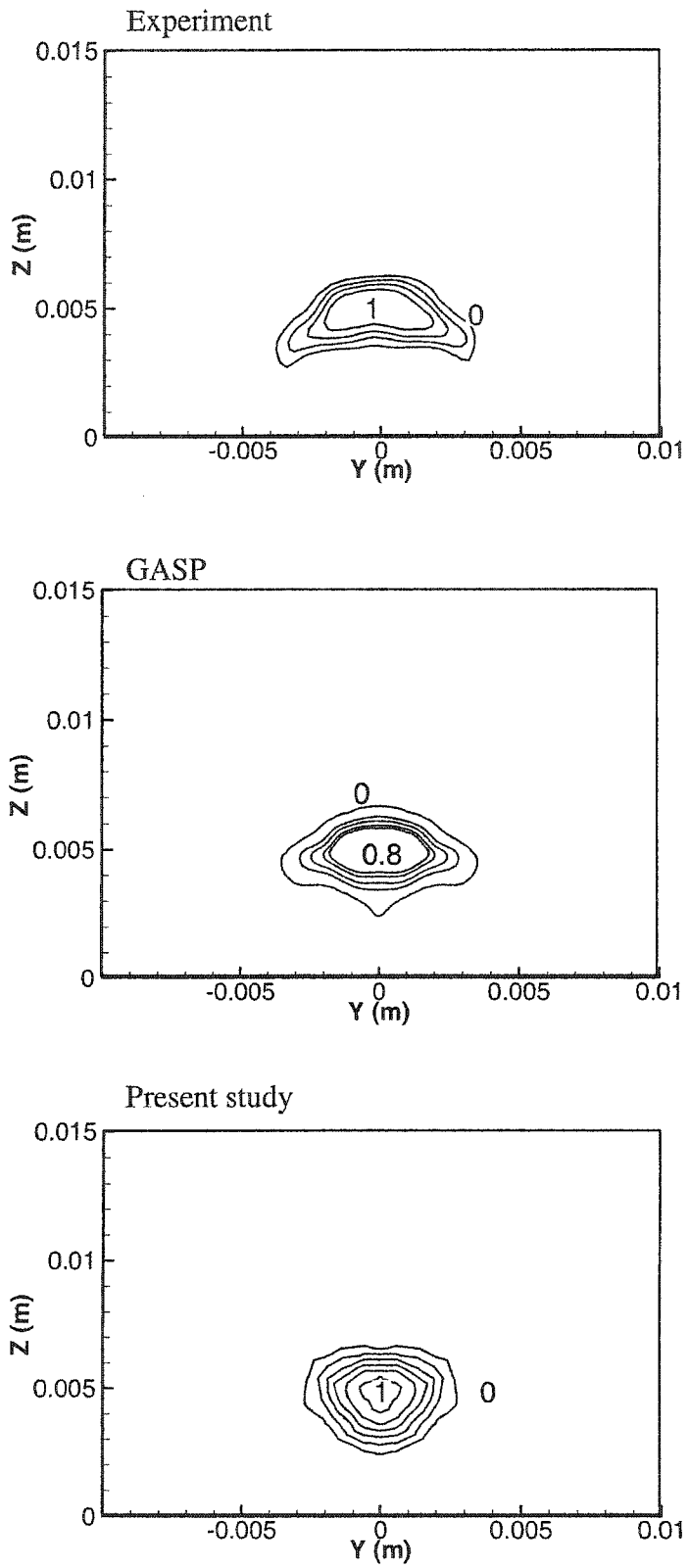

b. cross-section at X/H=2.0.

Fig. 4.20 (contd.) Contours of constant injectant mole fraction

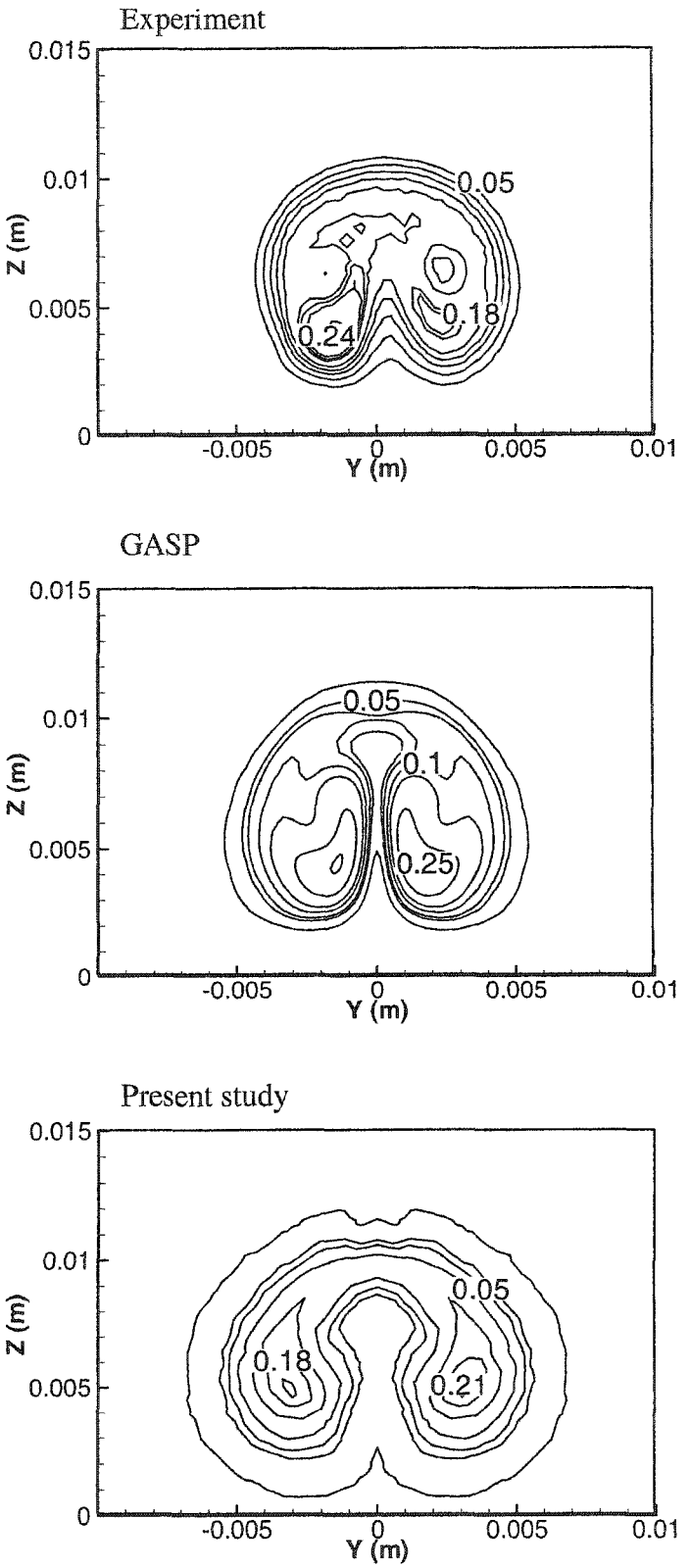

c. cross-section at X/H=8.0.

Fig. 4.20 (contd.) Contours of constant injectant mole fraction

fuel injector. Overall, agreement with the experimental and the numerical work is excellent. It is to be noted that the current calculations presented above are obtained with an unstructured grid of about 300,000 grid points. This grid size is less than 50% of the structured grid used for the numerical calculations of Mao[82].

4.4 Effects of Ramp Side Angle on Mixing and Combustion

The results presented here show the effects of the side angle on the mixing process for both nonreacting and reacting flows. Three ramps are investigated with side angles of 0, 5, and 10 degrees (Figs. 3.2-3.4). At the beginning, the main flow field results (without injection) are presented and compared with both the nonreacting flow and the reacting flow to give a clear idea of the flowfield structure. For nonreacting flows, inlet conditions are the same as in the previous section, shown in Table 4.2. Table 4.3 shows the flow conditions at the inlets for reacting flows. Figures 4.21- 4.22 show the contours of static pressure, and streamwise velocity at the plane of symmetry for the three flows. The flow field is the same before the fuel nozzle. The effect of the injectant is clearly seen in Fig. 4.21 where the shock waves and the reflections become much stronger and the values of the pressure contours become higher. In the reacting flow a shock train is seen in the combstor after the ramp due to the chemical reaction and the heat release. Figure 4.23 shows the distribution of the static temperature at the plane of symmetry for both nonreacting flow and reacting flow. The shape of the fuel jet is clear in the reacting flow along the combustor. Higher values of temperature are noticed around the fuel jet in the reacting zone.

Table 4.3 Reacting freestream and injectant conditions

Parameter	Freestream conditions	Injectant conditions
P_o (kPa)	305	750
T_o (K)	1200	460
P (kPa)	37	152
T (k)	647	285
Mach Number	2.07	1.7
Turbulence Intensity	1.6%	5%

No injection

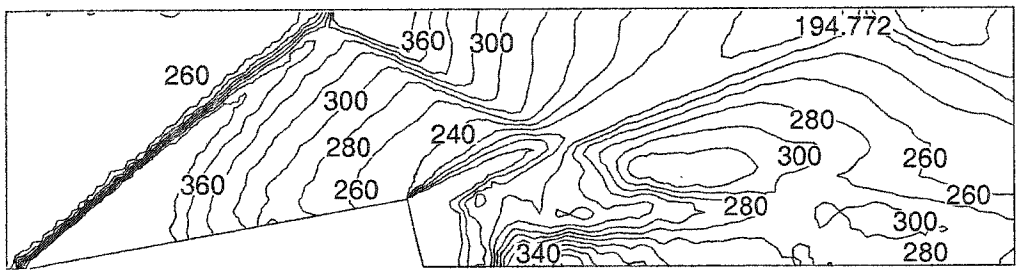

Non reacting flow

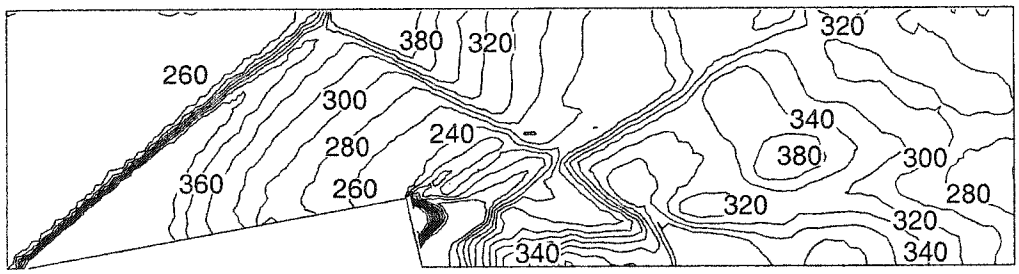

Reacting flow

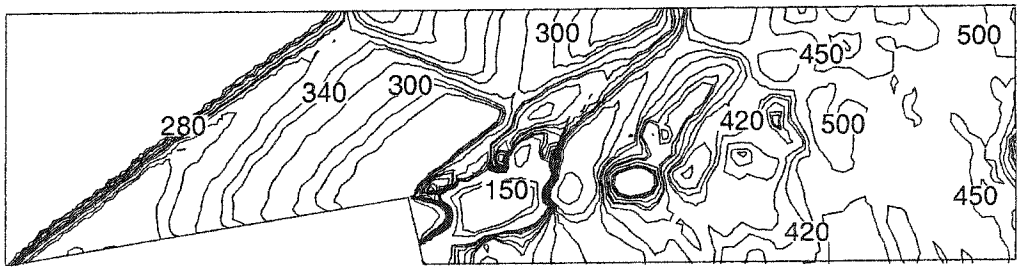

Fig. 4.21 Centerplane static pressure contours of the 10-degree ramp

No injection

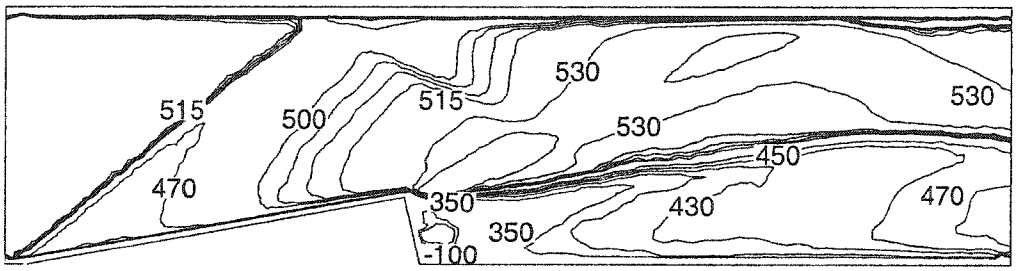

Non reacting flow

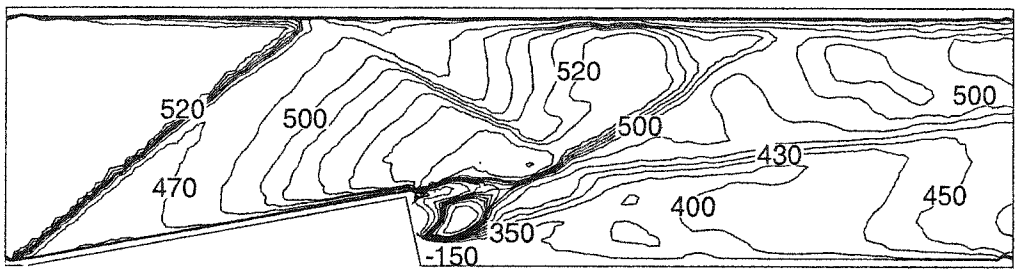

Reacting flow

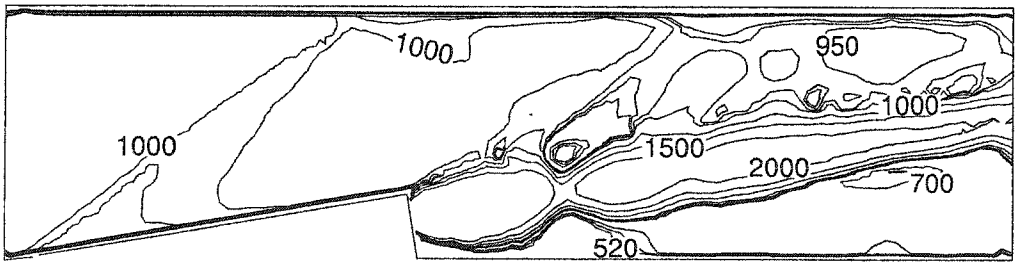

Fig. 4.22 Centerplane axial velocity contours of the 10-degree ramp

Non reacting flow

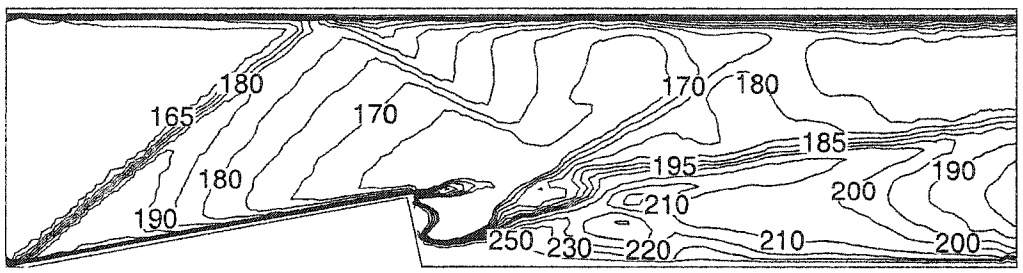

Reacting flow

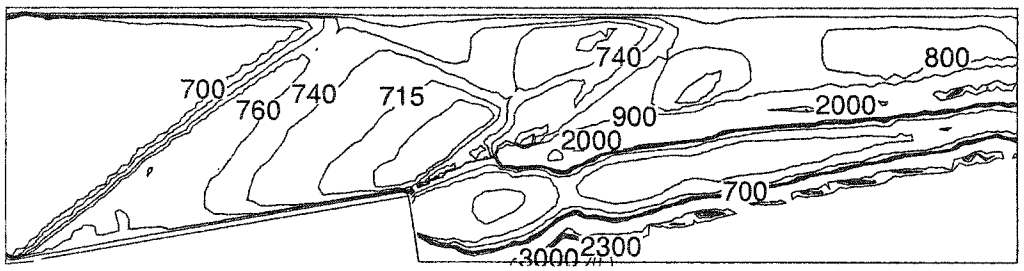

Fig. 4.23 Centerplane static temperature contours of the 10-degree ramp

Figure 4.24 shows the streamwise vorticity illustrated by the velocity vectors in different crossflow planes. The design goal of the ramp configuration is for the axial vortices to entrain the central fuel jet, ultimately leading to downstream mixing. The vortices are generated by the pressure gradient between the ramp surface and the ramp sides. The relative strengths can be seen clearly. As would be expected, the 10-degree swept ramp has the stronger vortex followed by the 5-degree swept ramp; also, the location of the vortex center moves outwards from the centerline and downwards to the side walls. In the X/H=0.5 plane, the two counter-rotating pairs of axial vortices are seen in the 10-degree ramp, and they slightly appear in the 5-degree ramp, while they are not seen in the unswept ramp which confirm the high mixing rate of the swept ramp. Downstream of the ramps the vortices become weaker.

The injectant mole fraction cross flow distribution for three ramp side angles is shown in Fig.4.25. Fuel is injected from the front base region of the ramp and is mixed into the freestream air by the ramp generated vortices. The figure compares the crossflow results of the three ramps at different axial locations from the ramp base, X/H=0.5, 2.0, 4.0, 6.0, and 8.0. The effect of the vortices created by the ramp side angle becomes very clear downstream of the ramp. At X/H=4.0 the kidney-shaped plume is formed at a shorter distance for the 10-degree swept ramp than in the 5-degree swept ramp while it is still not formed in the unswept ramp. Also, the spread of the injectant is wider in the 10-degree swept ramp than in the other two ramps. This is due to the effect of changing the side angle of the ramp. Further downstream, at X/H=8.0, the same trend of increased spread with larger angle is also obtained in this plane.

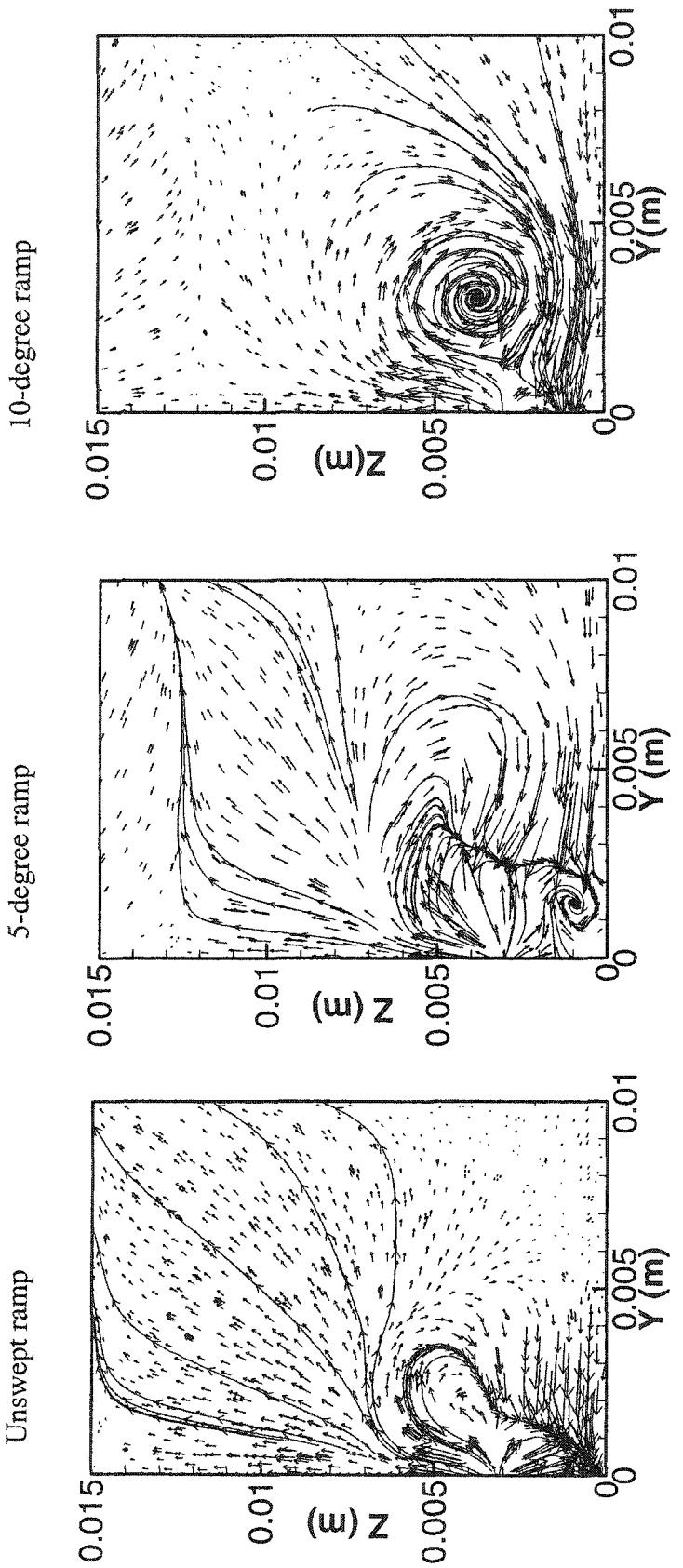

a. cross-section at X/H=0.5.

Fig. 4.24 Crossflow plane velocity vectors

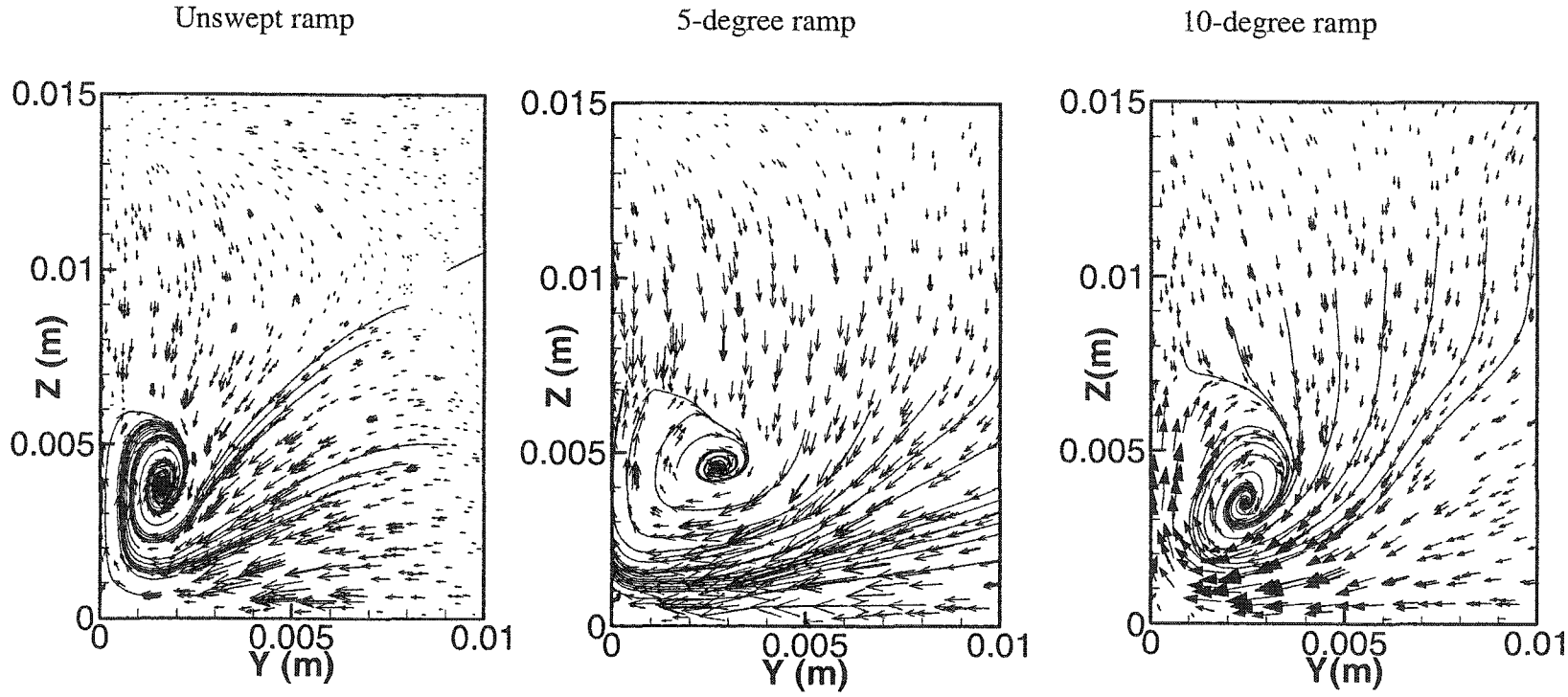

b. cross-section at X/H=2.0.

Fig. 4.24 (contd.) Crossflow plane velocity vectors

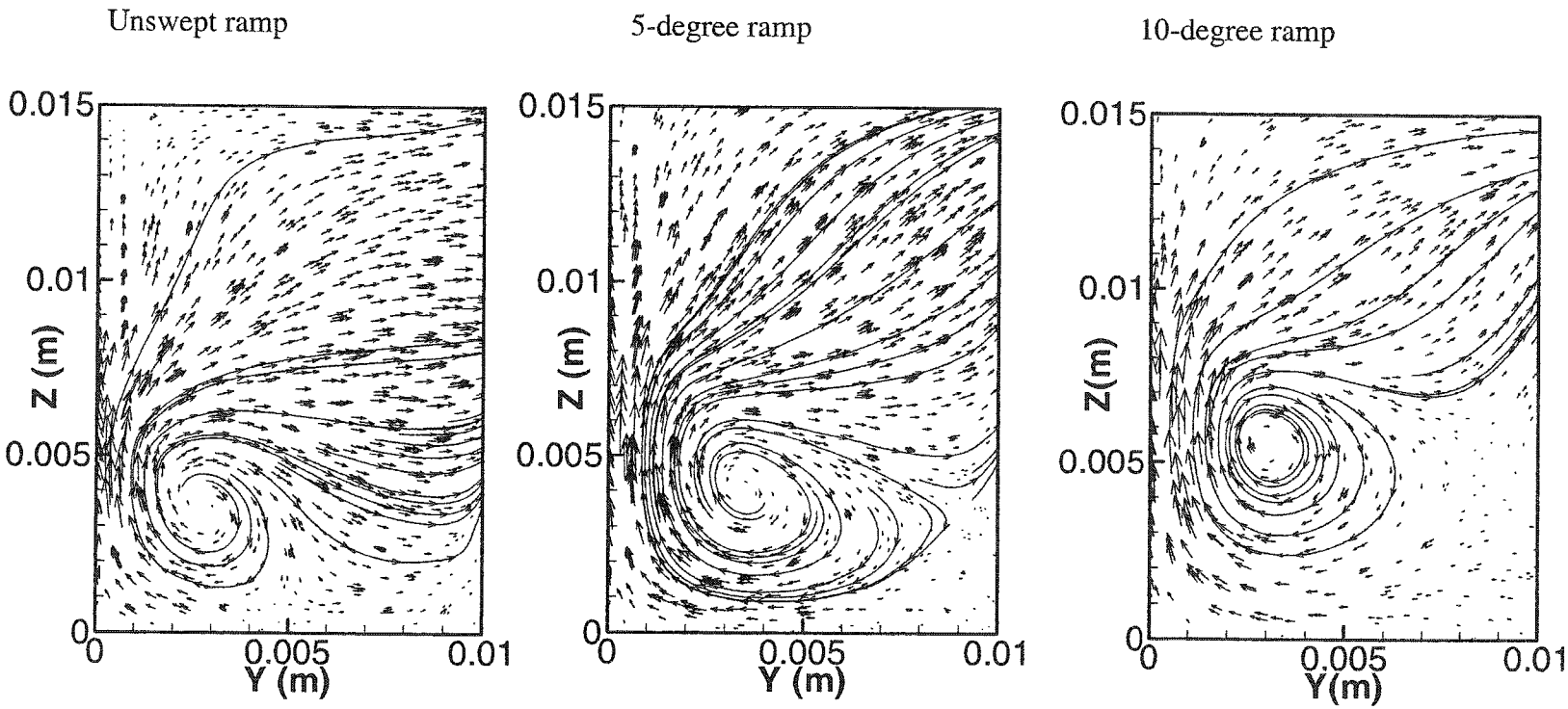

c. cross-section at X/H=8.0.

Fig. 4.24 (contd.) Crossflow plane velocity vectors

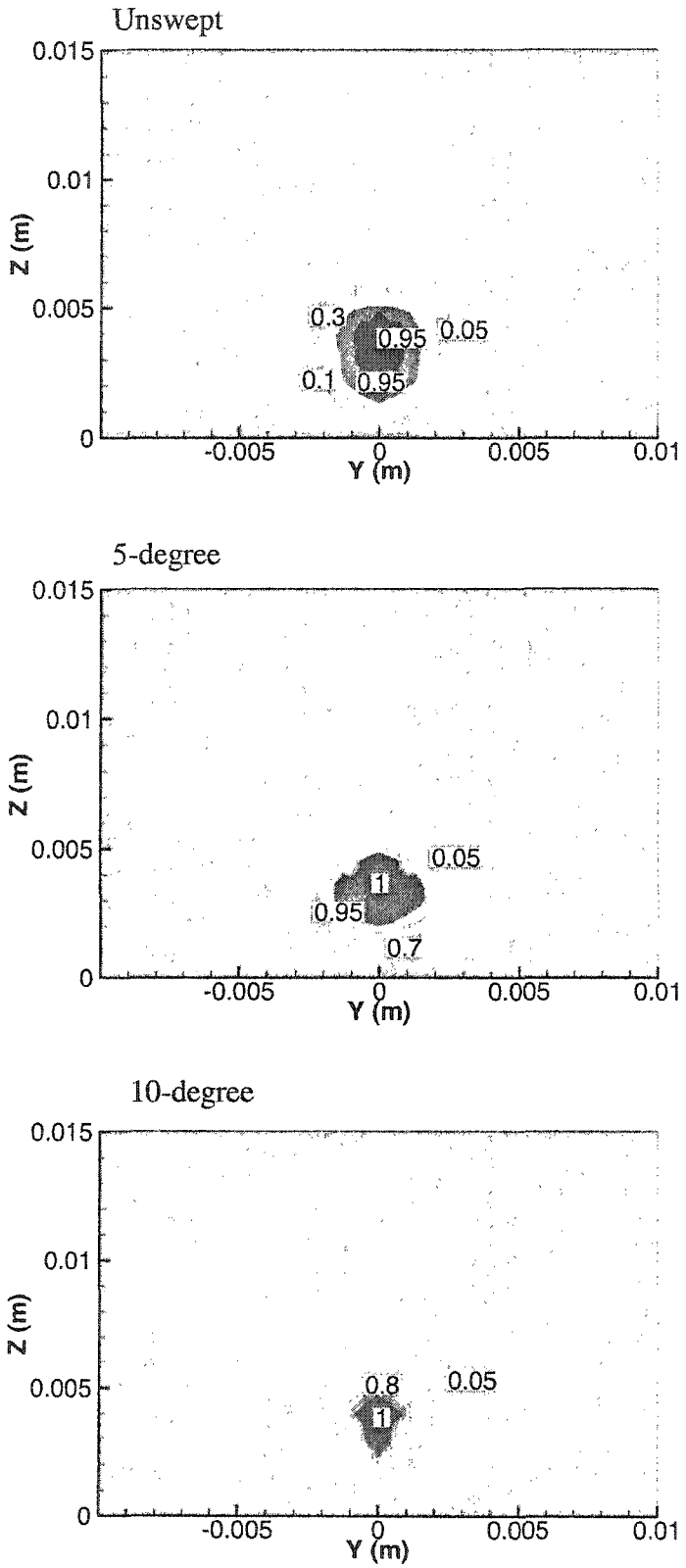

a. cross-section at X/H=0.5.

Fig. 4.25 Contours of constant injectant mole fraction

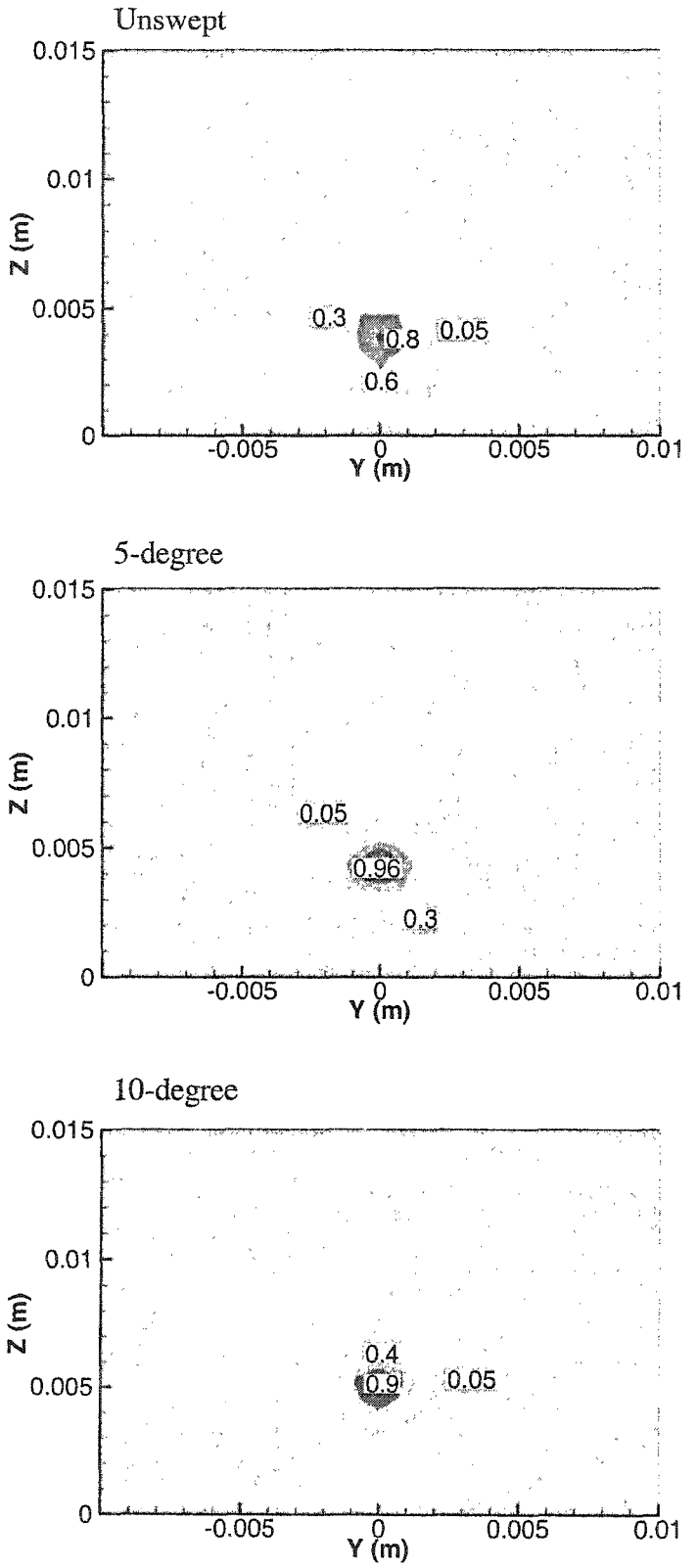

b. cross-section at X/H=2.0.

Fig. 4.25 (contd.) Contours of constant injectant mole fraction

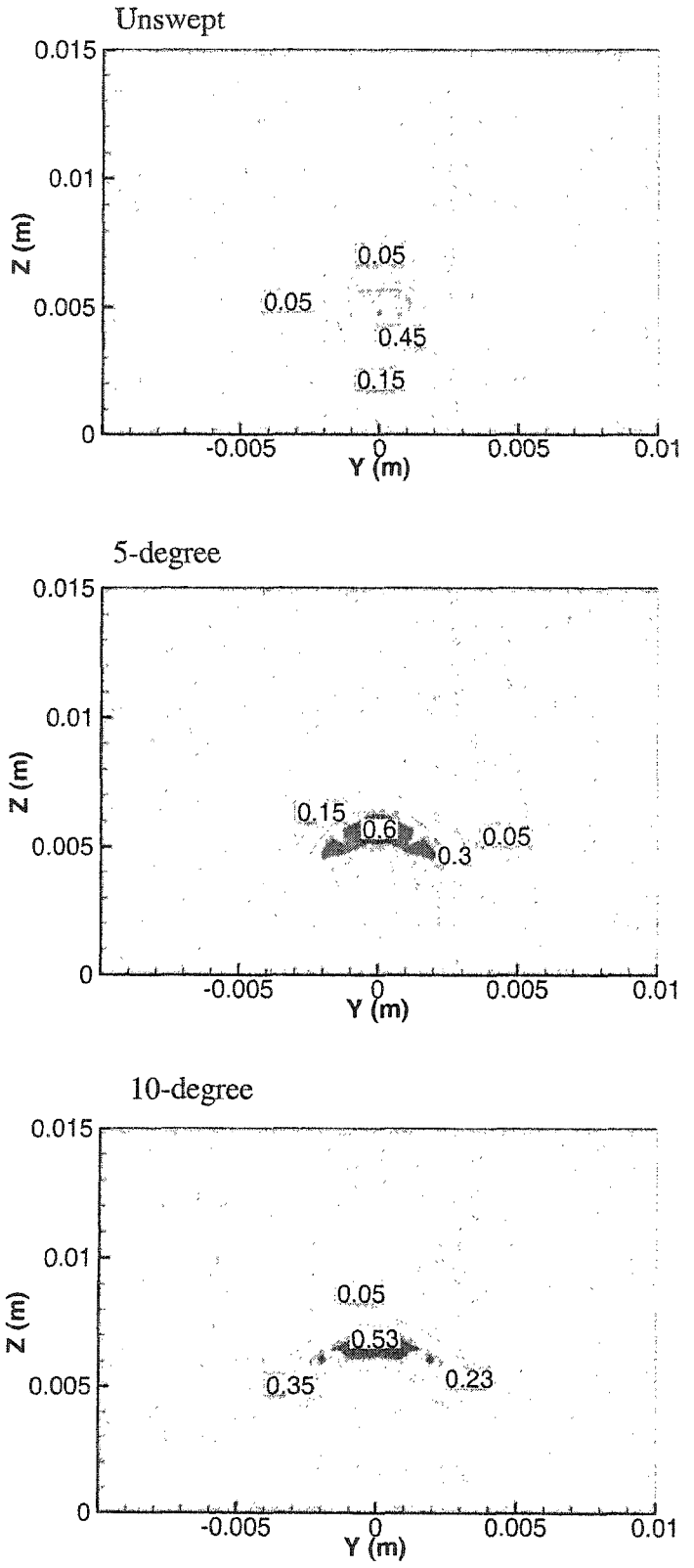

c. cross-section at X/H=4.0.

Fig. 4.25 (contd.) Contours of constant injectant mole fraction

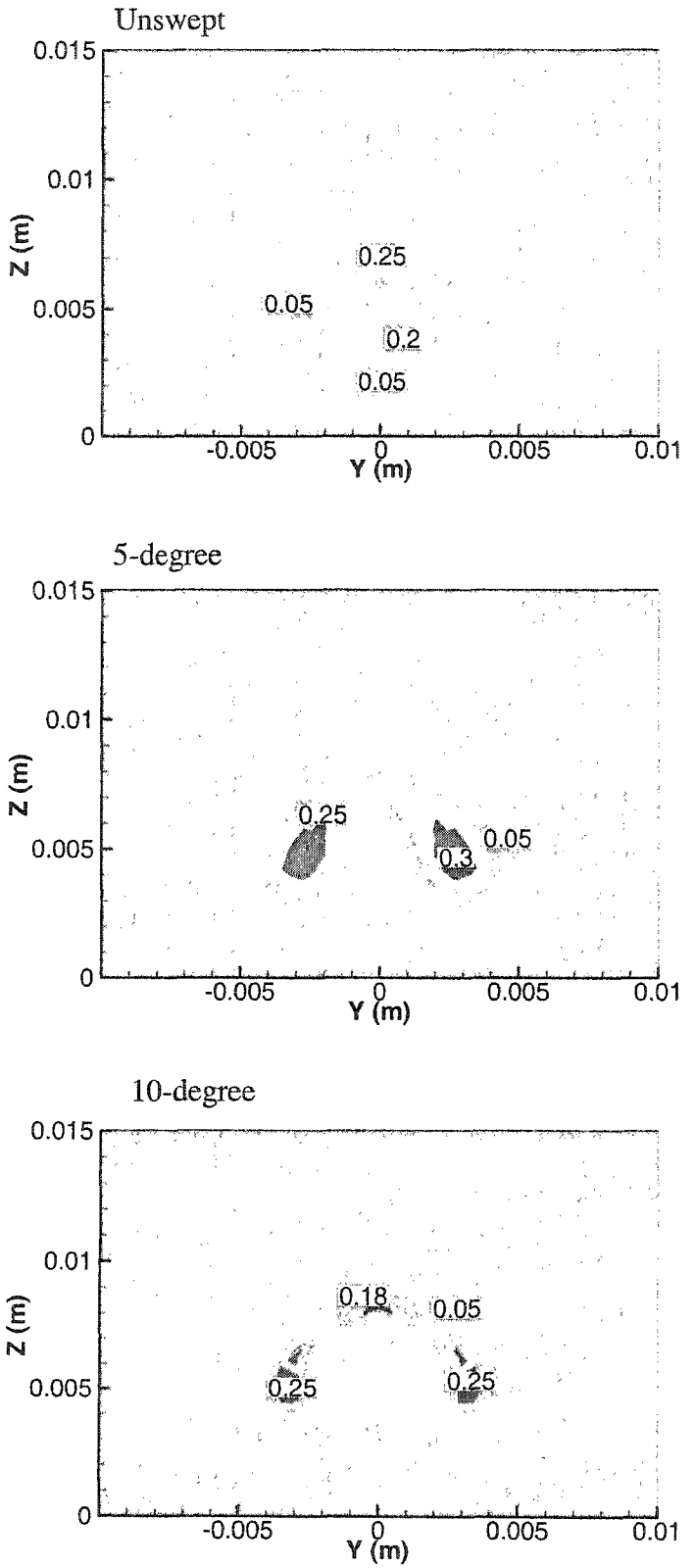

d. cross-section at X/H=6.0.

Fig. 4.25 (contd.) Contours of constant injectant mole fraction

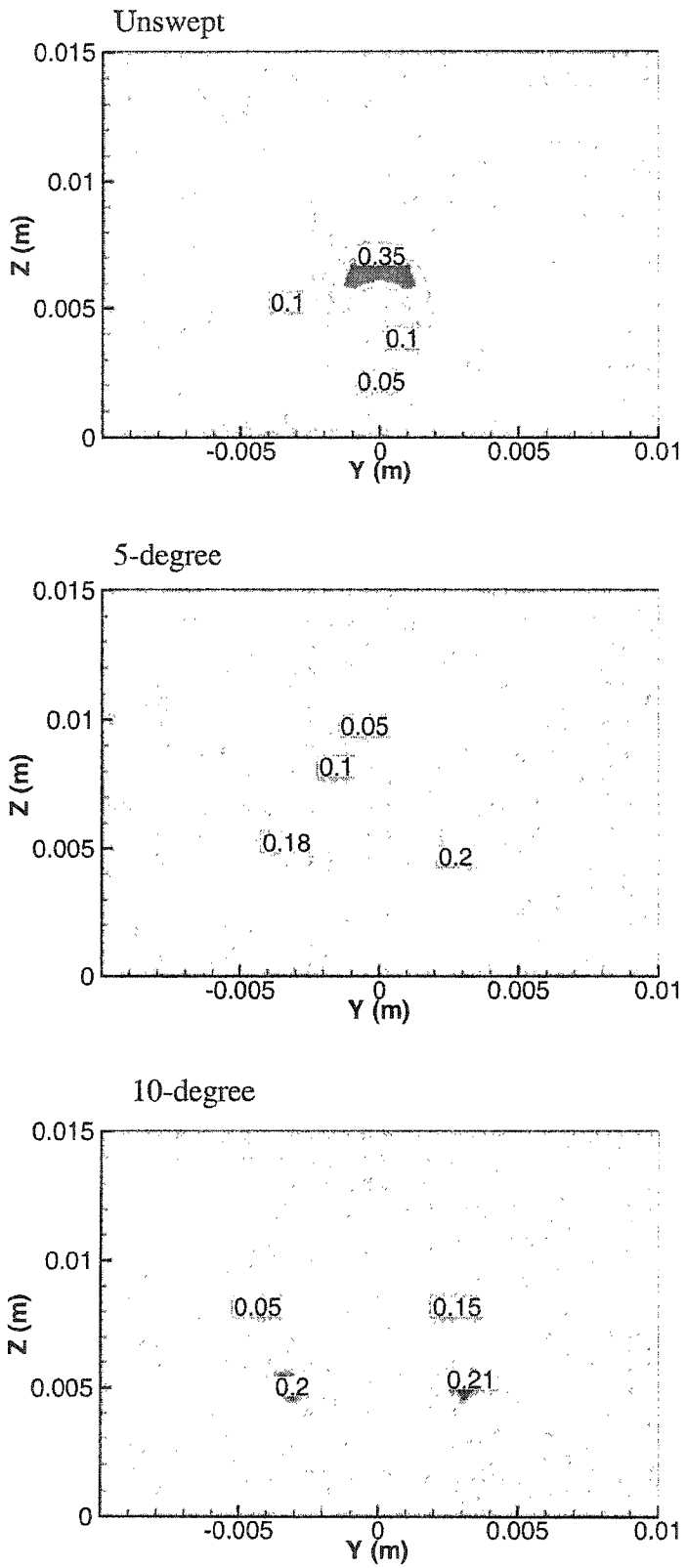

e. cross-section at X/H=8.0.

Fig. 4.25 (contd.) Contours of constant injectant mole fraction

The hydrogen mole fraction distribution for reacting flow is shown in Fig. 4.26 on different cross planes downstream of the jet location for the three cases. It is noted for the unswept case that the fuel jet remains in contact with the combustor wall through the boundary layer for a longer distance than the 5-degree swept ramp which can be seen at X/H= 0.5, 2.0, and 4.0. In the 10-degree swept ramp case the jet is lifted from the combustor wall after a short distance from the fuel nozzle. Also, the effect of the ramp side angle is clearly seen where the ramp vortex spreads the jet producing a kidney-shaped plume cross section, while there is almost no spreading occurs in the unswept case. The figure shows the same trend as in the nonreacting flow (Fig. 4.24), except that the spreading of the jet plumes is less than that in the nonreacting flow due to the effect of the chemical reaction at the surface of the fuel jet. The results presented in Figs. 4.25 and 4.26 can be explained as, with the swept ramp, the larger streamwise vortex has already begun to sweep the fuel across into the airstream and away from the lower wall while, with the unswept ramp, the smaller streamwise vortex also begins to transport injectant away from the jet, but not as much as does the swept ramp. As a result of the small vortex more fuel is transported towards the lower wall boundary layer in the unswept case. Clearly, the swept ramp significantly increases the overall spread and mixing of the fuel jet. However, some enhancement is also provided by the unswept ramp, but it is not as much as provided by the swept ramps.

Figure 4.27 shows the water vapor mole fraction generated from the reaction in a cross plane at X/H= 0.5, 20, 4.0, 6.0, and 8.0 for the three ramps. It is observed that the heat release dramatically reduced the mixing for the reacting case. This is due to the reduction in the streamwise vorticity. The reduction in streamwise vorticity as a result of

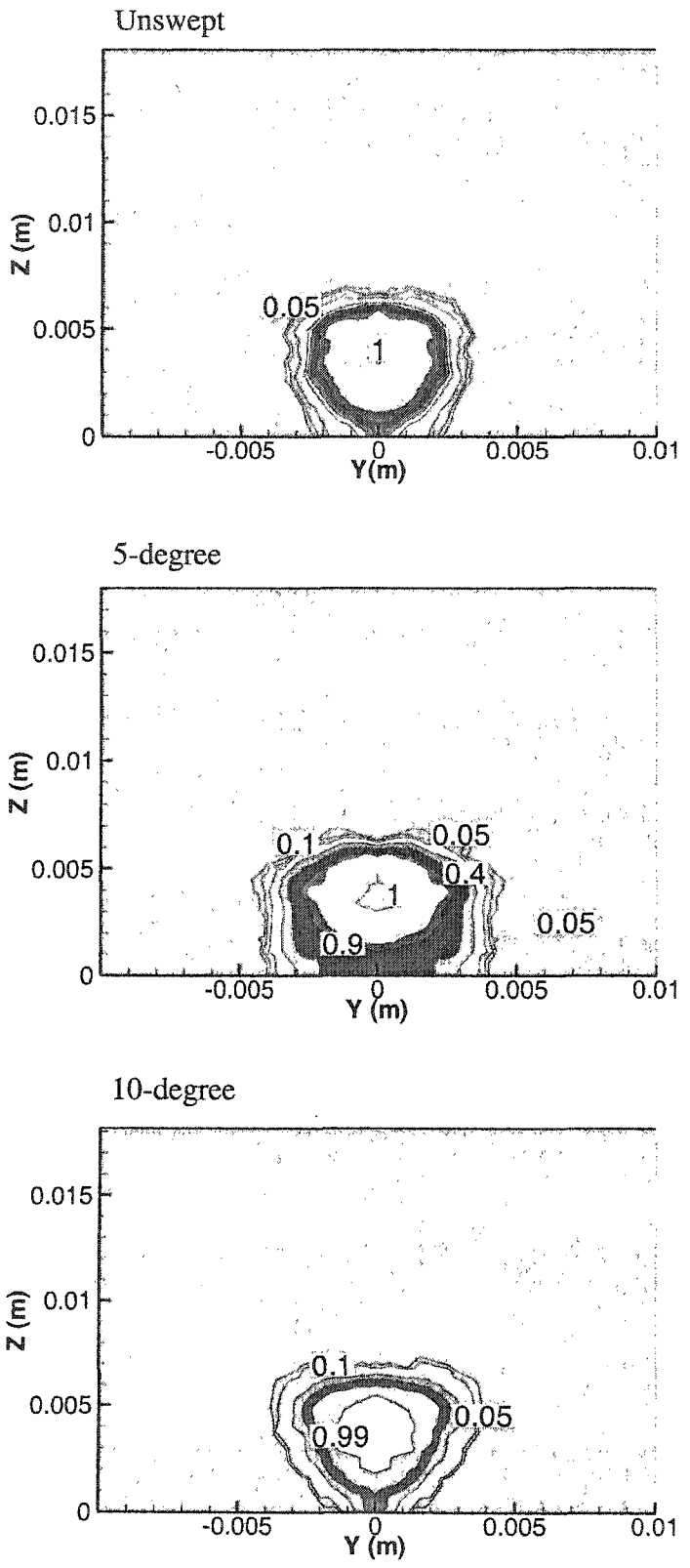

a. cross-section at X/H=0.5.

Fig. 4.26 Contours of constant injectant mole fraction (reacting flow)

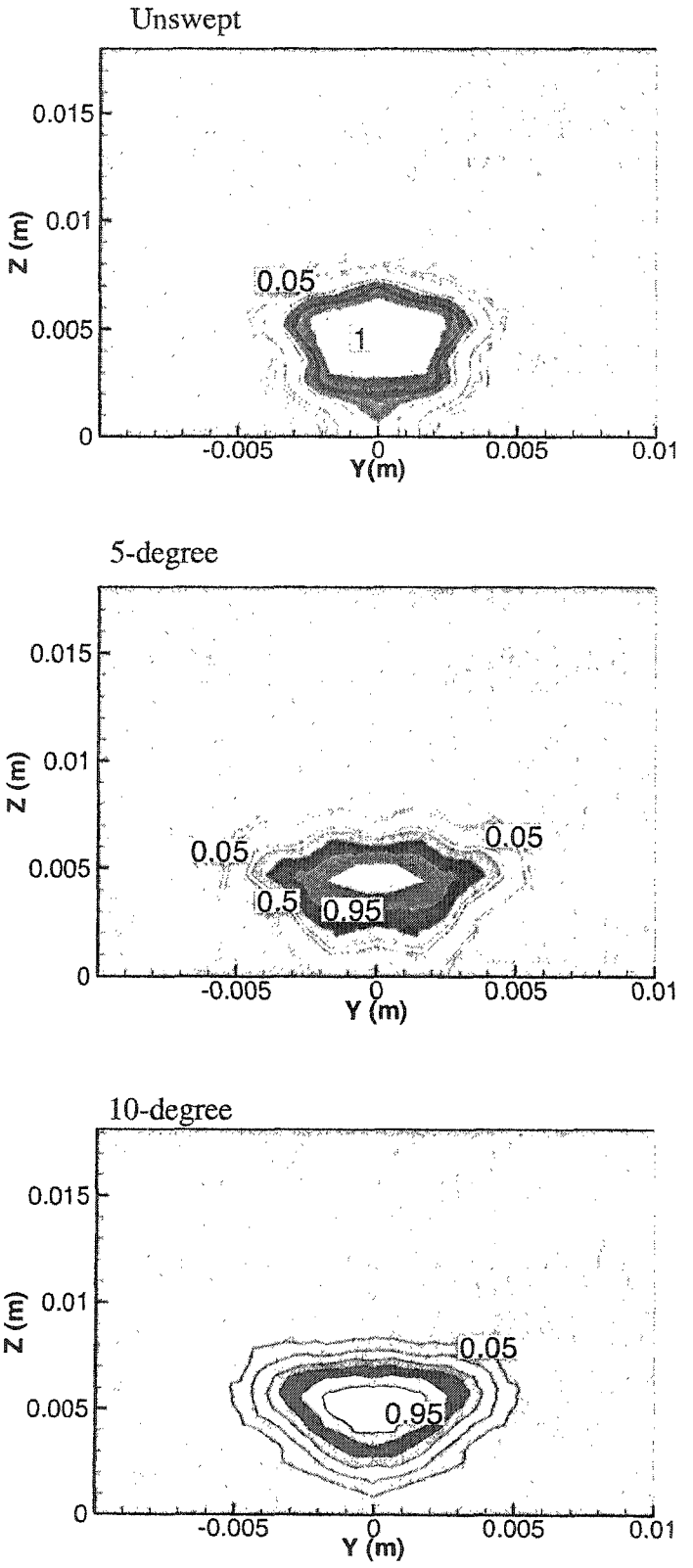

b. cross-section at X/H=2.0.

Fig. 4.26 (contd.) Contours of constant injectant mole fraction (reacting flow)

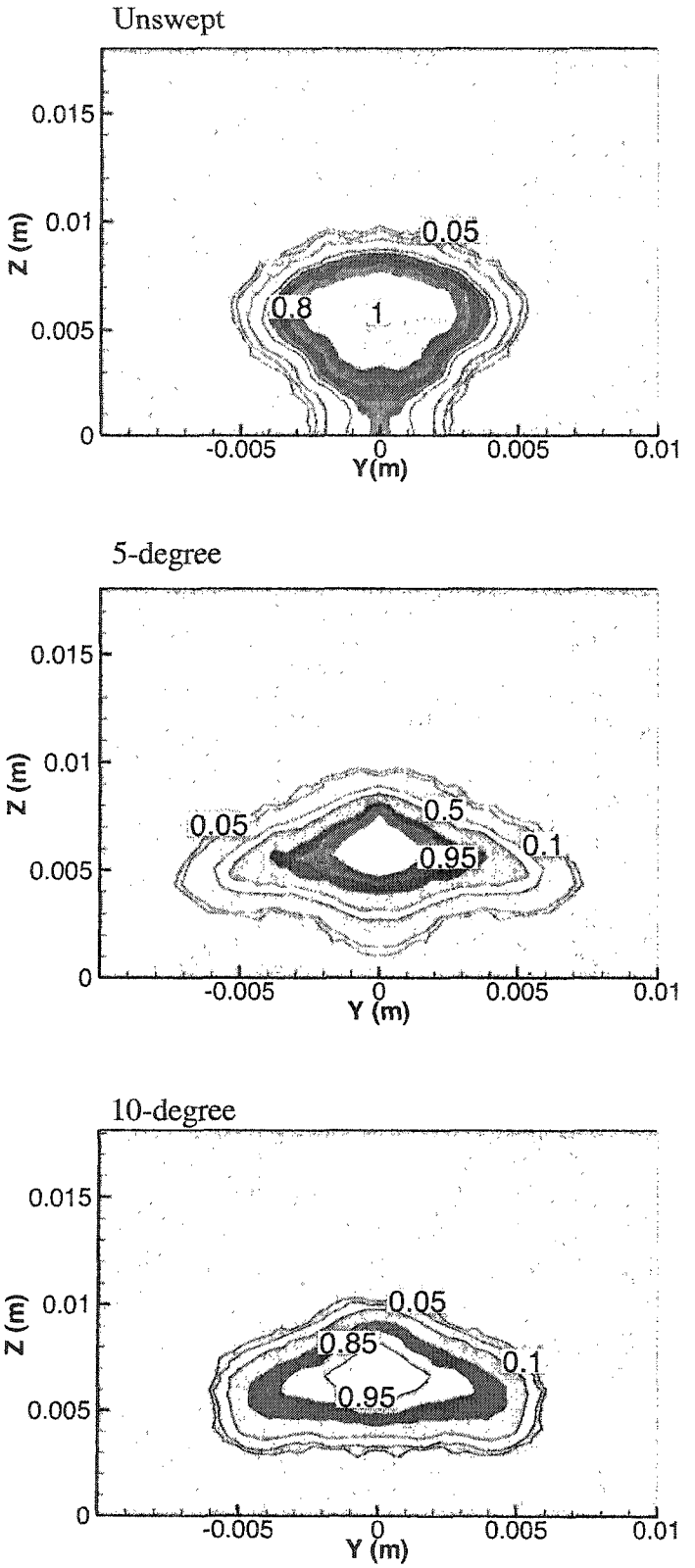

c. cross-section at X/H=4.0.

Fig. 4.26 (contd.) Contours of constant injectant mole fraction (reacting flow)

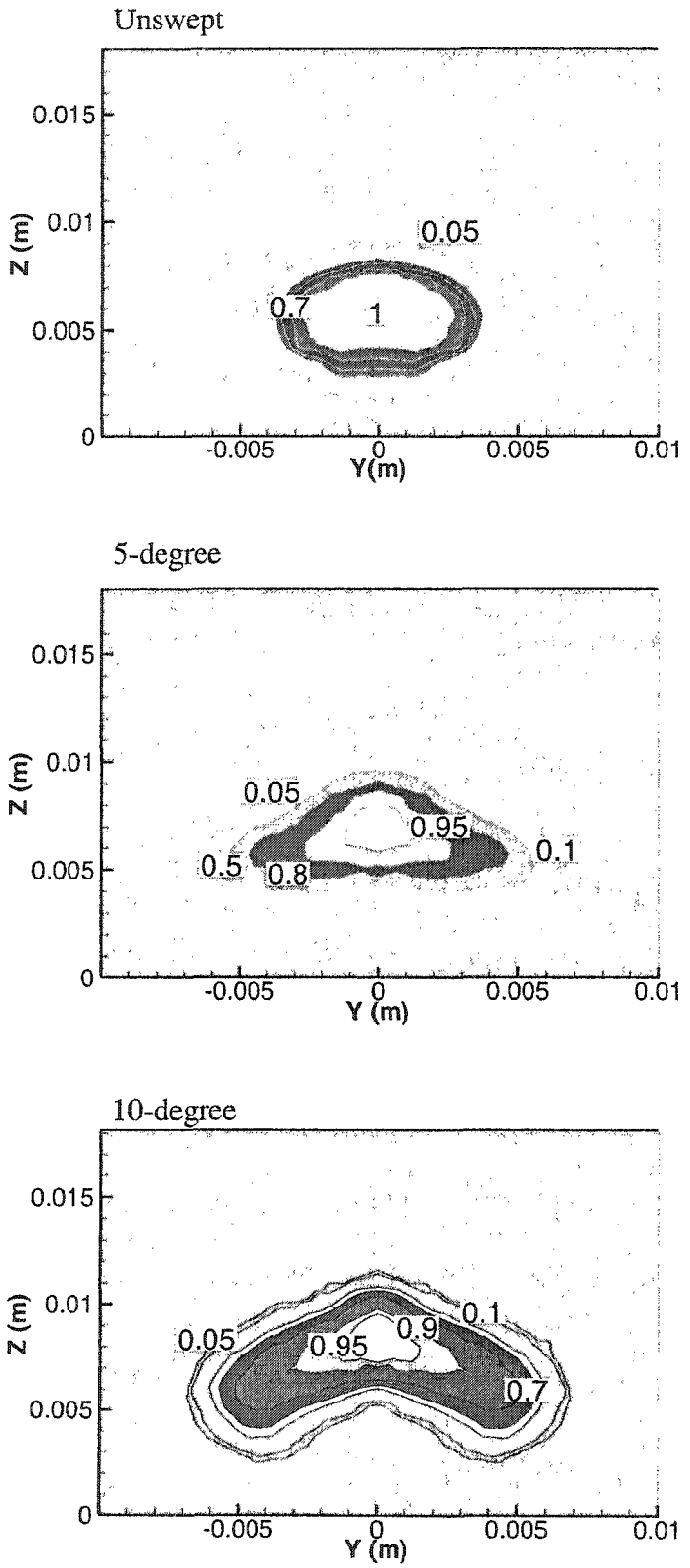

d. cross-section at X/H=6.0.

Fig. 4.26 (contd.) Contours of constant injectant mole fraction(reacting flow)

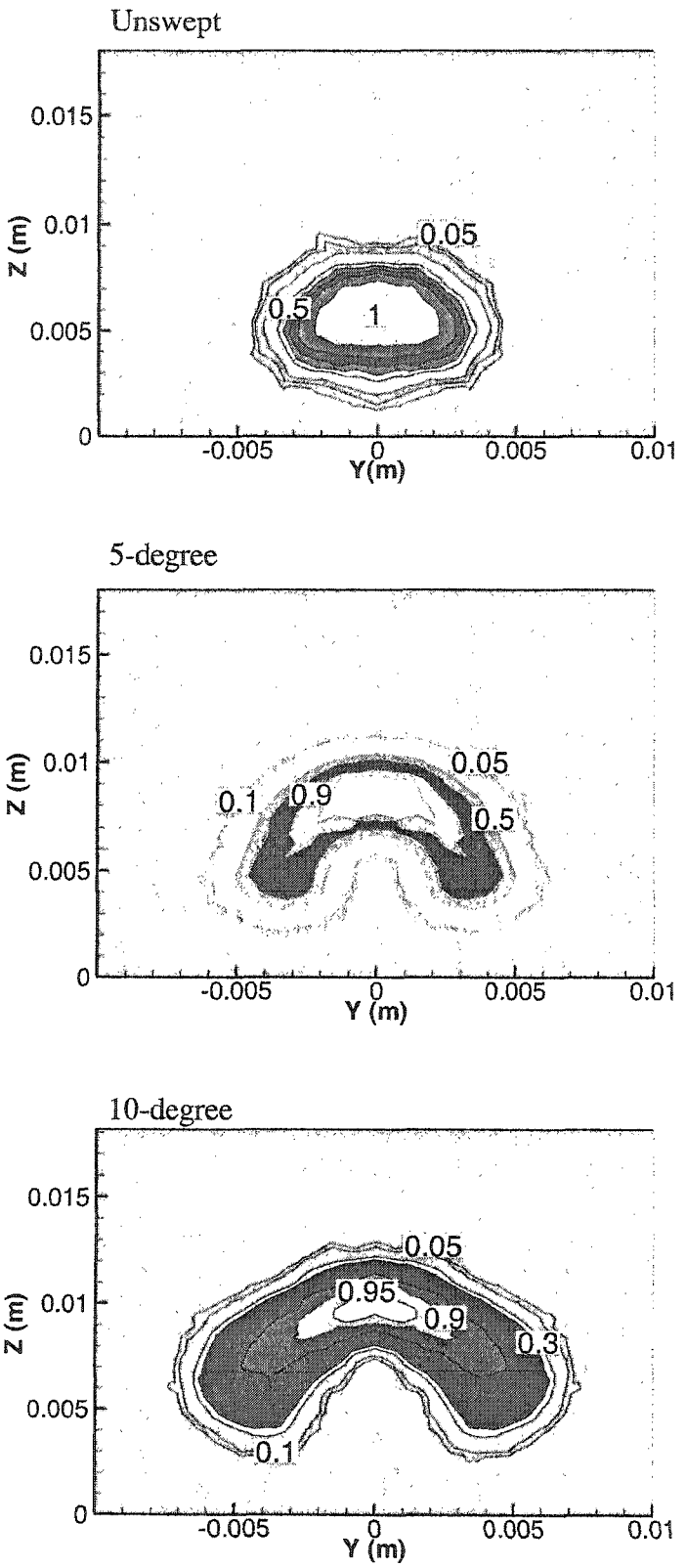

e. cross-section at X/H=8.0.

Fig. 4.26 (contd.) Contours of constant injectant mole fraction (reacting flow)

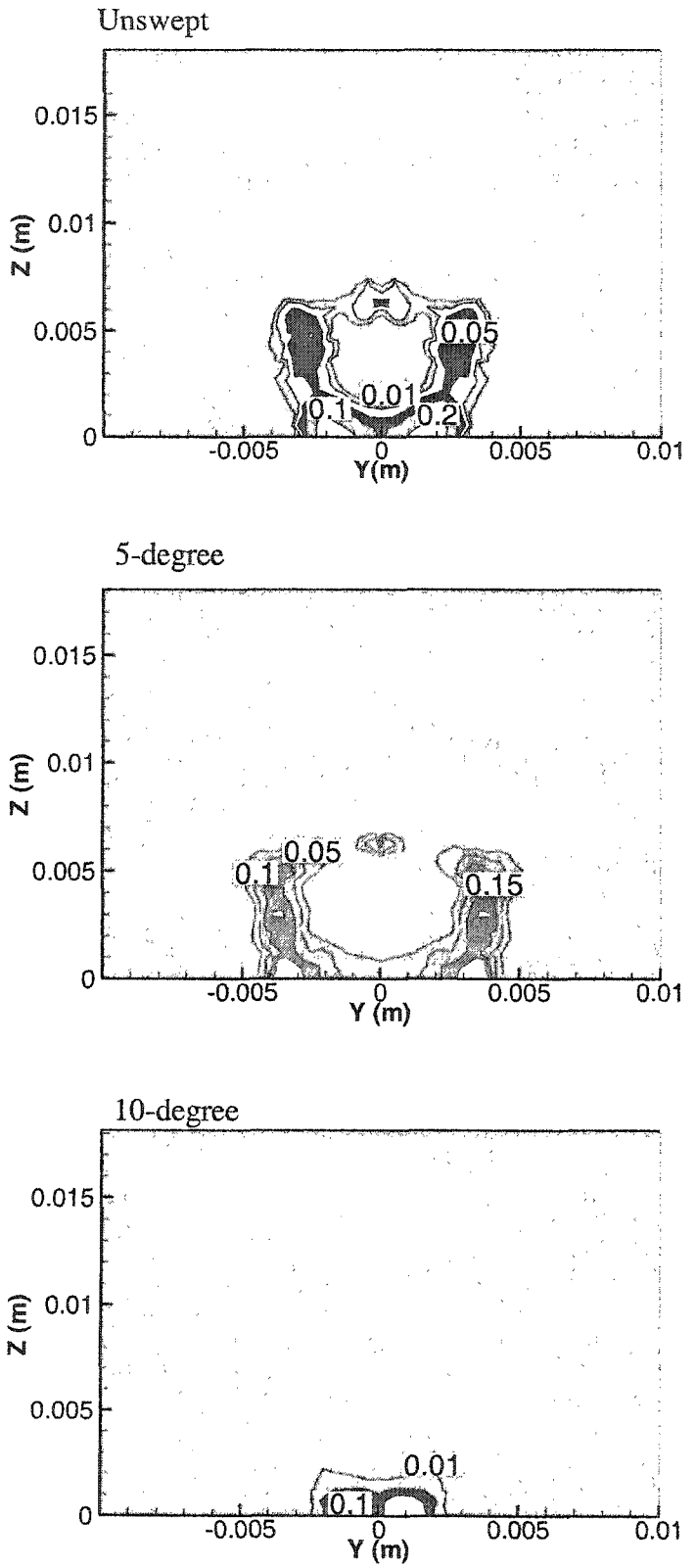

a. cross-section at X/H=0.5.

Fig. 4.27 Contours of constant water vapor mole fraction

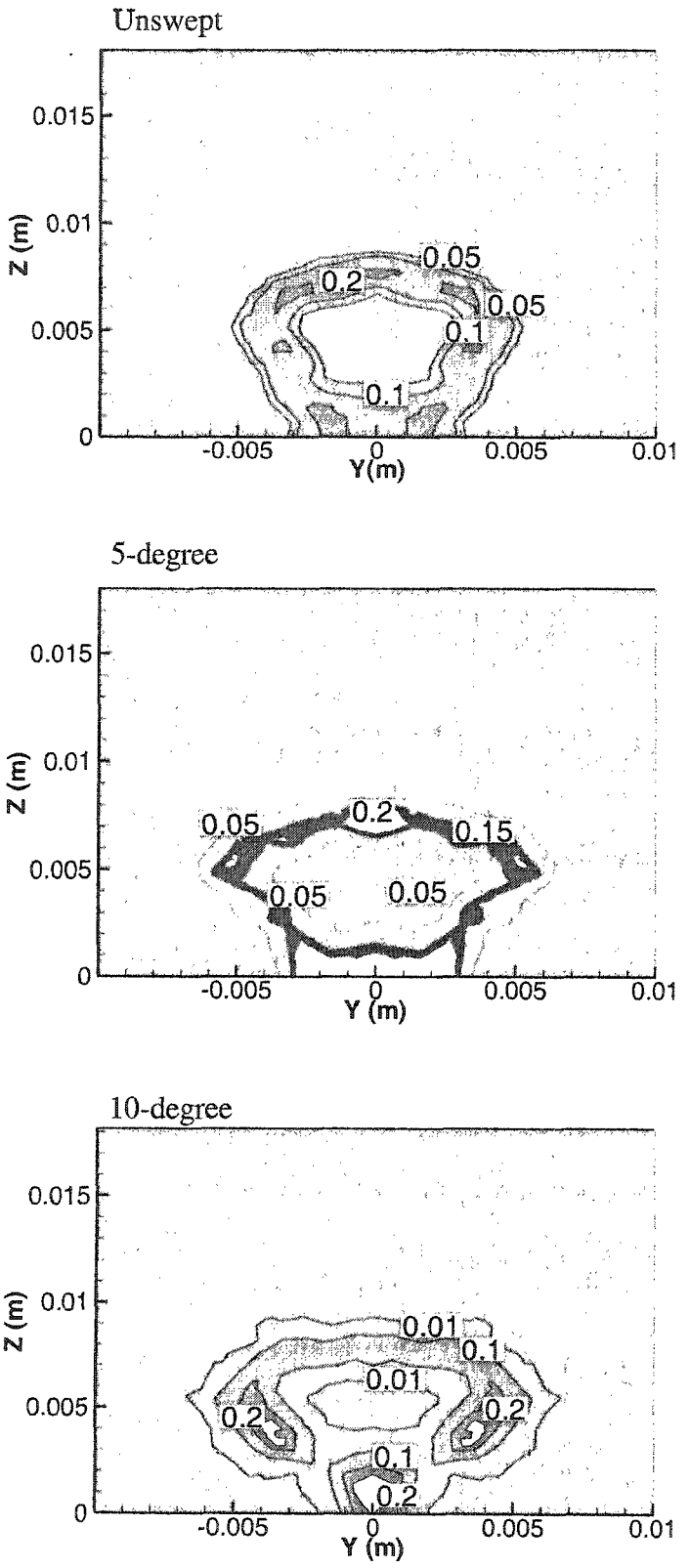

b. cross-section at X/H=2.0.

Fig. 4.27 (contd.) Contours of constant water vapor mole fraction

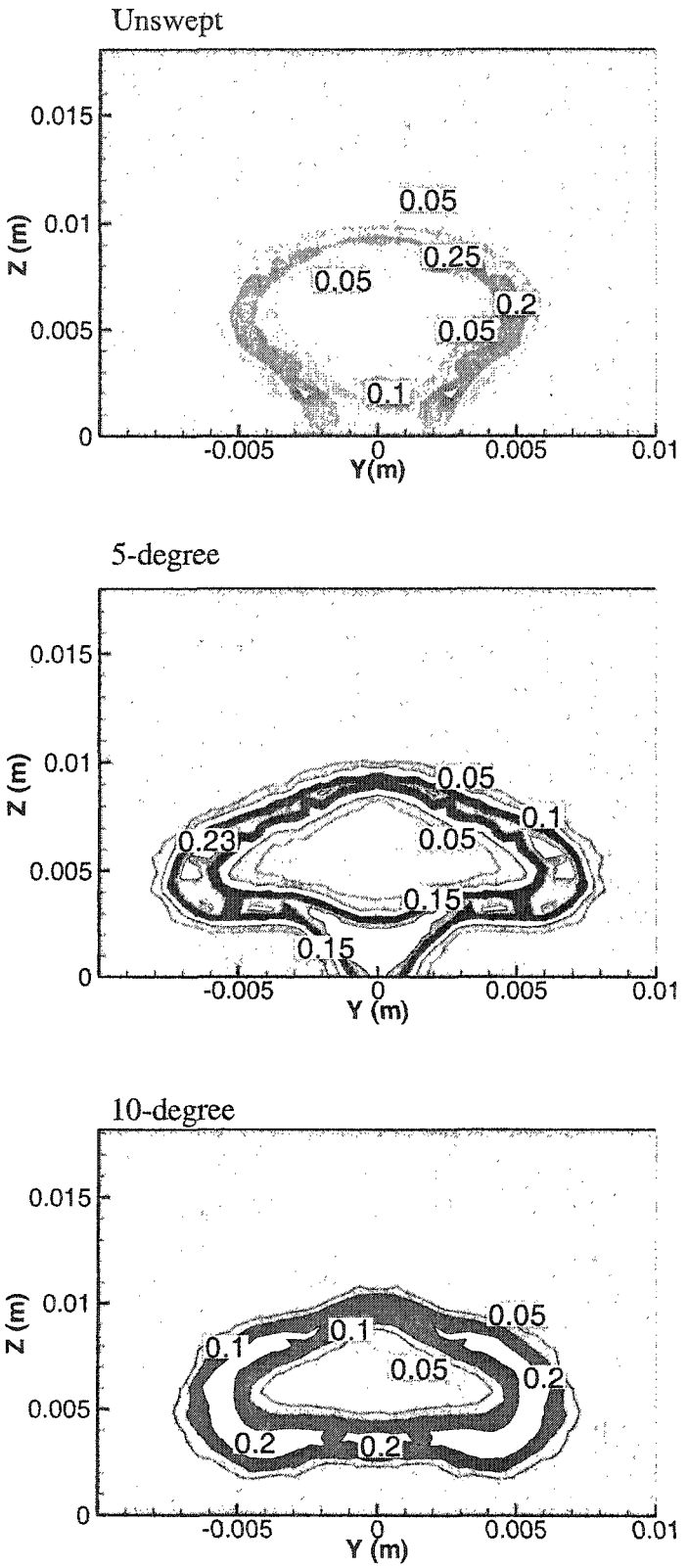

c. cross-section at X/H=4.0.

Fig. 4.27 (contd.) Contours of constant water vapor mole fraction

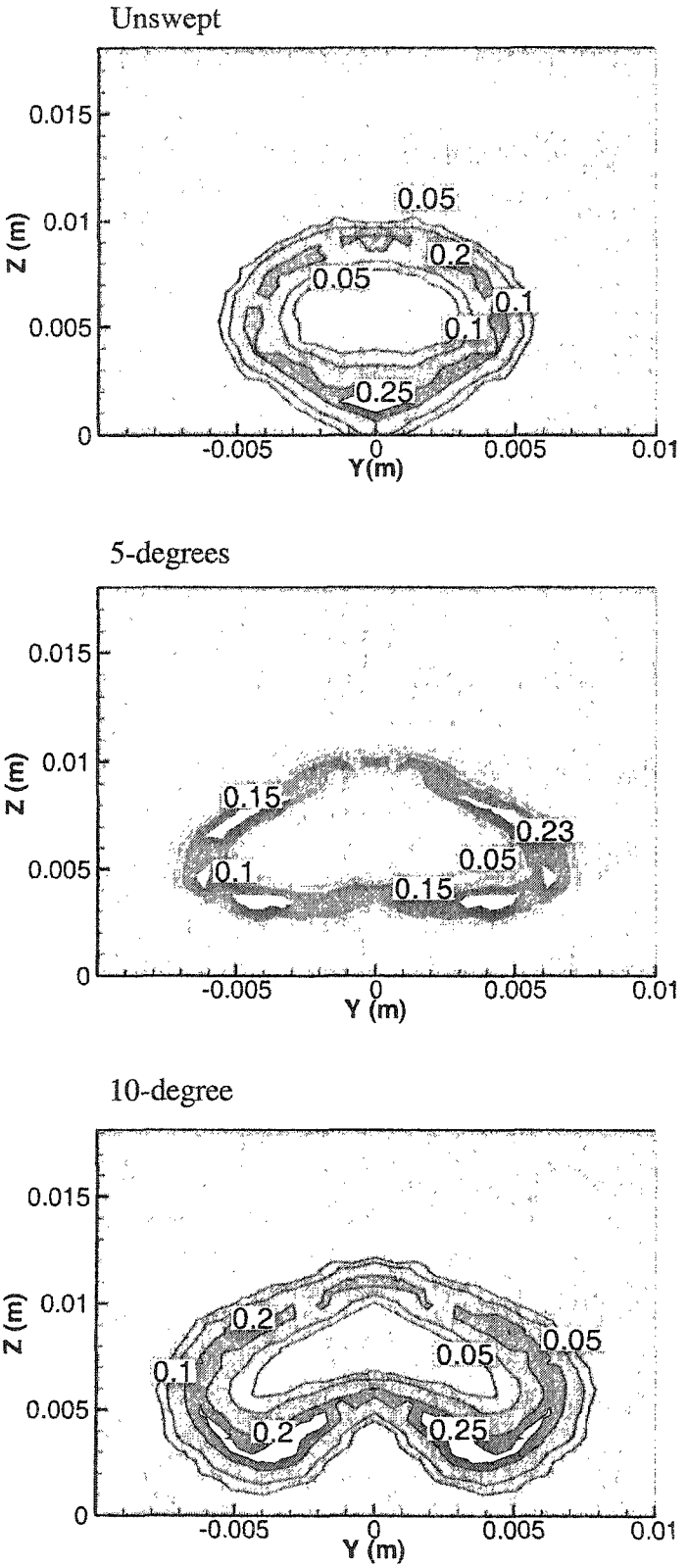

d. cross-section at X/H=6.0.

Fig. 4.27 (contd.) Contours of constant water vapor mole fraction

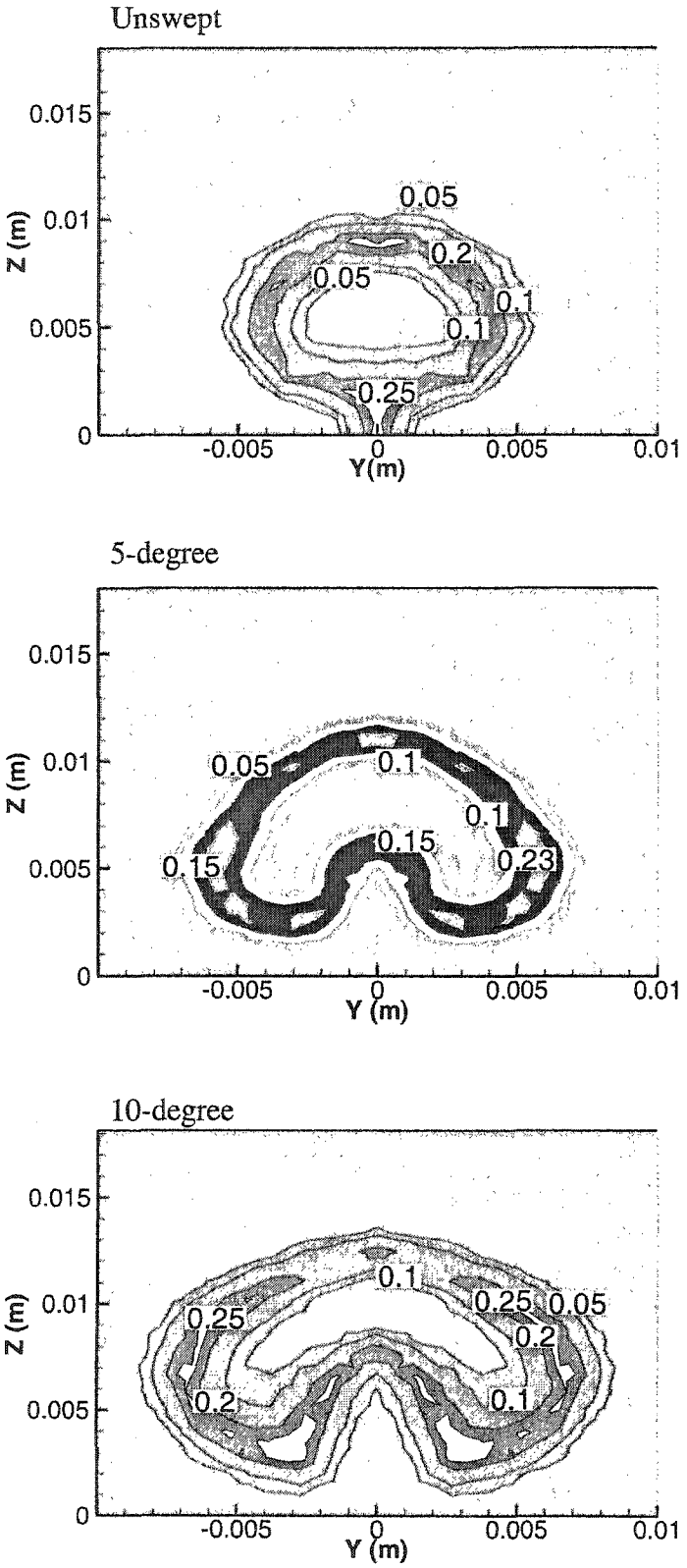

e. cross-section at X/H=8.0.

Fig. 4.27 (contd.) Contours of constant water vapor mole fraction

heat release was also observed by Riggins and McClinton [28]. The figure shows much less warping due to vorticity for the unswept ramp than the other two swept ramps. It should be noted that the water forms at the boundary around the fuel plume, and that the maximum water production occurs for all cases near the interface of the hydrogen core and the outer flow. Also, the burning layer for the 10-degree swept ramp is larger than that for the other two ramps.

Figure 4.28 shows the temperature contours for reacting flow at the same cross planes for the three ramps. The temperature contours take the shape of the fuel plume for the three ramps. The higher temperature, as expected, exists around the reacting layer.

The mixing rate of the three ramps is illustrated in Fig. 4.29. The figure shows the axial decay of the maximum injectant mole fraction for the three ramp side angles. It can be seen that as the distance from the ramp base increases the maximum mole fraction decreases rapidly in the two swept ramps as compared to the unswept ramp. At X/H=6.0, the mole fraction reduces to about 23% of its maximum value for the 10-degree swept ramp while it reduces to 60 % of its maximum value in the unswept ramp case. Further downstream, at X/H=8.0, these values become 20% and 32%, respectively. It should be noted that the difference in the mixing rate between the two swept ramps is not large, i.e., the effect of increasing the ramp side angle from 5 degrees to 10 degrees has slight effect on the mixing rate while the difference between unswept and the 5-degree swept ramps is remarkable. It can be concluded that the highest decay rate correlates with largest side angle, the 10-degree swept ramp.

Figures 4.30 and 4.31 show the axial decay of the injectant concentration and the axial distribution of the Mach number, respectively. The figures show the same trend as

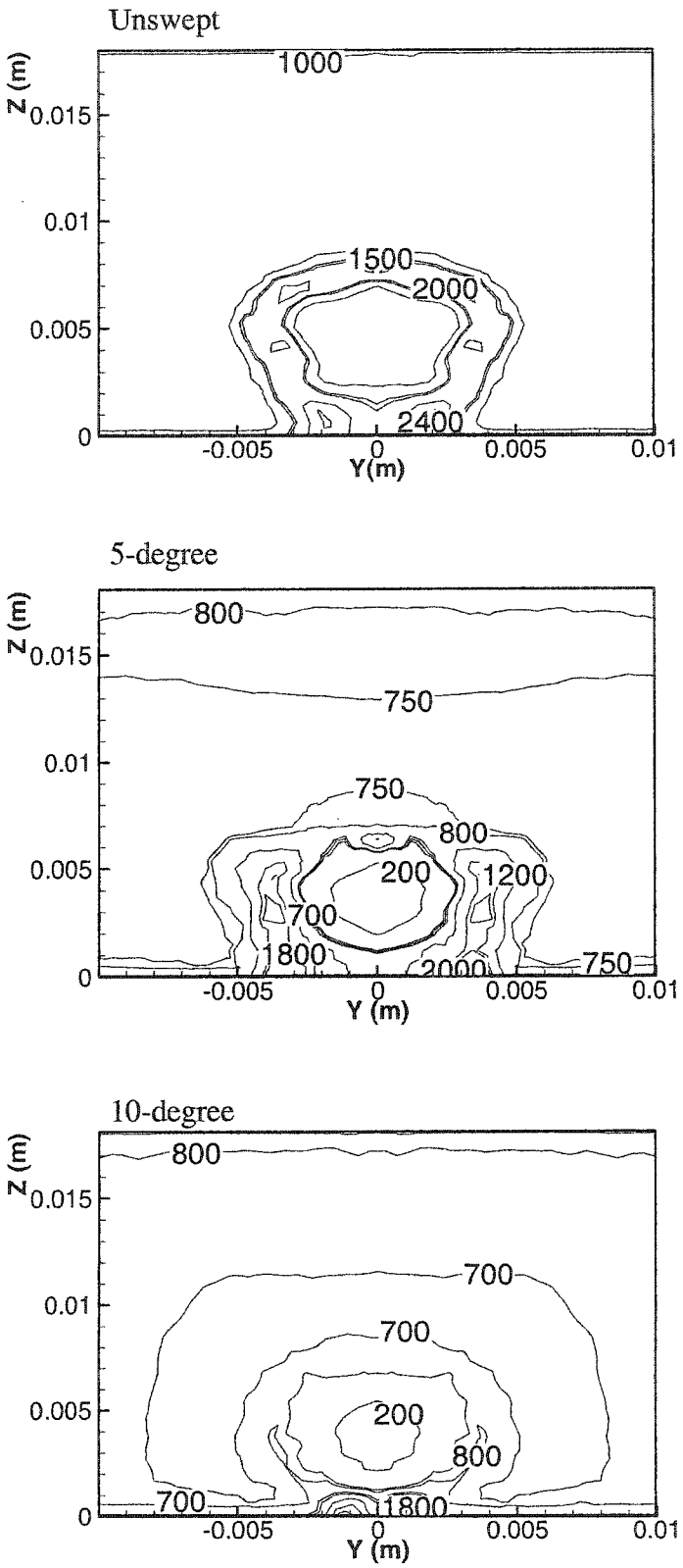

a. cross-section at X/H=0.5.

Fig. 4.28 Contours of constant static temperature(reacting flow)

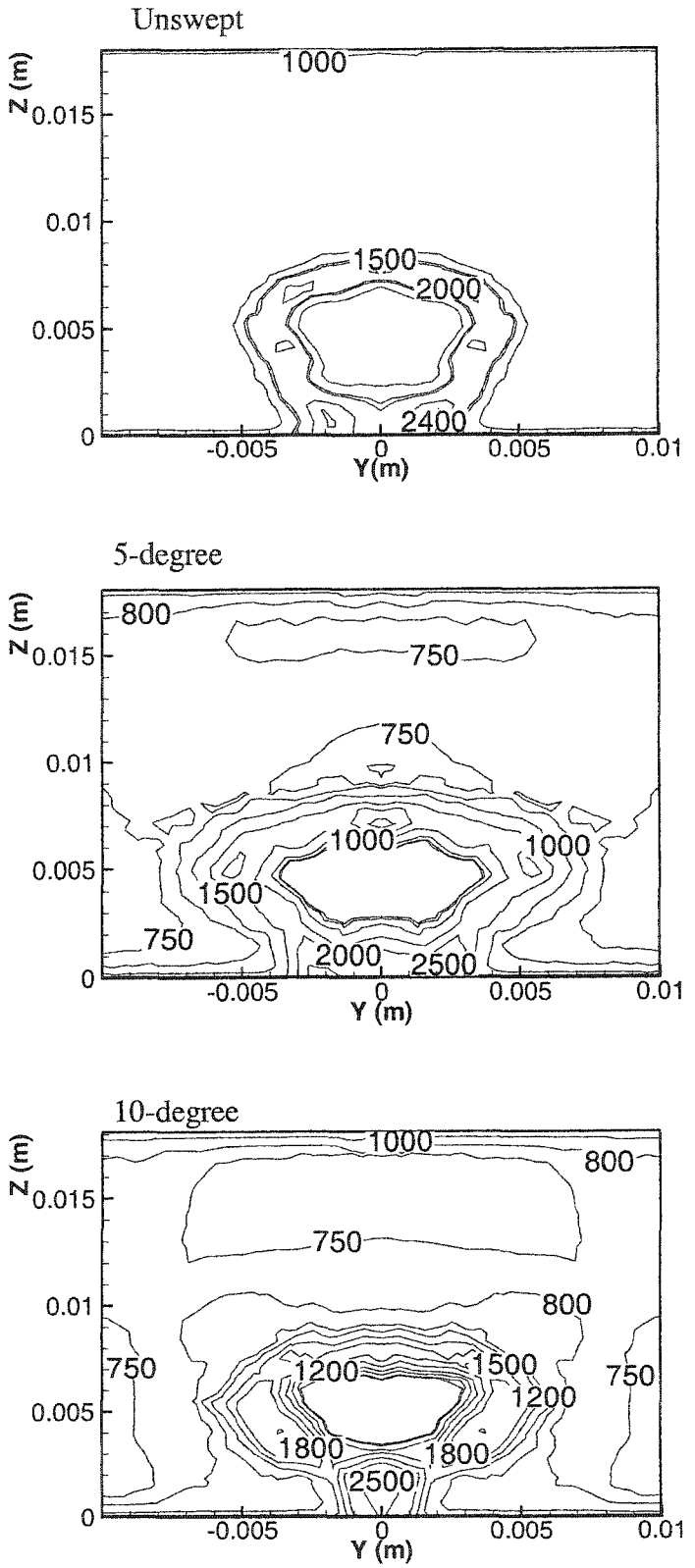

b. cross-section at X/H=2.0.

Fig. 4.28 (contd.) Contours of constant injectant mole fraction (reacting flow)

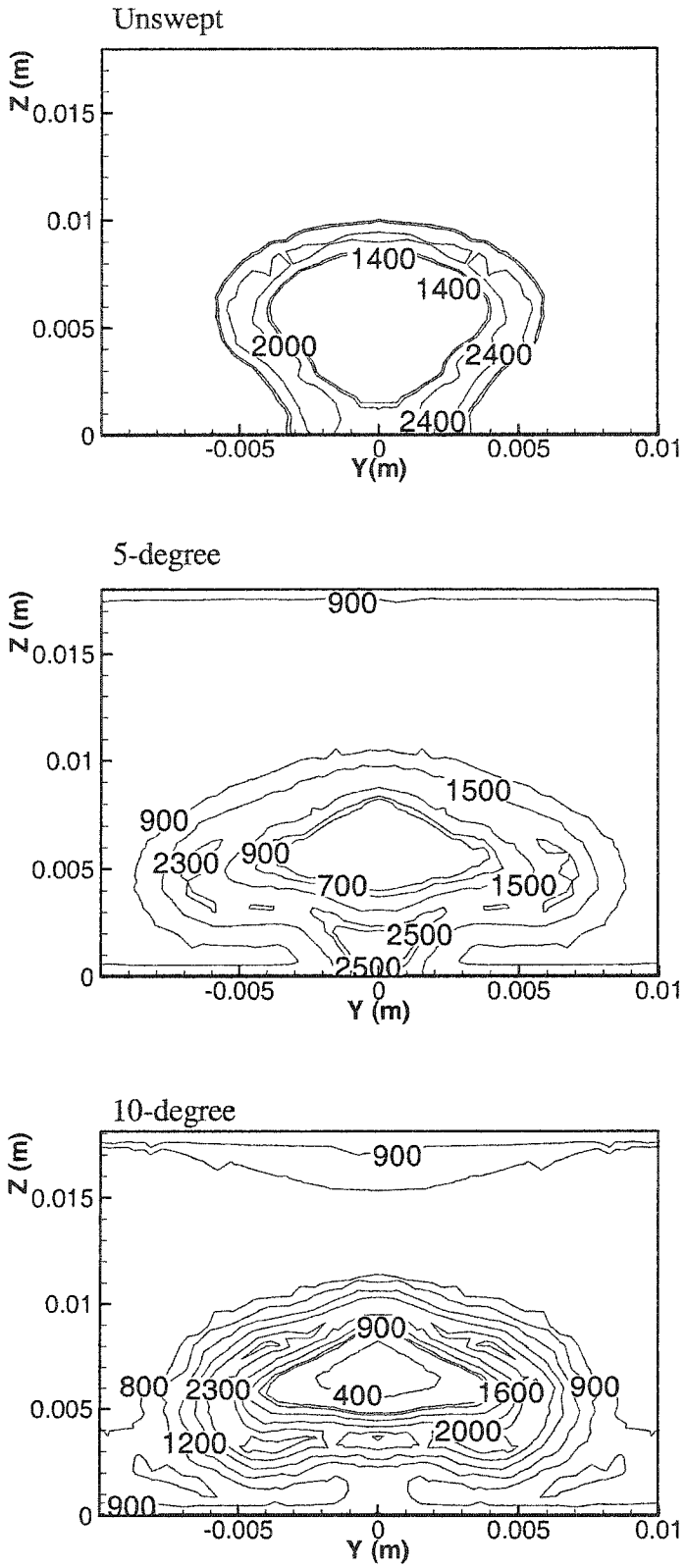

c. cross-section at X/H=4.0.

Fig. 4.28 (contd.) Contours of constant static temperature (reacting flow)

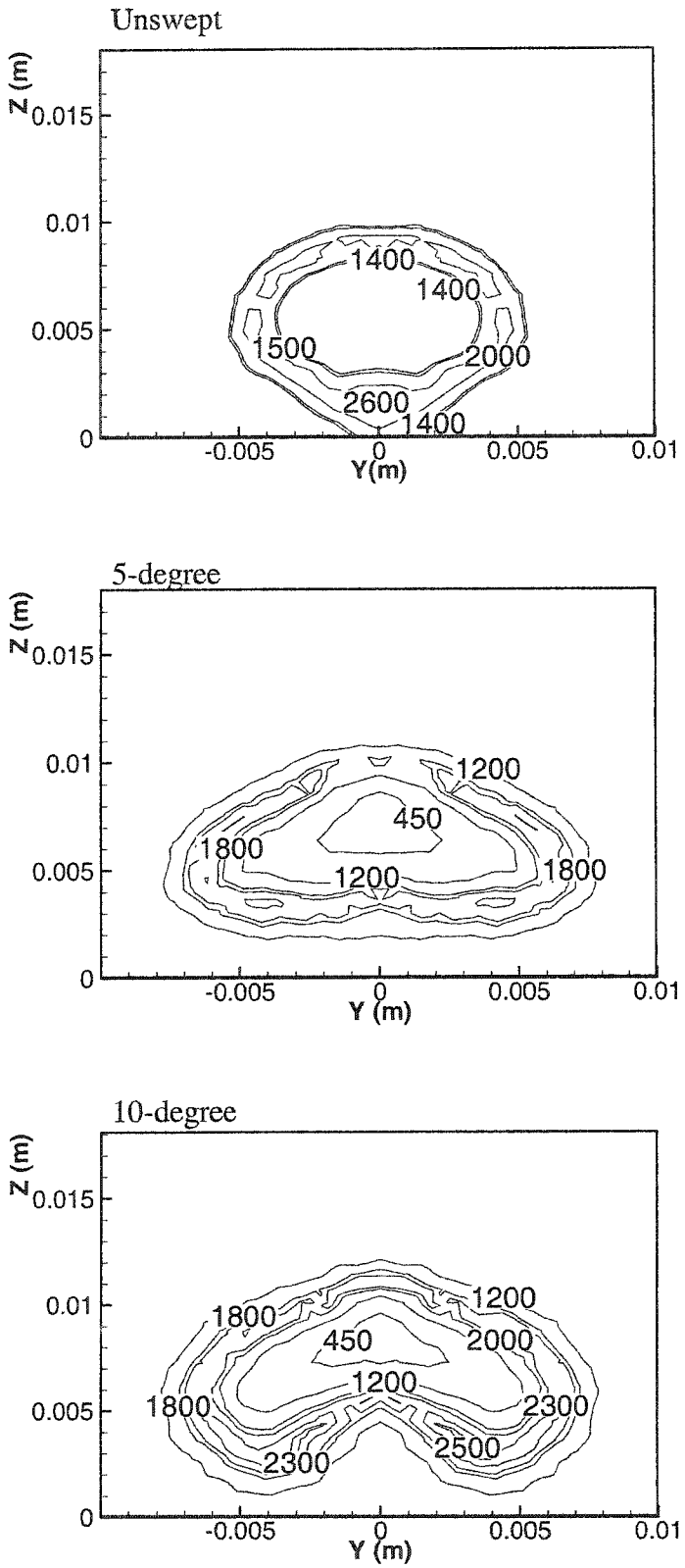

d. cross-section at X/H=6.0.

Fig. 4.28 (contd.) Contours of constant static temperature (reacting flow)

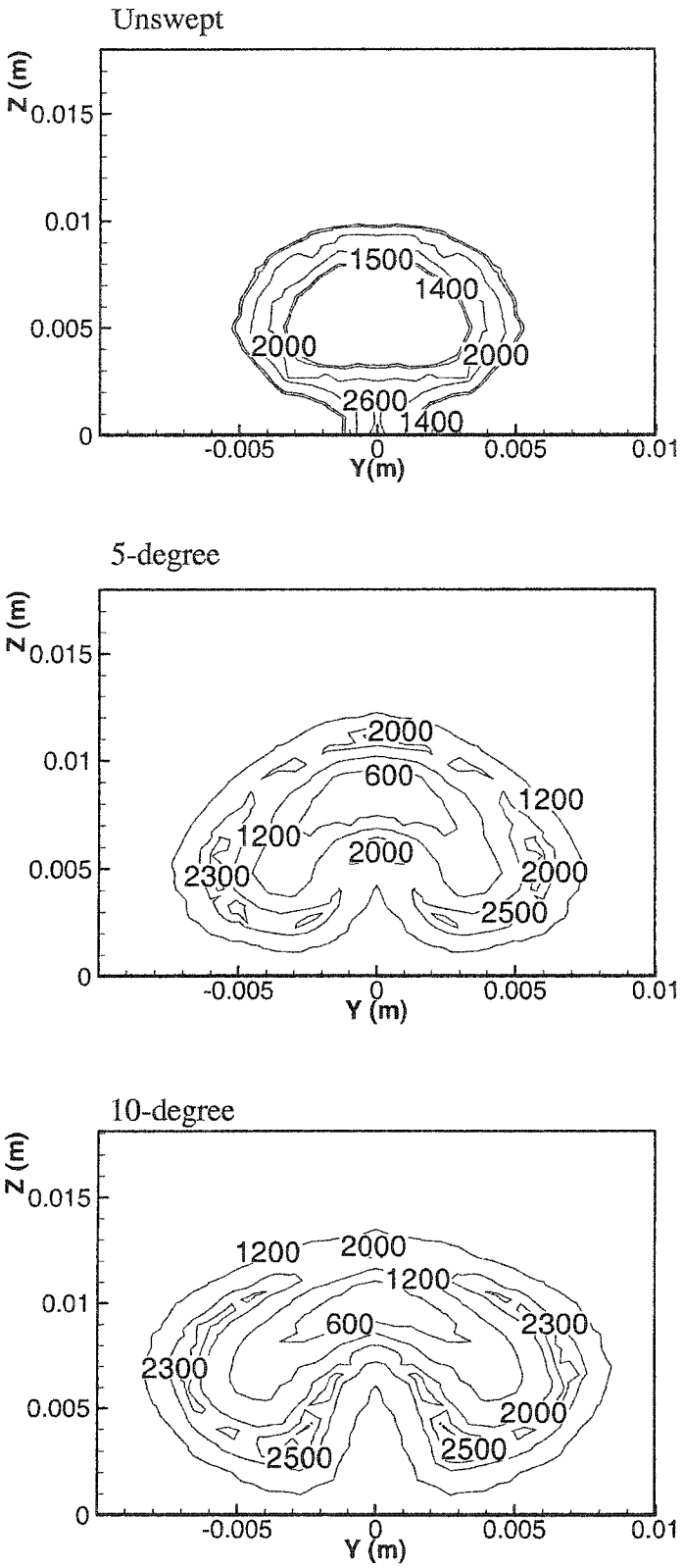

e. cross-section at X/H=8.0.

Fig. 4.28 (contd.) Contours of constant static temperature (reacting flow)

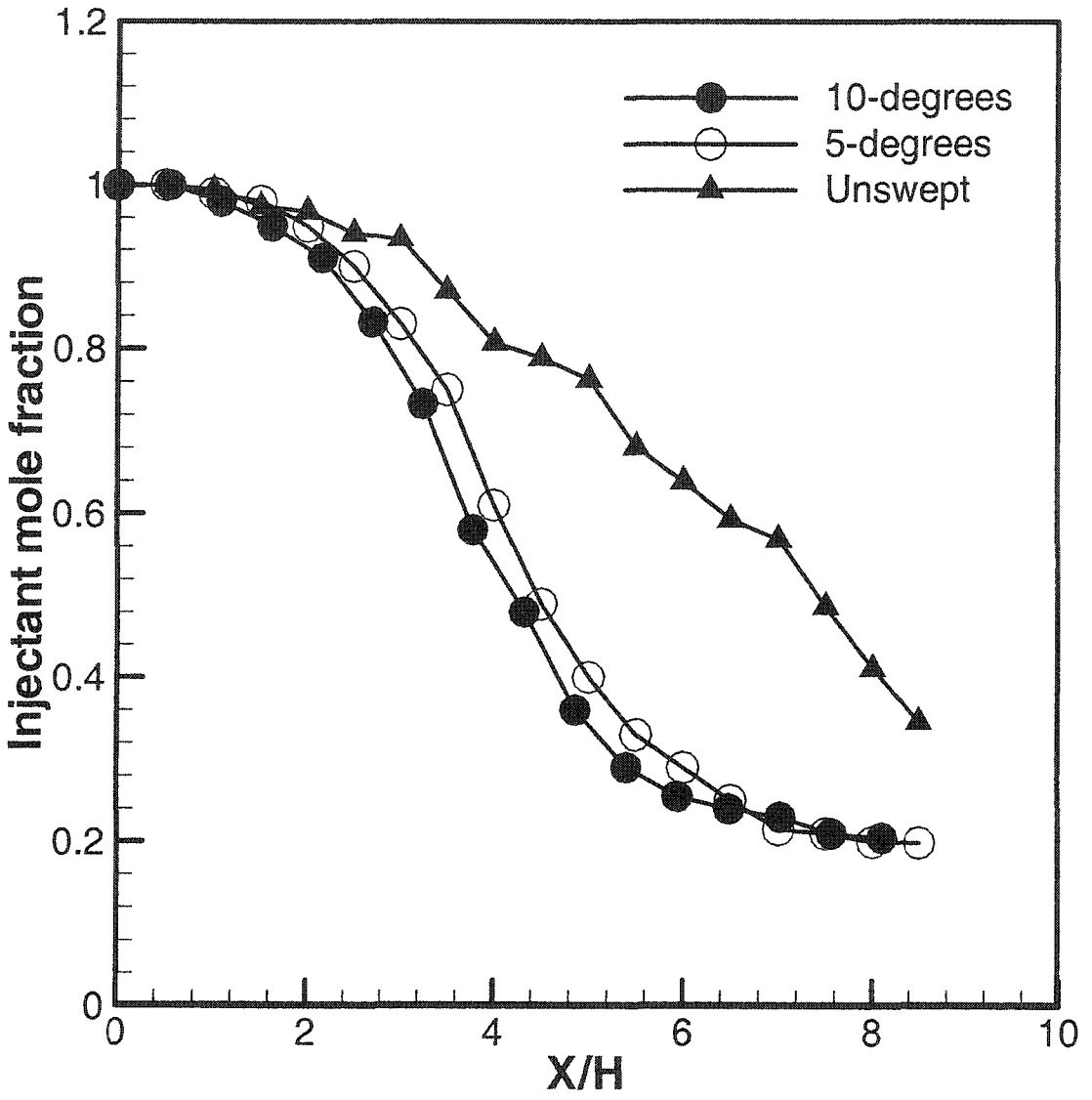

Fig. 4.29 Decay of maximum injectant mole fraction for different angles

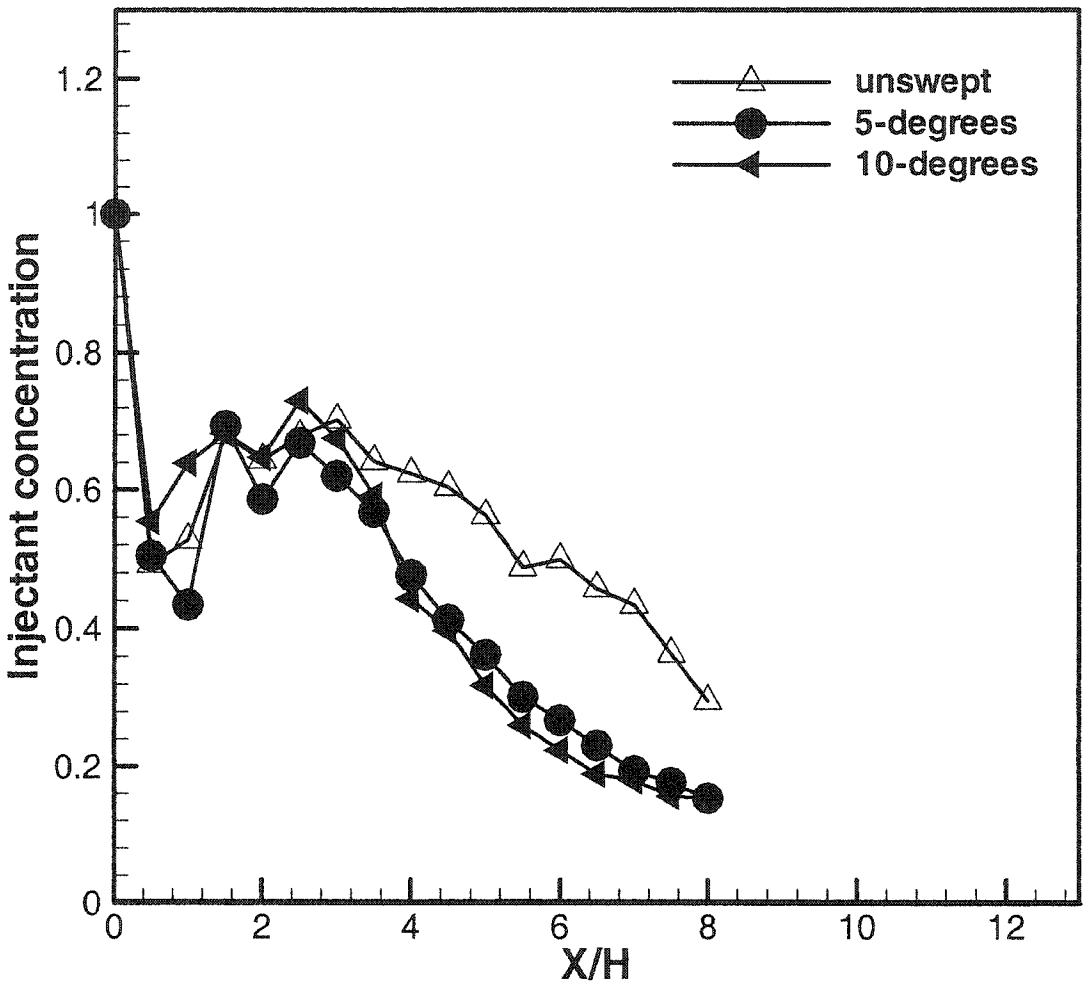

Fig. 4.30 Axial distribution of maximum injectant concentration for different angles

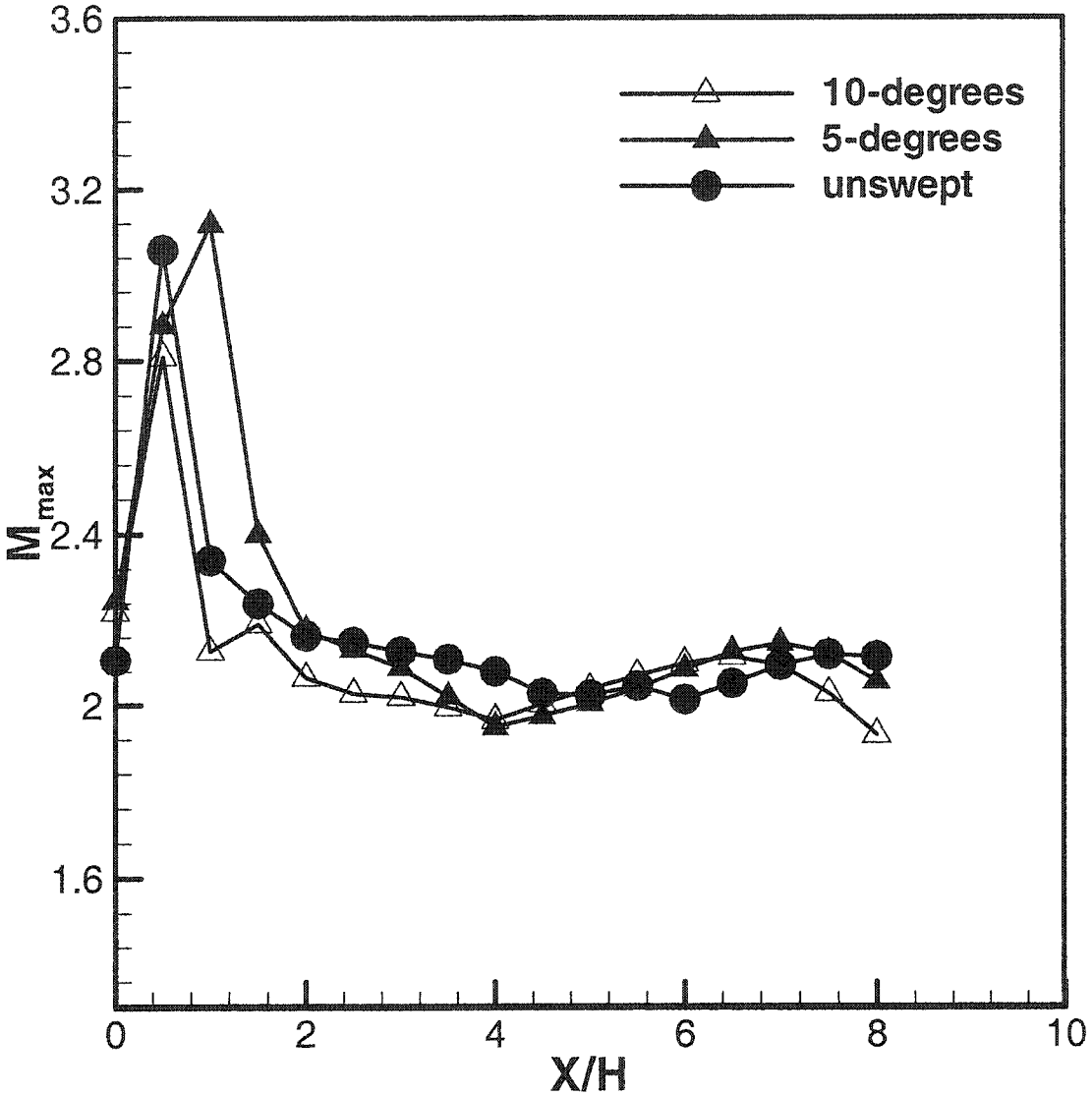

Fig. 4.31 Axial distribution of maximum Mach number for different angles

illustrated in Fig. 4.29. The difference between the two swept ramps and the unswept ramp is significant while the difference between the two swept ramps is small. This leads to a conclusion that there should be an optimum value after which further increase in sweep will not affect the mixing.

The axial distribution of the mass averaged static pressure and the mass averaged Mach number for the three ramps are illustrated in Figs 4.32 and 4.33. The mass averaged values are calculated with Eqs.(4.1) and (4.2). As shown in Fig. 4.32, all ramps calculations show the initial expansion of the jet downstream of the ramp base near X/H=3.0 followed by increase in the pressure due to the compression shock waves and the reflections. Especially, the 10-degree swept ramp shows the large scale values of the pressure. However, the 10-degree swept ramp shows lower values of the Mach number. This is expected due to the high losses relative to the other two ramps as shown in Figs. 4.34 - 4.36. Also, Fig.4.33 shows that the variation of spreading with the side angle affects the mean Mach number decay along the jet centerline.

Figure 4.34 shows the axial distribution of the mass-averaged vorticity magnitude. The vorticity is a measure of the rotation of a fluid element as it moves in the flowfield, and is defined as the curl of the velocity vector. The vorticity and the mass-averaged vorticity are obtained from using the following equations:

$$\zeta = \nabla \times \vec{V} \tag{4.3}$$

$$\bar{\zeta} = \frac{\int \xi \rho \vec{V} \cdot d\vec{A}}{\int \rho \vec{V} \cdot d\vec{A}} \tag{4.4}$$

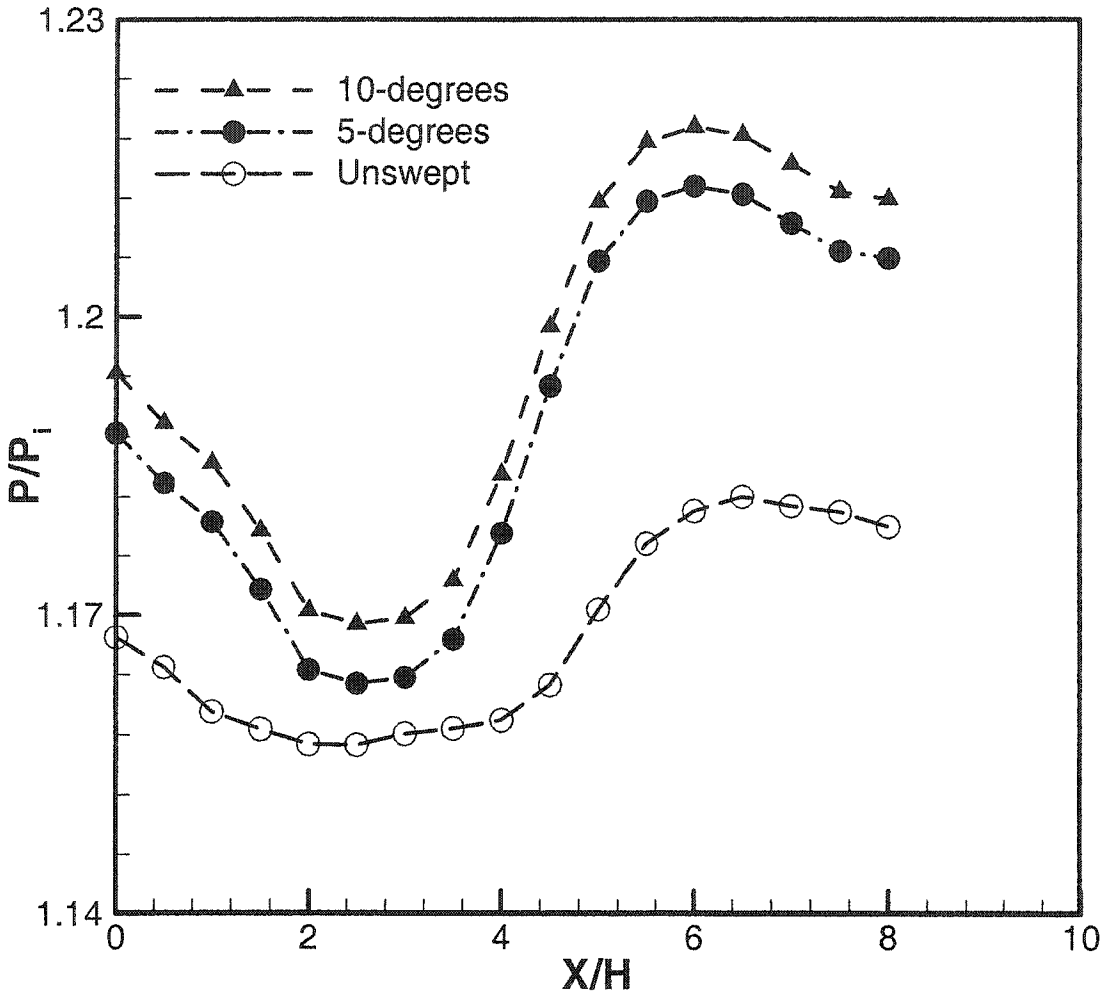

Fig. 4.32 Axial distribution of averaged static pressure for different angles

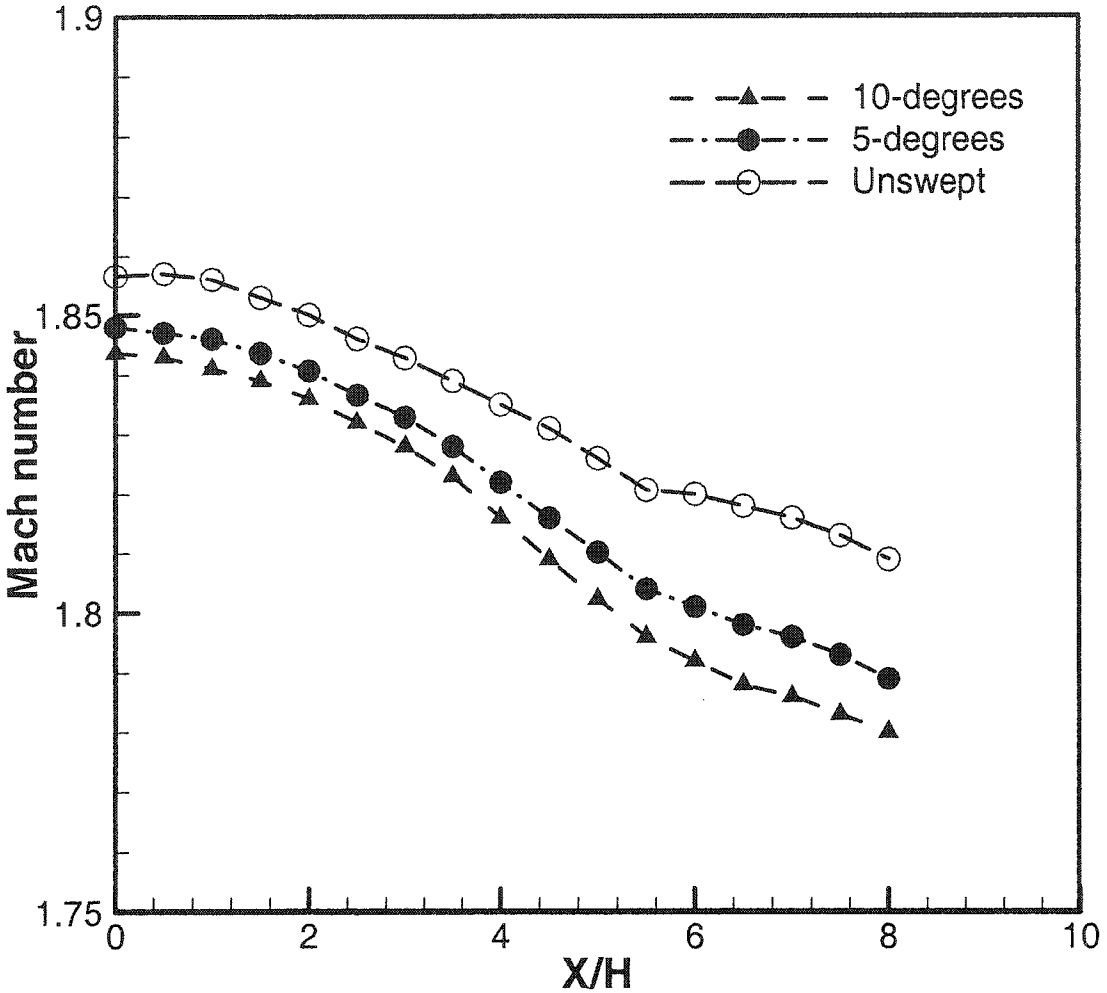

Fig. 4.33 Axial distribution of averaged Mach number for different angles

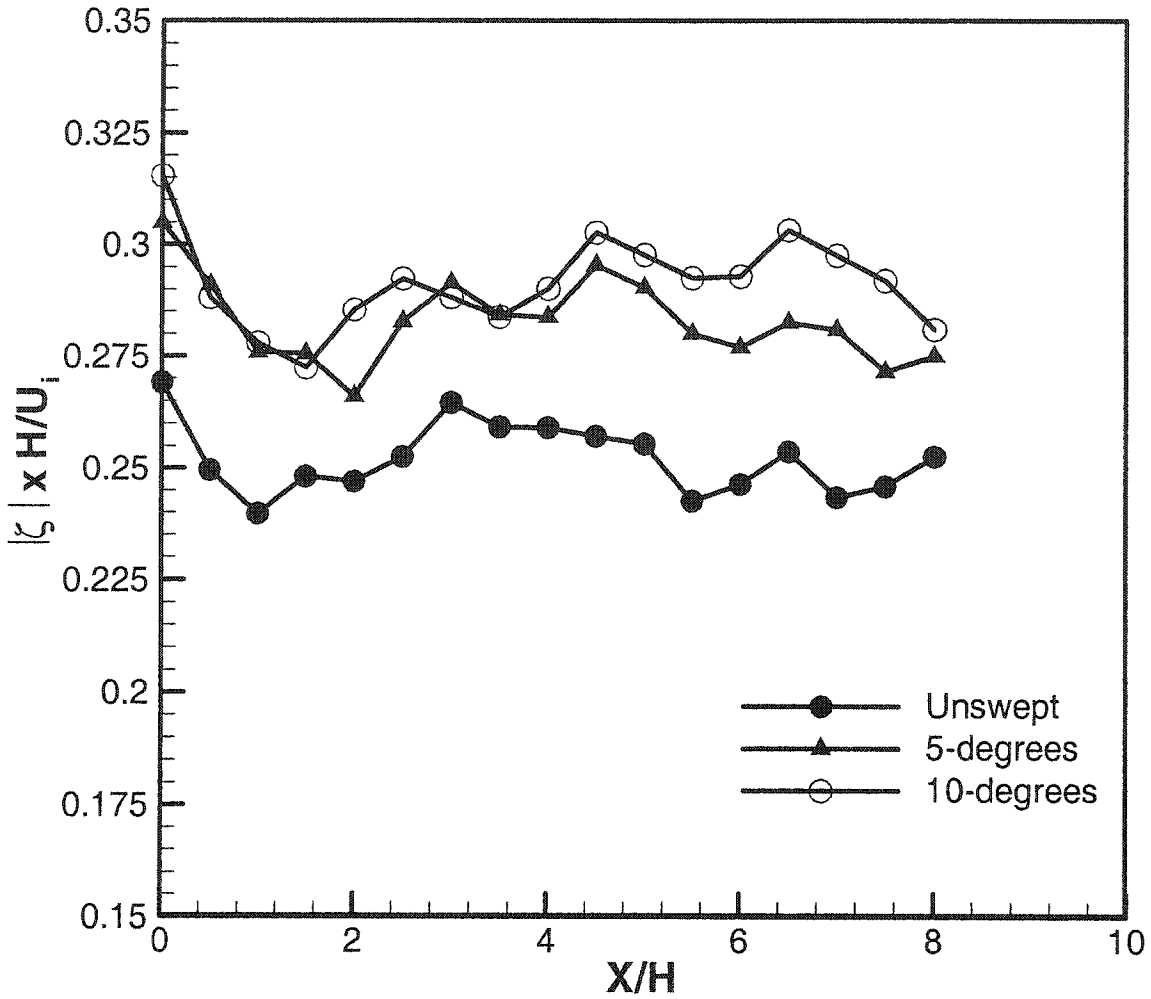

Fig. 4.34 Axial distribution of averaged vorticity magnitude for different angles

The vorticity magnitude is normalized with the ramp height "H" and the inlet streamwise velocity "u."

As expected, the unswept ramp has the weakest vorticity of the three cases examined. The axial distribution of the mass-averaged helicity is shown in Fig. 4.35. The helicity is defined by the dot product of vorticity and the velocity vector. The helicity provides insight into the vorticity aligned with the fluid stream. The helicity and the mass-averaged helicity are obtained from the following equations:

$$h = (\nabla \times \vec{V}) \cdot \vec{V} \tag{4.5}$$

$$\bar{h} = \frac{\int h\rho\vec{V} \cdot d\vec{A}}{\int \rho\vec{V} \cdot d\vec{A}} \tag{4.6}$$

The figure shows the same trend as in Fig. 4.34. The unswept ramp gives lower values than the other two swept ramps.

The losses associated with the mixing process are also can be shown by presenting the entropy increase for the three ramps. Figure 4.36 shows the increase of the entropy with the increase of the distance in the direction of the flow. The 10-degree swept ramp shows higher increase of entropy than the other two ramps.

In a conclusion, one would expect the 5-dgree swept ramp to be an intermediate case between the unswept ramp and the 10-degree swept ramp. However, the difference

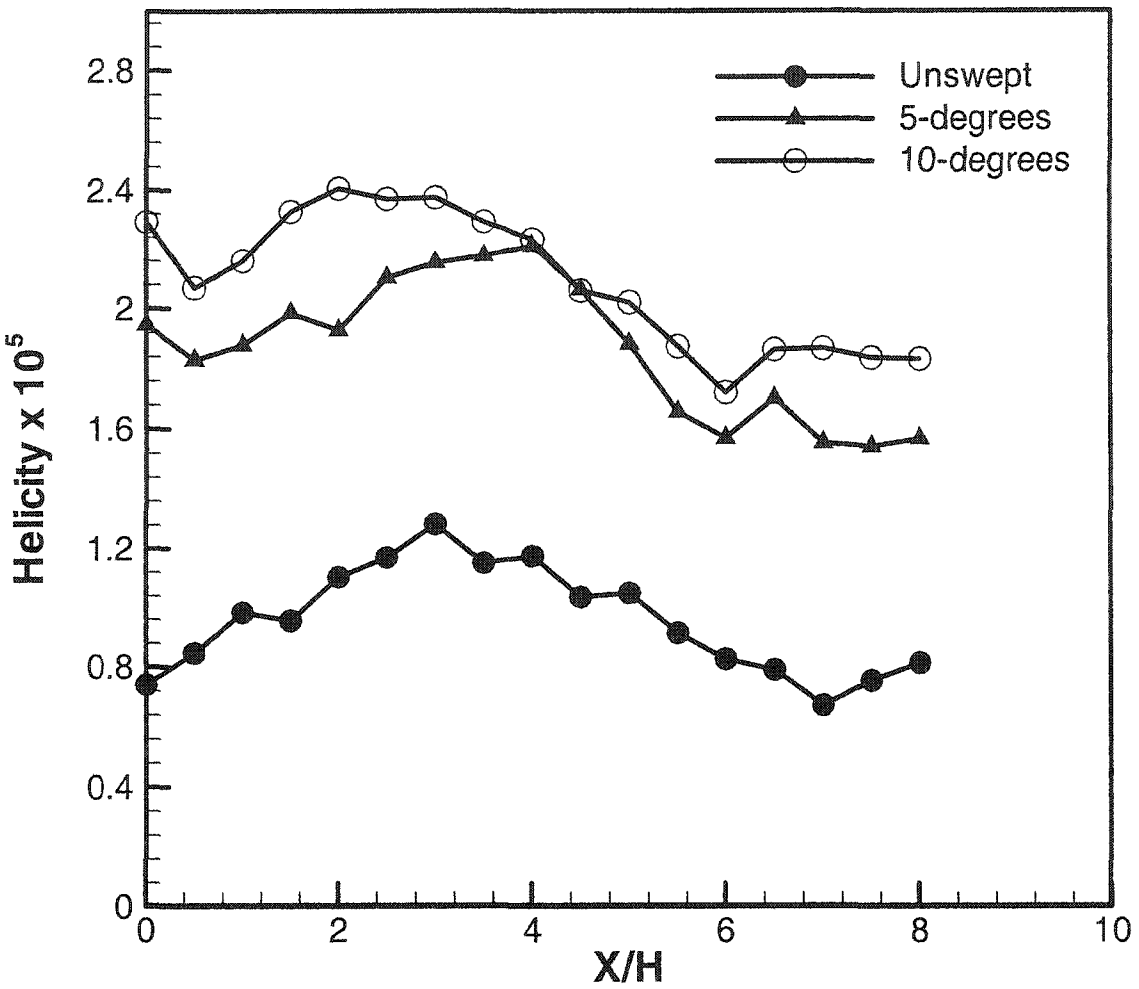

Fig. 4.35 Axial distribution of averaged helicity for different angles

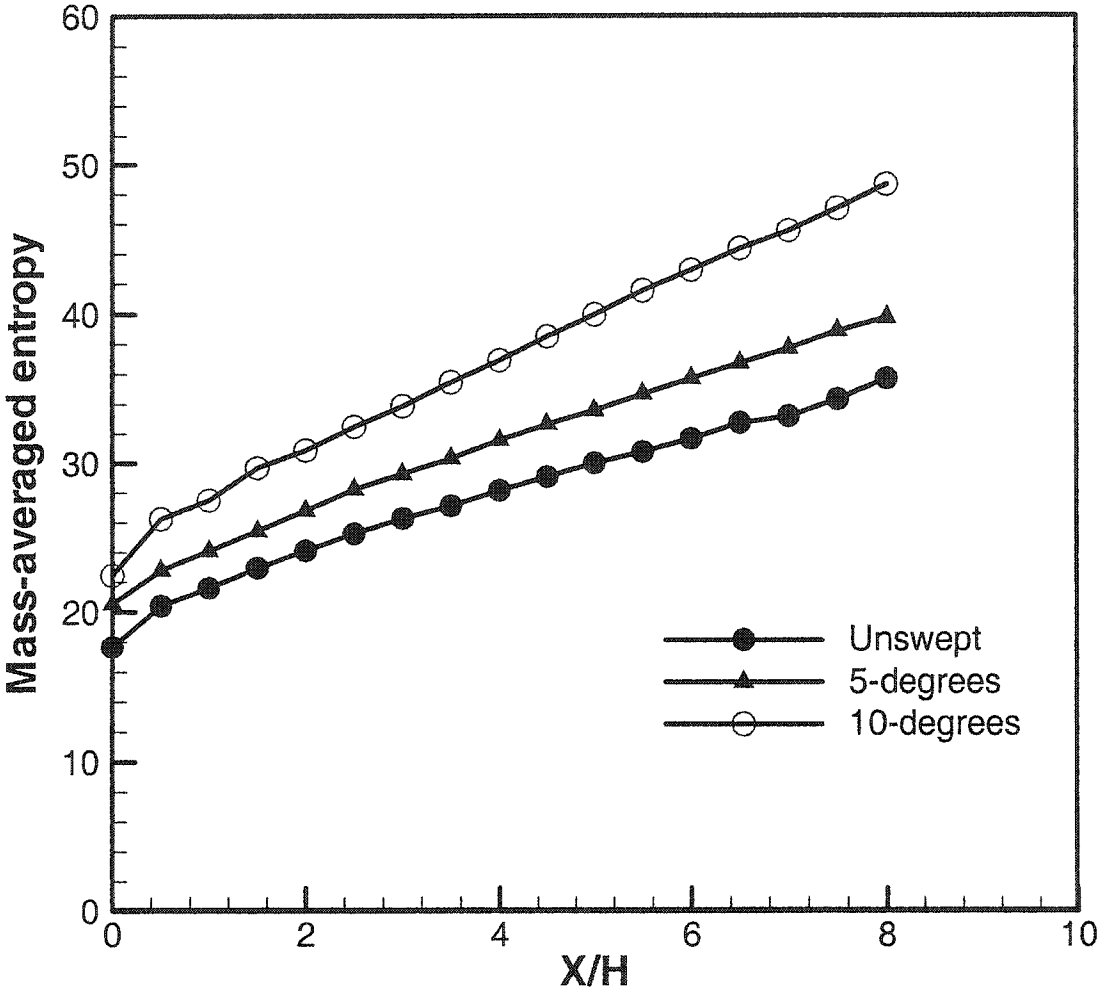

Fig. 4.36 Axial distribution of averaged entropy for different angles

between the two swept ramps is not significant as the difference between the swept ramps and the unswept ramp. This observation is verified by Figs. 4.24 - 4.36.

4.5 Results for Relieved Ramps

Results are obtained for the relieved ramp configuration with two different side-angles namely, 0 and 5 degrees (Figs. 3.6 and 3.7). The mass flow rate of both air and fuel and all flow parameters are kept equal to that of the cases of the raised ramps. Figure 4.37 shows the contours of the static pressure at the plane of symmetry. Figure 4.37 a shows the results of the unswept relieved ramp while Fig. 4.37 b shows the results of the unswept raised ramp in order to demonstrate the difference in the flow structure. The figure demonstrates clearly the difference between the two types of the wall-mounted ramps. The relieved ramp (Fig. 4.37 a) shows strong oblique shock wave introduced at the front base of the ramp due to the 10-degree turning angle of the wall and shows no shock reflections. The bow shock wave formed due to the fuel injection is much stronger than that of the raised ramp. In the second configuration, the raised ramp (Fig. 4.37 b), an oblique shock wave at the ramp base is captured also shock reflections are seen clearly in this configuration.

Figure 4.38 shows the contours of the injectant mole fraction for the unswept relieved ramp and the unswept raised ramp at the plane of symmetry. The decay of the mole fraction for the relieved ramp case occurs at a shorter distance than that for the raised ramp. It is to be noted that, in the relieved ramp configuration, the fuel is injected through an oblique shock wave as shown in Fig. 4.37. Moreover, the fuel is not injected parallel

a. Relieved ramp

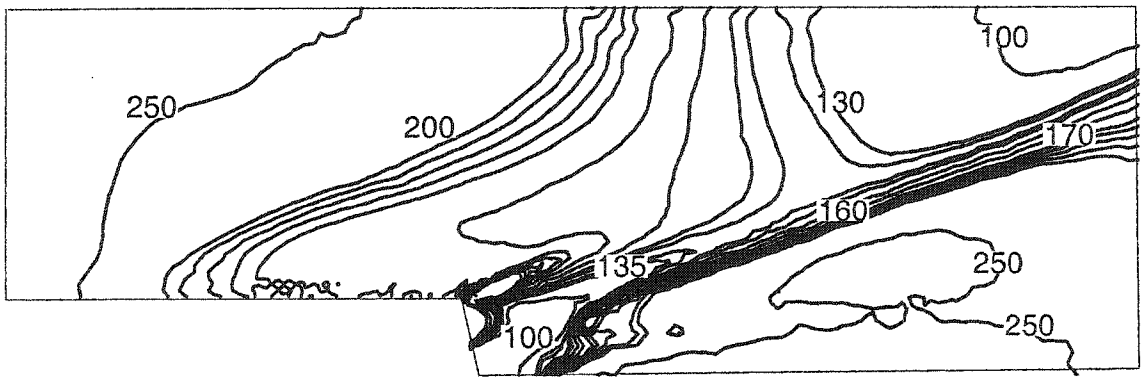

b. Raised ramp

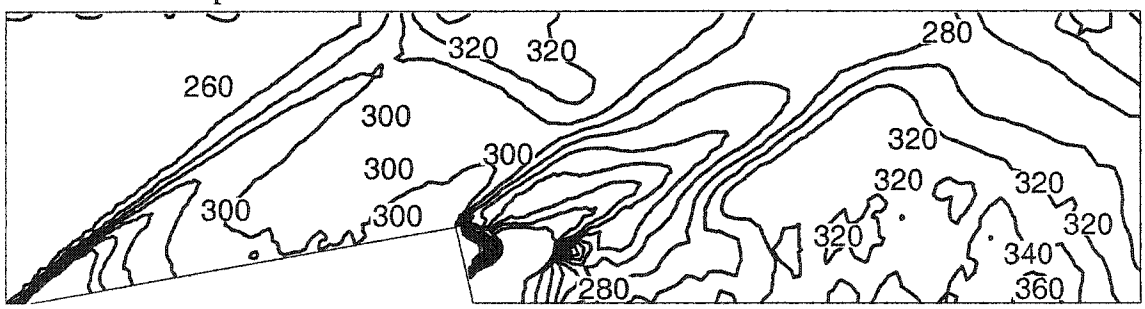

Fig. 4.37 Static pressure contours for relieved and raised ramp

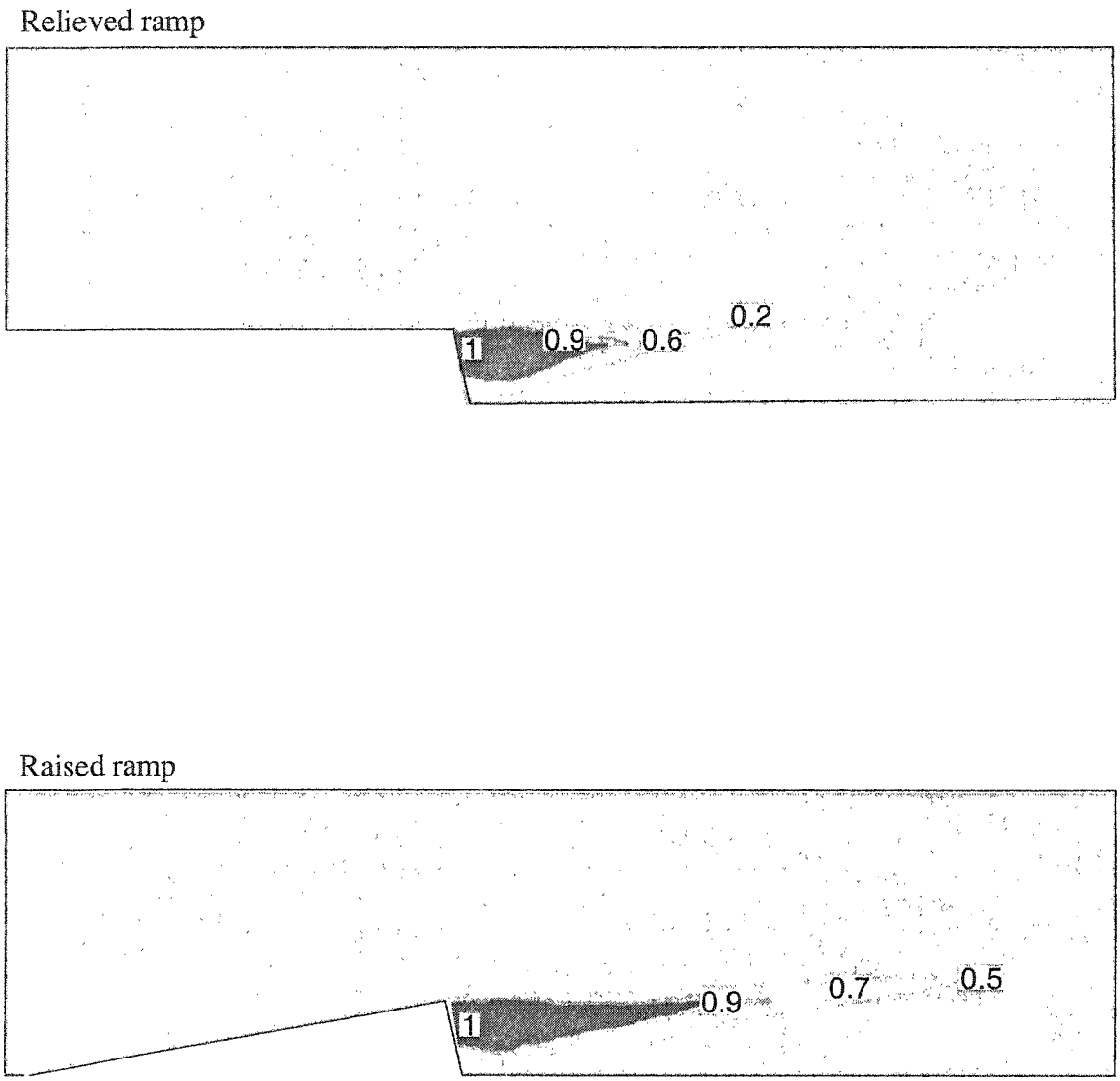

Fig. 4.38 Injectant mole fraction distribution at the palne of symmetry for relieved and raised ramps

to the upstream air as in the raised ramp configuration but inclined with an angle of 10 degrees.

The transport of injectant into the airstream can be observed more clearly by studying the location of the injectant mole fraction contours in different cross sectional planes. The contours of the injectant mole fraction are presented in Fig. 4.39 for the 5-degree swept relieved ramp at different downstream planes. As shown in the figure, streamwise vortex of the ramp begins to transport the fuel away from the jet. Clearly relieved ramp configuration gives faster spread and mixing of the fuel jet. The kidney shape of the fuel starts near the nozzle exit compared with the 5-degree raised ramp (Fig, 4.25)

Figures 4.40 and 4.41 show the streamwise vorticity illustrated by the velocity vectors for both the 5-degree swept and the unswept ramps in different crossflow planes. Similar to the raised ramp case, the vortices are generated by the pressure gradient between the top surface of the ramp and the ramp sides. The relative strengths can be seen clearly. The swept ramp has the stronger strength than the unswept relieved ramp. In the X/H=0.5 plane, the two counter-rotating pairs of axial vortices are seen in both configurations. The vortex formed by the swept ramp is considerably larger. It is to be noted that the spread of the vortices for the two angles is less than that in the raised ramp configurations which is shown in Fig. 4.24.

The mixing rates of the different ramps are illustrated in Figs. 4.42 and 4.43. Figure 4.42 compares the axial decay of the maximum injectant mole fraction for both the unswept raised and relieved ramps. The X axis is normalized with respect to the ramp height H which is kept constant for all ramps and is equal to 5 mm. It can be seen clearly that as the distance from the ramp base increases the maximum mole fraction decreases

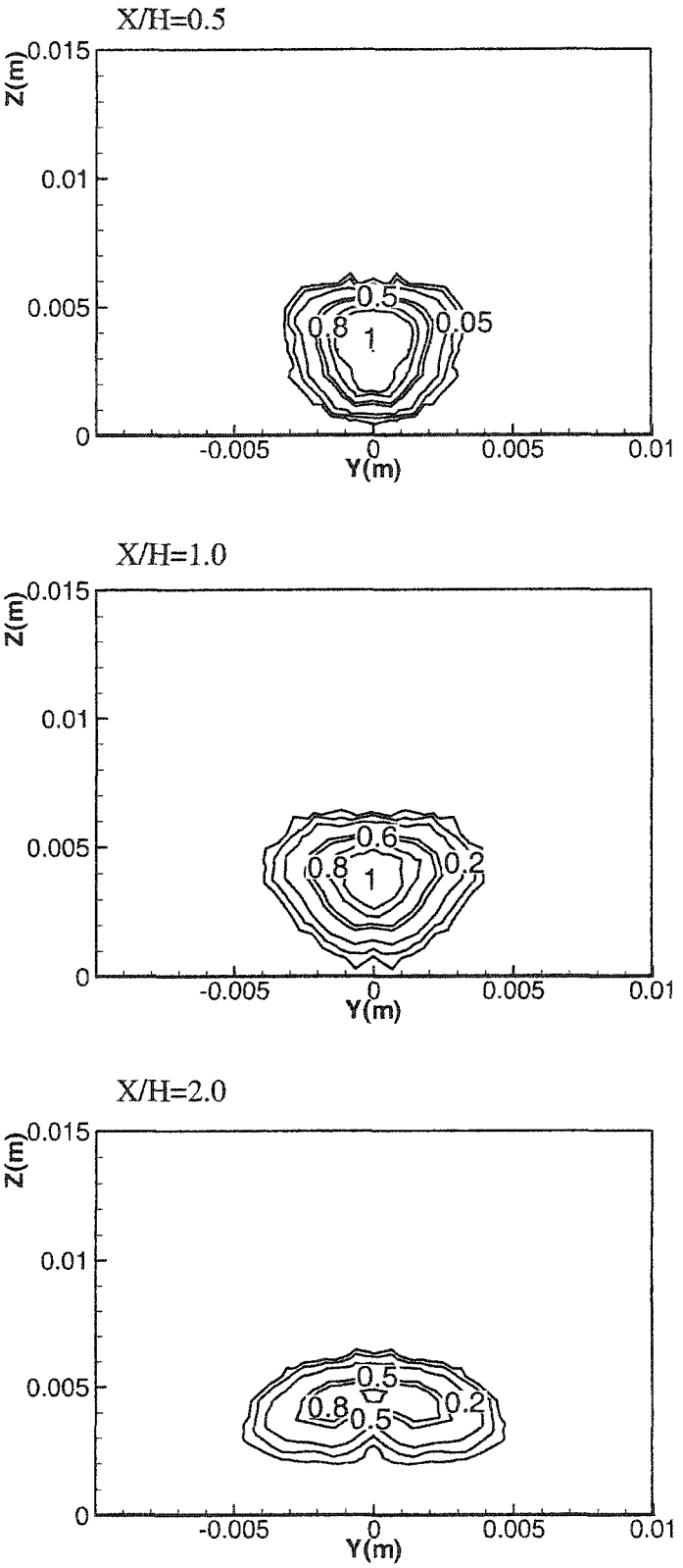

Fig. 4.39 Contours of constant injectant mole fraction for the swept relieved ramp

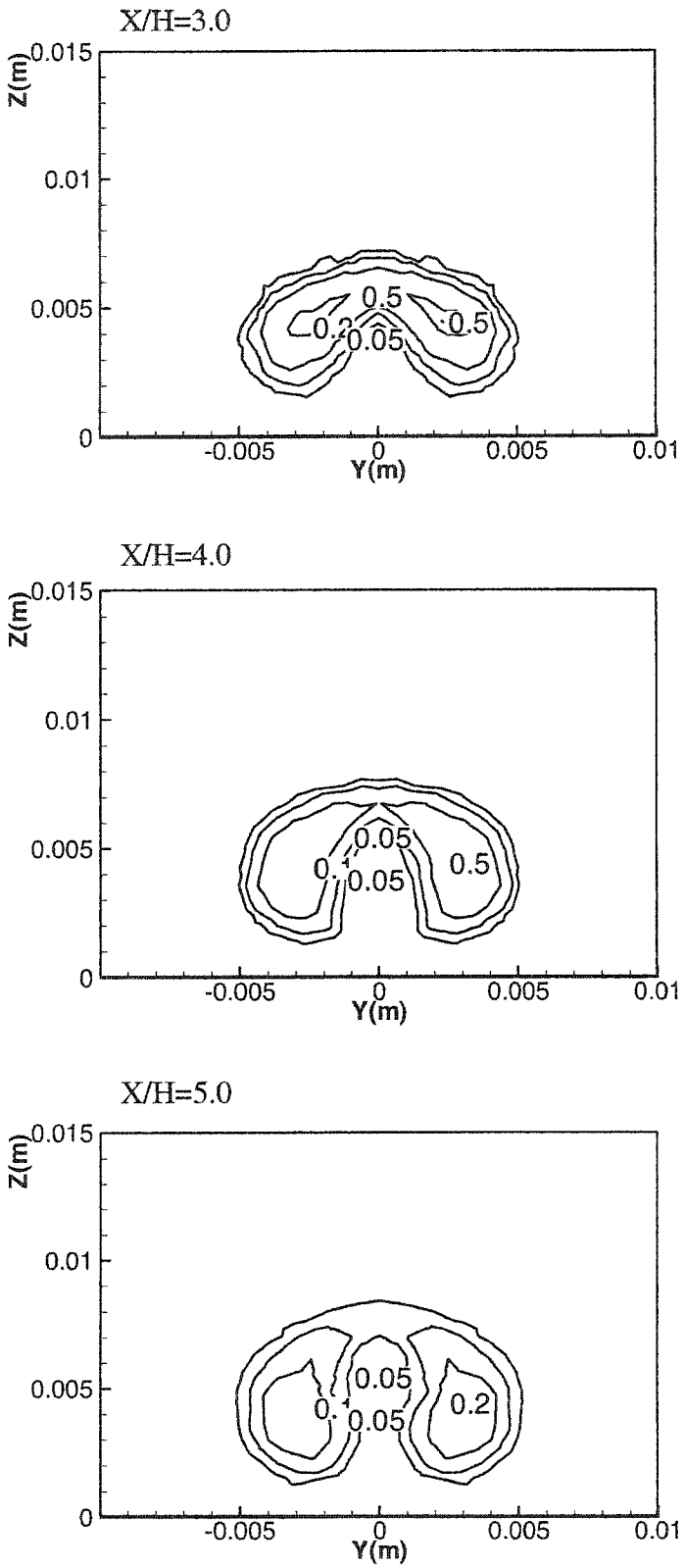

Fig. 4.39 (contd.) Contours of constant injectant mole fraction for the swept relieved ramp

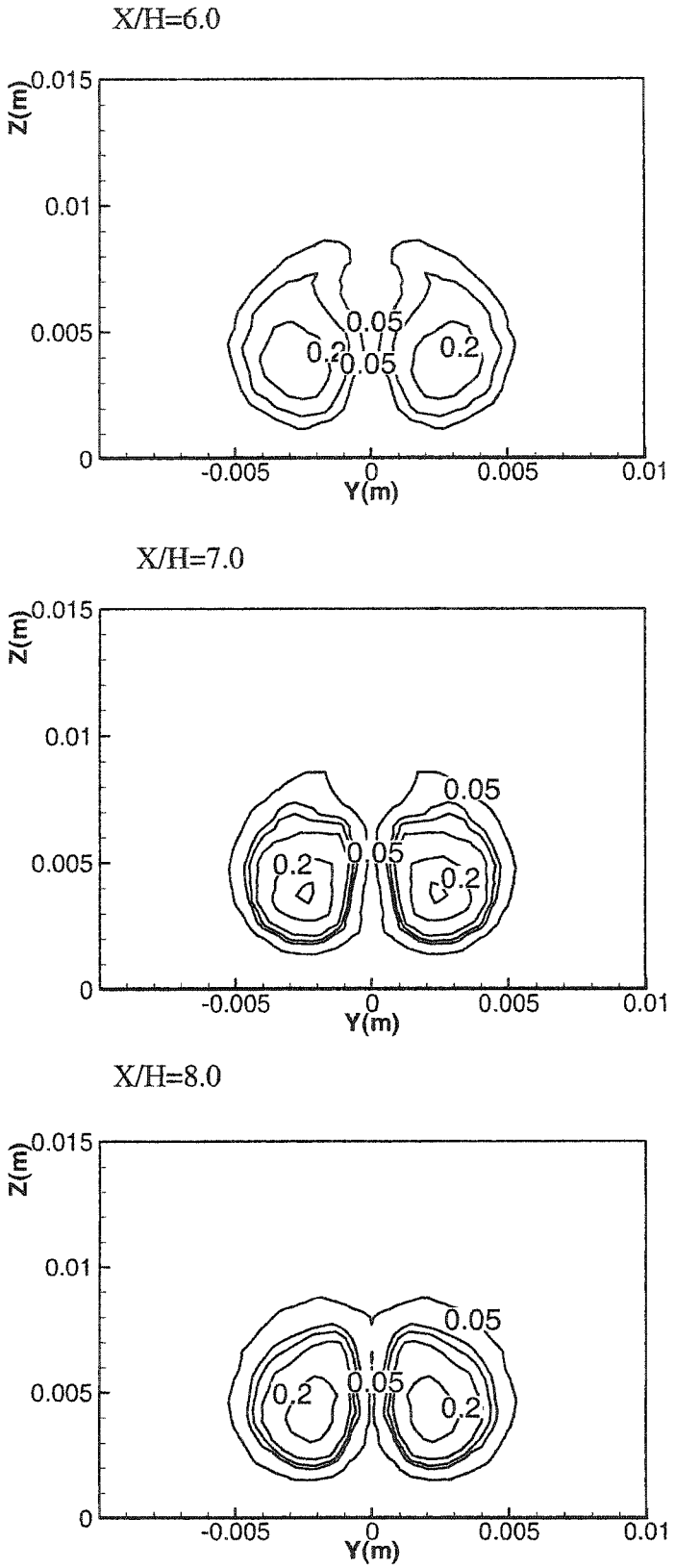

Fig. 4.39 (contd.) Contours of constant injectant mole fraction for the swept relieved ramp

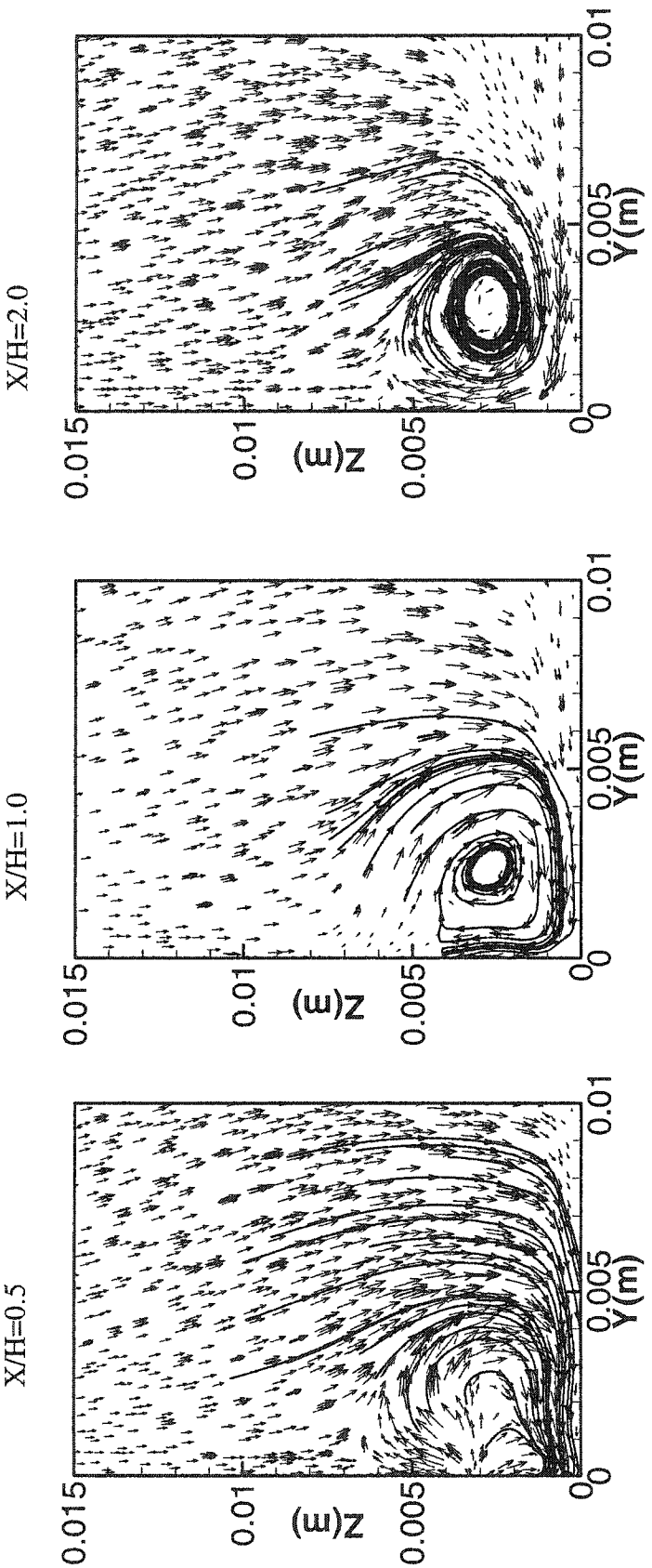

Fig. 4.40 Crossflow plane velocity vectors for the swept relieved ramp

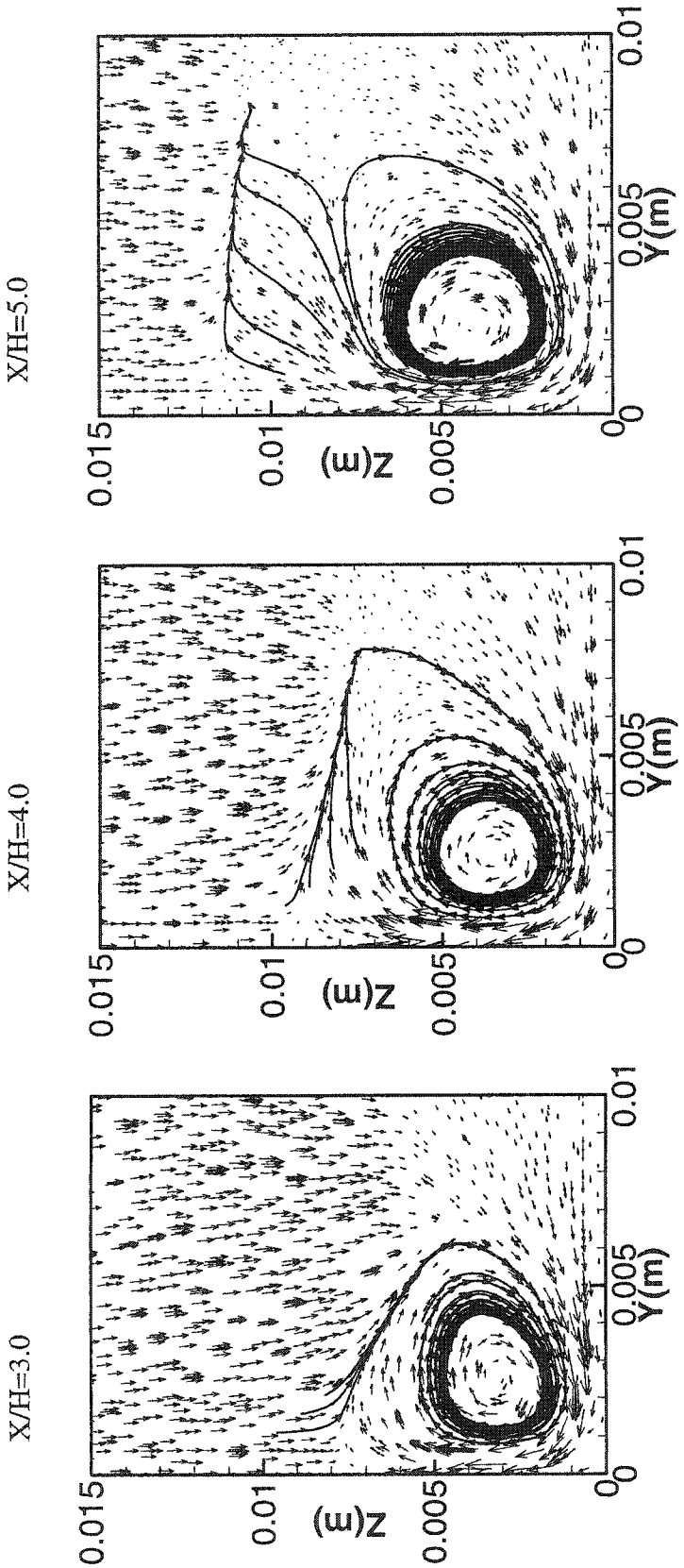

Fig. 4.40 (contd.)Crossflow plane velocity vectors for the swept relieved ramp

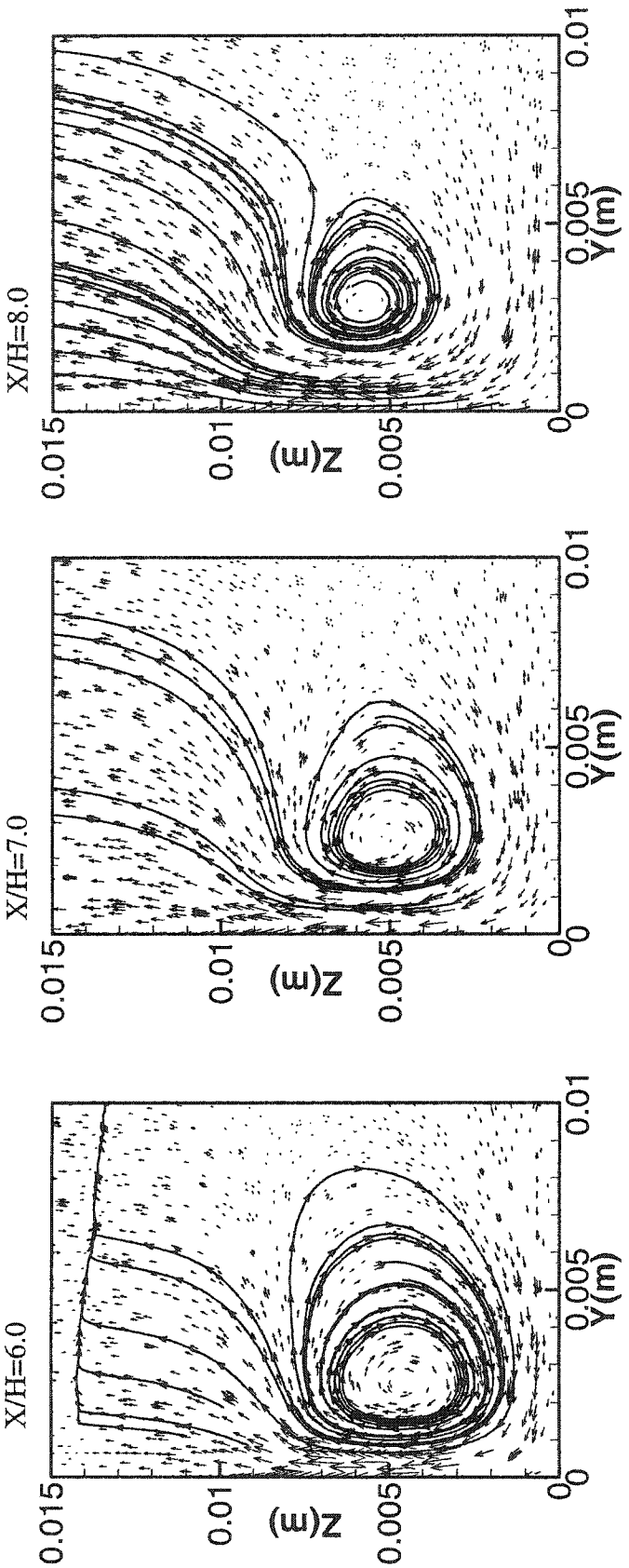

Fig. 4.40 (contd.)Crossflow plane velocity vectors for the swept relieved ramp

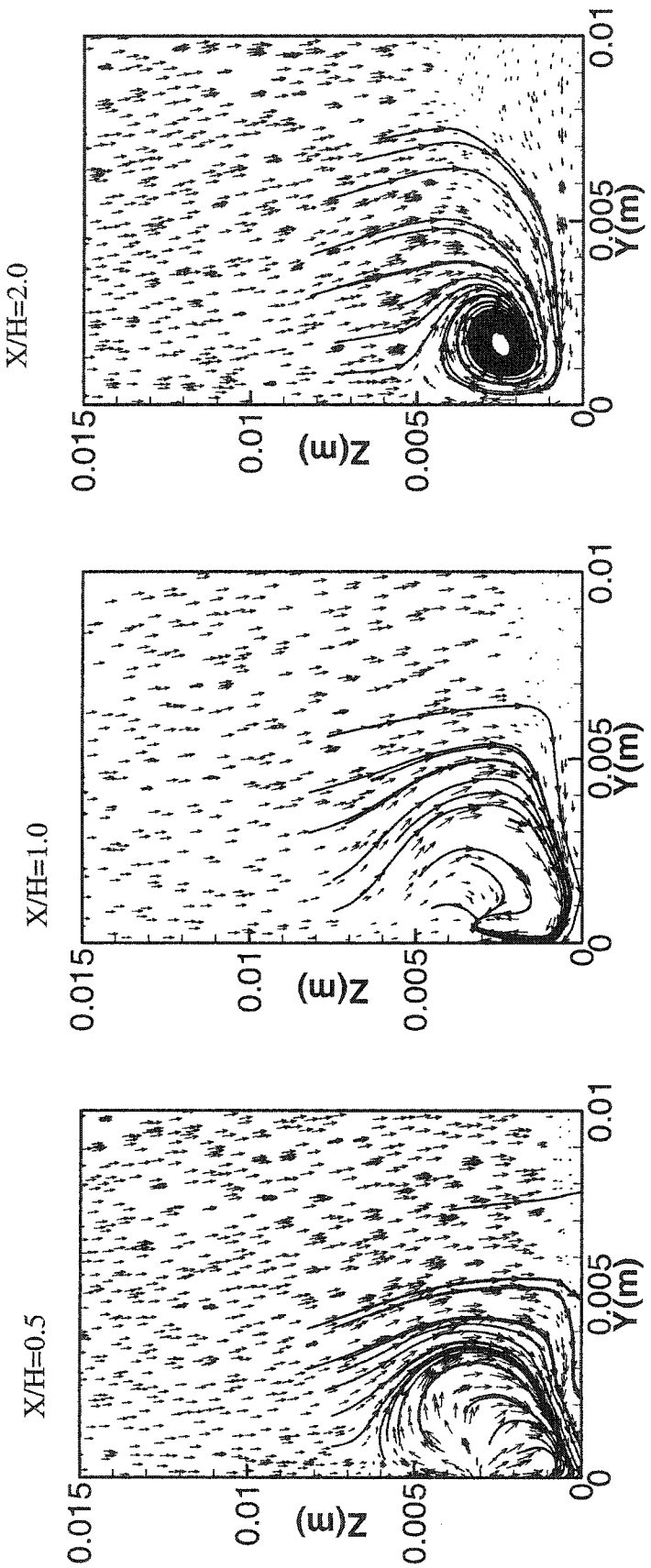

Fig. 4.41 Crossflow plane velocity vectors for the unswept relieved ramp

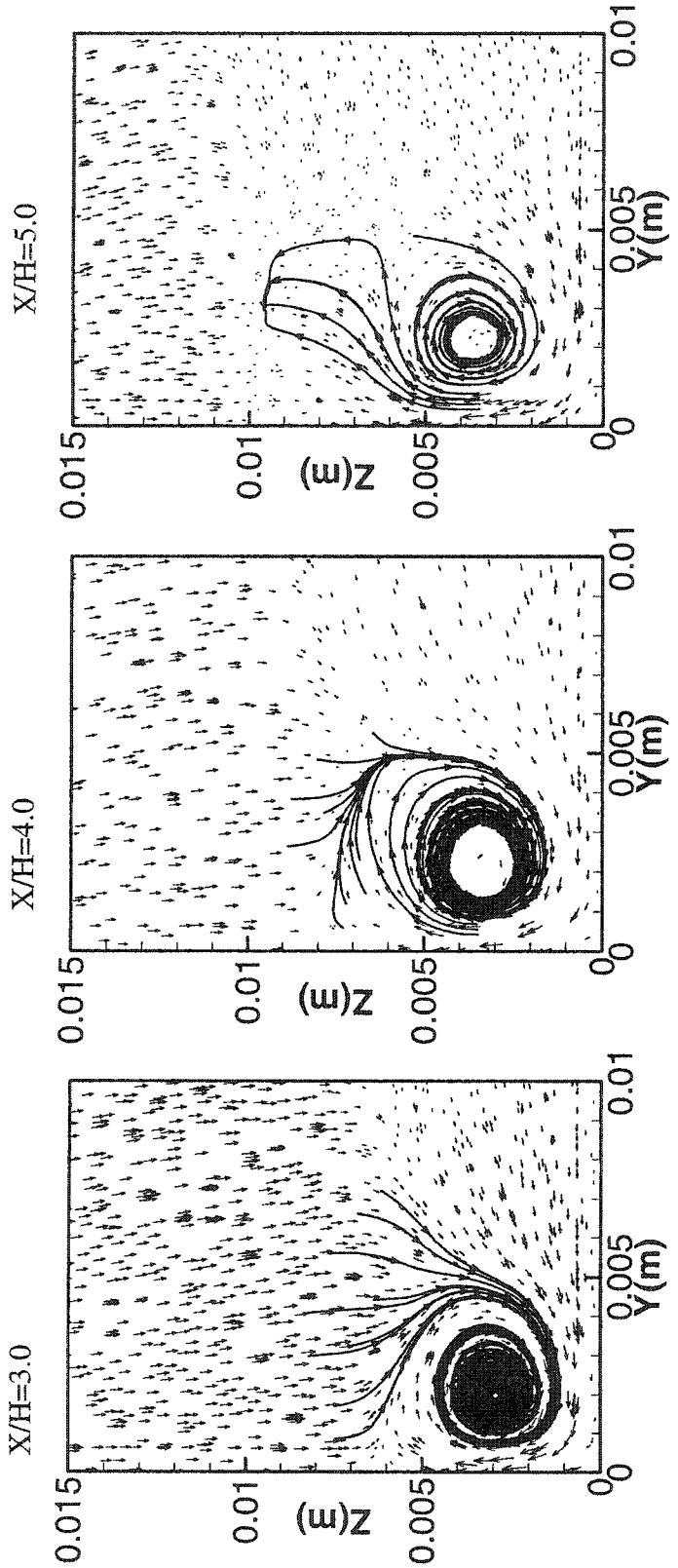

Fig. 4.41 (contd.)Crossflow plane velocity vectors for the unswept relieved ramp

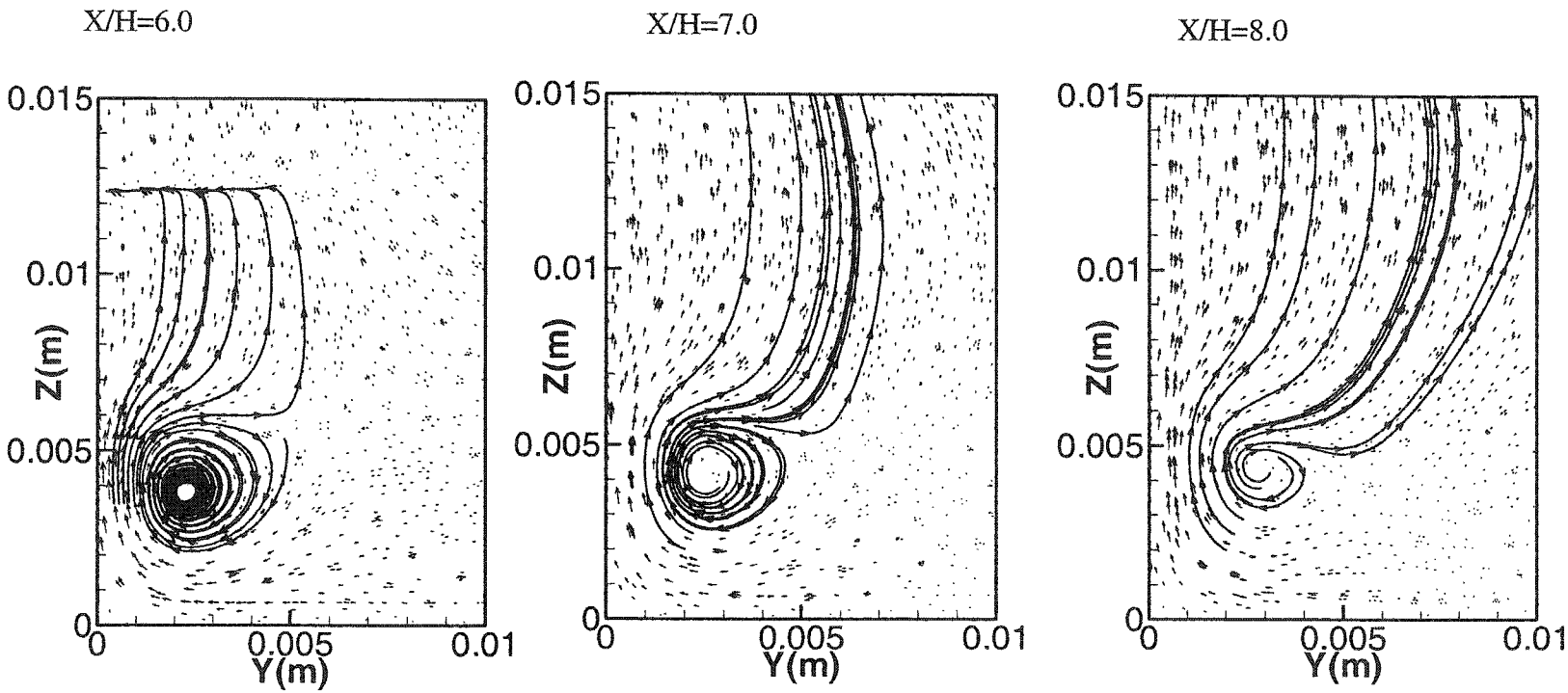

Fig. 4.41 (contd.)Crossflow plane velocity vectors for the unswept relieved ramp

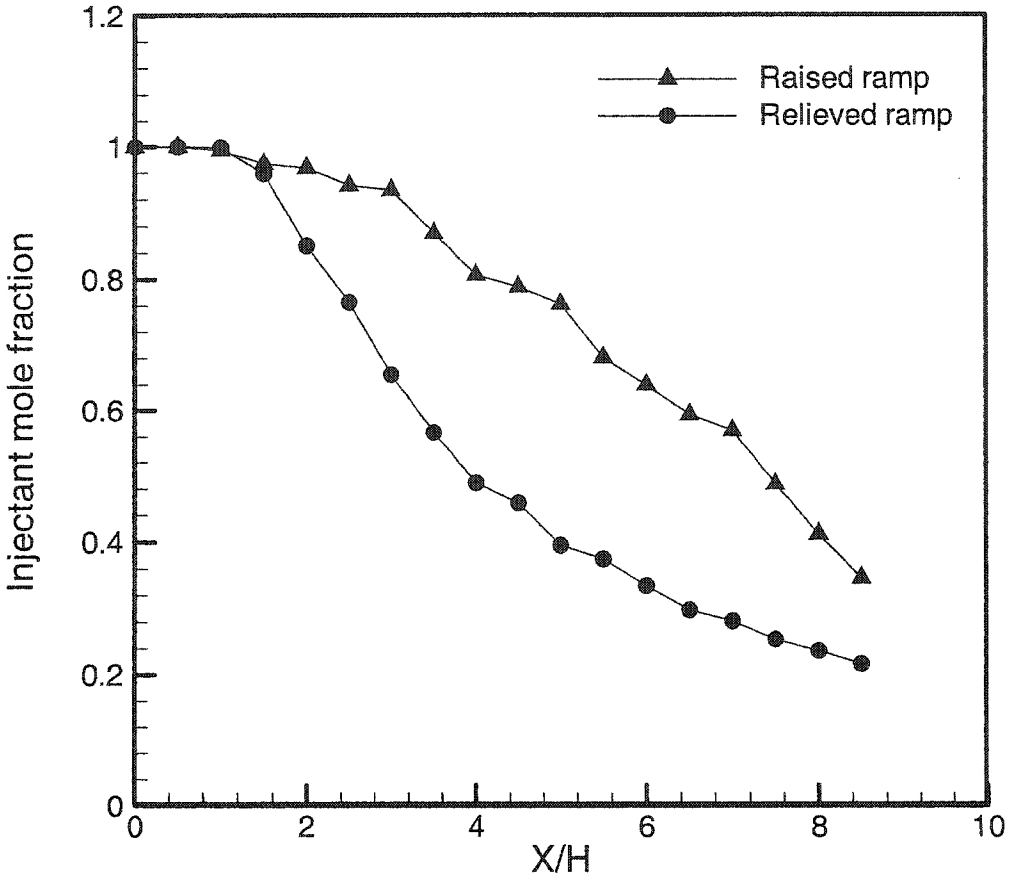

Fig. 4.42 Decay of maximum injectant mole fraction for the unswept ramps

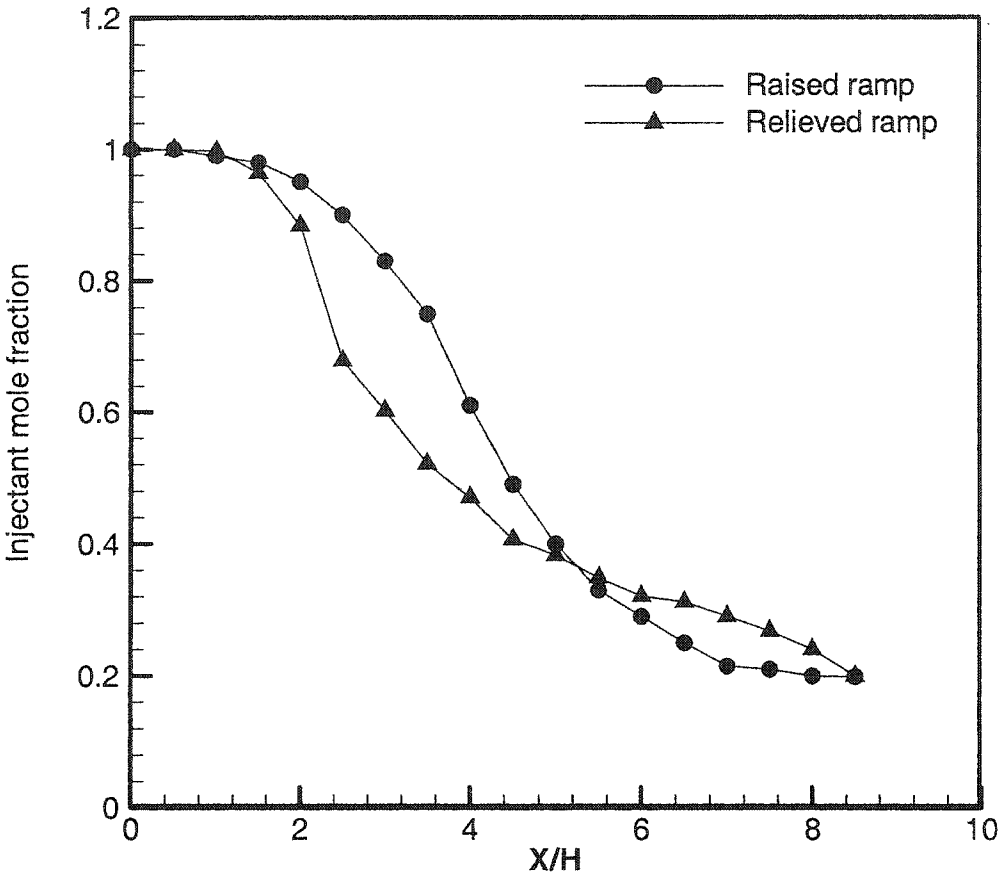

Fig. 4.43 Decay of maximum injectant mole fraction for the 5-degree swept ramps

rapidly in the relieved ramp compared to the raised ramp. This indicates the higher mixing rate of the unswept relieved ramp. The mixing rate near the ramp base is the same for the two ramps, while after X/H=1.6 the mixing rate of the unswept relieved ramp increases rapidly. This is due the difference in the structure of the flowfield. At X/H=4.0, the mole fraction reduces to about 44% of its maximum for the unswept relieved ramp while it reduces to about 80% of its maximum value in the unswept raised ramp case. Further downstream at X/H=8.0, these values become about 24% and 44% respectively. After this, the values become very close for the two cases. In Fig. 4.43, the mixing rate is presented for ramps with side sweep angle of 5 degrees. Similar to the case of unswept ramps, the swept 5-degree relieved ramp also gives higher mixing rate than the 5-degree swept raised ramp, although the difference between the two swept ramps is not significant as in the unswept ramps case. Further downstream, the injectant mole fraction decreases to about 20% of its maximum value which is relatively better than that of the unswept case.

The axial distributions of the vorticity magnitude and the helicity are shown in Figs. 4.44 and 4.45. As expected, similar to the raised ramp configuration, the values of the vorticity and the helicity are higher in the case of the swept ramp than the unswept ramp. Both figures verify that better mixing had occurred with swept ramps due to the strength of the vortex.

The averaged entropy and the averaged Mach number for both relieved ramps are shown in Figs. 4.46 and 4.47. With the swept relieved ramp, the increase in the entropy is much higher and steeper than that for the unswept relieved ramp. This means more losses associated with the mixing process of the swept ramp. Also, with the swept

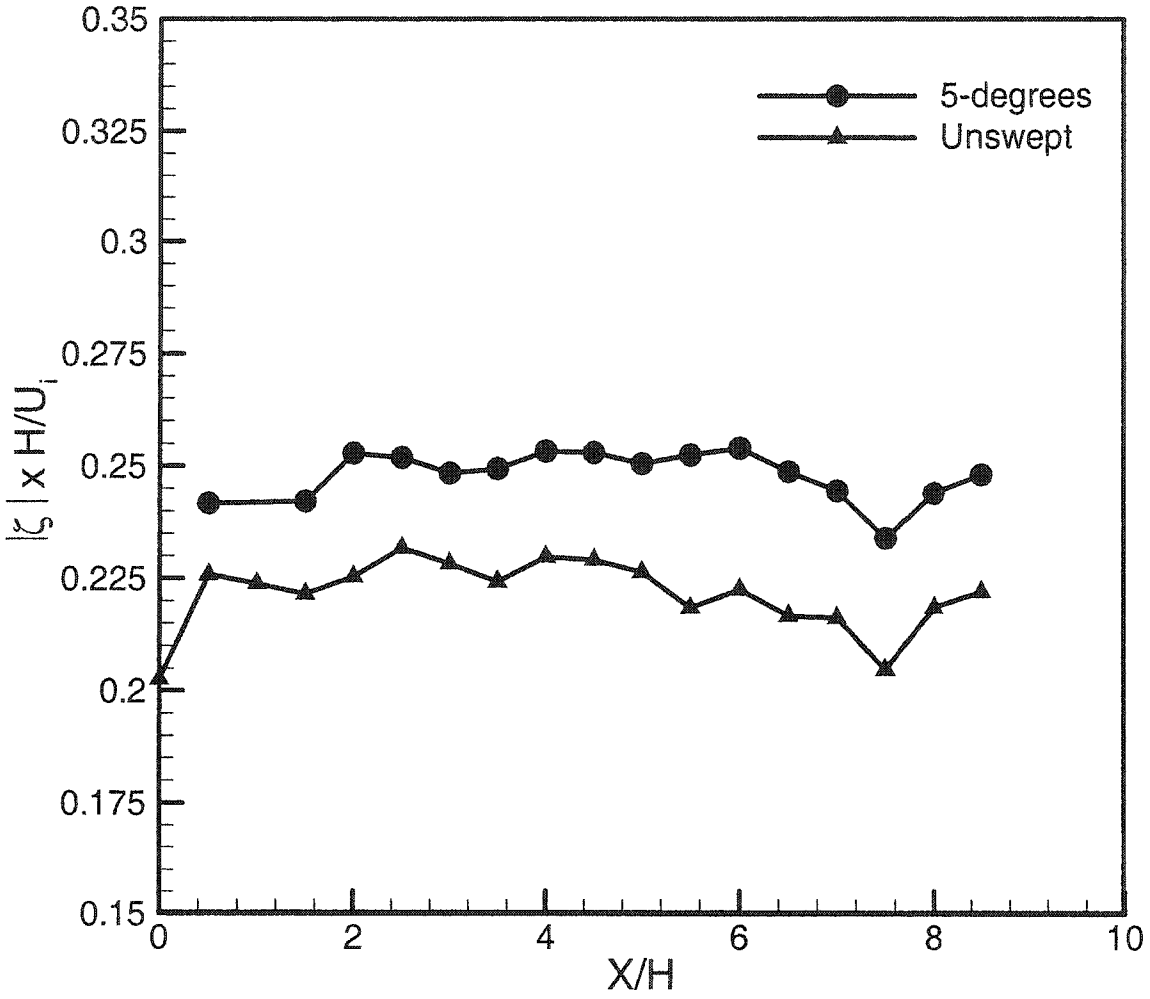

Fig. 4.44 Axial disribution of averaged vorticity magnitude for relieved ramps

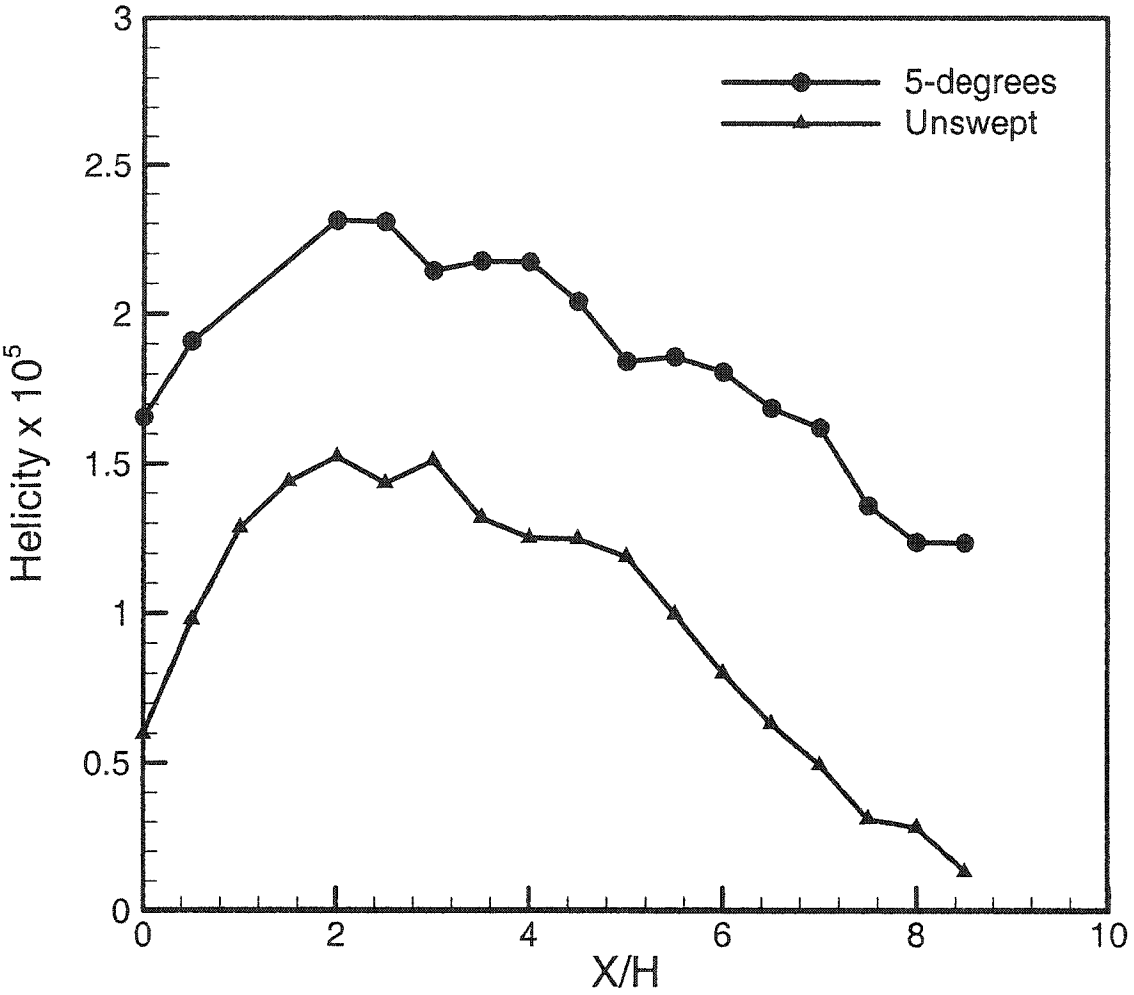

Fig. 4.45 Axial disribution of averaged helicity for relieved ramps

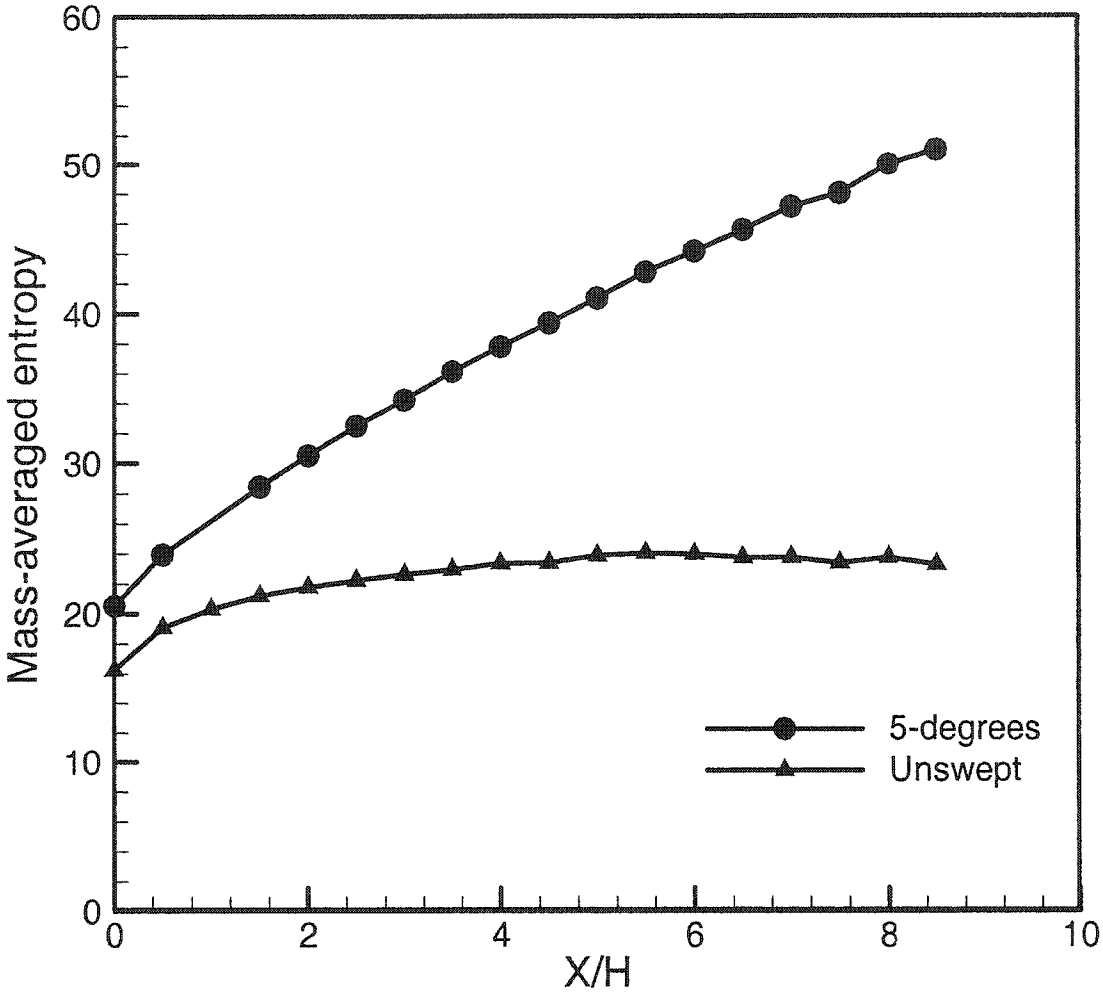

Fig. 4.46 Axial disribution of averaged entropy for relieved ramps

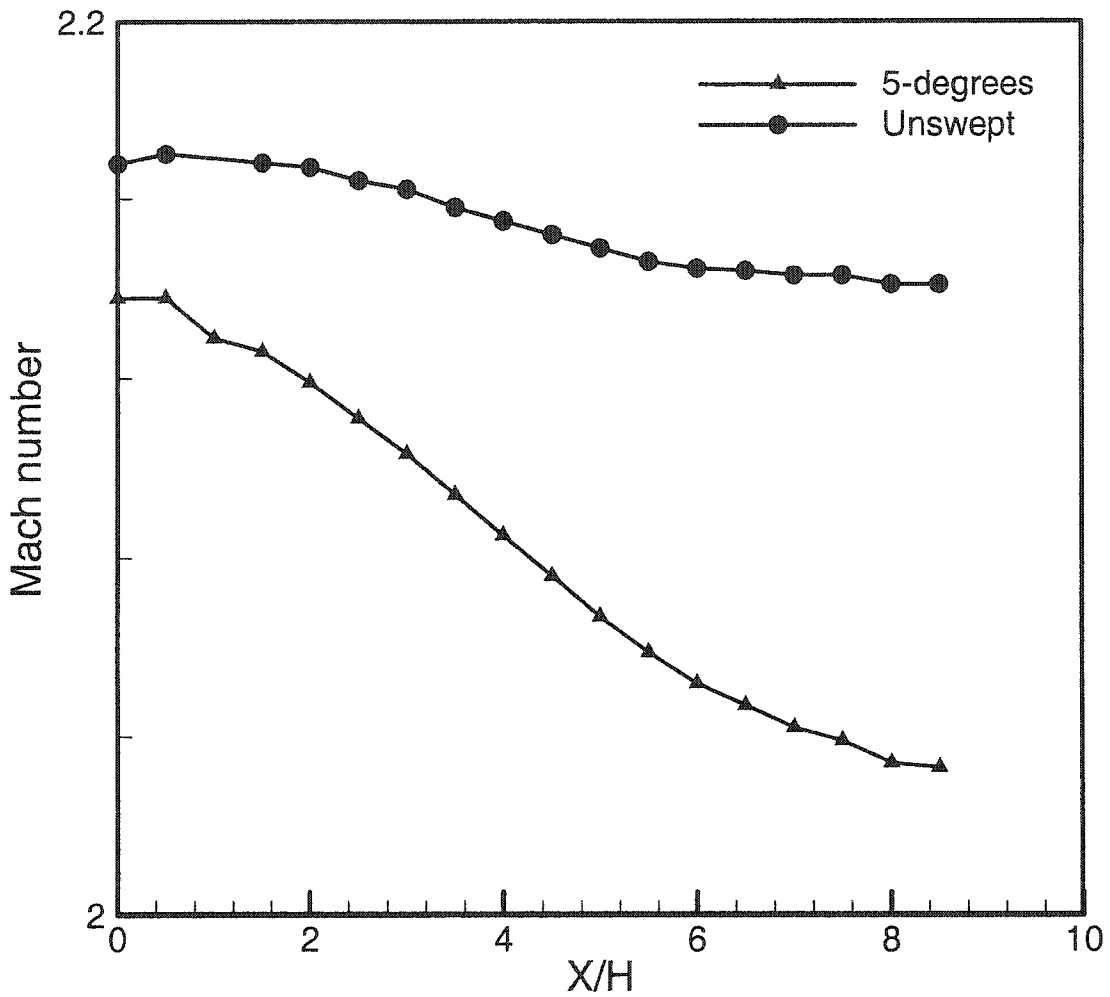

Fig. 4.47 Axial disribution of averaged Mach number for relieved ramps

relieved ramp the values of the averaged Mach number are much less than that of the unswept relieved ramp; however, the whole flow field for both ramps is supersonic.

From the results presented in Secs. 4.4 and 4.5, it can be concluded that better mixing and combustion can be achieved with the swept ramps. However, the unswept ramp also shows some enhancement in the mixing process for the supersonic mixing and combustion.

Chapter V

RESULTS FOR DUAL-MODE COMBUSTORS

Results for two different configurations of dual-mode combustors are presented in this chapter. In the first configuration fuel is injected through an unswept wall-mounted ramp parallel to the incoming airstream. In the second configuration, fuel is injected after a rearward facing step normal to the incoming airstream. Results for both reacting and nonreacting flows are presented.

5.1 Dual-Mode Combustor with Wall-Mounted Ramps

The geometry is similar, but not identical, to the University of Virginia's proposed dual-mode combustor [74]. Two combustor ducts are investigated with length of 10 and 20 ramp heights "H." Hydrogen fuel is injected through single unswept ramp with aspect ratio of 0.5 (see Fig. 3.8). Predicted results of nonreacting flow as well as for reacting flow are presented with two equivalence ratios ϕ=0.31 and ϕ=0.41. The inflow conditions for the two cases are given in Tables 5.1 and 5.2. Both nonreacting and reacting flow results are obtained with a grid size of about 400,000 cells. In this section, results are presented for the 20H combustor and with the two equivalence ratios (ϕ=0.31 and ϕ=0.41) followed by results of the 10H combustor.

Figure 5.1 shows the predicted duct centerline wall pressures. Agreement in peak pressure and the downstream trend is seen in both cases. A slight difference is seen inside the combustor at 4H<X<12H. Shock reflections can be seen only in the case with ϕ=0.31. The pressure remains constant inside the isolator followed by sudden increase to about

Table 5.1 Inlet flow conditions (ϕ=0.31)

Parameter	Freestream	Injectant
P_o [kPa]	390	1010
T_o [K]	1120	300
M	2	1.7
Turbulent Intensity	1 %	1 %
H_2 mass fraction	0	1.0
H_2O mass fraction	0.17315	0
O_2 mass fraction	0.24335	0

Table 5.2 Inlet flow conditions (ϕ=0.41)

Parameter	Freestream	Injectant
P_o [kPa]	333	1350
T_o [K]	1155	460
M	2	1.7
Turbulent Intensity	1 %	1 %
H_2 mass fraction	0	1.0
H_2O mass fraction	0.17315	0
O_2 mass fraction	0.24335	0

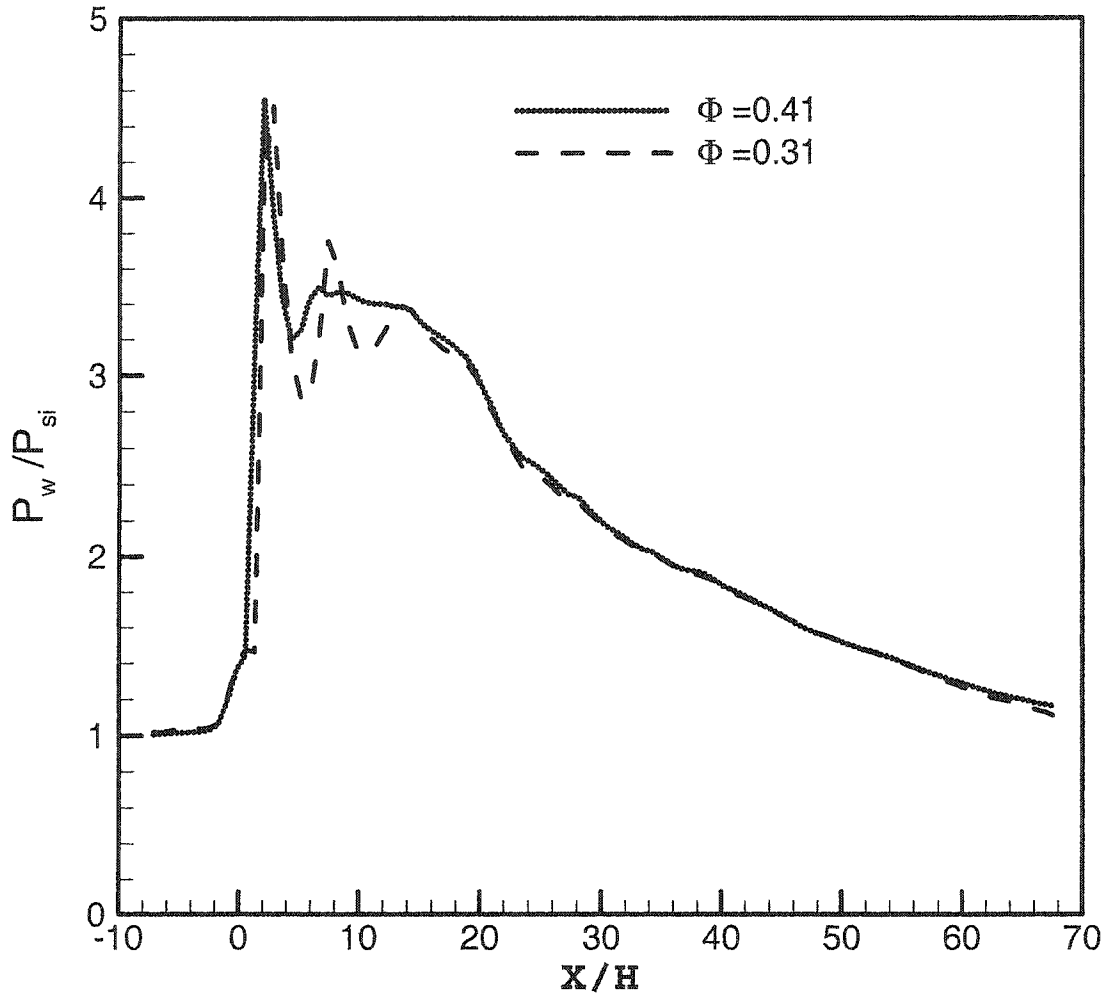

Fig. 5.1 Pressure distribution on the top wall (L_c=20H)

1.4 times its initial value due to the presence of a shock wave formed by the ramp. The pressure reaches its maximum value (4.6 times of the initial value) at a distance of about 4 ramp heights. This increase is due to the fuel injection and the combustion of the fuel.

The mass-averaged Mach number distribution is shown in Fig. 5.2. It can be seen that in both cases the flow is decelerated from supersonic to subsonic conditions within a very short distance near the combustor inlet due to the shock system. This subsonic region is characteristics of the dual-mode combustion. The averaged flow in the case with ϕ=0.31 is subsonic for 2<X/H<20. After that, the flow smoothly transitioned from subsonic to supersonic flow in the expanding duct due to heat release.

The mass-weighted static temperature is shown in Fig. 5.3. A high increase in the temperature occurs near the injector due to the flow deceleration and the released heat from the combustion of the fuel. The average temperature is raised from about 750K to 1160K within 4 ramp heights. Further increase of the temperature is seen with the increase of the axial distance due to the continuation of the combustion process.

In Figs. 5.4 and 5.5 velocity vectors and streamlines are presented for both equivalence ratios at three cross-flow planes. The two vortices generated by the ramp are clearly visible at theX/H=3 plane. The figures show that, as the distances downstream of the ramp increases, the two vortices attract each other and merged together as seen at X/H=6. The merging rate is seen higher in the case with ϕ=0.31 than the other one with ϕ=0.41(Fig. 5.5). To further investigate the rotation of the flow in the flowfield of the combustor, the averaged vorticity magnitude is shown in Fig. 5.6. The vorticity is normalized with the ramp height "H" and the inlet streamwise velocity "U." The maximum values are seen near X/H=2 in both cases. Although both cases show the same

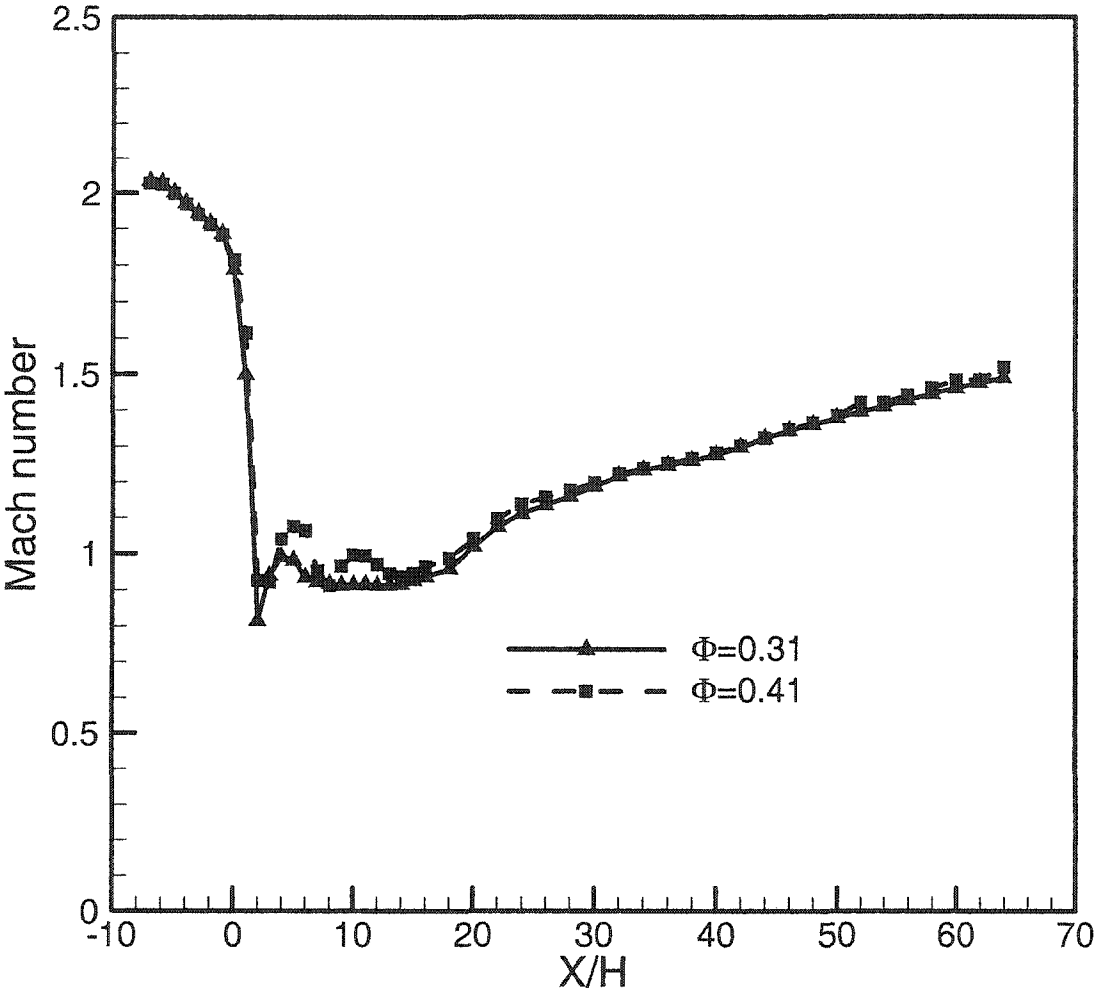

Fig. 5.2 Distribution of averaged Mach number (L_c=20H)

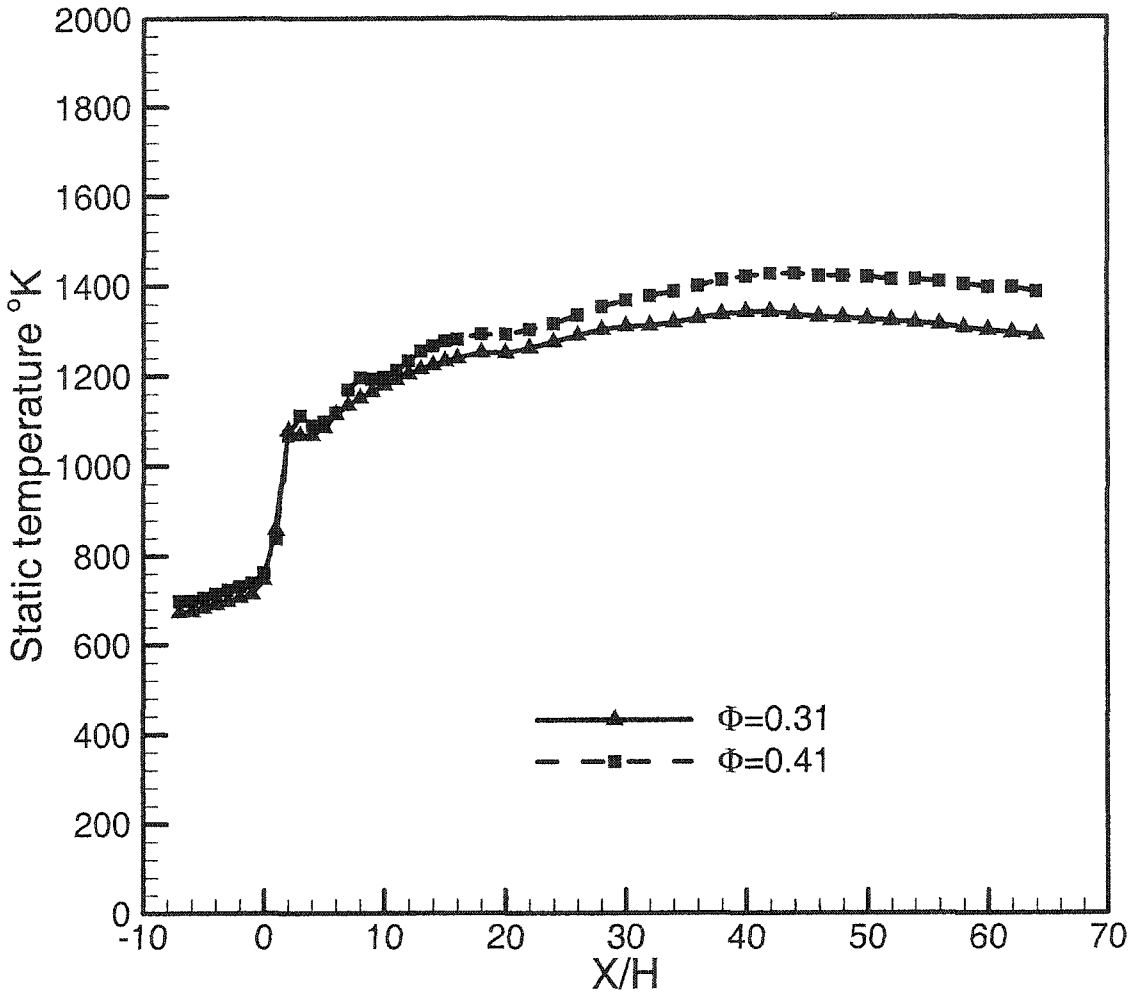

Fig. 5.3 Distribution of averaged static temperature (L_c=20H)

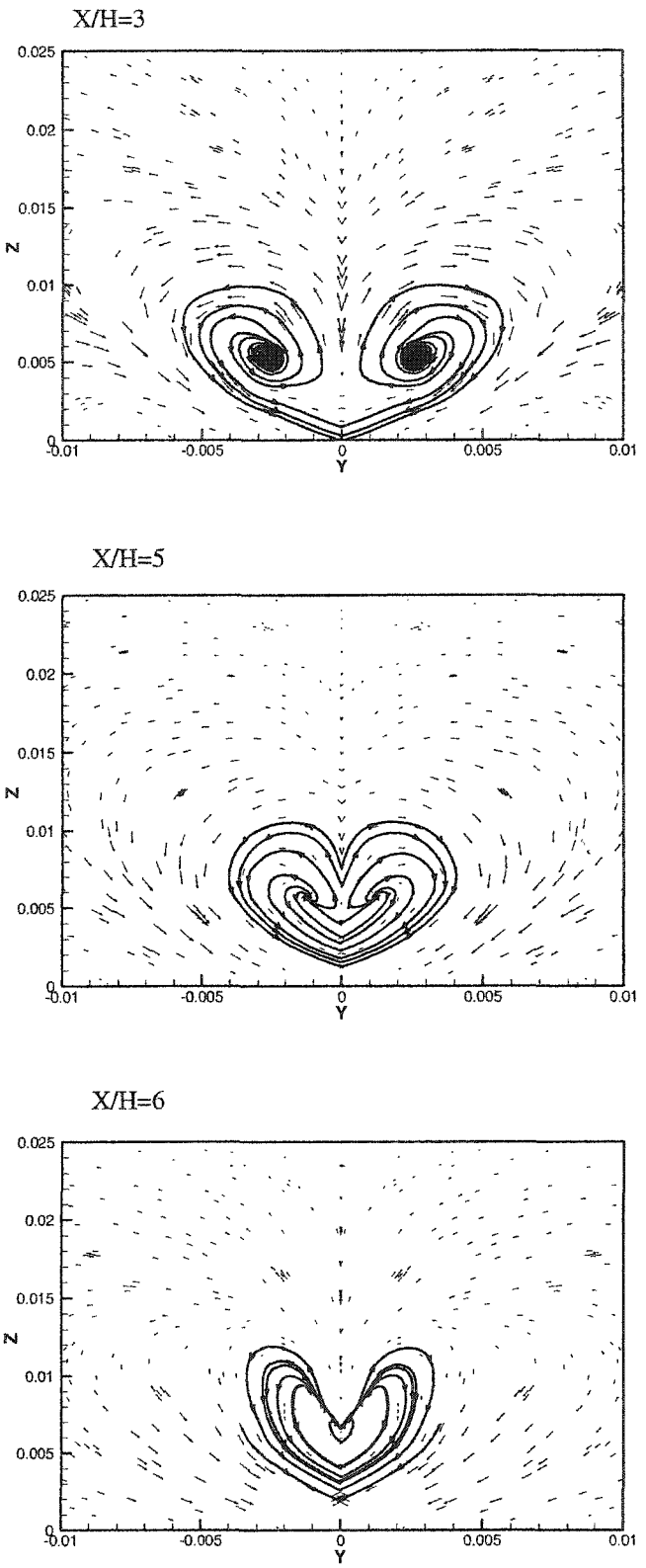

Fig. 5.4 Velocity vectors and streamlines(ϕ=0.31, L_c=20H)

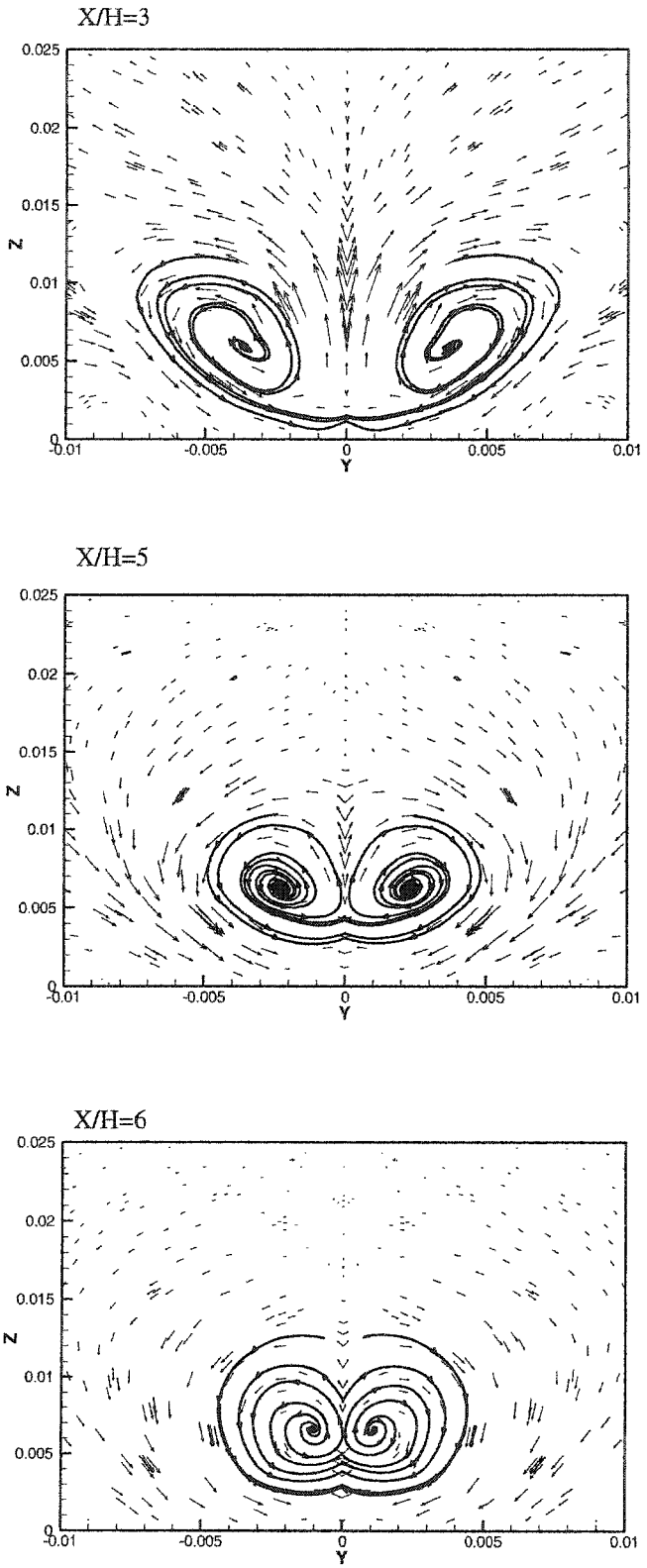

Fig. 5.5 Velocity vectors and streamlines(ϕ=0.41, L_c=20H)

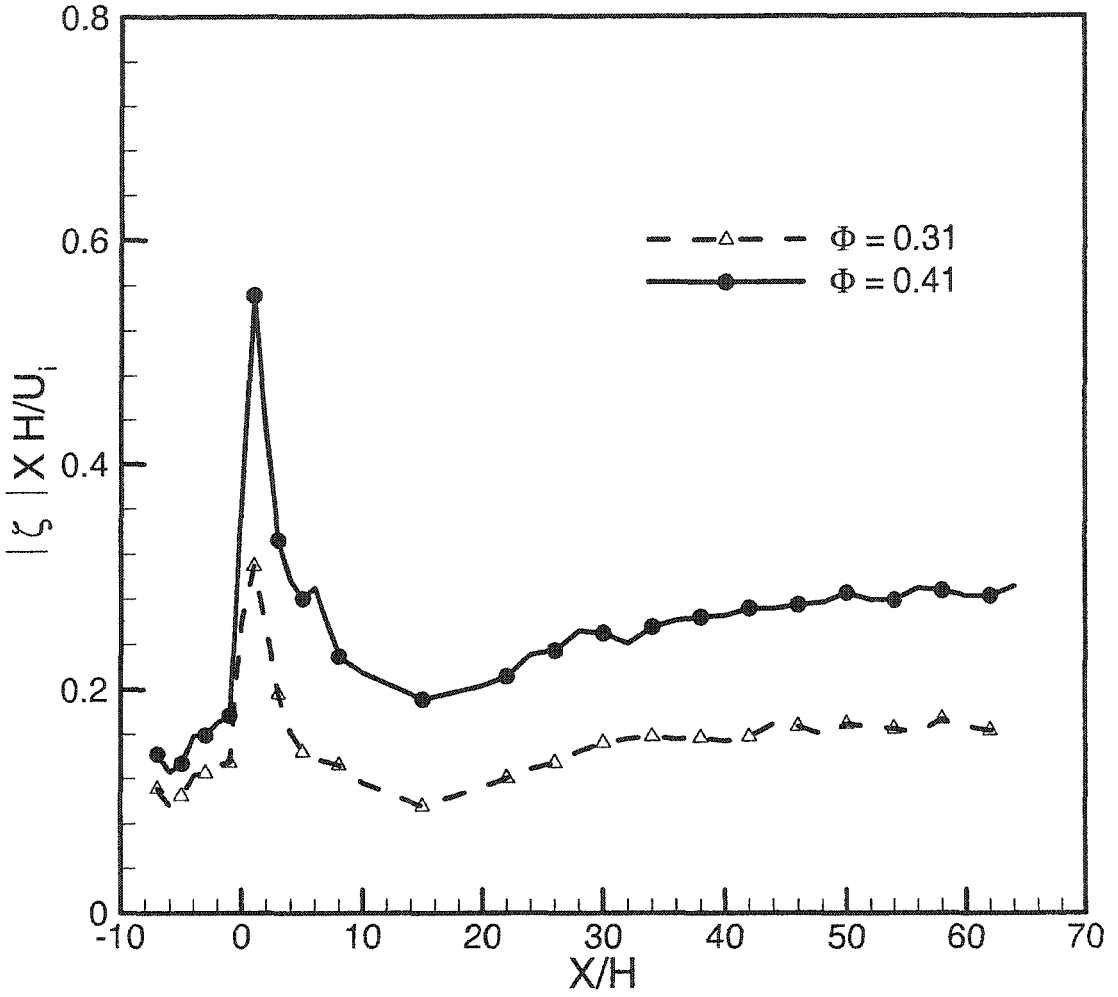

Fig. 5.6 Mass-averaged vorticity magnitude (L_c=20H)

trend, the magnitude of the vorticity in the case with ϕ=0.41 is higher than the other one with ϕ=0.31 which is due to the difference in the pressure between the two cases at the inlet.

Two overall parameters depicting effectiveness of fuel combustion over duration, and equivalently, a length of combustor are the heat released and the amount of the reference element such as hydrogen that is converted to water indicating completion of combustion of that element. The latter may also be expressed in terms of the amount of hydrogen that remains in any form other than that of water at a location of interest in the combustor in relation to the amount of hydrogen that available initially i.e.,

$$\eta_C = \frac{\text{amount of hydrogen converted to water}}{\text{amount of hydrogen supplied}} \tag{5.1}$$

Equation 5.1 implicitly includes the fuel to air ratio used and the effects of mixing of air and fuel in initially non-premixed cases. At the same time, Eq.(5.1) does not refer explicitly to the effects of ignition process or changes in combustion rate [7].

Figure 5.7 shows the combustion efficiency calculated with Eq.(5.1) for the two equivalence ratios. Combustion of hydrogen mixed is 68% complete at the end of the combustor duct. Further increase in the combustion efficiency is seen in the expanding duct. Both cases show the same values inside the combustor. However, slight difference is noted in the middle of the expanding duct between X/H =30 and X/H=50. Both cases have nearly the same combustion efficiency at the end of the expanding duct.

The benefits obtained in mixing performance must be weighted against the losses incurred. Averaged total pressure is presented in Fig. 5.8 as a preliminary examination of the losses associated with the large vertical mixing. The figure shows the total pressure

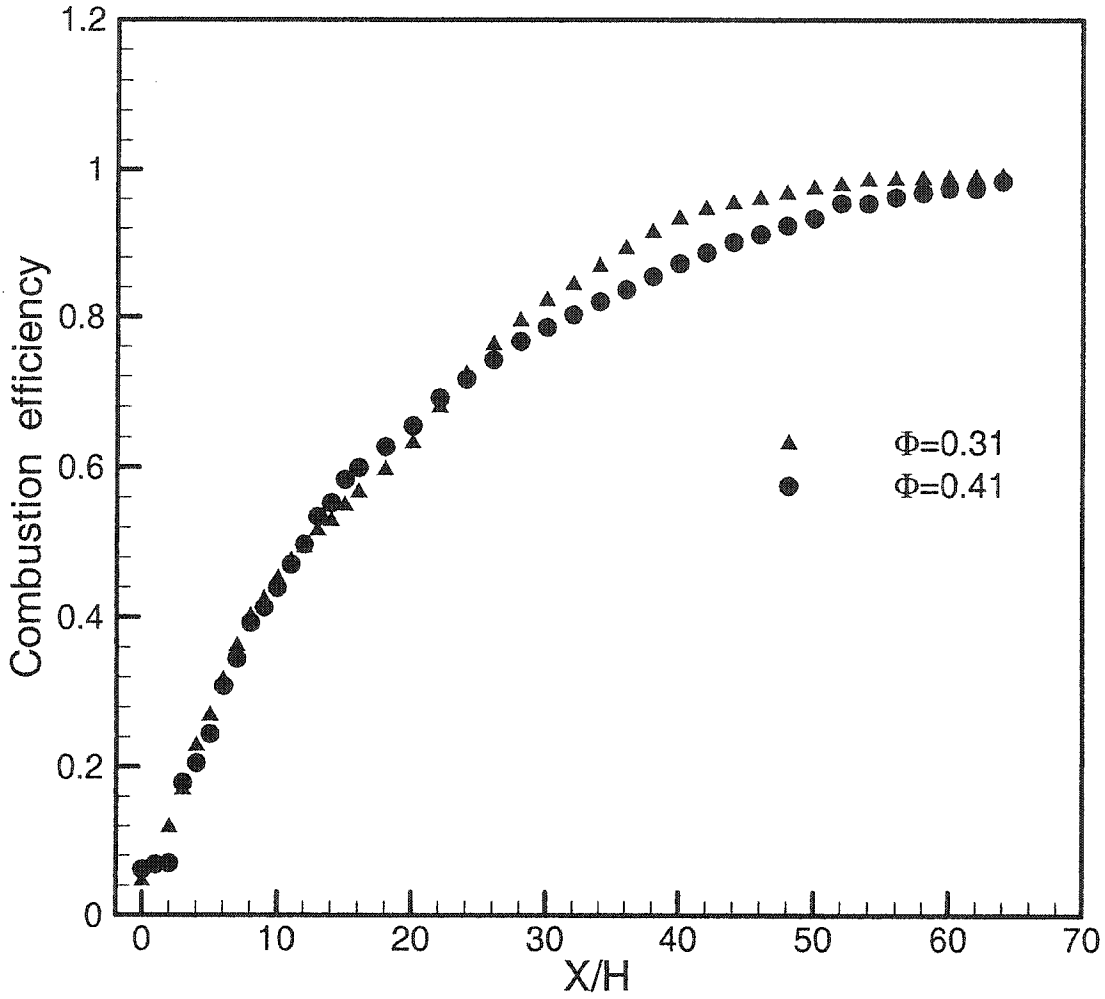

Fig. 5.7 Combustion efficiency as a function of the downstream distance (L_c=20H)

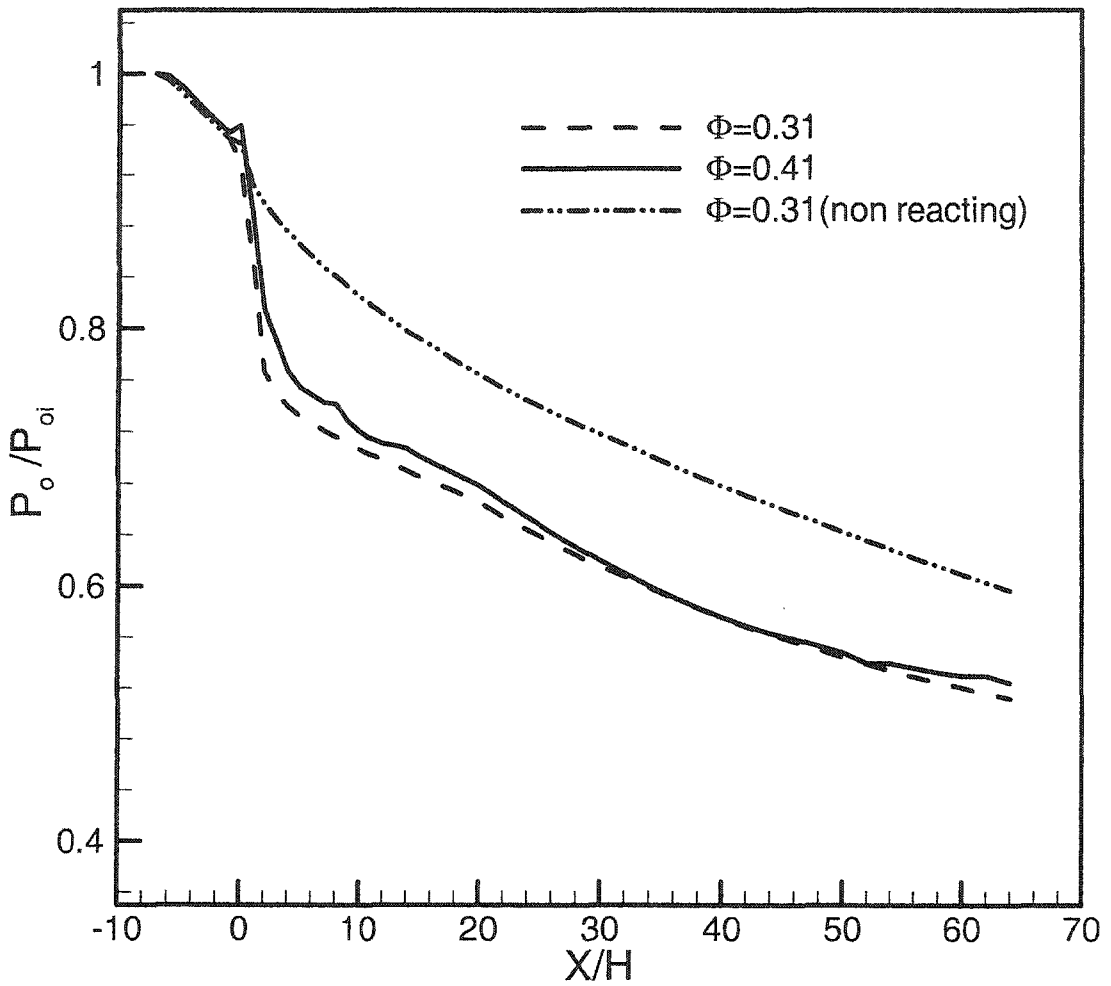

Fig. 5.8 Distribution of averaged total pressure (L_c=20H)

throughout the combustor for both equivalence ratios. The figure clearly shows that loss due to the reaction is considerable and that the loss in the total pressure is about 48% of the initial value. A significant part of the loss is seen in the combustor duct between the fuel injector and X/H= 4.0. The magnitude of the difference between the nonreacting flow and the reacting flow is almost constant with the axial location in the downstream combustor.

Next, the effect of the combustor length is presented in Figs. 5.9 -5.21. Figures 5.9 and 5.10 show the wall pressure for both the nonreacting flows and the reacting flows respectively. The figures compare the normalized wall pressure along the upper wall at the centerline of the duct. Figure 5.9 shows clearly that, in both cases, the pressure distribution is identical in the distance between the inlet of the isolator at X/H= –7 and X/H=10 which is the combustor exit in the first model. It should be noted that the length of the combustor has no effect on the upstream flow for the nonreacting flows. Further downstream the flow expands to a lower pressure in the 10H case than the 20H one. For the reacting flows, the length of the combustor is affecting the pressure as seen in Fig. 5.10. It is evident form Fig. 5.10 that the combustion process of the fuel and the heat release produces a significant pressure rise in the wall pressure. The sharp pressure rise just downstream of the injector seen in Fig. 5.10 is due to the formation of the combustion front. It is to be noted that, in this case, the isolator is said to be *shock-free*[6] since there is no shock train formed in the isolator.

Averaged Mach number distributions along the axial direction are shown in Fig. 5.11 for nonreacting flows. The same values of the Mach number are seen in the distance etween X/H=-7 and X/H=10, which confirms the results presented in Fig. 5.9. In both cases, Mach

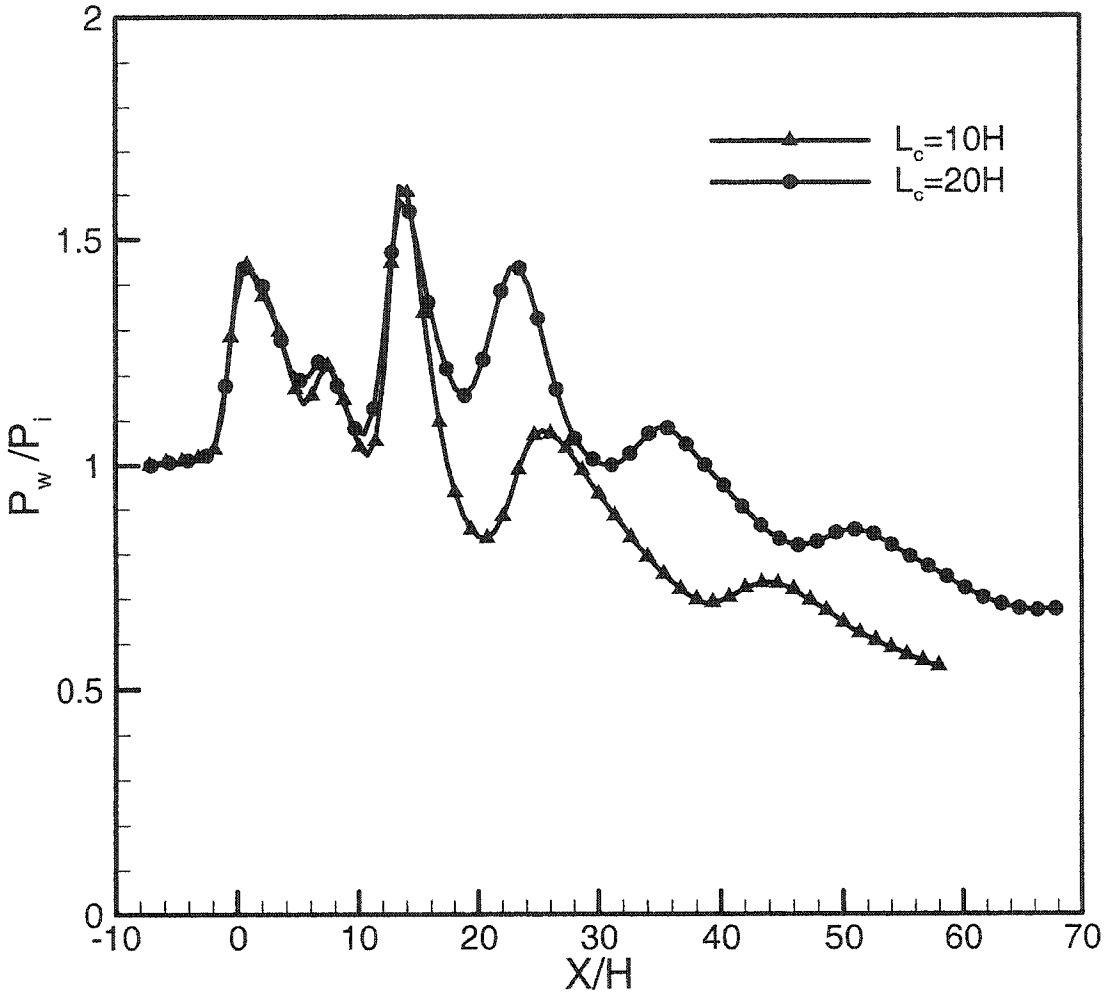

Fig. 5.9 Pressure distribution on the top wall (nonreacting flow, ϕ=0.31)

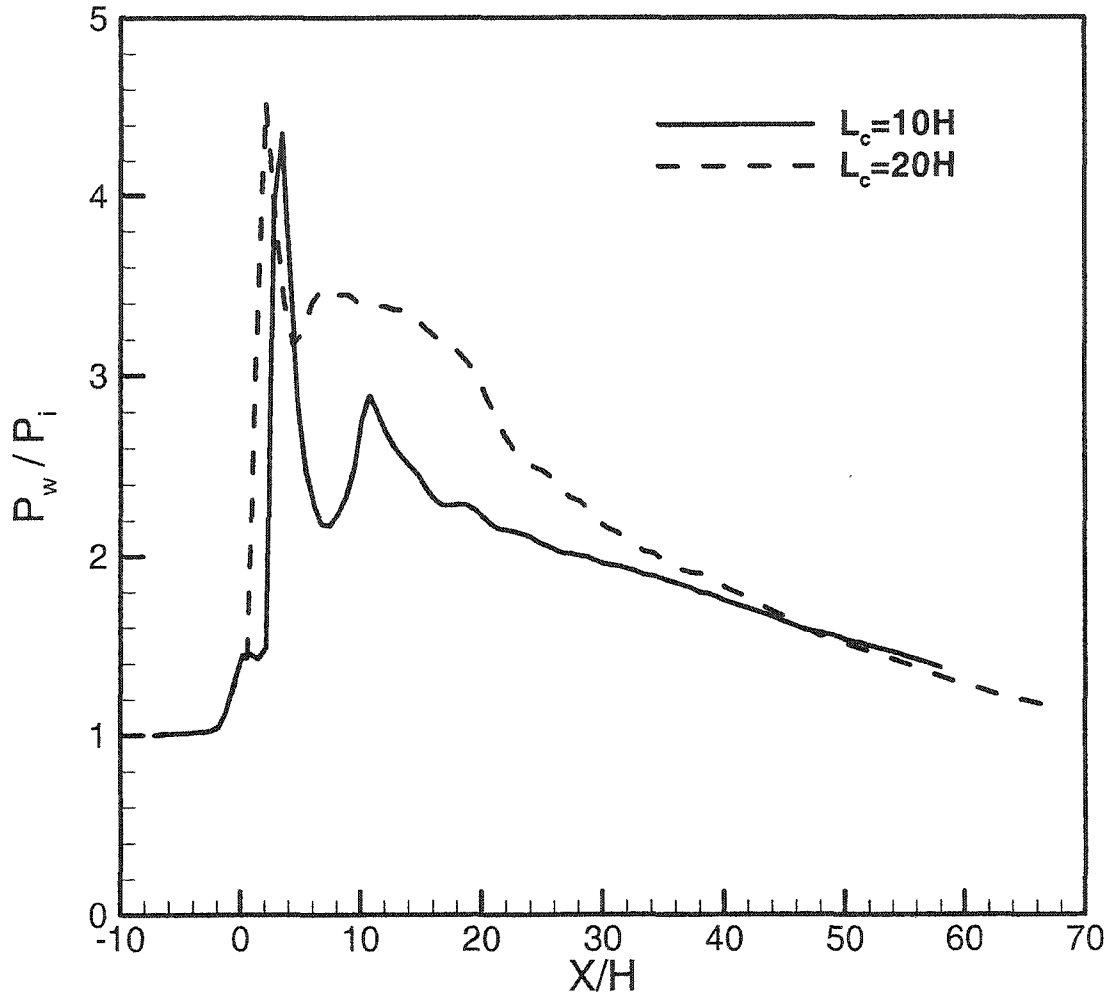

Fig. 5.10 Pressure distribution on the top wall (reacting flow, ϕ=0.31)

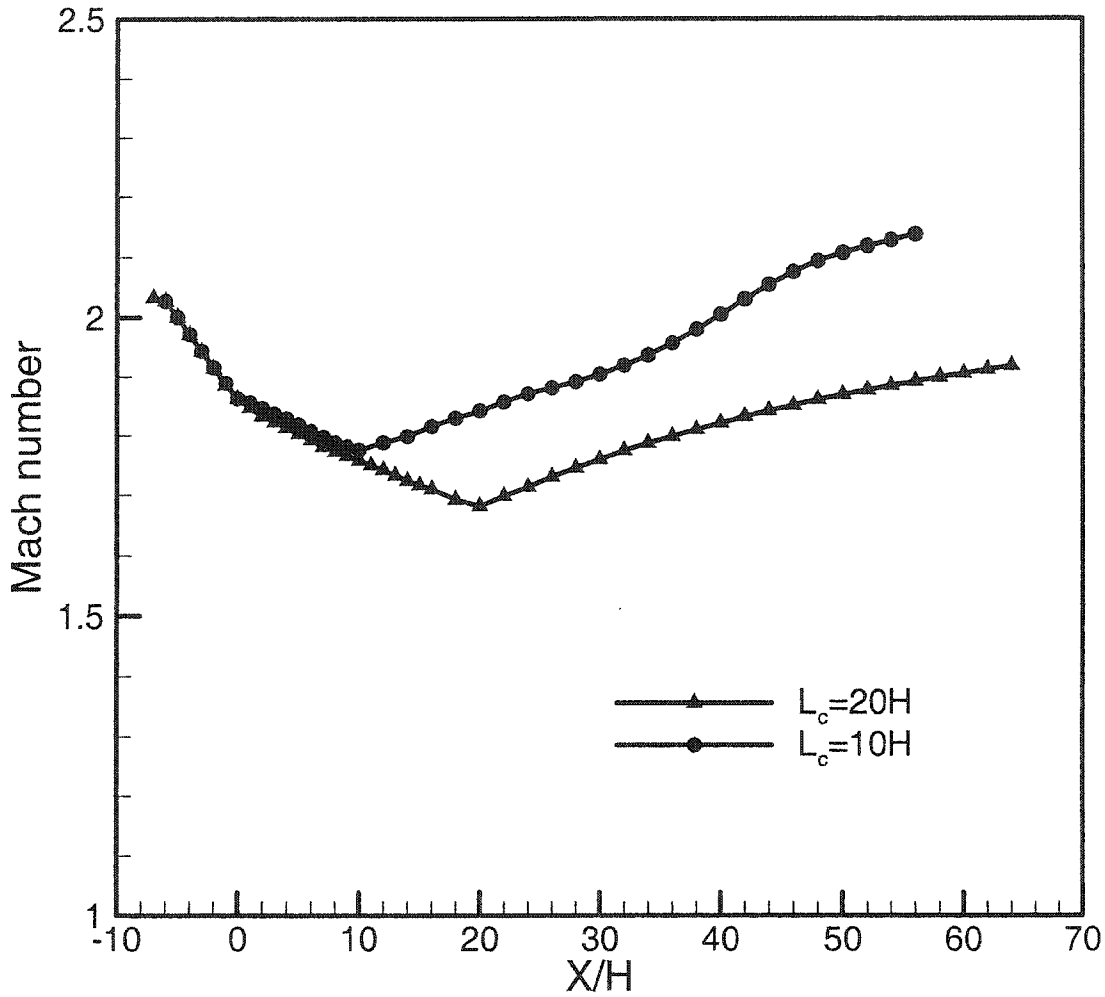

Fig. 5.11 Distribution of averaged Mach number (nonreacting flow, ϕ=0.31)

number decreases till the exit of the combustor then starts to recover again inside the expanding duct. Lower values are seen for the long combustor (L_c=20H). Figures 5.12 and 5.13 show Mach number contours for the two combustors at the centerplane of the ducts. Results are presented for nonreacting flows as well as for reacting flows. The figures show clearly significant subsonic portion of the flow in the two reacting cases. The subsonic regions are seen adjacent to the injection wall (lower wall) of the combustor and extend in the axial direction with the flow. The subsonic region in the short combustor (L_c=10H) extends to a longer distance.

In order to give clear view about the mixing process inside the two combustors, vorticity magnitude, velocity vectors, mixing rate, and the area of the fuel plumes are presented in Figs. 5.14-5.18. In Fig. 5.14, the vorticity magnitude is shown. In both models, the same trend of the vorticity is seen. The magnitude of the vorticity increases inside the isolator in both models and reaches its maximum value at the injection plane (X/H=0). The magnitude of the vortices decreases as it progress further downstream of the ramps. After the combustor and inside the expanding duct, the 10H combustor shows higher vorticity than the 20H one. In Figs. 5.15 and 5.16, velocity vectors and streamlines at different crossflow planes are presented. It can be seen clearly that the vortices are still developing near the injector in both cases. Downstream of the injector and after about three ramp heights, the vortices are seen completely developed, which is a reasonable distance for unswept ramp. The figures show clearly that, as the distance from the injector exit increases, the centers of the vortices move toward the lower wall. The vortices become closer to the lower wall in the case of the 10 H combustor than the other case.

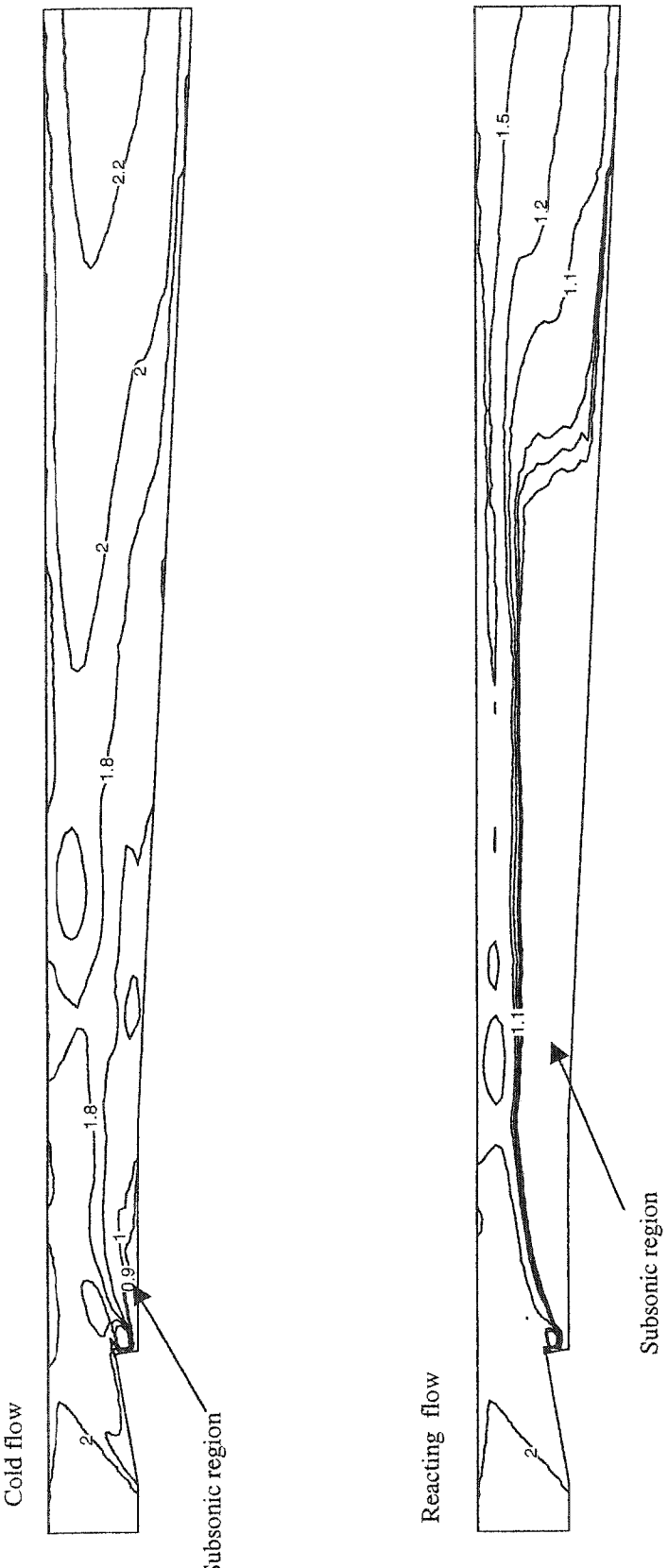

Fig. 5.12 Centerplane Mach number contours (L_c=10H)

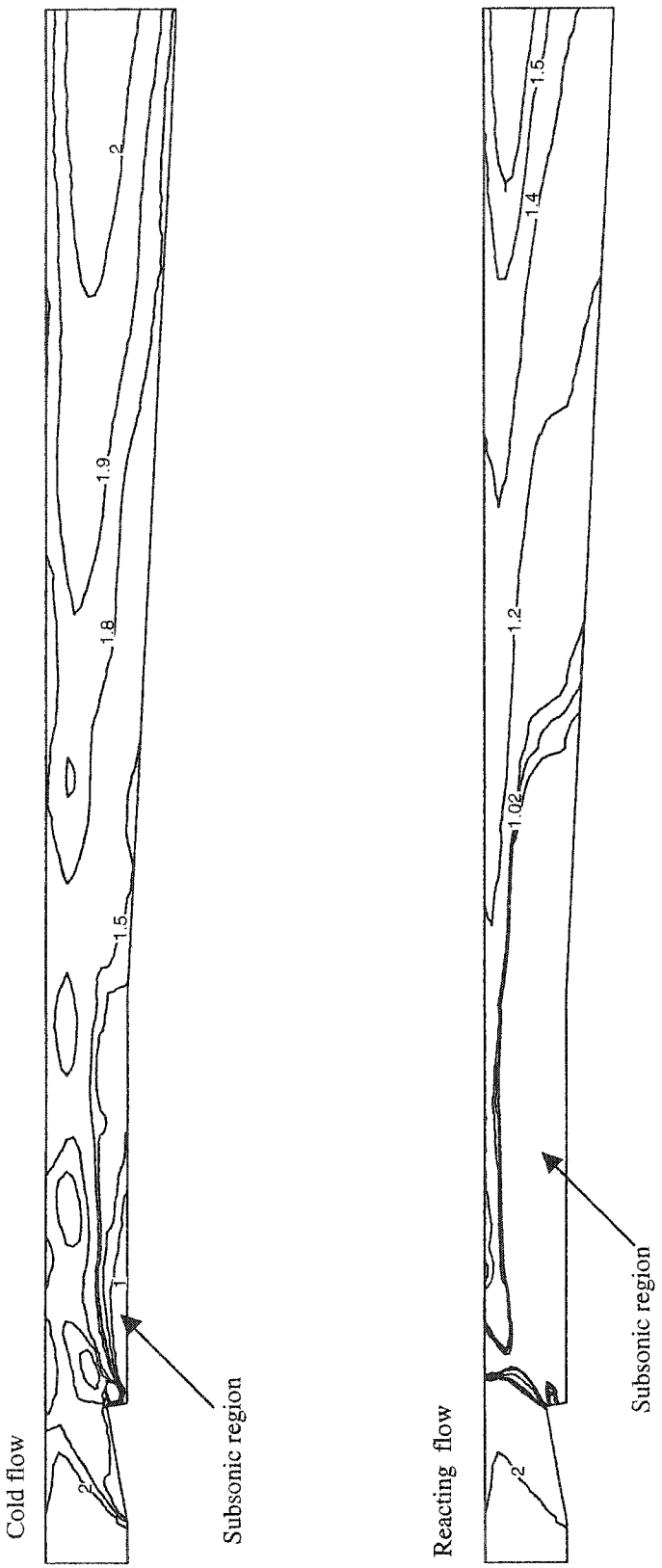

Fig. 5.13 Centerplane Mach number contours (L_c=20H)

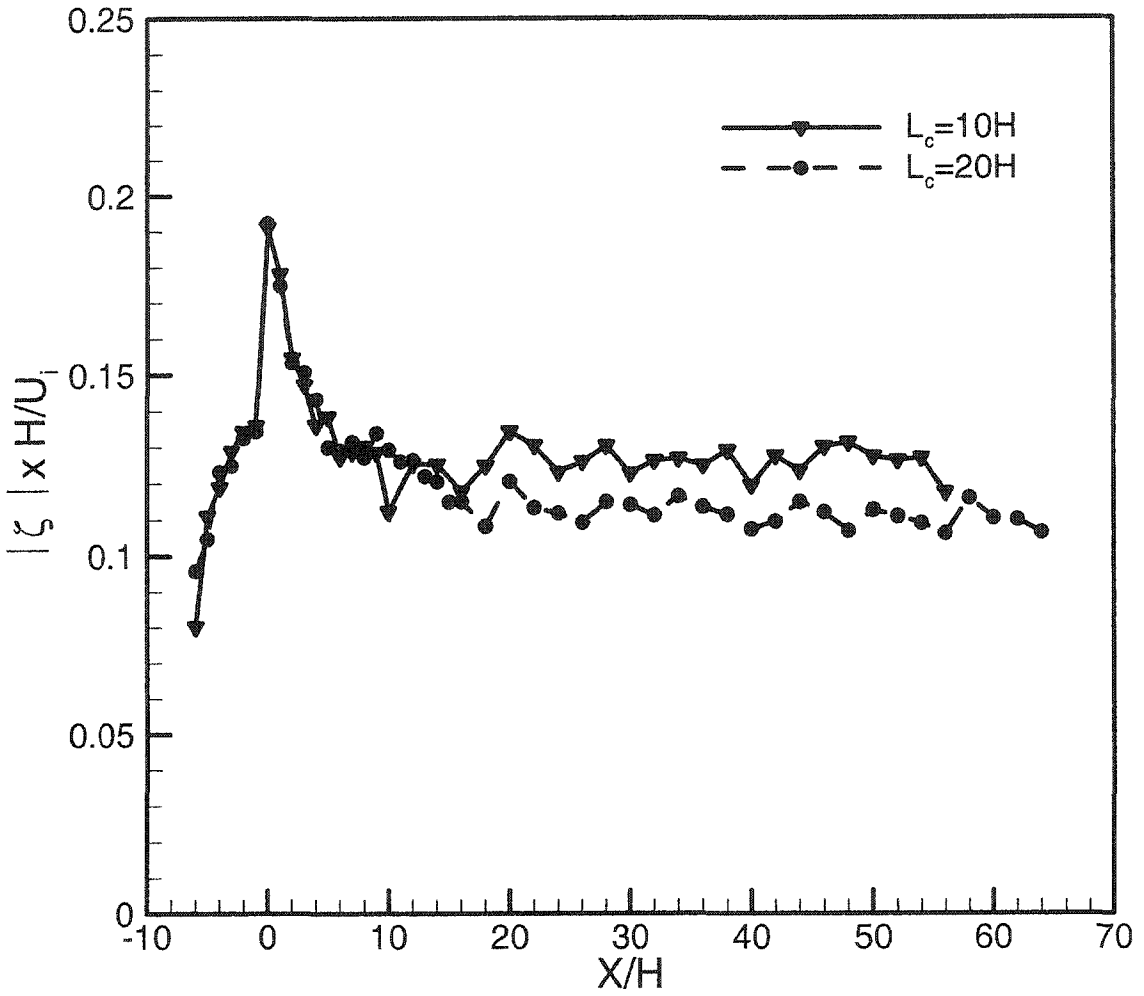

Fig. 5.14 Normalized vorticity magnitude (ϕ=0.41, L_c=20H)

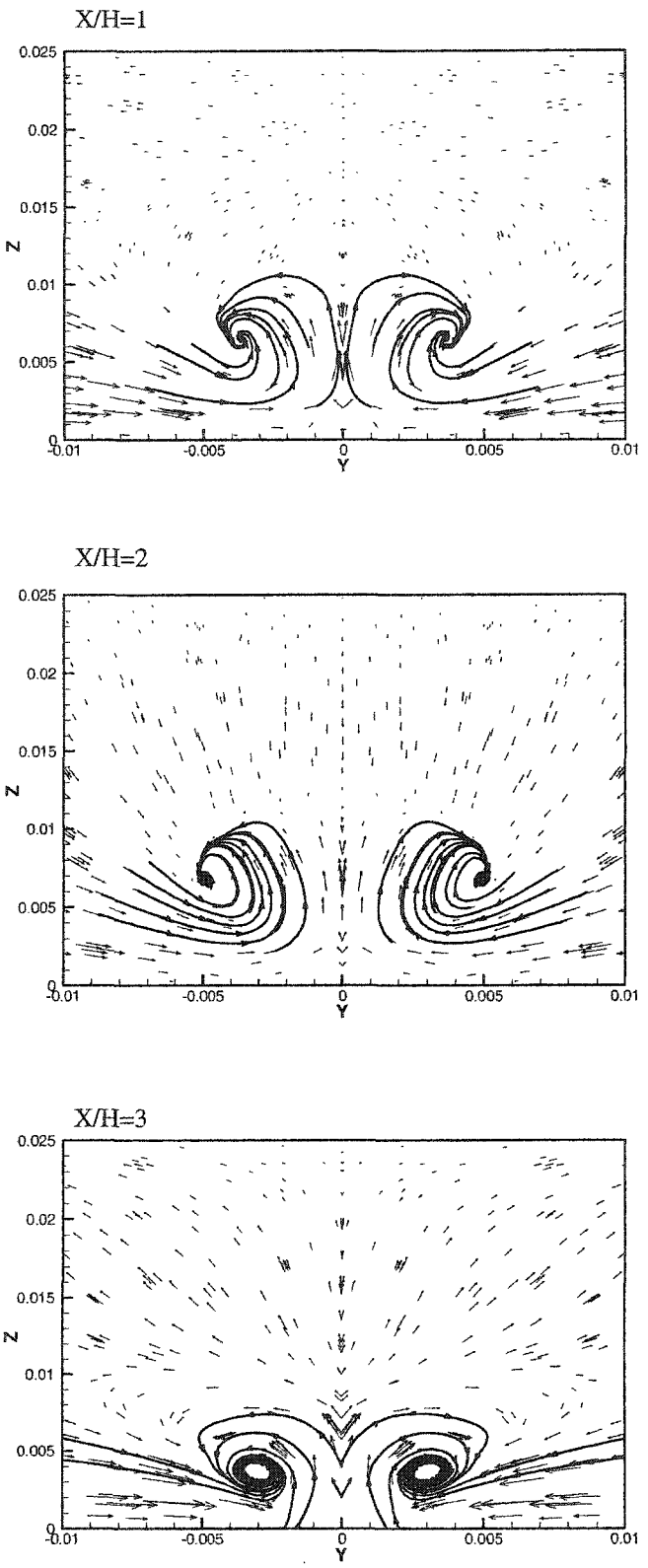

Fig. 5.15 Velocity vectors and streamlines(nonreacting flow, L_c=20H)

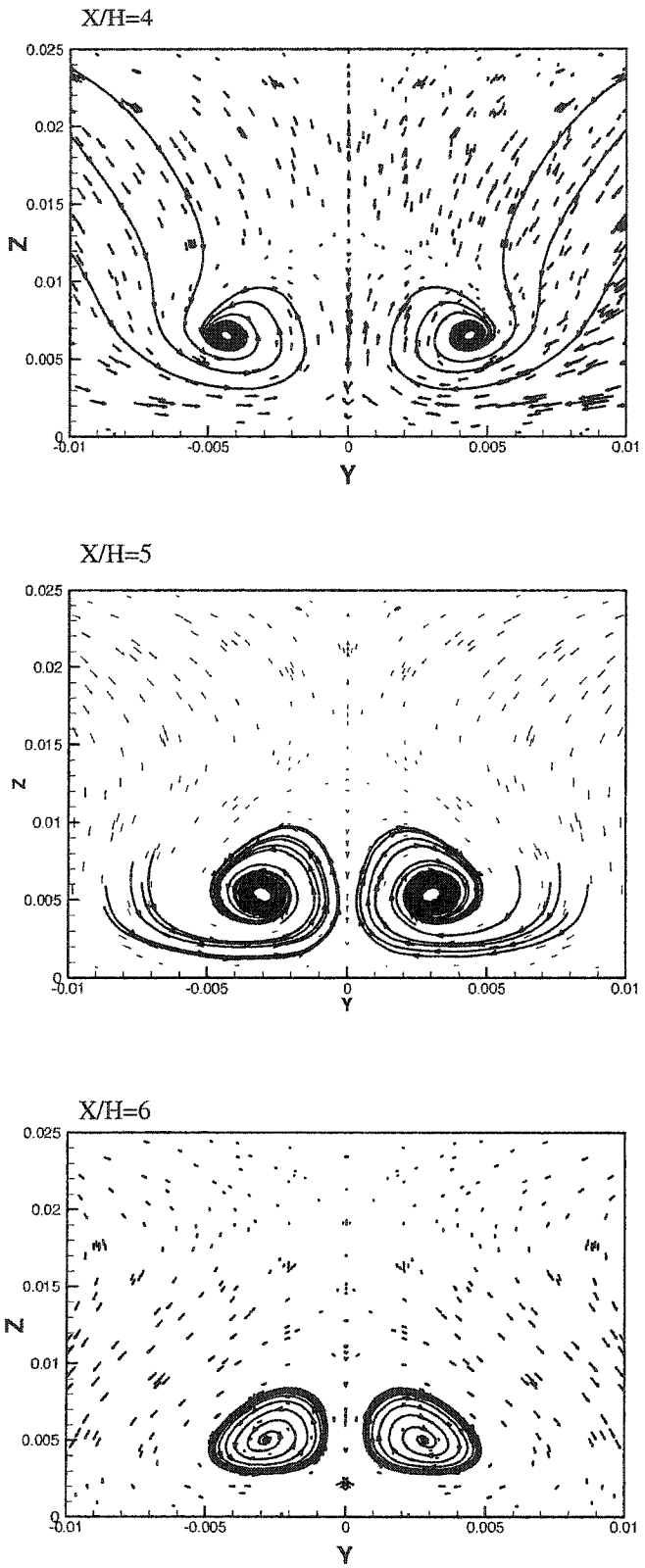

Fig. 5.15 (contd.)Velocity vectors and streamlines(nonreacting flow, L_c=20H)

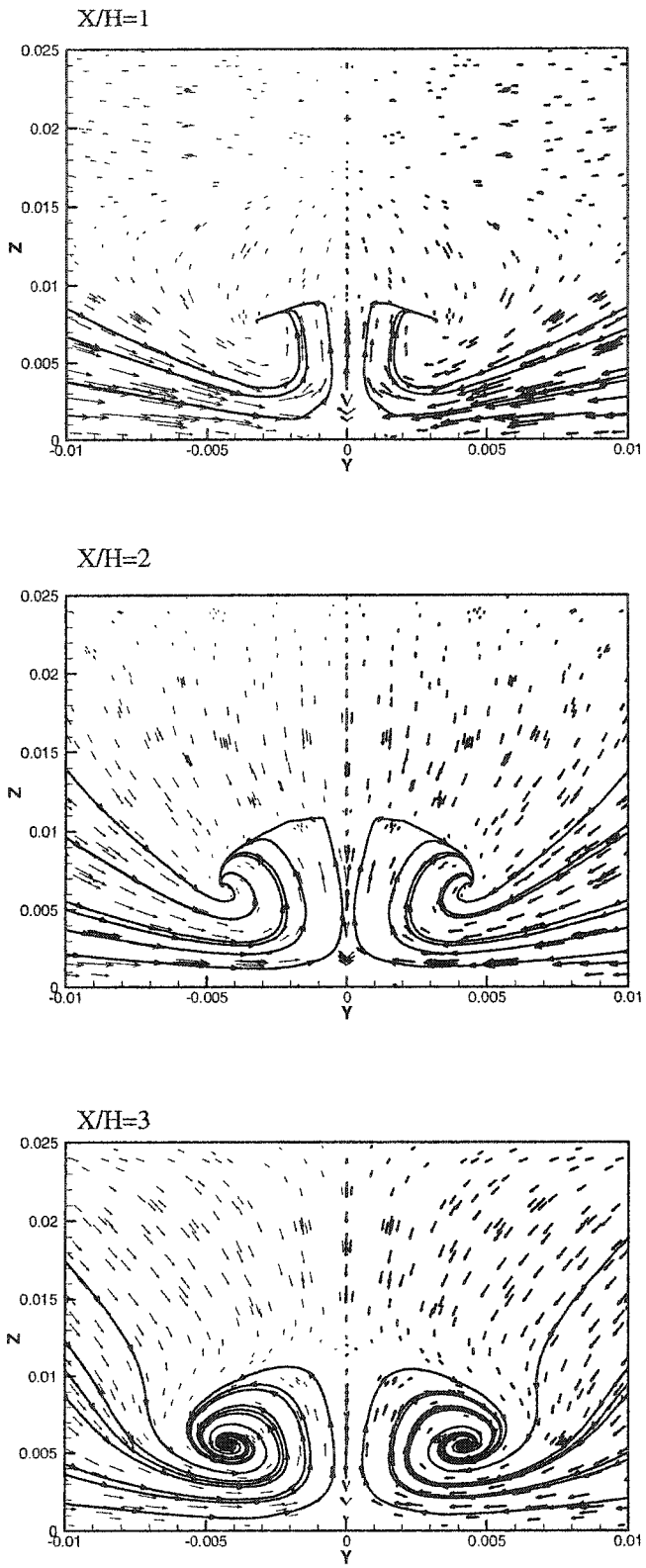

Fig. 5.16 Velocity vectors and streamlines(nonreacting flow, L_c=10H)

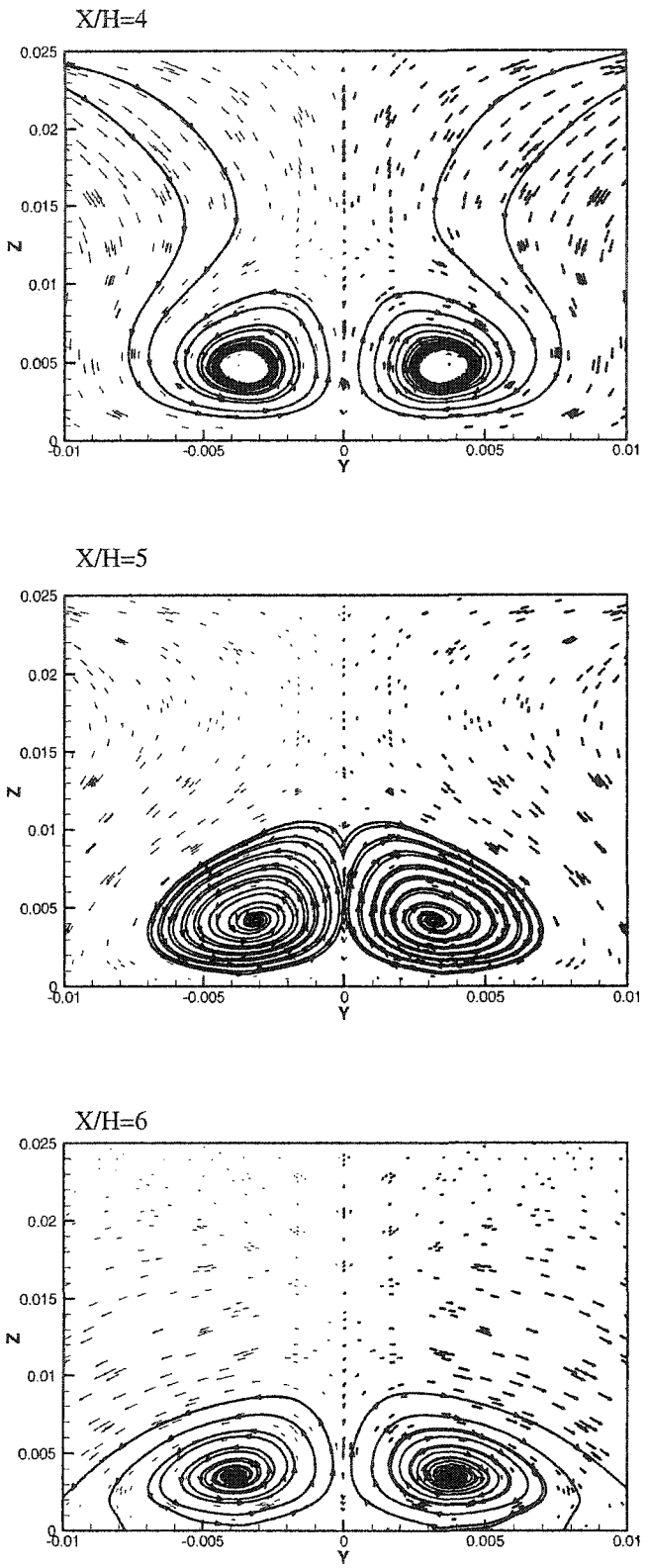

Fig. 5.16 (contd.)Velocity vectors and streamlines(nonreacting flow, L_c=10H)

Mixing rate is one of the most important parameters of mixing characteristics, since the combustion process strongly depends on the mixing process. The definition of the mixing rate is the decay of the maximum mass fraction of the fuel with the downstream distance. Figure 5.17 compares the mixing rate of the two combustors. Near the injector at 0<X/H<4, both models show nearly the same mixing rate. The 10H combustor shows higher rate than the 20H one; however, this difference is not significant. Further downstream, a slight difference is seen inside the expanding duct until X/H=44. After X/H=44, both models show the same rate again.

As a means of quantifying the differences between the two combustors, the cross-sectional area of the mixing and reacting plumes is determined inside the combustors and presented in Fig. 5.18. For this research, the boundary of the plume was defined as the point where the hydrogen mole fraction reaches 0.1 in each plume. The plume area is normalized by the cross-sectional area of the fuel injector. All cases show increase of the plume area with the increase of the axial distance. Both of the nonreacting cases show linear increase in the plume area. The influence of the combustion can be seen clearly in the figure. At any cross section, the plume area of the reacting flow cases is larger than the nonreacting flow cases. Also, more penetration in the cases of the 20H combustor can be seen than the 10H combustor.

Figure 5.19 shows the combustion efficiency calculated by Eq.(5.1). The combustion efficiency of the 20H geometry is higher than that of the 10H over the combustor and the expanding duct. This is expected because of the relatively large area of the fuel plume of the 20H model.

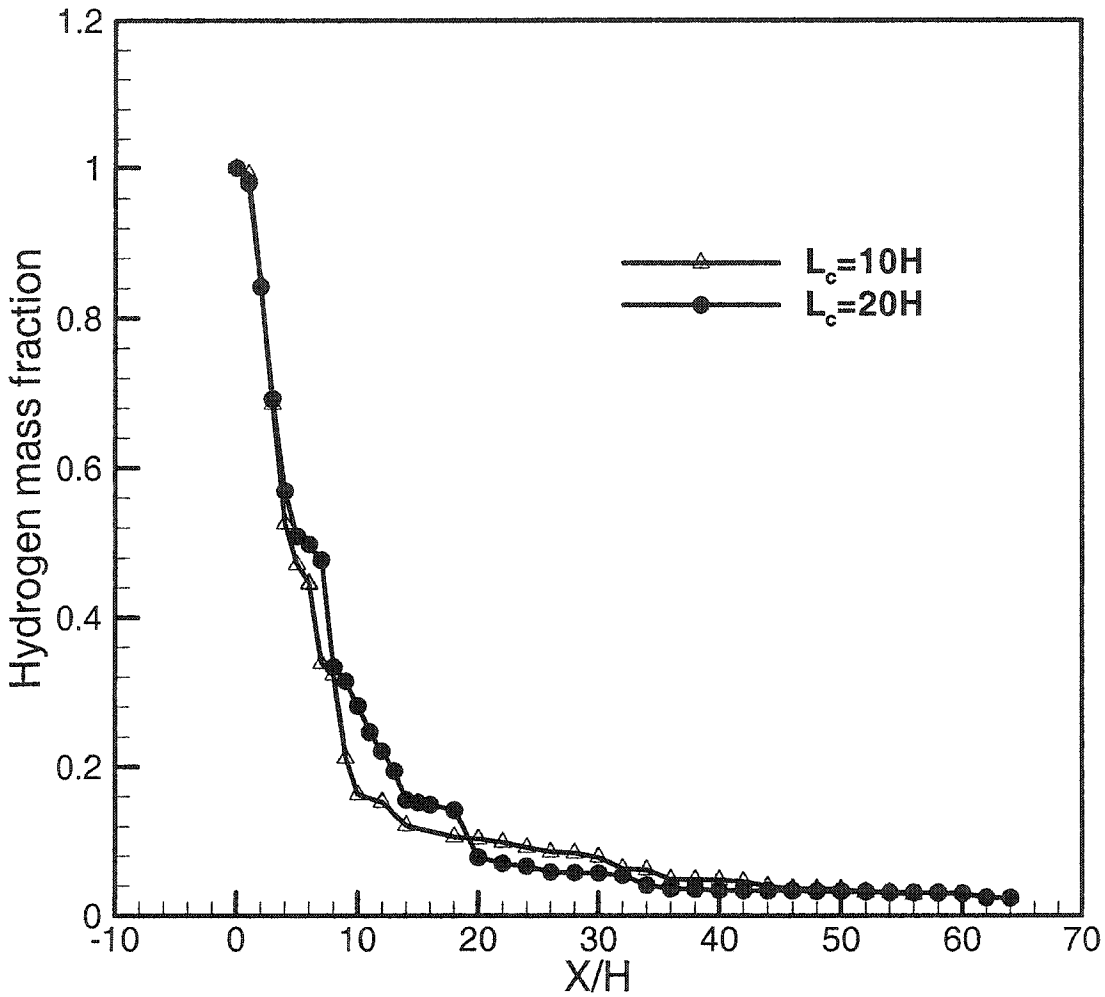

Fig. 5.17 Decay of fuel mass fraction (ϕ=0.31)

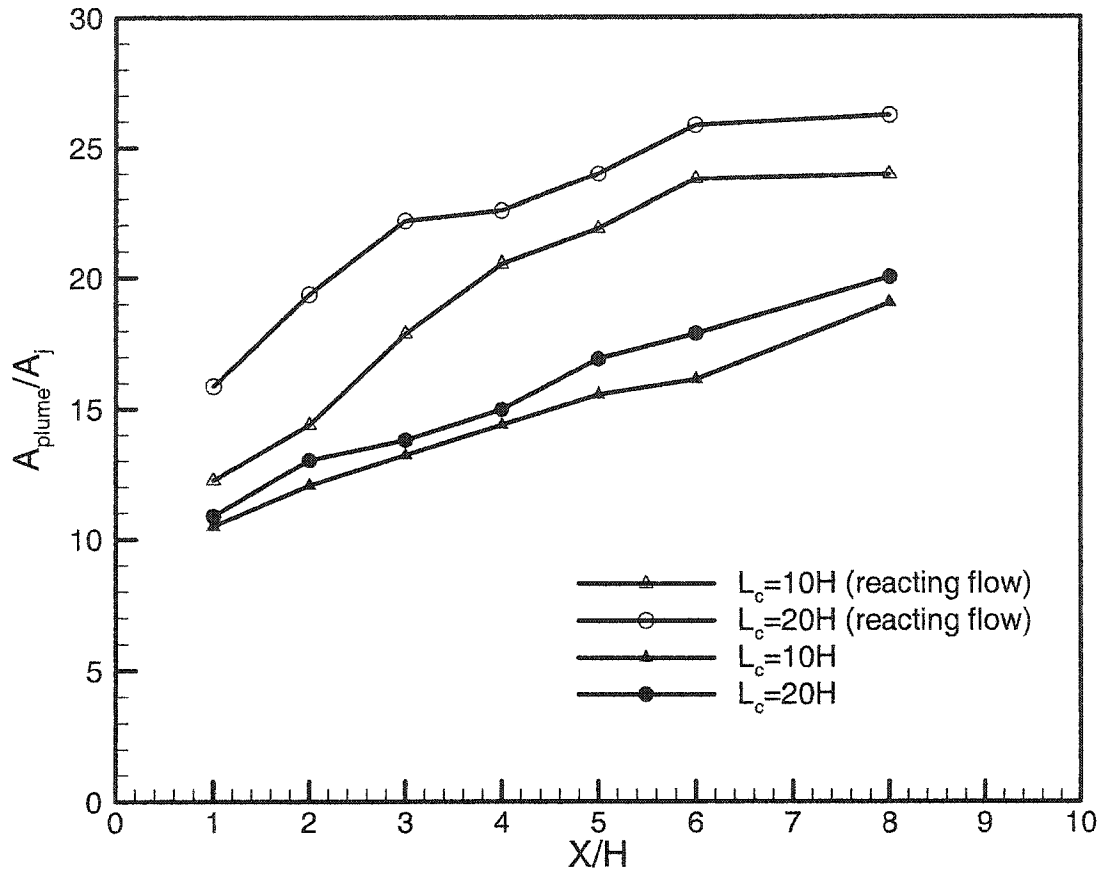

Fig. 5.18 Relative fuel jet area as a function of downstream distance.

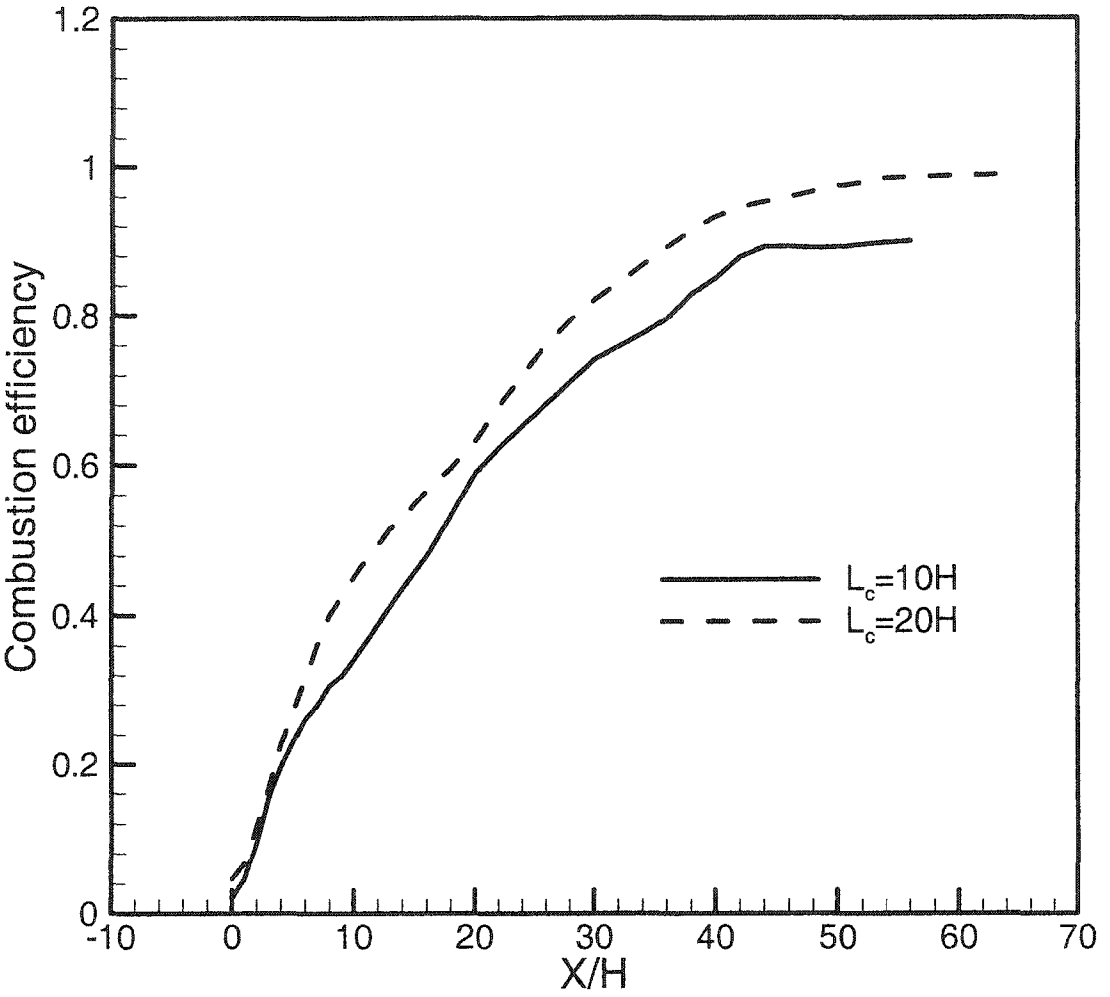

Fig. 5.19 Combustion efficiency as a function of downstream distance (ϕ=0.31)

In Figs. 5.20 and 5.21, integrated stream thrust F_x is shown. Thrust is calculated for planes perpendicular to the X-axis as[83]

$$F_x = \int (p + \rho u^2) dA \tag{5.2}$$

Current results confirm the results obtained in Ref. 83. An initial decrease of the thrust can be seen between the isolator inlet section and the injector plane (-7<X/H<0). This decrease is due to the drag generated by the ramp. Both models show the same thrust loss since they have the same ramp. A small increase is noted at X/H=0 because of the force exerted on the fluid by the back side of the ramp. The loss in momentum, because of friction, is seen in the decrease in the stream thrust for the combustor. After the exit plane of the combustor, a gradual increase in the stream thrust is seen. The increment in the reacting cases is higher than the nonreacting cases due to the heat release. The level of the stream thrust for 10H model in both reacting and nonreacting flows is relatively higher than that of the 20H one since the loss due friction is less in the first model. The increment in the stream thrust between the two reacting flows remains relatively constant.

5.2 Dual-Mode Combustor with Rearward Facing Step

This section describes the computational results of the dual-mode scramjet combustor configuration discussed in Sec.3.1.4 (Fig. 3.9). Two arrangements of the fuel injectors are investigated, the first configuration has 18 injectors while the second one has 10 injectors (see Fig. 3.10).

5.2.1 Results for the 18-Injector Combustor

Only half of the physical model is computed. The symmetry boundary condition is set at the duct half width (Y/2). Airflow and fuel conditions are presented in Table 5.3. First,

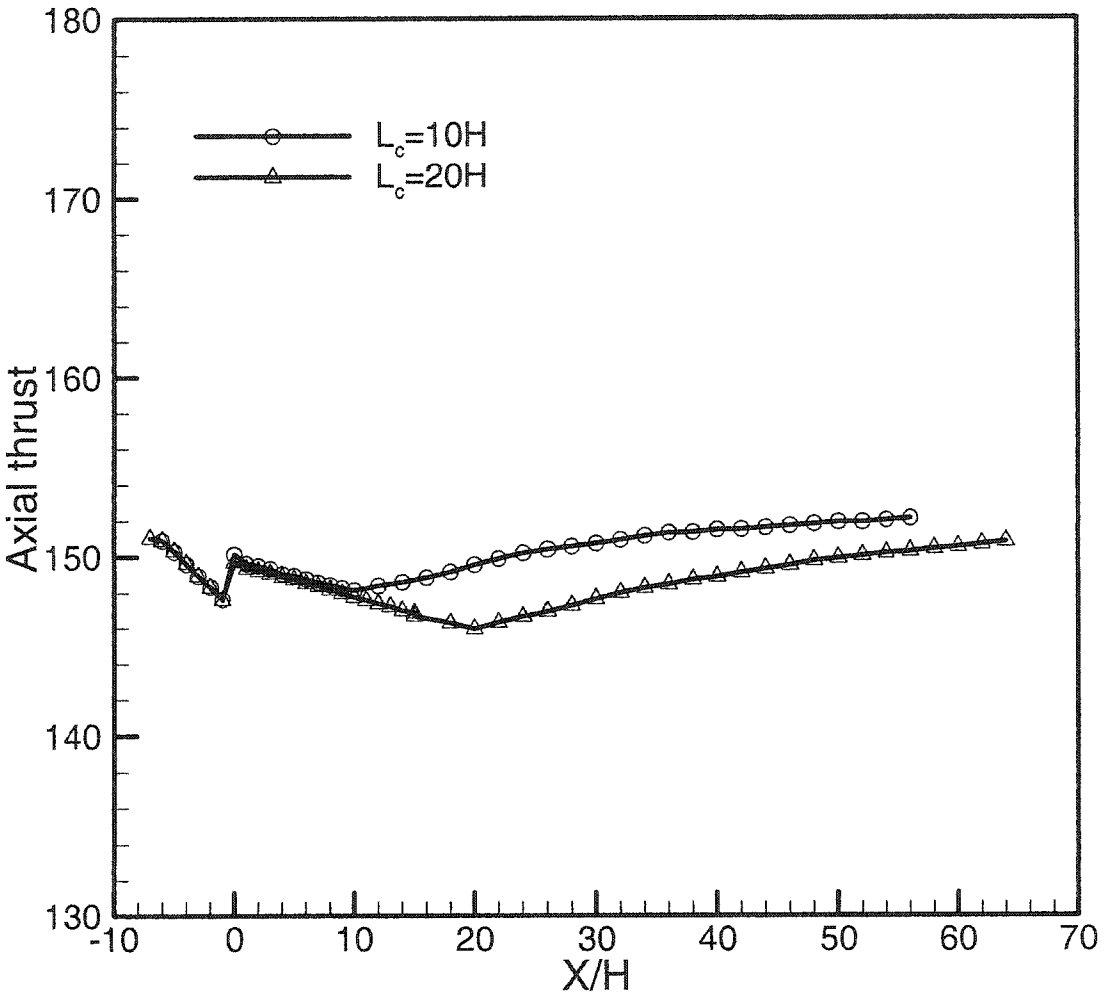

Fig. 5.20 Distribution of axial thrust (nonreacting, ϕ=0.31)

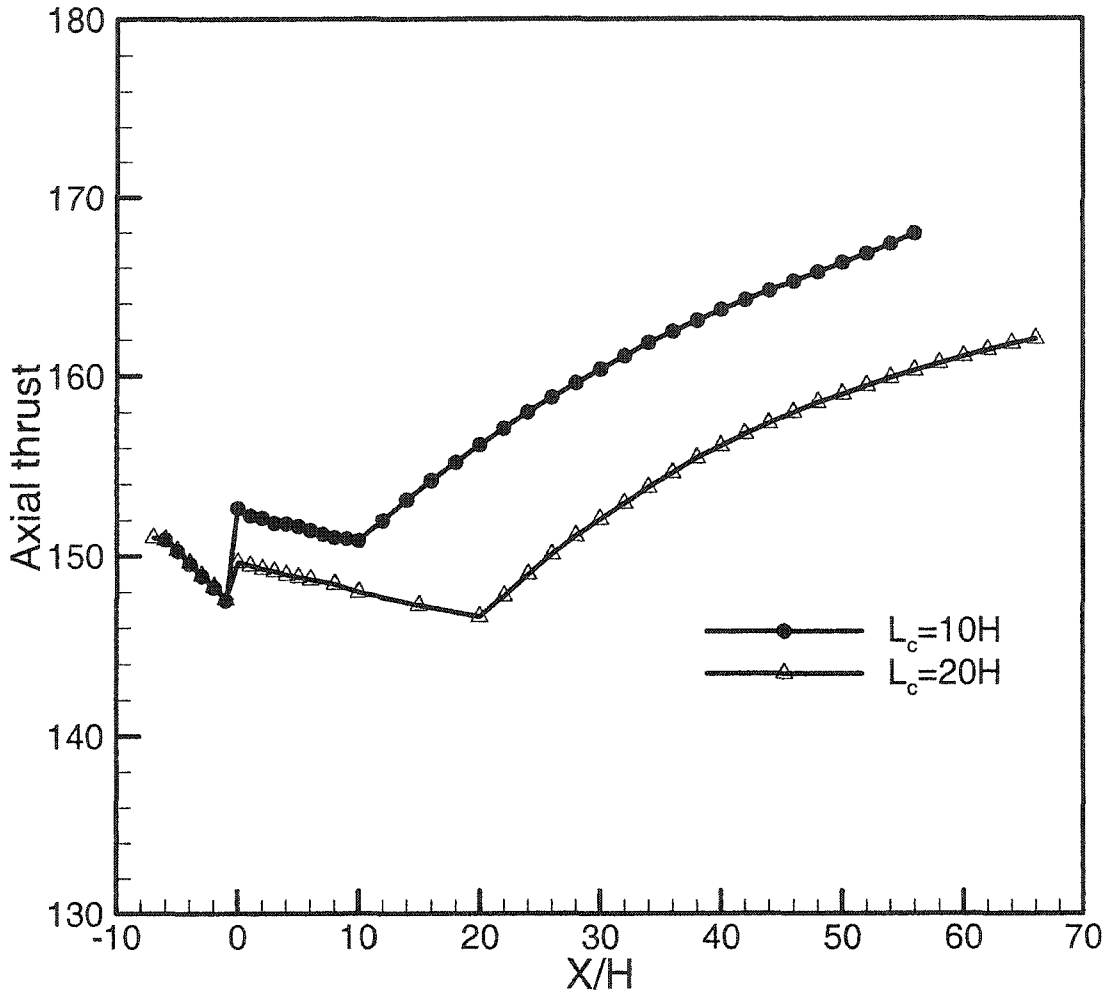

Fig. 5.21 Distribution of axial thrust (reacting, ϕ=0.31)

Table 5.3 Inlet flow conditions (transverse injection)

Parameter	Freestream	Injectant
P_o [kPa]	1000	6640
T_o [K]	2000	280
M	2	1
Turbulent Intensity	1 %	1 %
H_2 mass fraction	0	1.0
H_2O mass fraction	0.17315	0
O_2 mass fraction	0.24335	0

analysis is carried out for reacting flow with uniform inlet boundary conditions. The obtained results show no upstream interaction in the isolator as expected from this geometry. For this reason, the boundary conditions at the inlet are redefined using profiles instead of uniform conditions. The study of Riggins [69] is the only available work that performed numerical calculations on a similar geometry with inlet profiles. The results showed significant upstream interaction inside the isolator. The incoming boundary layer thickness of Riggins [69] is about 0.01 m (confinement parameter =0.625), which is relatively thick. The boundary layer thickness in the current study is about 0.005 m (confinement parameter =0.3125).

Three cases are presented: two reacting cases (with and without profile) and a nonreacting case with profile boundary conditions. In Fig. 5.22, the axial distribution of the mass-weighted averaged static pressure for the three cases is shown. A large amount of upstream interaction is seen in the reacting flow case with initial boundary layer. No upstream interaction is seen inside the isolator in the two cases with the uniform inlet conditions (nonreacting flow and reacting flow). In the two reacting flow cases, the static pressure has its maximum value at the inlet section of the combustor. This value of the maximum static pressure is the same in both reacting flow cases. This is due to the effect of the fuel injection and the heat release from the chemical reaction. At combustor inlet section, the pressure of the two reacting flow cases is much higher than that for the nonreacting flow case and is about five times the inlet value. In both reacting flow cases, the pressure decreases inside the combustor while in the nonreacting flow case the pressure slightly increases.

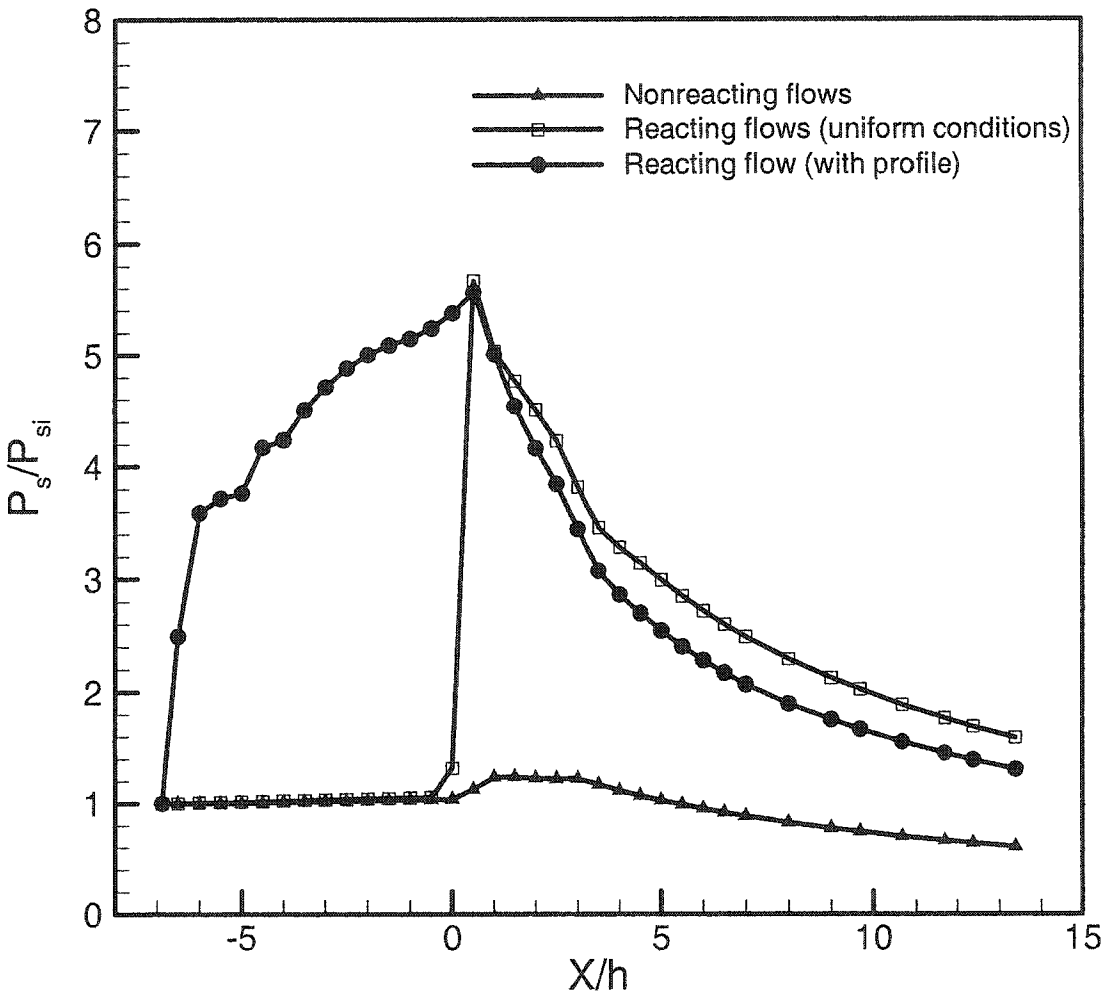

Fig. 5.22 Axial distribution of static pressure for the 18-injector combustor

In Fig. 5.23, velocity vectors and streamlines are shown inside the isolator for the two reacting flow cases. The figure shows clearly the effect of the initial boundary layer thickness on the flow structure. A large upstream interaction is seen in the reacting flow case with inlet profile. The same behavior was also observed in Ref. 69. Also, asymmetric flow is clearly seen which confirms the results of [72]. A large circulation region is formed near the lower wall. No isolator bubbles are seen in the case with uniform conditions.

The averaged total pressure is shown in Fig. 5.24. The figure shows clearly that, in the cases with uniform inlet conditions, major losses in the total pressure occur near the combustor inlet. There is about 30% decrease in the total pressure inside the isolator followed by a sharp decrease at the combustor inlet to about 50% and 65 % of its initial value in both the reacting flow case and the nonreacting flow case, respectively. The pressure decreases again in the combustor and in the expanding duct until it reaches about 36% and 50% of its initial value at the exit plane. Inside the isolator section, the distribution of the total pressure in the reacting flow case with initial boundary layer is completely different than in the other two cases. There is a rapid decrease just after the inlet section to about 50% of its initial value followed by a very slight decrease in the rest of the isolator. The pressure decreases again inside the combustor and the expanding duct and its value is very close to the other reacting flow cases.

The axial distribution of Mach number is shown in Fig. 5.25. In the cases with uniform inlet conditions, insignificant decrease is noted in the isolator section followed by a rapid decrease near the combustor inlet. At the combustor inlet, the flow becomes completely subsonic in the reacting flow case, while it is still supersonic in the

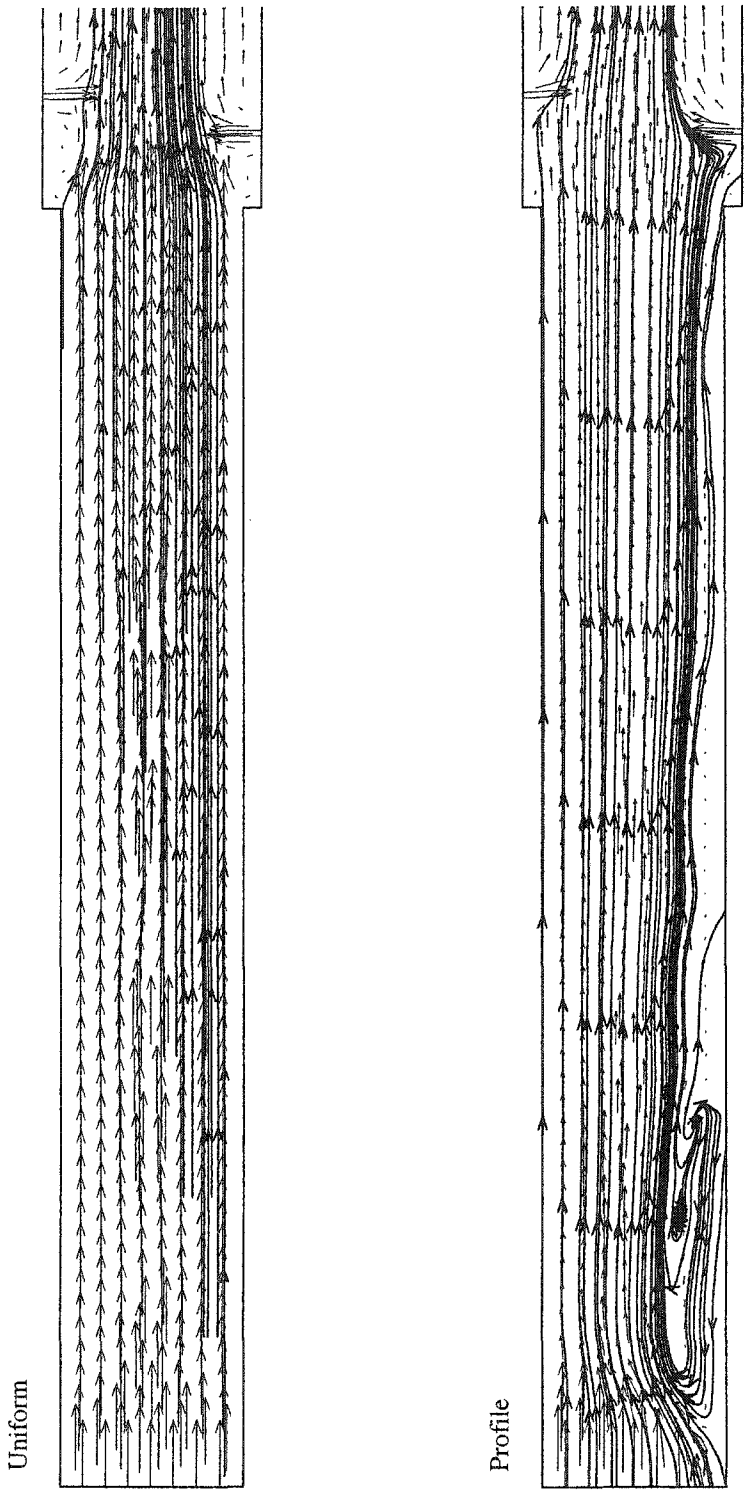

Fig. 5.23 Velocity vectors at the plane of symmetry for the 18-injector combustor

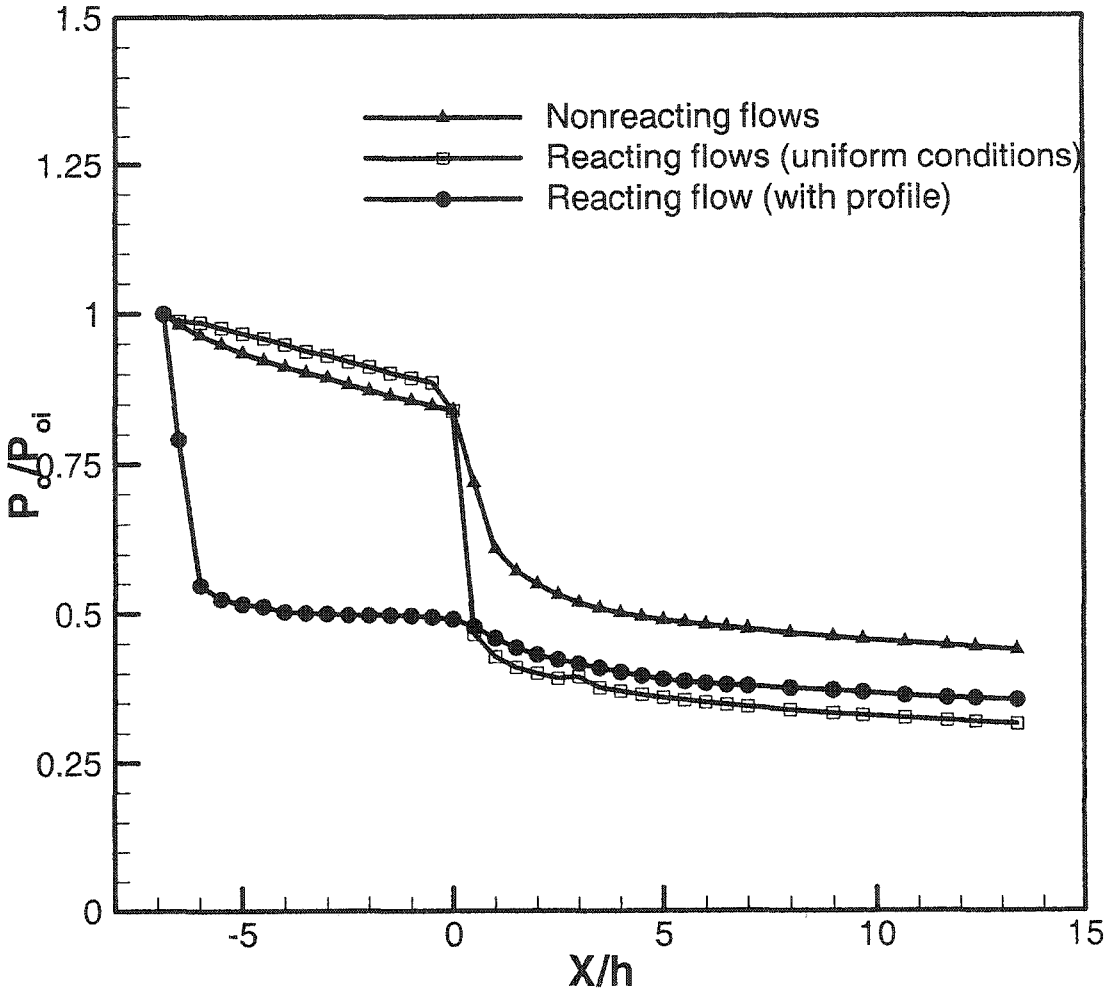

Fig. 5.24 Total pressure distribution for the 18-injector combustor

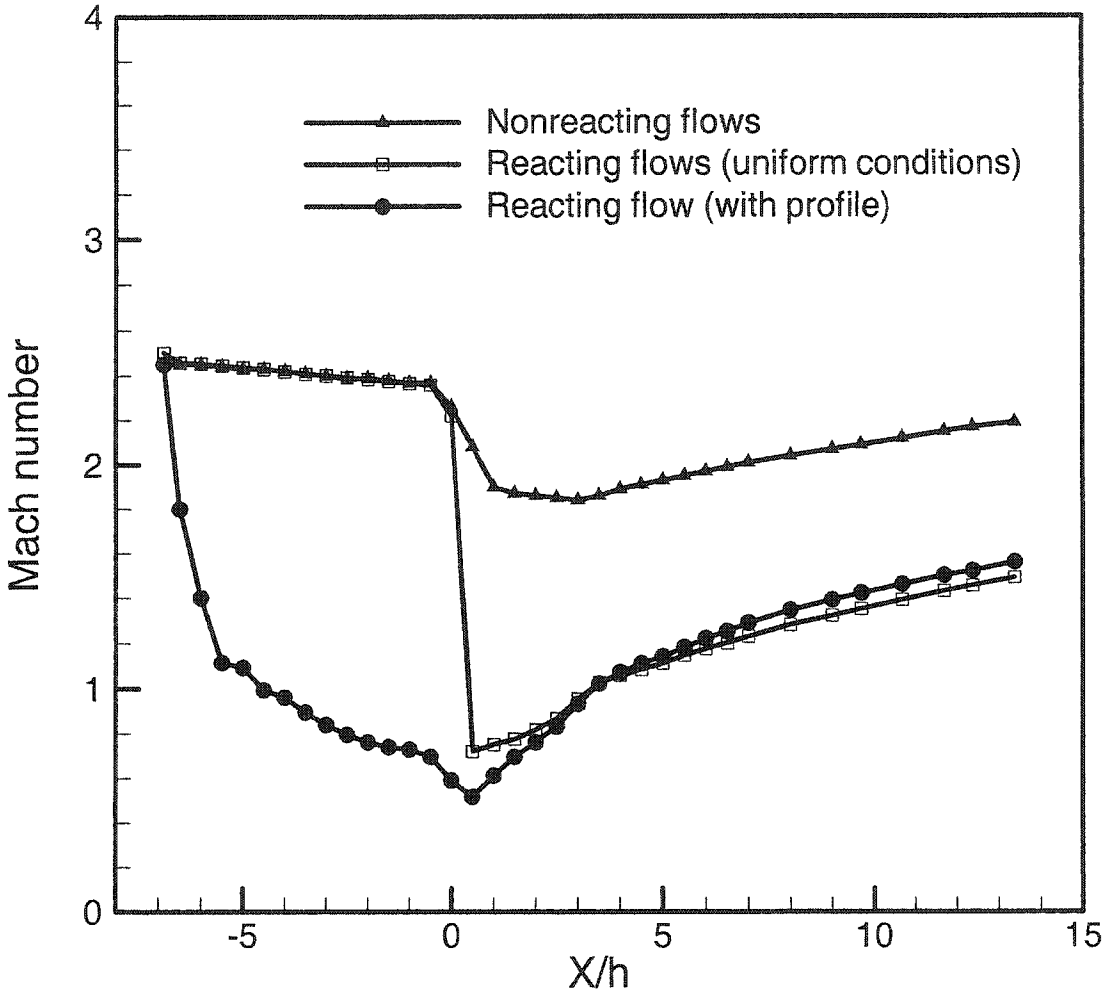

Fig. 5.25 Axial distribution of Mach number for the 18-injector combustor

nonreacting flow case. In the reacting flow case with initial boundary layer, there is a rapid decrease in the averaged Mach number to subsonic speeds near the combustor inlet. After that the, Mach number recovery starts inside the combustor in both reacting flow cases, however; the combustion process takes place in a subsonic streams. The Mach number increases again in the expanding duct to supersonic speeds until it reaches about 1.5 at the exit plane of the duct. For the nonreacting case, the Mach number recovers in the expanding duct to about 2.3 at the exit plane of the duct.

Figure 5.26 compares the decay of the fuel mole fraction in the axial direction for both reacting cases. The decay rate is the same in both cases which means that the combustion process is not affected by the boundary layer thickness inside the isolator. Also, it is quite evident that injecting the fuel normal to the oncoming airstream leads to fast mixing.

In Figs. 5.27 and 5.28, the crossflow contours of the hydrogen mass fraction for both reacting flow cases inside the combustor are shown. The injected hydrogen from the first row of jets (four on the top wall and five on the bottom wall) is very clear at X/h=0.4. It is seen that among these jets there is a small fraction of hydrogen coming back from the second row of injectors which is seen at X/h=0.6. After that, the fuel jets start to merge and combine with the increase of the axial distance. In both cases, no symmetry is seen at all planes, which leads to the recommendation of running the whole geometry. Also the figure shows clearly the effect of the side wall on the spread of the fuel jet. In the reacting case with initial boundary layer, both jets beside the wall are lifted and the spread of the lower jet is much more than that of the upper one (due the circulation region in the lower part of the isolator and the combustor).

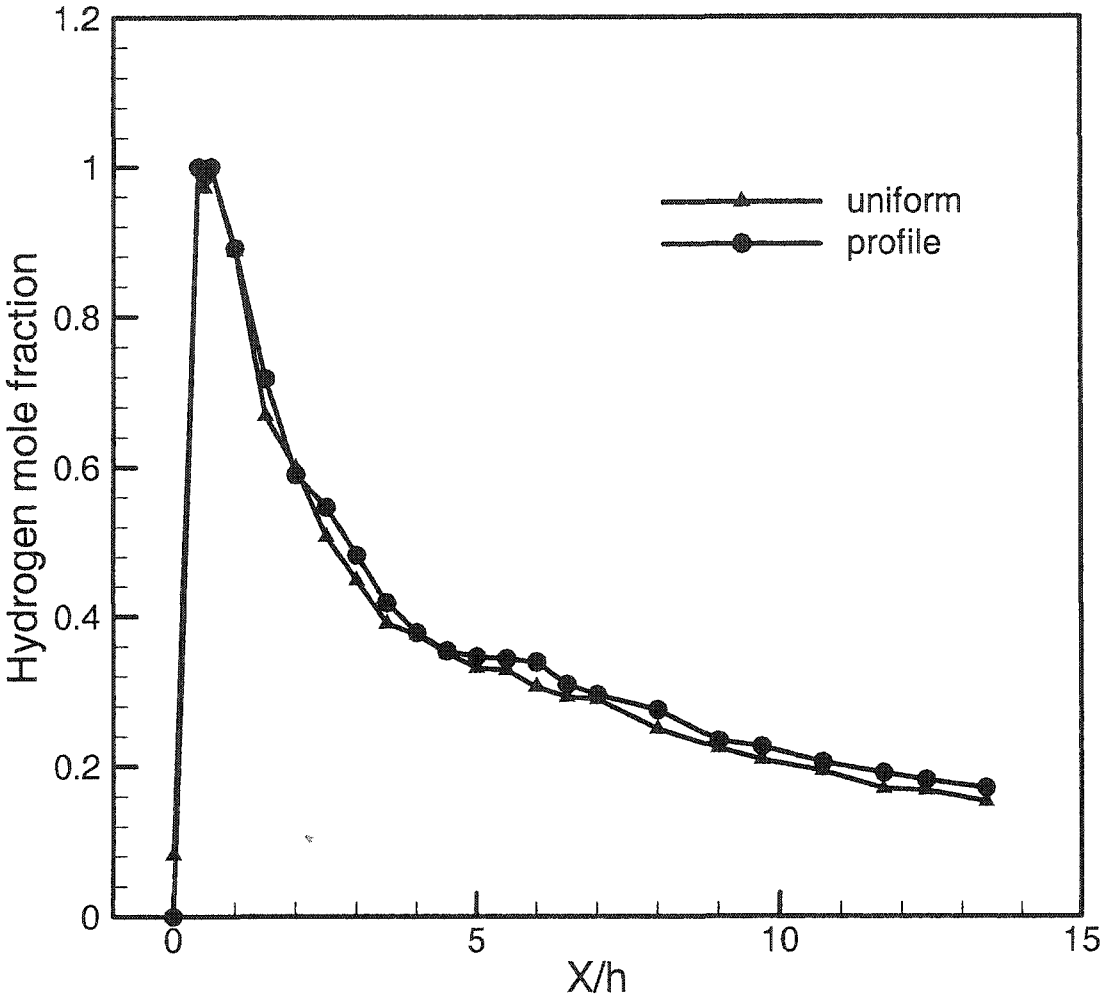

Fig. 5.26 Axial distribution of fuel mass fraction for the 18-injector combustor

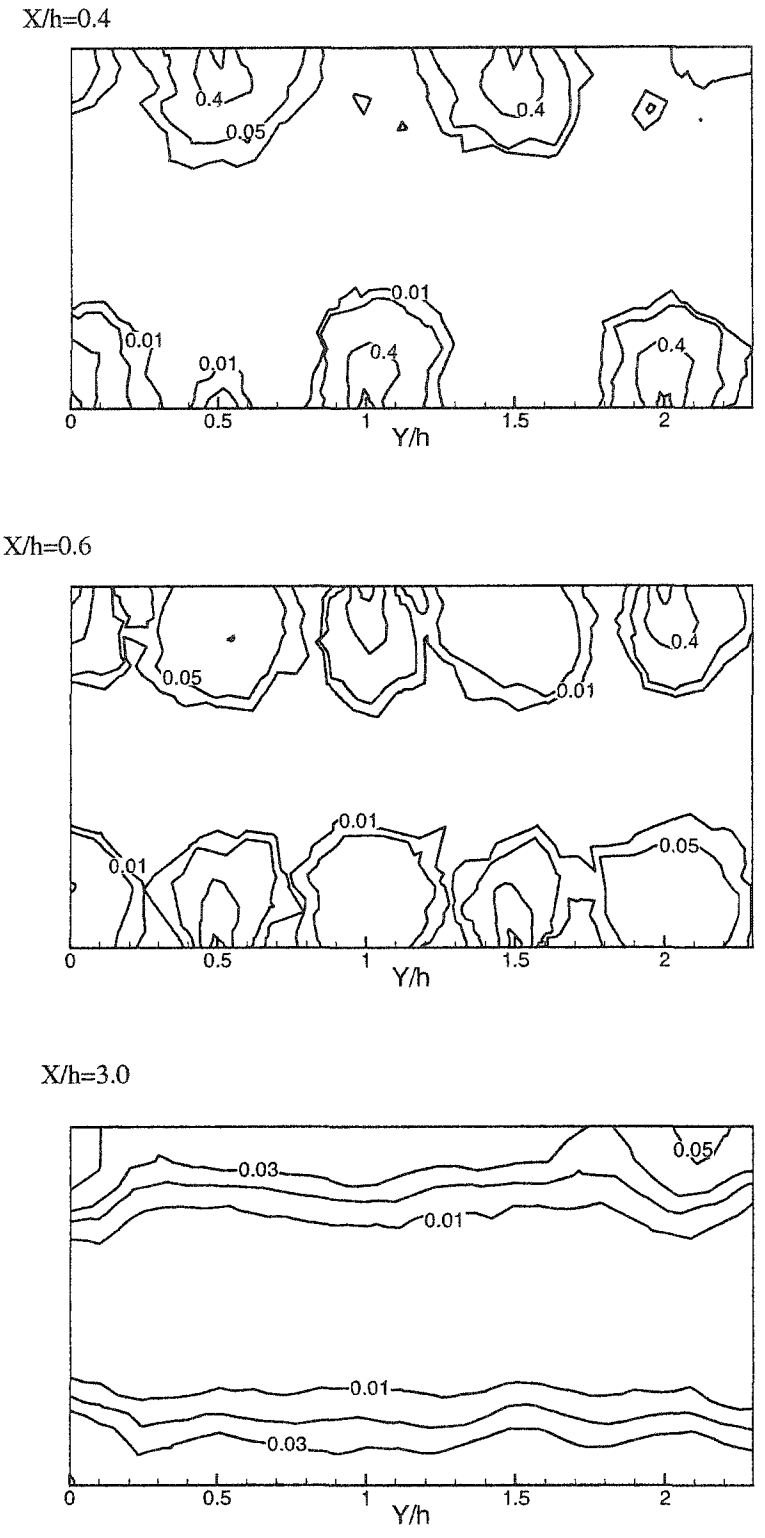

Fig. 5.27 Contours of hydrogen mass fraction ;uniform conditions case

X/h=0.4

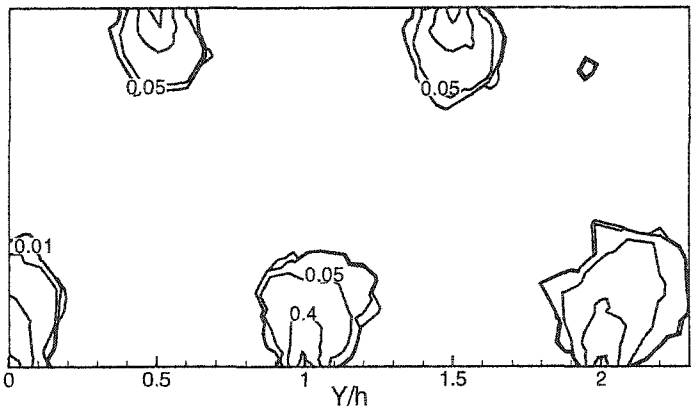

X/h=0.6

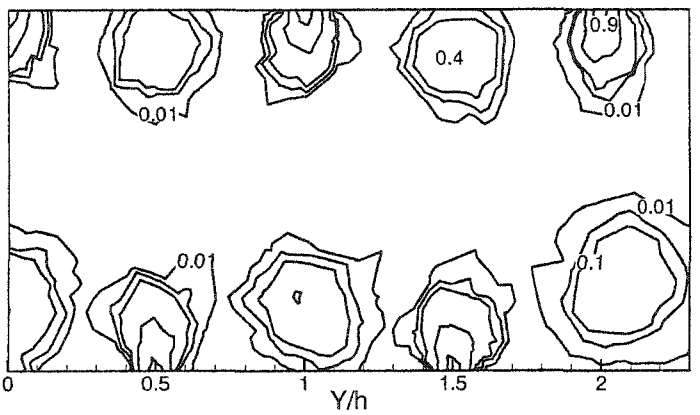

X/h=3.0

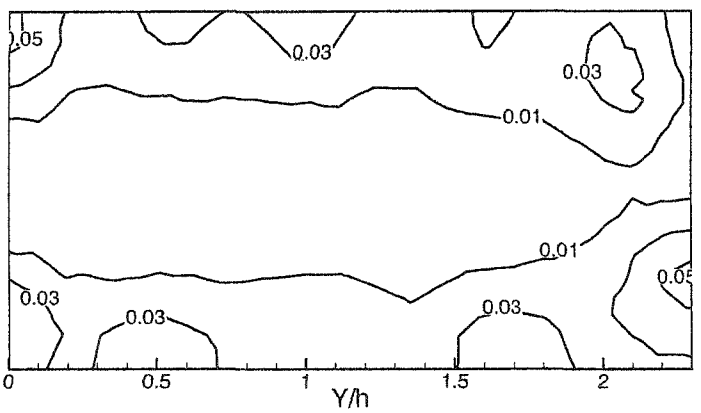

Fig. 5.28 Contours of hydrogen mass fraction inlet profile case

5.2.2 Comparison with the 10-Injector Combustor

Velocity vectors and streamlines for the two combustors are shown in Fig. 5.29. Results of both combustors are obtained with an inlet boundary profile. The figure shows clearly the asymmetric flow and the circulation region inside the isolator in both cases. In the 18-injector combustor the circulation region occupies nearly most of the isolator near the lower wall. In the other case, the circulation extends to half length of the isolator and adjacent to the upper wall.

Figure 5.30 shows the combustion efficiency for the two configurations, the 10-injector combustor and 18-injector combustor. The combustion efficiency is calculated with Eq.(5.1). The combustion efficiency shows higher values for the case with 18 injectors than with 10 injectors. For the same fuel mass flow rate, increasing the number of injectors increases the surface area of the injected fuel, which leads to better and faster mixing. Also, it is seen that the combustion efficiency is slightly affected by the flow inside the isolator. The combustion efficiency is affected mainly by the method of fuel injection.

In Figs. 5.31 and 5.32, the effect of the fuel injectors on the local fuel equivalence ratio is shown. The figures show distributions of local values of the equivalence ratio and the combustion efficiency for the two configurations. The overall fuel equivalence ratio is the same in both cases and is equal to 1.0. The local values of the equivalence ratio and the combustion efficiency are calculated from the mixture composition in terms of mole fraction ratios [84]. These values are calculated using the following equations:

$$\varphi_l = 1 + \left[0.5\left(\frac{X_{H2}}{X_{N2}}\right) - \left(\frac{X_{O2}}{X_{N2}}\right)\right] \cdot \left(\frac{X_{N2}}{X_{O2}}\right)_{air} \tag{5.3}$$

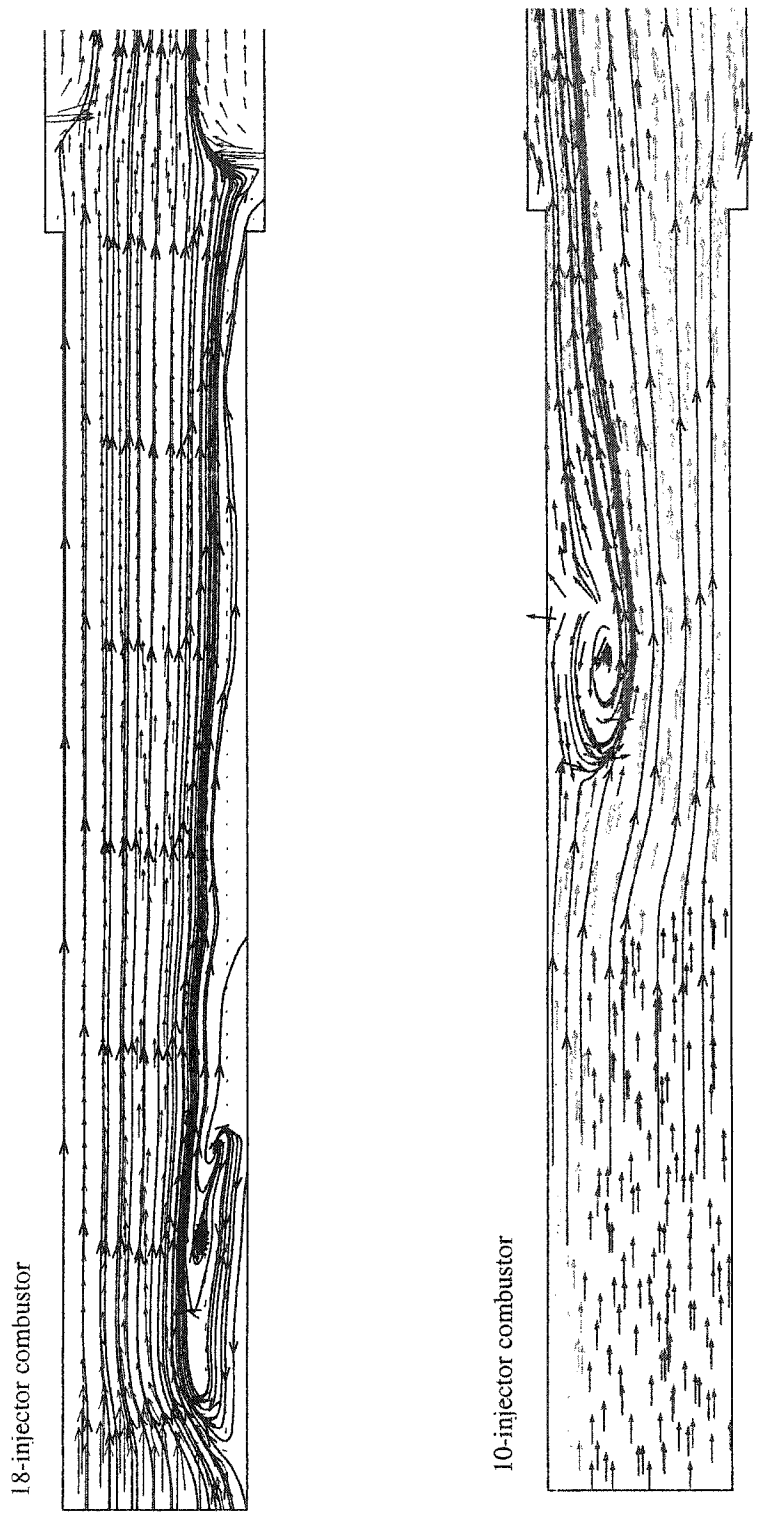

Fig. 5.29 Velocity vectors at the center plane for the two combustors

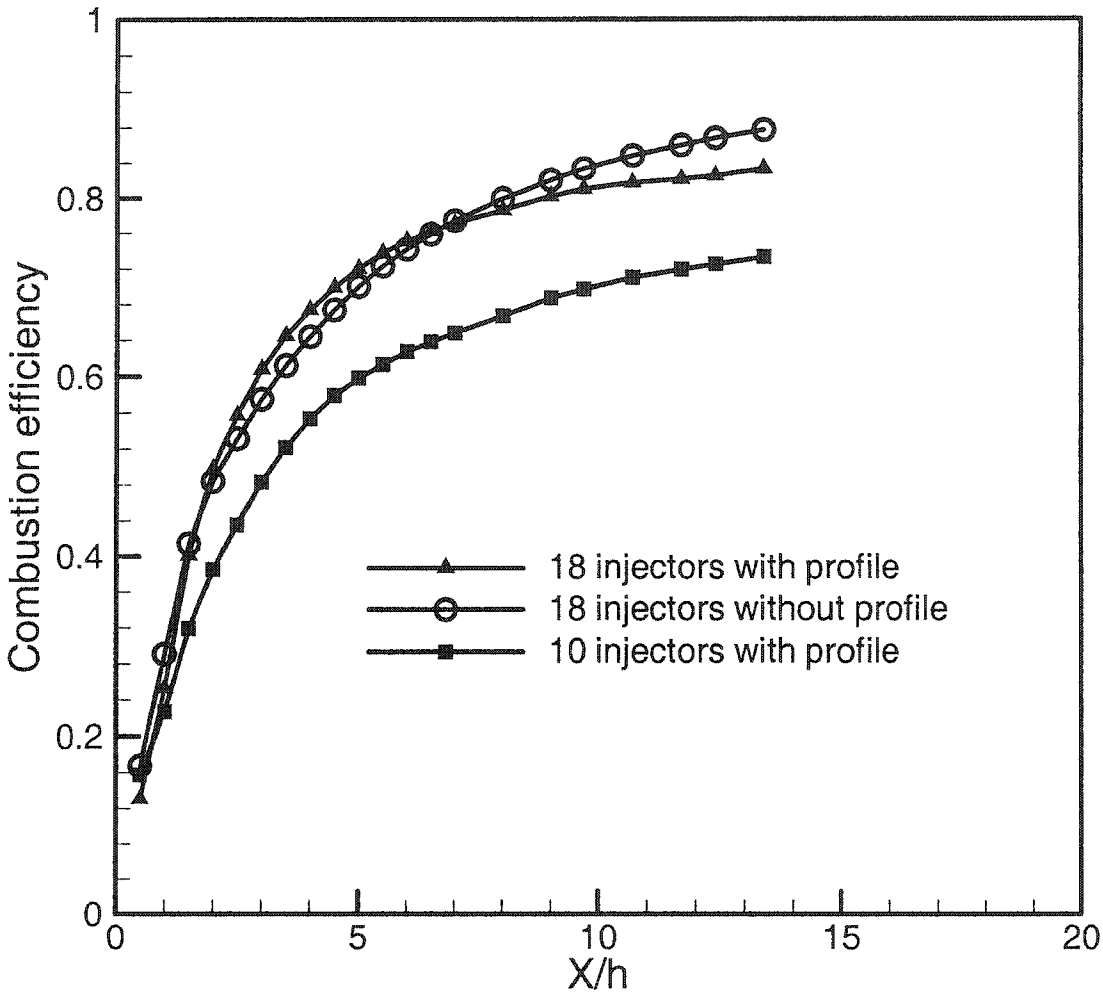

Fig. 5.30 Combustion efficiency for the two combustors

10 injectors

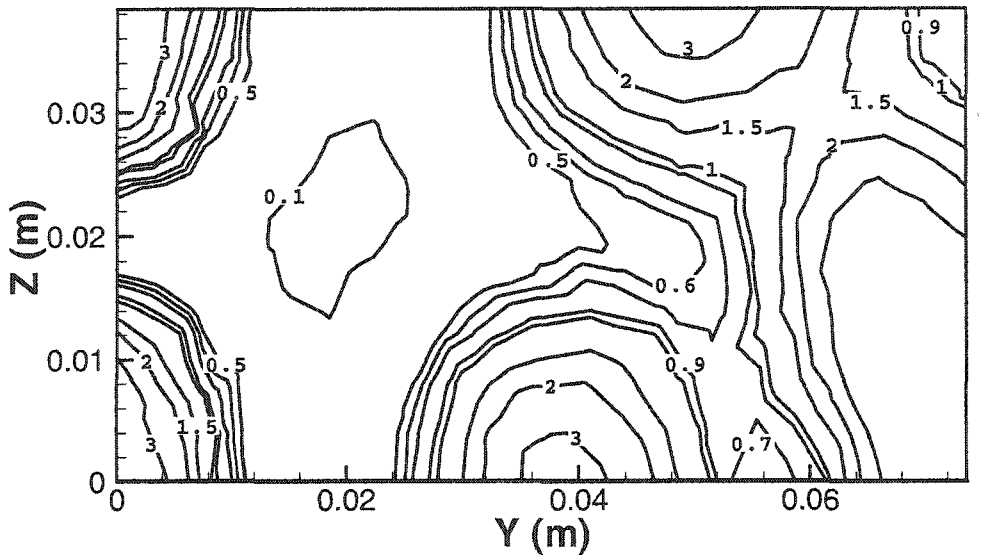

18 injectors

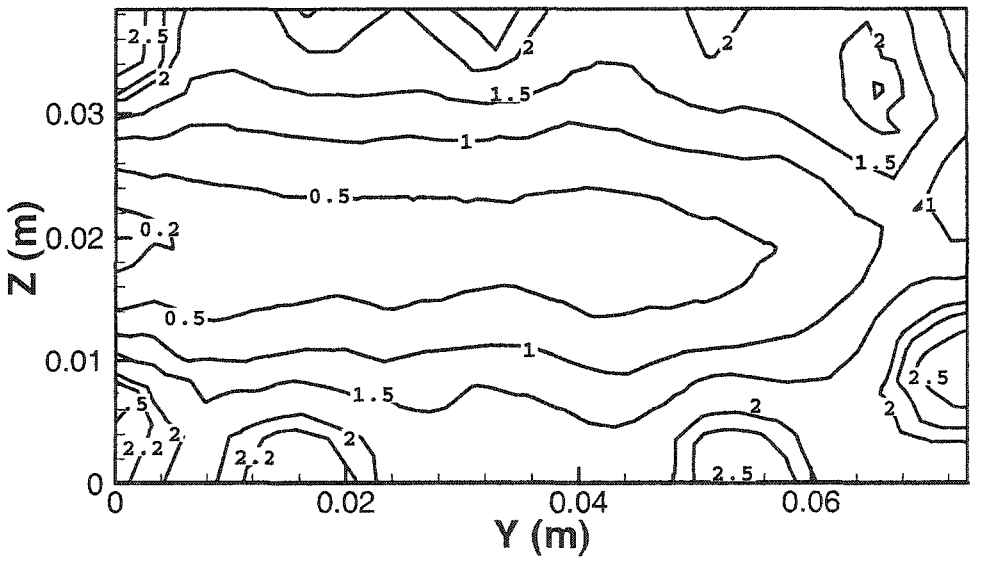

Fig. 5.31 Distribution of fuel local equivalence ratio at the combustor exit plane

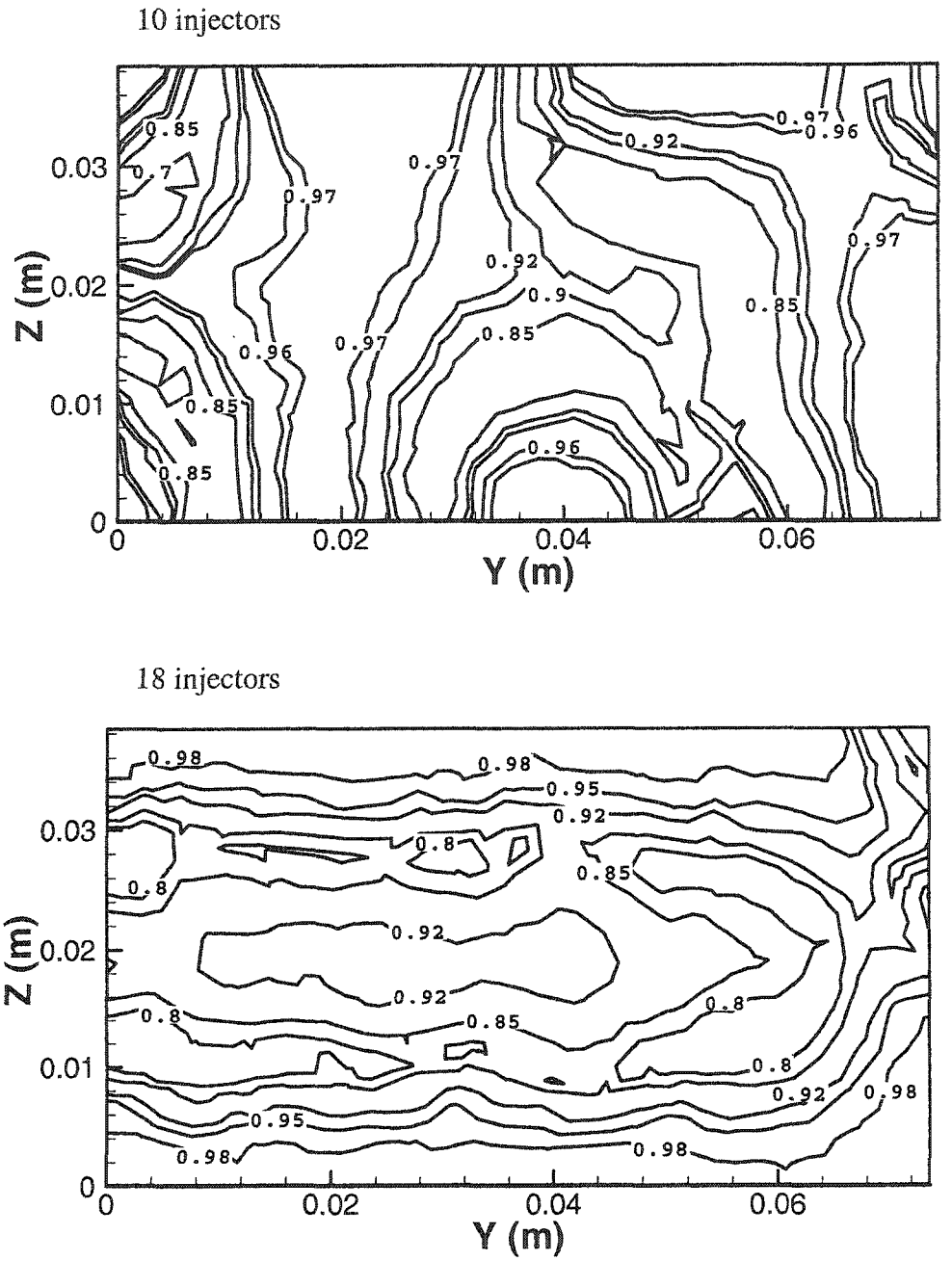

Fig. 5.32 Distribution of fuel local combustion efficiency at the combustor exit plane

$$\eta_{CI} = \left[1 - \left(\frac{X_{O2}}{X_{N2}}\right) \cdot \left(\frac{X_{N2}}{X_{O2}}\right)_{air}\right] / \varphi_l \tag{5.4}$$

$$\eta_{CI} = 1 - \left(\frac{X_{O2}}{X_{N2}}\right) \cdot \left(\frac{X_{N2}}{X_{O2}}\right)_{air} \tag{5.5}$$

Figure 5.31 presents the distribution of the local equivalence ratio at the exit plane of the combustor. Although the fuel is injected from uniformly distributed orifices on the top and the bottom walls, hydrogen is confined near the walls and around the corners in the 10-injector combustor. It can be seen that the distribution of the hydrogen is more uniform in the 18-injector geometry than that in the second case. In the 18-injector combustor, the hydrogen lean region (φ <0.1) covers a non significant region at the center of the cross section. It is to be noted that this uniform distribution and the rapid mixing of the 18-injector combustor is seen with overall fuel equivalence ratio of 1.0 and may be different with lower values. Figure 5.32 illustrates distribution of local combustion efficiency. Comparisons with equivalence ratio distribution (Fig. 5.31) indicates that location of the highest combustion efficiency coincides with the region with φ =1.5. The combustor exit is occupied by a region with local efficiency higher than 80%.

Figure 5.33 compares the averaged static pressure along the axial direction. In both cases, the pressure increases inside the isolator section then reaches its maximum value just after the combustor inlet and very close to the location of the injectors. The pressure then decreases inside the combustor and the expanding duct. It can be seen that the

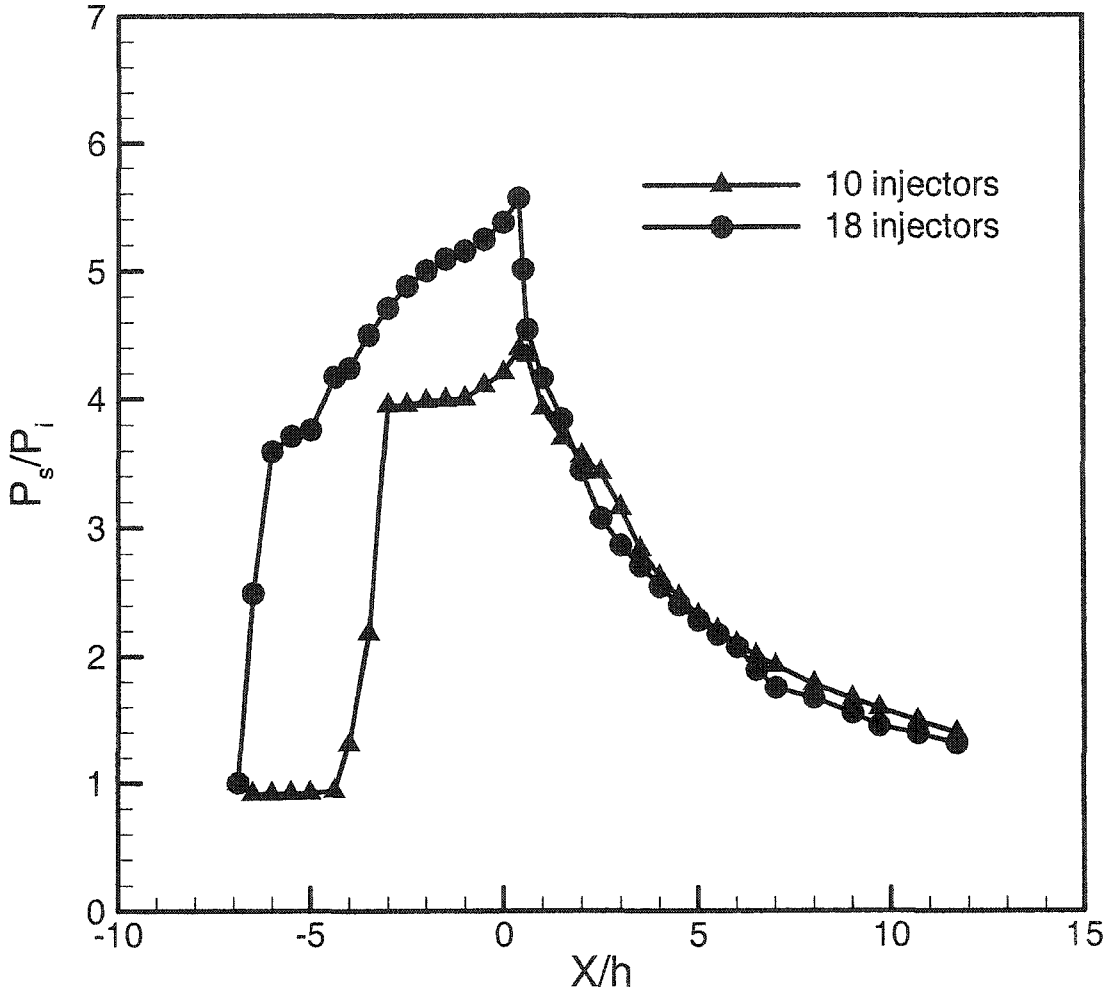

Fig. 5.33 Axial distribution of static pressure for the two combustors

upstream interaction inside the isolator is very significant in the 18-injector case. This increase starts very close to the isolator inlet. However, in the 10-injector case the upstream interaction starts after a distance equal to about half duct length. The maximum value of the pressure inside the isolator in the 18-injector model is higher than that in the 10-injector model. The pressure rise in both cases is due to the fuel injection and the heat release from the combustion. The difference in the pressure can be due to the arrangement and the number of the fuel injectors.

Figure 5.34 shows the integrated stream thrust F_x for both cases. Thrust is calculated for planes perpendicular to the X-axis with Eq.(5.2). Inside the isolator, the thrust force has the same value in both configurations. A slight decrease is seen because of friction. The stream thrust increases just after the combustor inlet caused by the momentum of the jets. It is seen that increasing the number of injectors caused an increase in the stream thrust inside the combustor and the expanding duct. It can be concluded that the improved mixing and combustion efficiency produced the higher thrust performance in the 18-injector combustor. It can be seen that the thrust inside the isolator is not affected by the distribution of the injectors inside the combustor.

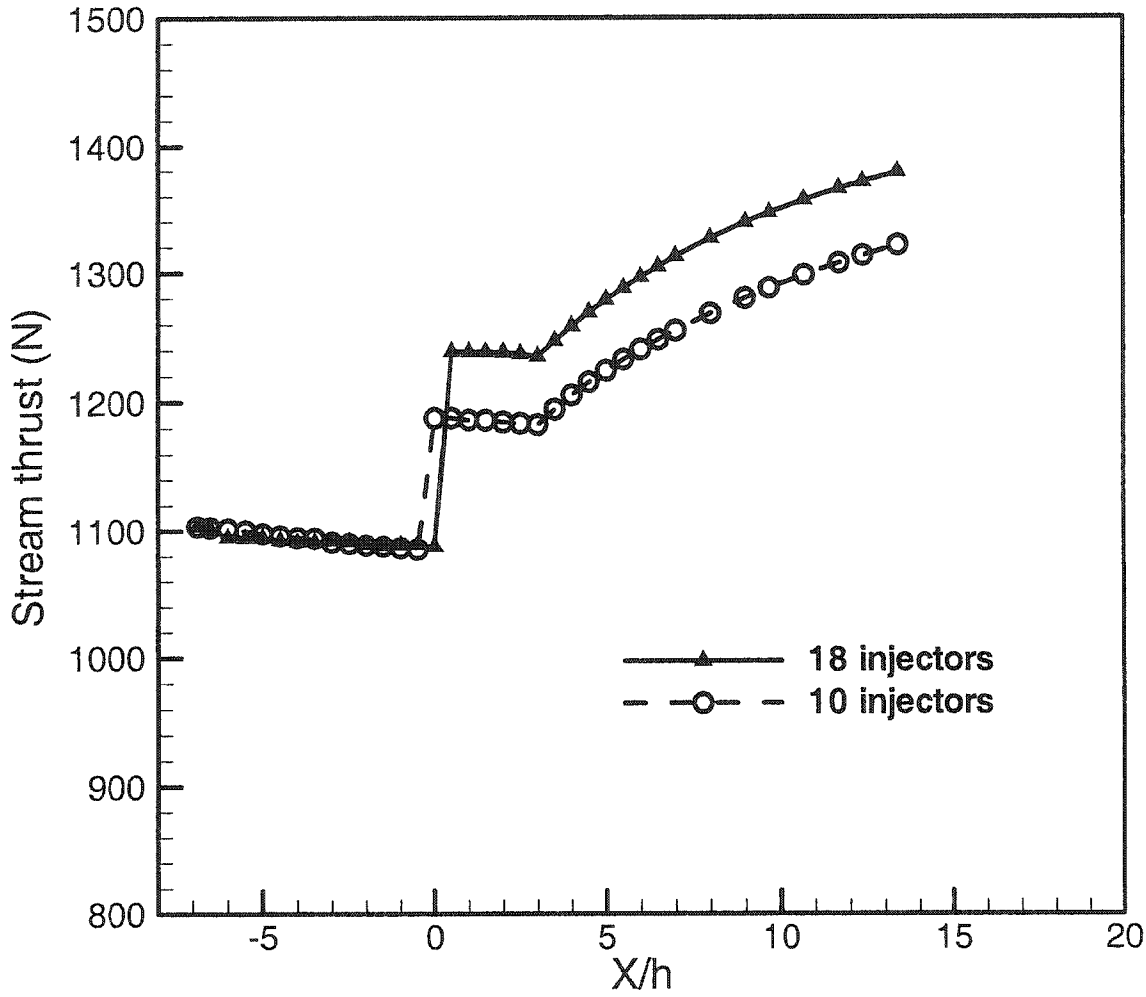

Fig. 5.34 Axial distribution of streamwise thrust for the two combustors

Chapter VI

CONCLUSIONS

Mixing and flow characteristics in scramjet engines combustors are numerically investigated. Results are obtained with a finite volume CFD code and using unstructured grids.

In the first part of this study, the supersonic mixing of fuel and air with wall-mounted ramps is addressed. Two types of the wall-mounted ramps have been used: raised (compression) ramp and relieved (expansion) ramp. The effects of the ramp side angle in both mixing and combustion processes are investigated. Three side angles have been used, 0 (unswept), 5, and 10 degrees. The conclusions drawn from this part of the study could be summarized by the following points:

1. Current results confirm the turbulence nature of the flowfield inside the combustor model. Results of laminar flows underpredict the flow velocity and the flow temperature by 6% and 5%, respectively, when compared with experimental results. Furthermore, the magnitude of the static pressure is seen to be highly underpredicted, especially in the front region of the ramp.
2. The importance of selecting a suitable turbulence model is addressed by different researchers. In the current study, a two-equation turbulence model is used as recommended by Donohue et al. [39]. Three forms of the k-ε turbulence model are examined using the 10-degree swept ramp. All forms of the model show no significant difference and agree well with the experimental results.

3. The mole fraction of the injectant is used to demonstrate the mixing rate. The effect of the side angle of the ramp is not significant near the exit plane of the injector (from X/H=0 to X/H=2.0).
4. Downstream of the injector, after X/H=2.0, the effect of the side angle of the ramp becomes significant. At X/H=6.0, the mole fraction reduces to about 23% of its maximum value for the 10-degree swept ramp while it reduces to about 60% of its maximum value in the unswept case.
5. Slight improvement in the mixing rate is seen when increasing the side angle from 5 degrees to 10 degrees. The difference in the mixing rate between the two swept ramps is not significant as the difference between the unswept ramp and the swept ramps.
6. As expected, the losses associated with the 10-degree swept ramp, presented by the entropy increase, are higher than those of the other two ramps. Both the unswept ramp and the 5-degree ramp show the same rate of increase. This demonstrates that the 5-degree swept ramp gives relatively good mixing rate and low losses compared to the 10-degree ramp.
7. Both raised and relieved unswept ramps show the same mixing rate near the injector until two ramp heights (X/H=2.0). After that, fast mixing is obtained by the relieved ramp. This leads to important conclusion that all of the wall-mounted ramps investigated in this study (regardless of the side angle) give the same mixing rate in the region between X/H=0 and X/H=2.0. Also, the ramp injectors give poor mixing rate in the near field of the injector.

8. Although fast mixing can be achieved with the relieved ramps, the losses associated with mixing process (presented by the entropy increase) are higher than those of the raised ramps.

Further study is needed with different side angles greater than 10 degrees to determine if this increase of the angle will lead to further improvement of the mixing process.

In the second part, two different configurations of dual-mode combustors are investigated. In the first configuration, fuel is injected through an unswept wall-mounted ramp parallel to the incoming airstream. In the second configuration, fuel is injected behind a rear ward facing step normal to the incoming airstream. The effects of the equivalence ratio, the length of the combustor, the initial boundary layer thickness, and the arrangement of the injectors are studied. The conclusions drawn from the dual-mode combustor with the ramp fuel injector could be summarized by the following points:

1. The flow is decelerated from supersonic to subsonic condition within a very short distance of the combustor inlet. This subsonic region is a characteristic of the dual-mode combustion. Considerable total pressure loss is seen in the combustor duct mainly due to the chemical reaction.
2. The change in the equivalence ratio by 10% slightly affects the combustion efficiency near the end of the combustor duct.
3. Increasing the length of the combustor increases the plume area of the fuel. This can be seen in reacting as well as non reacting cases. A linear increase is seen only in the nonreacting cases.
4. The combustion efficiency is improved by increasing the length of the combustor which is a result of increasing the plume area.

5. Both reacting and nonreacting results show that the calculated magnitude of the axial thrust in the long combustor model is less than that of the short combustor model.

Finally, the results of the dual-mode combustor with rearward facing step are summarized by the following points:

1. As a result of using incoming boundary layer thickness, a significant amount of upstream interaction occurs in the isolator; this finding confirms the results obtained by Riggins [69]. In addition, asymmetric flow is seen inside the isolator duct with a large circulation region formed near the lower wall of the isolator. The same observation is found by Mohieldin et al. [72].
2. It is noted that all flow properties inside the combustor are slightly affected by the initial thickness of the boundary layer. Also, the mixing rate is not affected by the initial boundary layer thickness. This observation confirms the ability of the isolator in the dual-mode combustor to isolate the inflow from the combustor and to prevent the engine unstart condition.
3. For the same air and fuel flow rates, increasing the number of the injectors from 10 injectors to 18 injectors leads to faster mixing rate and higher combustion efficiency. Also, higher axial thrust and larger upstream interaction are obtained when using the 18-injector model.

REFERENCES

1. Archer, R. Douglas, and Saarlas, Maido, Introduction to Aerospace Propulsion, Prentice-Hall Inc., New Jersey, 1996.

2. Deiwert, G. S., Cavolowsky, J. A., and Loomis, M. P., "Large Scale Scramjet in the Ames 16-Inch Shock Tunnel," AIAA 18th Aerospace Ground Testing Conference, AIAA Paper No. 94-2519, June 1994.

3. McClinton, C. R., Hunt, J. L., Ricketts, R. H., Reukauk, P., and Peddie, C. L., "Airbreathing Hypersonic Technology Vision Vehicles and Development Dreams," AIAA 9th International Space Planes and Hypersonic Systems and Technologies Conference, AIAA Paper No. 99-4978, November 1999.

4. Stalker, R. J., Simmons, J. M., Paull, A., and Mee, D. J., "Measurement of Scramjet Thrust in Sock Tunnels," AIAA 18th Aerospace Ground Testing Conference, AIAA Paper No. 94-2516, June 1994.

5. Drummond, J. P., Northam, G. B., and Rogers, R. C., "Research Opportunities in Supersonic Mixing and Combustion," 32nd Aerospace Sciences Meeting, AIAA Paper No. 94-0708, January 1994.

6. Heiser, W. H., and Pratt, D. T., Air Breathing Propulsion, AIAA Education Series, 1994.

7. Curran, E. T., and Murthy, S. N. B., Scramjet Propulsion, AIAA Progress in Astronautics and Aeronautics, Vol. 189, 2001.

8. Seiner, J. M., Dash, S. M., and Kenzakowski, D. C., "Historical Survey on Enhanced Mixing in Scramjet Engines," AIAA Journal of Propulsion and Power, Vol. 17, No. 6, Nov.-Dec.2001, pp.1273-1286.

9. Lee, M. P., McMillin, B. K., Palmer, J. L., and Hanson, R. K., "Planar Fluorescence Imaging of a Transverse Jet in a Supersonic Crossflow," AIAA Journal of Propulsion and Power, Vol. 8, No.4, 1992, pp. 729-735.

10. Segal, C., McDaniel, J. C., Krauss, R. H., and Whitehurst III, R. B., "Combustion Efficiency Determined from Wall Pressure and Temperature Measurement in a Mach 2 Combustor," AIAA 29th Aerospace Sciences Meeting, AIAA Paper No. 91-0017, January 1991.

11. Hermanson, J. C., and Winter, M., "Mie Scattering Imaging of a Transverse Sonic Jet in Supersonic Flow," AIAA Journal, Vol. 31, No. 1, January 1993, pp. 129-132.

12. Gruber, M. R., Nejad, A. S., Chen, T. H., and Dutton, J. C., "Mixing and Penetration Studies of Sonic Jets in a Mach 2 Freestream," AIAA Journal of Propulsion and Power, Vol. 11, No. 2, 1995, pp. 315-323.

13. VanLerberghe, W. M., Santaigo, J. G., Dutton, J. C., and Lucht, R. P., " Mixing of a Sonic Transverse Jet Injected into a Supersonic Flow," AIAA Journal, Vol. 38, No. 3, March 2000, pp. 470-479.

14. Abbitt III, J. D., McDaniel, J. C., Krauss, R. H., Whitehurst, R. B., and Segal, C., "Experimental Investigation of a Supersonic Combustion Flowfield Employing Staged Transverse Injection Behind a Rearward-Facing Step," 30th AIAA Aerospace Sciences Meeting, AIAA Paper No. 92-0090, January 1990.

15. Uenishi, K., Rogers, R. C., and Northam, G. B., "Numerical Prediction of a Rearward-Facing-Step Flow in a Supersonic Combustor," AIAA Journal of Propulsion and Power, Vol.5, No. 2, March-April 1989, pp. 158-164.

16. Vinogradov, V. A., Owens, M., Mullagiri, S., and Segal, C., "Effects of Fuel Pre-injection on Mixing in a Mach 1.6 Airflow," 9th International Space Planes and Hypersonic Systems and Technologies Conference, AIAA Paper No. 99-4918, November 1999.

17. Segal, C., Haj-Hariri, H., and McDaniel, J. C., "A Numerical Investigation of Hydrogen Combustion in a Mach 2 Airflow," 30th AIAA Aerospace Sciences Meeting, AIAA Paper No. 92-0341, Jan. 1992.

18. Yu, G., Li, J. G., Zhang, X. Y., Chen, L. H., and Sung, C. J., "Investigation on Combustion Characteristics of Kerosene-Hydrogen Dual Fuel in a Supersonic Combustor," AIAA 36 Joint Propulsion Conference, AIAA Paper No. 2000-3620, July 2000.

19. Lee, S-H, Kim, H-B., and Mitani, T., "Mixing and Combustion Augmentations of Transverse Injection in Scramjet Combustor," AIAA 39th Aerospace Sciences Meeting, AIAA Paper No. 2001-0384, January 2001.

20. Gutmark, E., Schadow, K. C., Parr, T. P., Parr, D. M., and Wilson, K. J., "Combustion Enhancement by Axial Vortices," AIAA Journal of Propulsion and Power, Vol. 5, No. 5, September 1989, pp 555- 560.

21. Northam, G. B., Greenberg, I., and Byington C. S., "Evaluation of Parallel Injection Configurations for Supersonic Combustion," AIAA 25th Joint Propulsion Conference, AIAA Paper 89-2525, July 1989.

22. Rogers, R. C., Capriotti, D. P., and Guy, R. W., "Experimental Supersonic Combustion Research at NASA Langley," 20th AIAA Advanced Measurement and Ground Testing Technology Conference, AIAA Paper No. 98-2506, June 1998.

23. Drummond, J. P., Carpenter, M. H., Riggins, D. W., and Adams, M. S., "Mixing Enhancement in a Supersonic Combustor," 25th AIAA Joint Propulsion Conference, AIAA Paper No. 89-2794, July 1989.

24. Riggins, D. W., Mekkes, G. L., McClinton, C. R., and Drummond, J. P., "A Numerical Study in a Supersonic Combustor," 28th AIAA Aerospace Sciences Meeting, AIAA Paper No. 90-0203, January 1990.

25. Riggins, D. W., and McClinton, C. R., "A Computational Investigation of Flow Losses in a Supersonic Combustor," AIAA Paper No. 90-2093, July 1990.

26. Riggins, D. W., and McClinton, C. R., "Analysis of Losses in Supersonic Mixing and Reacting Flows," AIAA Paper No. 91-2266, June 1991.

27. Riggins, D. W., McClinton, C. R., Rogers, R. C., and Bittner, R.D., "A Comparative Study of Scramjet Injection Strategies for High Mach Number Flows," AIAA Paper No 92-3287, 1992.

28. Waitz, I. A., Marble, F. E., and Zukoski, E. E., "A Systematic Experimental and Computational Investigation of a Class of Contoured Wall Fuel Injectors," AIAA 30th Aerospace Sciences Meeting, AIAA Paper No. 92-0625, January 1992.

29. Donohue,J.M., Haj-Hariri, H., and McDaniel, J.C., "Vorticity Generation Mechanisms in Parallel Injection Schemes for Supersonic Mixing," AIAA Paper No. 92-3286, July 1992.

30. Stouffer, D. S., Baker, N .R., Capriotti, D. P., and Northam,G. B., " Effects of Compression and Expansion-Ramp Fuel Injector Configurations on Scramjet Combustor and Heat Transfer," 31st AIAA Aerospace Sciences Meeting, AIAA Paper No. 93-0609, January 1993.

31. Stouffer, D. S., and Northam, G. B., "Comparison of Wall Mixing Concepts for Scramjet Combustors," 32nd AIAA Aerospace Sciences Meeting, AIAA Paper No. 94-0587, January 1994.

32. Cox, S. K., Fuller, R. P., Schetz, J. A., and Walters, R. W., "Vortical Interactions Generated by an Injector Array to Enhance Mixing in Supersonic Flow," AIAA 32nd Aerospace Sciences Meeting and Exhibit, AIAA Paper No. 94-0708, January 1994.

33. Eklund, D. R., and Stouffer, S. D., "A Numerical and Experimental Study of a Supersonic Combustor Employing Swept Ramp Fuel Injector," AIAA Paper No. 94-0587, January 1994.

34. Baurle, R. A., Alexopoulos, G. A., and Hassan, H. A., "Analysis of Supersonic Combustors with Swept Ramp Injectors," AIAA 31st Joint Propulsion Conference, AIAA Paper No. 95-2413, July 1995.

35. McDaniel, J. C., Gauba,G., Quagliaroli, T.M., Grinstead, J.H., Laufer, G., Krauss, R. H., Whitehurst, R. B., and Victor, K.G., "Combustion of Hydrogen in Mach 2 Air Using an Unswept Ramp Fuel Injector: A Test Case for CFD Validation," AIAA Paper No. 94-2521, June 1994.

36. Gauba, G., Haj-Hariri, H., and McDaniel, J. C., "Numerical and Experimental Investigation of Hydrogen Combustion in a Mach 2 Airflow with an Unswept Ramp Fuel Injector," 31st AIAA Joint Propulsion Conference, AIAA Paper No. 95-2562, July1995.

37. Hartfield, R.J., Hollo ,S.D., and McDaniel, J.C "Experimental Investigation of a Supersonic Swept Ramp Injector Using Laser-Induced Iodine Fluorescence," Journal of Propulsion and Power, Vol. 10, No.1, Jan.-Feb. 1994, pp. 129-135.

38. Donohue,J.M., McDaniel, J.C. and Haj-Hariri, H., "Experimental and Numerical Study of Swept Ramp Injection into a Supersonic Flowfield," AIAA Journal, Vol. 32, No. 9, September 1994, pp.1860-1867.

39. Donohue, J.M., and McDaniel, J. C., "Complete Three-Dimensional Multiparameter Mapping of a Supersonic Ramp Fuel Injector Flowfield," AIAA Journal, Vol. 34, March 1996, pp. 455-462.

40. Sekar, B., "Three Dimensional Computation of Parallel and Non-Parallel Injection in Supersonic Flow," 33rd AIAA Aerospace Sciences Meeting, AIAA Paper No. 95-0886, January 1995.

41. Haimovitch, Y., Gartenberg, E., Roberts, A.S., and Northam G. B., "Effects of Internal Nozzle Geometry on Compression-Ramp Mixing in Supersonic Flow," AIAA Journal, Vol. 35, No. 4, April 1997, pp. 663-670.

42. Drummond, J. P., " Enhancement of Mixing and Reaction in High-Speed Combustor Flowfields," International Colloquium on Advanced Computation and Analysis of Combustion, May 12-15, 1997, Moscow, Russia.

43. Laufer, G., Quagliaroli, T. M., Krauss, R. H., Whitehurst, R. B., and McDaniel, J. C., "Planar OH Density and Apparent Temperature Measurements in a Supersonic Combusting Flow," AIAA Journal, Vol. 34, No. 3, March 1996, pp. 463-469.

44. Cox-Stouffer, S. K., and Gruber, M. R., "Effects of Spanwise Injector Spacing on Mixing Characteristics of Aerodynamic Ramp Injector," 34th AIAA Joint Propulsion Conference, AIAA Paper No. 98-3272, July 1998.

45. Cox-Stouffer, S. K., and Gruber, M. R., "Effects of Injector Yaw on Mixing Characteristics of Aerodynamic Ramp Injectors," AIAA 37 th Aerospace Sciences Meeting, AIAA Paper No. 99-0086, January 1999.

46. Cox-Stouffer, S. K., and Gruber, M. R., "Further Investigation of the Effects of "Aerodynamic Ramp" Design Upon Mixing Characteristics," AIAA 35th Joint Propulsion Conference, AIAA Paper No. 99-2238, June 1999.

47. Waltrup, P. J., "Liquid-Fueled Supersonic Combustion Ramjets: A Research Perspective," AIAA Journal of Propulsion and Power, Vol. 3, No. 6, Nov.-Dec. 1987, pp. 515-524.

48. Billing, F. S., and Dugger, G. L. "The Interaction of Schock Waves and Heat Addition in the Design of Supersonic Combustors," Proceedings of 12th Symposium on Combustion, Combustion Institute, Pittsburgh, PA, 1969, pp. 1125-1134.

49. Billing, F. S., Dugger, G. L., and Waltrup, P. J., "Inlet-Combustor Interface Problems in Scramjet Engines," Proceeding of the 1st International Symposium on Airbreathing Engines, Marseilles, France, June 1972.

50. Waltrup, P. J., and Billing, F. S., "Prediction of Precombustion Wall Pressure Distribution in Scramjet Engines," Journal of Spacecraft and Rockets, Vol. 10, No. 9, 1973, pp. 620-622.

51. Waltrup, P. J., and Billing, F. S., "Structure of Shock Waves in Cylindrical Ducts," AIAA Journal, Vol. 11, No. 9, September 1973, pp. 1404-1408.

52. Anderson, G. Y., "Experimental Investigation of a Swept-Strut Fuel Injector Concept for Scramjet Application," NASA TN D-8454, August 1977.

53. Billing, F. S., "Research on Supersonic Combustion," AIAA Paper No. 92-0001, January 1992.

54. Stockbrige R. D., "Experimental Ivestigation of Shock Wave/Boundary-Layer Interactions in an Annular Duct," AIAA Journal of Propulsion and Power, Vol. 5, No.3, May-June 1989, pp. 346-352.

55. Carol, B. F., and Dutton, J. C., "Characteristics of Multiple Shock Wave/Turbulent Boundary-Layer Interactions in Rectangular Ducts," Journal of Propulsion and Power, Vol. 6, No. 2, March-April 1990, pp. 186-193.

56. Hunter, L. G., and Couch, B. D., "A CFD Study of Precombustion Shock-Train from Mach 3-6," AIAA 26th Joint Propulsion Conference, AIAA Paper No. 90-2220, July 1990.

57. Lin, P., Rao, G.V., and O'Connor, G. M., " Numerical Investigation on Shock Wave/Boundary Layer Interaction in a Constant Area Diffuser at Mach 3," AIAA 22nd Fluid Dynamics Conference, AIAA Paper No. 91-1766, June 1991.

58. Pratt, D. T., and Heiser, W. H., "Isolator-Combustor Interaction in a Dual-Mode Scramjet Engine," 31st Aerospace Sciences Meeting and Exhibit, AIAA Paper No. 93-0358, January 1993.

59. Chinzei, N., Komuro, T., Kudou, K., Murakami, A., Tani, K., Masuya, G., and Wakamatsu, Y., "Effects of Injector Geometry on Scramjet Combustor Performance," Journal of Propulsion and Power, Vol. 9, No. 1, Jan.-Feb. 1998, pp. 146-152.

60. Lin, P., "Geometric Effects on Precombustion Shock Train in Constant Area Isolator," 29th Joint Propulsion Conference, AIAA Paper No. 93-1838, July 1993.

61. Emami, S., Trexler, C., Auslender, A., and Weidner, J. P., "Experimental Investigation of Inlet-combustor Isolator for a Dual- Mode Scramjet at a Mach Number of 4," NASA Technical Paper 3502, May 1995.

62. Eklund, D. R., and Gruber, M. R., "Study of a Supersonic Combustor Employing an Aerodynamic Ramp Pilot Injector," 35th AIAA Joint Propulsion Conference, AIAA Paper No. 99-2249, June 1999.

63. Gruber, M., Donbar, J., Jackson, T., Mathur, T., Eklund, D., Billing, F., "Performance of an Aerodynamic Ramp Fuel Injector in a Scramjet Combustor," AIAA 36th Joint Propulsion Conference, AIAA Paper No. 2000-3708, July 2000.

64. Eklund, D. R., Baurle, R. A., and Gruber, M. R., "Numerical Study of a Scramjet Combustor Fueled by an Aerodynamic Ramp Injector in a Dual-Mode Combustion," 39th AIAA Aerospace Sciences Meeting, AIAA Paper No. 2001-0379, January 2001.

65. Cox-Stouffer, S. K., and Hagenmaier, M. A., "The Effect of Aspect Ratio on Isolator Performance," 39th AIAA Aerospace Sciences Meeting, AIAA Paper No. 2001-0519, January 2001.

66. Kumauro, T., Kudo, K., Masuya, G., Chinzei, N., Murakami, A., and Tani, K., "Experiment on a Rectangular Cross Section Scramjet Combustor," (in Japanese), National Aerospace Lab., NAL TR-1068, Tokyo, Japan, 1990.

67. Murakami, A., Kumauro, T., and Kudo, K., "Experiment on a Rectangular Cross Section Scramjet Combustor (II) Effects of Fuel Injector Geometry," (in Japanese), National Aerospace Lab., NAL TR-1220, Tokyo, Japan, 1993.

68. Mizobuchi, M., Matsuo, Y., and Ogawa, S., "Numerical Estimation of Turbulence Temperature Fluctuation Effect on Hydrogen-Oxygen Reaction Process," 35th Aerospace Sciences Meeting, AIAA Paper No. 97-0910, January 1997.

69. Riggins, D. "The Numerical Investigation of a Dual-Mode Scramjet Combustor," JANNAF Joint Meetings, Tucson, AZ, December 10, 1998, pp. 409-426.

70. Olynciw, M. J., Mohieldin, T. O., McClinton, C. R., and Tiwari, S. N., "Effects of Scaling on Numerical Modeling of Transverse Jet into Supersonic Cross Flows," AIAA 14th Computational Fluid Dynamics Conference, AIAA Paper No. 99-3368, June 1999.

71. Rodriguez, C. G., White, J. A., and Riggins, D. W., "Three-Dimensional Effects in Modeling of Dual-Mode Scramjets," 36th AIAA/ASME/SAE/ASEE Joint Propulsion Conference and Exhibit, AIAA Paper No. 2000-3704, July 2000.

72. Mohieldin, T. O, Tiwari, S. N., and Olynciw, M. J., "Asymmetric Flow-Structures in Dual Mode Scramjet Combustor with Significant Upstream Interaction," 37th AIAA Joint Propulsion Conference, AIAA Paper No. 2001-3296, July 2001.

73. Nickol, C. L., "Unswept Ramp Fuel Injector Base Aspect Ratio Parametric Study in a Mach 2.9 Freestream," M. Sc. Thesis, University of Virginia, Charlottesville, VA, 1994.

74. McDaniel, J. C., " Combustor Data Bases for Hypersonic Airbreathing Propulsion Systems," 8th AIAA International Space Planes and Hypersonic Systems and Technologies Conference, AIAA Paper No. 98-1646, April 1998.

75. Tannehill, J., Anderson, D., and Pletcher, R., Computational Fluid Mechanics and Heat Transfer, Hemisphere Publishing Co., New York, 1984.

76. FLUENT 5 User's Guide, Fluent Incorporated, Lebanon, New Hampshire, 1999.

77. Hinze, J. O., Turbulence, McGraw-Hill Inc., Second Edition, 1987.

78. Wilcox, D. C., Turbulence Modeling for CFD, DCW Industries Incorporation, October1998.

79. Launder, B. E., and Spalding, D. B, Lectures in Mathematical Models of Turbulence, Academic Press, London, England, 1972.

80. Yakhot, V. and Orszag, S.A., "Renormalization Group Analysis of Turbulence. I. Basic Theory," Journal of Scientific Computing, Vol. 1 No.1, pp.3-51.

81. GAMBIT User's Guide, Fluent Incorporated, Lebanon, New Hampshire, 1999.

82. Mao, M., "Validation of GASP on Mach 2 Swept Ramp Injection Flow Field," HNAG Report 98-0xy Rev. 0, November1998.

83. Eklund, D. R., Stouffer, S. D., and Northam, G. B, "Study of a Supersonic Combustor Employing Swept Ramp Fuel Injectors," AIAA Journal of Propulsion and Power, Vol. 13, No. 6, November-December 1997, pp. 697-704.

84. Mitani, T., Hiraiwa, T., Sato, S., Tomioka, S., Kanda, T., and Tani, K., "Comparison of Scramjet Engine Performace in Mach 6 Vitiated and Storage-Heated Air," AIAA Journal of Propulsion and Power, Vol. 13, No. 5, September-October 1997, pp. 635-642.

CURRICULUM VITA
for
Tarek Abdel-Salam

DEGREES:

Doctor of Philosophy (Mechanical Engineering), Old Dominion University, Norfolk, VA, May 2003

Master of Science (Mechanical Engineering), Cairo University, Cairo, Egypt, March 1994

Bachelor of Science (Mechanical Engineering), Cairo University, Cairo, Egypt, July 1988

PROFESSIONAL CHRONOLOGY:

Department of Mechanical Engineering, Old Dominion University, Norfolk, Virginia
Graduate Teaching Assistant, August 1997 – Present

Department of Mechanical Engineering, Old Dominion University, Norfolk, Virginia
Graduate Research Assistant, May 1998 – August 1999

Industrial Assessment Center, Old Dominion University, Norfolk, Virginia
Project Engineer, April 2000 – May 2001

Energy Conservation and Environment Project, Cairo University, Cairo, Egypt
Senior Environmental Engineer, October 1995 – August 1997

Department of Mechanical Engineering, The Higher Technological Institute, Tenth of Ramadan City, Egypt.
Teaching Assistant, January 1989-Present

CONSULTING/PART TIME EMPLOYMENT:

Department of Mechanical Engineering Technology, Old Dominion University, Norfolk, Virginia
Adjunct Professor, August 2002 – Present

Department of Mechanical Engineering, The American University at Cairo, Cairo, Egypt
Teaching Assistant, September 1992 – August 1997

SCIENTIFIC AND PROFESSIONAL SOCIETIES MEMBERSHIP:

American Institute of Aeronautics and Astronautics. (AIAA)
American Society of Mechanical Engineers. (ASME)
Virginia Academy of Science (VAS)

COURSES TAUGHT DURING LAST FIVE YEARS:

Dynamics, Engineering Graphics, Thermo-Fluids Lab, Fluids Lab, Thermodynamics and Fluid Mechanics.

MAJOR SERVICE ACTIVITIES:

President, Mechanical Engineering Graduate Student Association, Old Dominion University, September 1999-October 2000.

SELECTED PUBLICATIONS:

Abdel-Salam, T. M., Tiwari, S. N., and Mohieldin, T. O., "Three-Dimensional Numerical Study of a Scramjet Combustor," The 40th AIAA Aerospace Sciences Meeting and Exhibit, Paper No. 2002-0805 Reno, Nevada, January 2002.

Tiwari, S.N., Taha, A. A., Abdel-Salam, T. M., and Mohieldin, T. O., "Supersonic Mixing and Combustion Characteristics in Scramjet Engines," Proceeding of the 15th International Symposium on Airbreathing Engines (XV ISABE), ISABE Paper No. 2001-1002, September 2001, Bagalore, India

Abdel-Salam, T. M., Tiwari, S.N., and Mohieldin, T. O., "Analysis of a Dual-Mode Scramjet Combustor," 37th AIAA/ASME/SAE/ASEE Joint Propulsion Conference, AIAA Paper No. 2001-3194, July 2001.

Abdel-Salam, T. M., Tiwari, S.N., and Mohieldin, T. O., "Dual-Mode Flowfield in a Scramjet Combustor," 35th AIAA Thermophysics Conference, AIAA Paper No. 2001-2966, June 2001.

Tiwari, S. N., Abdel-Salam, T. M., Taha, A. A., and Mohieldin, T. O., "Supersonic Mixing and Combustion in Scramjet Combustors Using Unstructured Grids," Proceedings of the 9th Annual Conference of the CFD Society of canada, Paper No. 2001-066, Waterloo, Ontario, Canada, May 2001.

Abdel-Salam, T. M., Tiwari, S.N., and Mohieldin, T. O., "Study of Dual-Mode Flowfield In Scramjet Combustors," 39th Aerospace Sciences Meeting , AIAA Paper No. 2001-0380, January 2001.

Abdel-Salam, T. M., Tiwari, S.N., Mohieldin, T. O., and S.K. Chaturvedi., "Numerical Study of the Effects of Ramp Swept Angle in Supersonic Mixing and Combustion," Proceeding of the 34th National Heat Transfer Conference, ASME Paper No. 2000-12028, Pittsburgh, PA, August 20-22, 2000 (On CD-Rom).

Mohieldin, T. O., Abdel-Salam, T. M., and Tiwari, S.N. "Numerical Study of Supersonic Mixing Using Unstructured Grid," Hyper-X program Office, NASA Langley Research Center, Hampton, Virginia, HX Report HX-781, March 2000.